Advanced Sciences and Technologies for Security Applications

Edward C. Morse

Analytical Methods for Nonproliferation

EXTRAS ONLINE

Springer

Advanced Sciences and Technologies for Security Applications

The series Advanced Sciences and Technologies for Security Applications focuses on research monographs in the areas of

- Recognition and identification (including optical imaging, biometrics, authentication, verification, and smart surveillance systems)
- Biological and chemical threat detection (including biosensors, aerosols, materials detection and forensics),

and

- Secure information systems (including encryption, and optical and photonic systems).

The series is intended to give an overview at the highest research level at the frontier of research in the physical sciences.

The editors encourage prospective authors to correspond with them in advance of submitting a manuscript. Submission of manuscripts should be made to the Editor-in-Chief or one of the Editors.

More information about this series at http://www.springer.com/series/5540

Edward C. Morse

Analytical Methods for Nonproliferation

Springer

Edward C. Morse
Department of Nuclear Engineering
University of California, Berkeley
Berkeley, CA
USA

Additional material to this book can be downloaded from http://extras.springer.com.

ISSN 1613-5113 ISSN 2363-9466 (electronic)
Advanced Sciences and Technologies for Security Applications
ISBN 978-3-319-29729-3 ISBN 978-3-319-29731-6 (eBook)
DOI 10.1007/978-3-319-29731-6

Library of Congress Control Number: 2016934945

© Springer International Publishing Switzerland 2016
This work is subject to copyright. All rights are reserved by the Publisher, whether the whole or part of the material is concerned, specifically the rights of translation, reprinting, reuse of illustrations, recitation, broadcasting, reproduction on microfilms or in any other physical way, and transmission or information storage and retrieval, electronic adaptation, computer software, or by similar or dissimilar methodology now known or hereafter developed.
The use of general descriptive names, registered names, trademarks, service marks, etc. in this publication does not imply, even in the absence of a specific statement, that such names are exempt from the relevant protective laws and regulations and therefore free for general use.
The publisher, the authors and the editors are safe to assume that the advice and information in this book are believed to be true and accurate at the date of publication. Neither the publisher nor the authors or the editors give a warranty, express or implied, with respect to the material contained herein or for any errors or omissions that may have been made.

Printed on acid-free paper

This Springer imprint is published by Springer Nature
The registered company is Springer International Publishing AG Switzerland

To my father, Robert A. Morse

Preface

This book has its roots in a course that was taught at Lawrence Livermore National Laboratory in the summer of 2005 entitled "Analytic Methods for Nonproliferation." This course was an intensive two-week experience for 22 graduate students from around the United States, with two foreign nationals included. The instruction was shared among 36 people, with three Berkeley faculty (Michael Nacht, Stan Prussin, and me), and 33 LLNL scientists. It was an impressive tour de force of scientific knowledge and technical capability in the area of nonproliferation and arms control. The Berkeley students followed up with another week on the Berkeley campus (a required element for them to get course credit through the university), which allowed a more "hands-on" approach to detection experiments, but without large quantities of weapons-grade material available. While at first it was thought that we would hold this class at Livermore in subsequent summer sessions, the tremendous amount of time, effort, and money required resulted in this being a one-off experience. It became clear that there was a need for this type of education on the Berkeley campus in a regular semester-long course. This resulted in a course at Berkeley with the same title as this book, which has now been taught in each of the 10 years since the 2005 course at Livermore. It became clear that the course needed a textbook, and this book is the result.

The level of this book assumes knowledge of some concepts of basic nuclear engineering, such as the cross-section concept and alpha, beta, and gamma decay. While some background on gamma and neutron transport is provided here, it is done so only to show some of the simplified forms of these mathematically rich subjects, which can lead to approximations that can be used to evaluate detection schemes in applications relevant to nonproliferation, arms control, and treaty verification. Thus the book is not intended as a replacement for standard textbooks such as Lamarsh (for neutron transport and reactor theory) and Knoll (for detector physics). The exercises in the book are best carried out with a mathematical processing language such as Mathematica or Matlab.

This book should be accessible to advanced undergraduates as well as graduate students in nuclear engineering or applied physics. There is a good bit of material outside the normal exposure that students in these disciplines have, such as seismology, chemical engineering, and materials processing techniques. Again, this book is not intended to be a substitute for stand-alone courses in these areas. Also, the chapter on public policy is not a replacement for a well-rounded education in this field, but rather to help a reader with an engineering or science background understand how the organizations responsible for global nuclear security fit together, and perhaps help potential job seekers understand what is out there.

I have many people to thank in the preparation of this manuscript. First, I would like to thank the 10 year's worth of graduate and undergraduate students who have helped shape the contents of this book through their input as students exposed to most of this material in the graduate and undergraduate courses in this area at Berkeley. I would also like to thank some experts in the fields covered in this book who have given certain chapters a critical review. These include Mike Moran "Nuclear Explosives" and "Nuclear Testing," Rhonda Righter "Detection Statistics," Joon-Hong Ahn "The Nuclear Fuel Cycle," and Dennis Slaughter "Active Interrogation." I am grateful for the conversation with Siegfried Hecker regarding the plutonium metallurgy material in "Nuclear Forensics". Also, I am grateful for the data and insight from Rick Norman and for the data from Ryan Pavlovsky.

I am grateful for careful editing of the manuscript by Lisa Zemelman and for encouragement and moral support from many friends, especially Wendy Reid.

Berkeley, CA, USA Edward C. Morse
December 2015

Contents

Acronyms

ARIX	(Russian) Radio-xenon measurement device
AUC	Area Under Curve: metric for ROC performance
AVLIS	Atomic Vapor Laser Isotope Separation
CANDU	CANada Deuterium Uranium: heavy water reactor
CEC	Center for Export Controls
CITS	Center for International Trade and Security
CLLB	$Cs_2LiLaBr_6:Ce^{3+}$: scintillator material
CLLC	$Cs_2LiLaCl_6:Ce^{3+}$: scintillator material
CLYC	$Cs_2LiYCl_6:Ce^{3+}$: scintillator material
CNS	Center for Nonproliferation Studies
CTBT(O)	Comprehensive Test Ban Treaty (Organization)
DHS	Department of Homeland Security
DNDO	Domestic Nuclear Detection Office
DoD	Department of Defense
FSU	Former Soviet Union
FWHM	Full Width at Half Maximum (probability distributions)
GYGGAG	$Gd_{1.5}\ Y_{1.5}Ga_{2.2}Al_{1.8}O_{12}:Ce$ (scintillator material)
HEU	Highly Enriched Uranium
ICPMS	Inductively Coupled Plasma Mass Spectrometry
ICRP	International Commission on Radiological Protection
IMS	International Monitoring System
ISIS	Institute for Science and International Security (ISIS)
ITDB	Illicit Trafficking Database
MCNP	Monte Carlo N-Particle Transport Code
MIRV	Multiple Independent Re-entry Vehicle
MLIS	Molecular Laser Isotope Separation
MVRDS	Machine Vision Radiation Detection system
MWd/THM	Megawatt-days per Ton of Heavy Metal
NATO	North Atlantic Treaty Organization
NNSA	National Nuclear Security Administration
NNWS	Non-Nuclear Weapon States

NORM	Naturally Occurring Radioactive Material
NRF	Nuclear resonance Fluorescence
NTI	Nuclear Threat Initiative (NTI)
NWS	Nuclear Weapon States
Pu300/600/900	Tests to determine properties of plutonium (numbers are gamma energies in keV)
PUREX	Plutonium Uranium Redox EXtraction
REM	Radiation Equivalent Man
RF	Russian Federation
ROC	Receiver Operating Characteristic
SAUNA	(Swedish) Radio-xenon measurement system
SIPRI	Stockholm International Peace Research Institute
SNM	Special Nuclear Material
SOFAR	Sound Fixing and Ranging
SPALAX	(French) Radio-xenon measurement system
SWU	Separative Work Unit
TENORM	Technologically Enhanced Naturally Occurring Radioactive Material
TIMS	Thermal Ion Mass Spectrometry
UN	United Nations
USSR	Union of Soviet Socialist Republics

Introduction

Abstract This chapter describes the international development of nuclear weapons technology, the early history of the US-USSR arms race, and the proliferation of nuclear weapon technology into other countries. Some of the motivation for other countries to obtain nuclear weapons is also described. The early efforts at controlling this nuclear weapons buildup through international diplomacy efforts is then discussed. Efforts at nuclear weapon and stockpile reduction by the US and Russian Federation, through treaties such as START are described. Next, the possibility of non-state groups such as terrorist organizations procuring nuclear weapon technology is outlined. Incidents involving interdiction of nuclear material, in a database maintained by the International Atomic Energy Agency, are outlined. The commonality of nuclear smuggling with other criminal activities, such as human trafficking and drug smuggling, is discussed. Regions particularly vulnerable to nuclear smuggling are noted.

1 Nuclear Proliferation

Since July 1945 there have been weapons with a destructive power that exceeds that of all weapons which had come before by many orders of magnitude. These weapons utilize energy release from atomic nuclei. The awesome and terrifying power of these weapons has stimulated a re-thinking of what the outcome of isolated acts of violence can be. While the United States government and its post-World War II allies had sole access to these weapons at first, there became rather quickly a "nuclear club" of other nations with their own arsenal of nuclear weapons and stockpiles of nuclear weapon materials (see Fig. 1). Many countries had leaders that believed that nuclear weapons were key to their survival. Nuclear weapon production efforts, coupled with other related efforts such as delivery systems, early warning systems, and monitoring programs, often nearly bankrupted countries as they "went nuclear".

Five early developers of nuclear weapon technology are known as "Nuclear Weapon States" in the Nuclear Non-Proliferation Treaty, ratified under the aegis of the United Nations and in force since 1970 (see Appendix A). These are the United States, the Russian Federation, the United Kingdom, France, and China. Since that

E.C. Morse, *Analytical Methods for Nonproliferation*, Advanced Sciences and Technologies for Security Applications, DOI 10.1007/978-3-319-29731-6_1

Fig. 1 Political cartoon by Herbert Block depicting Nikita Khruschev and John F. Kennedy trying to keep the lid on the Pandora's box of nuclear weapon proliferation. A 1962 Herblock Cartoon, ©The Herb Block Foundation

time, other nations have developed nuclear capability, including India, Pakistan, North Korea, Israel (unofficially), and South Africa. During the past decade, other countries including Libya, Iraq, and Iran have been suspected of trying to develop nuclear weapons. South Africa, on the other hand, has eliminated its nuclear weapon capability.

Today (2015) there are approximately 16,300 nuclear weapons stored at 98 sites in 14 countries worldwide [10]. In addition to the nine producers of nuclear weapons listed above, there are five more NATO allies with about 180 American-made nuclear weapons in US custody at airbases on their soil: these are Belgium, Germany, Italy, Netherlands, and Turkey. Table 1 gives a synopsis of the total nuclear weapons in

Table 1 Estimated worldwide nuclear weapon inventories as of August 2014

Russia	8000
United States	7300
France	300
China	250
United Kingdom	225
Israel	80
Pakistan	100–120
India	90–110
North Korea	<10

From [10]

stockpiles and in deployment. It should be noted that some arms reduction activities are in progress; the Russian number includes 3,700 weapons slated for dismantlement and the American number includes 2,540 to be dismantled.

There are several different reasons why a state may develop nuclear weapons [12]. The first and probably most common reason is that the state fears that an adversary is developing, or already has developed, nuclear weapons capability and poses a current or future nuclear threat. The development of nuclear weapons in the United States was largely motivated by the threat that Germany was involved in a similar effort during World War II. Germany was defeated before the American bomb was ready, but the decision to deploy the bomb on Japan could be considered as a transference of that threat. Similarly, the USSR felt that the American bomb was a destabilization of a power balance, and Joseph Stalin ordered the rapid development of a Soviet nuclear weapon. As former U.S. Secretary of State George Shultz stated in a 1984 article, “Proliferation begets proliferation” [14].

However the development of nuclear weapons can also serve a political purpose. A leader or a political party may develop nuclear weapons without a clear threat from other nations, hoping to establish themselves as showing great leadership in the eyes of the people. Examples in the current political climate of this approach might best fit Iran and North Korea. In both cases religion and ideology take on a more prominent role than an actual threat of invasion by a neighboring country or a superpower. Indira Gandhi, prime minister of India in the 1970 s and 1980s, denied that the 1974 nuclear test was done for political gain, although she admitted that the 1974 nuclear test “…would have been useful for elections. But we did not have any” [5].

A third reason to develop nuclear weapons is the perception that possessing nuclear weapons puts that country in a position of prestige and that the country gains regional and international respect by doing so. Charles de Gaulle, the former president of France, was known to have communicated with his leadership that having nuclear capability was a requirement that France be viewed as a great country, even though France was a member of NATO and would be protected under NATO’s nuclear umbrella [6].

Apart from developing nuclear weapons, the tests of these weapons present another facet of the political and global security issues surrounding nuclear weapons. While the development of nuclear weapons may take years, test shots can be timed to the microsecond, and often this timing is done to satisfy some agenda. While India conducted its first test in 1974, it did not test again until 1998. But significantly, the 1998 tests were done just weeks before the first Pakistan test (May 11 for India, May 28 for Pakistan).

There has been a downward trend in the total number of nuclear weapons on the planet since the mid-1980s. This has been largely due to reductions in the U.S. and former Soviet Union stockpiles. There have been calls for nuclear disarmament from many statesmen, foreign policy experts, and even many former weapon scientists. So far eight Nobel Peace Prizes have been awarded for efforts related to nuclear disarmament [11].

2 The Threat of Nuclear Terrorism

The threat of nuclear weapon production and usage should be considered not only from the viewpoint of new nations developing nuclear weapons but also the possibility that terrorist groups might try to acquire them as well. There is some evidence that terrorist organizations have tried, or at least declared their intention of trying, to obtain nuclear material and build weapons with it. On May 29, 1998, Osama bin Laden, then leader of the terrorist group Al-Qaeda, released a statement entitled "The Nuclear Bomb of Islam," in which he stated that "it is the duty of Muslims to prepare as much force as possible to terrorize the enemies of God" [4]. Subsequently Al-Qaeda members have attempted to purchase stolen nuclear material [3]. Terrorist groups in the North Caucasus (including Chechnya) and a Japanese cult known as Aum Shinrikyo, infamous as the group behind the sarin gas attacks in the Tokyo subway system in 1995, have made similar attempts at securing weapon-grade material as well [3].

A common cultural stereotype is to think of terrorist groups being comprised of poor, uneducated people with no other place to turn, making unsophisticated makeshift weapons with black powder and ball bearings. Both Al-Qaeda and Aum Shinrikyo serve as counterexamples to that notion. In the case of Al-Qaeda, the leader was a man with a degree in engineering born into a billionaire's family. The organization included assistance from Pakistani nuclear experts. While the leader of Aum Shinrikyo was a yoga instructor, the cult collected a wide following of individuals from the computer and high-tech industries in Japan, and its inner circle included a Ph.D. in microbiology, an astrophysicist, and a chemist. The organization owned several businesses and had assets of around $1 billion [13]. The businesses, some of which were in the food sector, may have helped mask the true purpose for purchasing expensive chemical equipment ultimately used for manufacturing sarin and other agents.

This points to the historical existence of motive for nuclear terrorism. What about the opportunity factor? How much material is out there and how well-guarded is this material? The current estimate is that there is a global inventory of 1390 metric tons of highly enriched uranium (HEU) and 494 metric tons of plutonium [9]. Figures 2 and 3 show the distribution of this material by country; about 93 % of the HEU resides in either the US or Russia, and 54 % of the plutonium stockpile is in the US or Russia as well. (In the case of plutonium, the military and civilian quantities are combined. This can be somewhat misleading, because much of the civilian material is the result of transmutation from uranium in reactors at high irradiation levels, making material that is more difficult to use in weapons, as explained in the next chapter.)

Former Secretary-General of the IAEA and Nobel Prize winner Mohamed ElBaradei has stated that "Nuclear terrorism is the most serious danger the world is facing [1]. Almost all world leaders have voiced similar opinions. This has led to repeated calls to the UN Security Council to act on the problem of nuclear terrorism. The Security Council has passed many resolutions on this subject. In one of the more

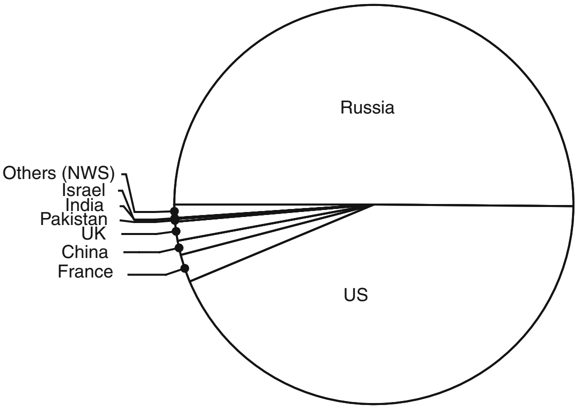

Fig. 2 Pie chart showing distribution of HEU among nations. Note that NWS = non-weapon states. Data from [9]

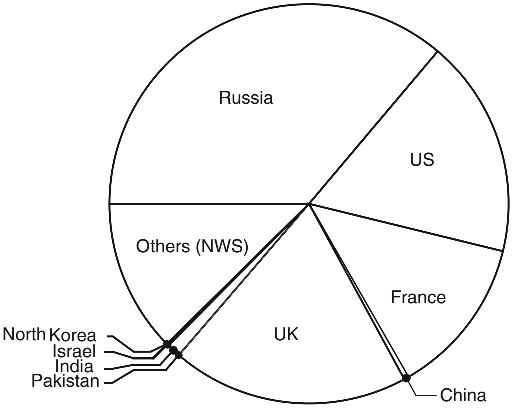

Fig. 3 Pie chart showing distribution of Pu among nations. Note that NWS = non-weapon states. Data from [9]

recent of these, Article 24 of the UN Security Council Resolution 1887 (2009) "Calls upon Member States to share best practices with a view to improved safety standards and nuclear security practices and raise standards of nuclear security to reduce the risk of nuclear terrorism, with the aim of securing all vulnerable nuclear material from such risks within 4 years" [16]. The 4 years are now up, but the problem of nuclear terrorism has not gone away.

3 Interdiction of Nuclear Material

The International Atomic Energy Agency (IAEA) maintains a list of incidents involving improper possession and movement of nuclear material and radioactive sources, known as the IAEA Incident and Trafficking Database (ITDB) [8]. The 2014 report outlines 2477 incidents of this type reported to IAEA over a period from January 1993 to December 2013. Of these, 424 incidents involved illegal possession, unlawful transportation, attempts to sell material, and related criminal activities. Of these, 16 incidents involved HEU or plutonium. Of the total number of cases, 664 involved theft or loss of nuclear or radioactive material, and 1337 cases involved other unauthorized activities, such as unauthorized disposal of radioactive materials or discovery of uncontrolled sources.

Of the 16 cases involving HEU or plutonium, the majority involved gram quantities of material, but a small number involved kilogram quantities. Some of the gram-quantity seizures have been thought of as "sales samples", where the seller might have represented that he/she might have a great deal of the same material elsewhere and wanted to negotiate a price for a large quantity before showing it. In other cases, the packaging of the material (such as glass ampoules and other laboratory methods) probably indicated that the material was stolen from a production quality control laboratory, out of the normal chain of custody at the time of the theft, and might never have been missed. In some cases, nearly identical samples have turned up at different locations, implying that there is a cache of this material at some other location. For example, a seizure in France in 2001 involved a sample that was almost identical to one found in Bulgaria 2 years before [2, 7, 15]. In both cases there was a link back to Moldova [17].

If one examines other criminal activities such as drug trafficking, human trafficking, and other types of contraband movement and smuggling, one finds that nuclear smuggling can occur along similar lines, with similar routes and sometimes carried out by some of the same people. The French seizure involved a man who was "well known as a crook by the police" [2]. Reference [17] points out that an unusually large number of incidents have occurred in the Black Sea region (Georgia, Russia, Bulgaria, and Moldova have had confirmed incidents involving HEU trafficking), an area associated with a great deal of the drug smuggling and human trafficking to and from western Europe. Turkey has a special role to play in the nuclear smuggling scenario. It has served as a destination for nuclear materials, but probably not as a final resting place. With close ethnic and cultural ties to the Middle East, Turkey has more than 900,000 visitors a year from Arabic countries. Thus Turkey might serve as the ideal transfer point for terrorist groups operating in the Middle East to connect with traffickers in nuclear materials coming in from the Black Sea region.

References

1. Allison G (2010) Nuclear Terrorism Fact Sheet, Policy memo, Belfer Center for Science and International Affairs. Harvard Kennedy School. http://belfercenter.ksg.harvard.edu/publication/20057/nuclear_terrorism_fact_sheet.html. Accessed 24 Oct 2014
2. Baude S, Chartier B, Mariotte F, Masse D, Kimmel D, Peron H, Tilly D (2008) The French response in cases of illicit nuclear trafficking: lessons learned from a real case. In: International Conference on Illicit Nuclear Trafficking: Collective Experience and the Way Forward, pp 363–371. http://www-pub.iaea.org/MTCD/publications/PDF/Pub1316_web.pdf
3. Bunn M, Morozov Y, Mowatt-Larssen R, Saradzhyan S, Tobey W, Yesin V, Zolotarev R (2011) The U.S.-Russia Joint Threat Assessment on Nuclear Terrorism, Belfer Center for Science

and International Affairs. Harvard University. http://belfercenter.ksg.harvard.edu/files/Joint-Threat-Assessment%20ENG%2027%20May%202011.pdf. Accessed 24 Oct 2014

4. CNN Library: Osama bin Laden Fast Facts. http://www.cnn.com/2013/08/30/world/osama-bin-laden-fast-facts/. Updated 12:25 PM EST, Tue December 24, 2013. Accessed 24 Oct 2014
5. Goldblat J (1985) Stockholm International Peace Research Institute: Non-Proliferation: The why and the wherefore. Stockholm International Peace Research Institute, Taylor and Francis. http://books.google.com/books?id=eIKPAAAAMAAJ
6. Gordon P (1999) Cold war statesmen confront the bomb: nuclear diplomacy since 1945, chapter 10: Charles de Gaulle and the nuclear revolution. Oxford University Press. doi:10.1093/0198294689.001.0001
7. Hoskins RA (2008) Threats & risks in trafficking. IAEA Bull 49(2). http://www.iaea.org/Publications/Magazines/Bulletin/Bull492/49203543236.html
8. International Atomic Energy Agency: IAEA incident and trafficking database (ITDB) 2014 fact sheet. http://www-ns.iaea.org/downloads/security/itdb-fact-sheet.pdf. Accessed 27 Oct 2014
9. International panel on fissile material: “Fissile material stocks”. http://fissilematerials.org. Accessed 26 Oct 2014
10. Kristensen H, Norris RS (2014) Worldwide deployments of nuclear weapons, 2014. Bull Atom Sci 70. doi:10.1177/0096340214547619
11. Nobelprize.org: the development and proliferation of nuclear weapons. http://www.nobelprize.org/educational/peace/nuclear_weapons/readmore.html. Accessed 20 Oct 2014
12. Sagan SD (1996/1997) Why do states build nuclear weapons? Three models in search of a bomb. Int Secur 21:54–86
13. Senate government affairs permanent subcommittee on investigations: global proliferation of weapons of mass destruction: a case study on the Aum Shinrikyo, october 31, 1995 staff statement. http://fas.org/irp/congress/1995_rpt/aum/
14. Shultz G (1984) U.S. Dept. of State Office of Public Communication, Editorial Division: preventing the proliferation of nuclear weapons: november 1, 1984. Current policy. U.S. Department of State, Bureau of Public Affairs, Office of Public Communication, Editorial Division. http://books.google.com/books?id=79ed3mOcphMC
15. The Nuclear Threat Initiative (NTI): five grams HEU seized in Paris. http://www.nti.org/analysis/articles/five-grams-heu-seized-paris/. Accessed 01 Nov 2014
16. United Nations Security Council: resolution 1887 (2009). http://www.un.org/en/ga/search/view_doc.asp?symbol=S/RES/1887(2009). Accessed 27 Oct 2014
17. Zaitseva L, Steinhäusler F (2014) Nuclear trafficking issues in the Black Sea region. In: EU Nonproliferation Consortium: Nonproliferation Papers, vol 39. Accessed 03 Nov 2014

Nuclear Explosives

Abstract The history of the development of the first nuclear devices in the US are discussed from the standpoint of both the science and the politics behind this decision to move towards developing such devices. The Hiroshima and Nagasaki weapons were developed through completely different processes–one with uranium and one with plutonium. The different paths are compared and contrasted. The basic physics of nuclear weapons is discussed from the vantage point of the now-declassified Los Alamos Primer. The development of fusion-boosted weapons is also described, along with the historical backdrop of the Cold War and the arms race in the 1960s and beyond. The impact of the dismemberment of the Soviet Union on the availability of weapons-usable nuclear material is outlined, and the classification of nuclear material is described from the viewpoint of various national and international regulatory bodies.

1 History

1.1 The Dawn of the Atomic Age

The Atomic Age officially started with the test and subsequent deployment of fission-based nuclear explosives by the United States in 1945. The first nuclear attack came on the largely civilian population of Hiroshima, Japan on August 6, 1945. The death toll is uncertain, with estimates of 70,000 killed immediately by the blast and at least 20,000 more dead from burns and radiation sickness over the next few months. On August 9, 1945, a second nuclear explosive was deployed at Nagasaki, Japan, resulting in a cumulative death toll of between 60,000 and 80,000. While these numbers are small compared to the total deaths in World War II ($\sim$60 million), this demonstration of nuclear explosives as the most terrifying and lethal weapons in mankind's history has changed the world permanently.

The possibility of a weapon based on nuclear fission had occurred to many physicists after the discovery of nuclear fission. An experiment in Germany by Hahn and Strassman in 1938 showed that bombardment of uranium with neutrons created enormous energy release compared to other known reactions and created reaction

E.C. Morse, *Analytical Methods for Nonproliferation*, Advanced Sciences
and Technologies for Security Applications, DOI 10.1007/978-3-319-29731-6_2

products such as barium. By 1939, Lise Meitner and Otto Frisch gave a theoretical explanation for this process as the breakup of the heavy uranium nucleus due to the its large coulombic forces, and the production of two lighter nuclei as a result. An experiment by Enrico Fermi and Leo Szilard at Columbia University in the United States showed that more than one neutron was produced per neutron-induced fission, thus paving the way for a nuclear chain reaction. Szilard and Eugene Wigner then approached Albert Einstein and asked if Einstein would sign a letter addressed to then-President Franklin Roosevelt, advising him to develop uranium resources and technology for development of a nuclear explosive. The letter was sent on August 2, 1939. Roosevelt asked Lyman Briggs of the National Bureau of Standards to chair a committee (the "Advisory Committee on Uranium") to examine the possibility for a nuclear explosive. In November of that year, the committee reported back to Roosevelt that the fission concept was very likely to yield a bomb of immense explosive power. Meanwhile, parallel efforts were going on in England, and Frisch and Rudolf Peierls had calculated the critical mass for a ^{235}U device to be about 10 kg, much smaller than other prevailing estimates of the day. While this result was ignored in the United States, an Australian physicist, Mark Oliphant, working in Birmingham, England at the time, visited Berkeley, California in 1941 and communicated this result to Ernest Lawrence, who then became a believer in the prospects of a fission explosive. Lawrence then persuaded several key scientists in the government to start a large-scale program, and Roosevelt approved what would become known as the Manhattan Project in October 1941. By the summer of 1942, large numbers of physicists gathered at the University of Chicago and at Berkeley to discuss theoretical aspects of nuclear fission. In order to preserve secrecy about the project, most participants were relocated to Los Alamos, New Mexico starting in late 1942, in a new secret laboratory under the direction of J. Robert Oppenheimer from Berkeley. Overall direction of the Manhattan project was done by Leslie Groves of the U. S. Army.

Another important development had occurred in 1941 in Berkeley. Nuclear chemist Glenn Seaborg and his group had isolated a new element, plutonium. It was produced by exposing ^{238}U nuclei to neutrons. It quickly became apparent that this new element also had a high probability of fissioning under exposure to neutrons, similar to ^{235}U. This made it clear that there would be two paths to developing the critical material for an atomic bomb: either by enriching uranium to obtain a product containing mostly ^{235}U or by producing plutonium in a fission reactor. By late 1942, Fermi and Szilard had demonstrated the first nuclear reactor at the University of Chicago. By early 1943, a site at Hanford, Washington was commissioned to build plutonium production reactors.

An initial approach to uranium isotope production was developed at Berkeley using a method based on ion mass spectrometry and called the Calutron. Large-scale versions of these machines were built at Oak Ridge, Tennessee and known as the Y-12 plant. The magnet coils for these machines were made with pure silver conductors, representing about 395 million troy ounces in silver (worth roughly $ 10 billion in today's market) on loan from the repository at West Point, New York.

(After the war, the silver was returned to West Point, and gaseous diffusion replaced electromagnetic separation.)

The difficulty of producing adequate quantities of weapon-grade uranium resulted in the decision not to test the uranium weapon, which was ultimately used at Hiroshima and called Little Boy. However, the design of Little Boy was not sophisticated, and relied upon the combination of two subcritical components by firing an explosive behind one of the components, causing it to mate with the other with a linear trajectory. This "gun-type" design was very heavy (almost five tons), required a great deal of enriched uranium (64 kg of 80 % enriched U), and was inefficient (its nuclear yield was around sixteen kilotons TNT equivalent, or a little over one percent burnup of its nuclear fuel).

The Nagasaki weapon, known as Fat Man, was a very different device. It was made with plutonium produced mostly in reactors at Hanford. It also used a more sophisticated system of implosion of the subcritical components in a symmetrical way. The timing of the shock waves had to be carefully controlled, and the design of the explosive lens had to be carefully worked out. However, there were significant advantages to the Fat Man design. Firstly, it used a much smaller amount of fissile material (only about 6.2 kg, less than a tenth of Little Boy), secondly, that material could be plutonium, which was easier to obtain at the time, and thirdly, the device would only detonate if all of the chemical explosives worked together, so that an accidental criticality during handling was very unlikely. Enough plutonium was available at the time to perform a test before the actual deployment in Japan, and this test (of a device called "Gadget") was performed at the White Sands test site near Alamogordo, New Mexico on July 16, 1945. The code name for this test was Project Trinity. The test was successful, and produced about 20 kilotons of TNT equivalent energy. Preparations began immediately following this test to deploy both Little Boy and Fat Man in Japan, and both devices were used three weeks later.

At this point it is interesting to consider the resources that were available for this endeavor. On the one hand, financing for this project was practically unlimited. Almost $2 billion (equivalent to about $25 billion today) was spent on the Manhattan Project from its start until August 1945, an unprecedented amount for a government-supported research and development program at that time. The human capital for the project was also impressive, representing some of the brightest physicists, chemists, mathematicians, and engineers on the planet. But compared to today's technology, one can see some great disadvantages. "Computers" were not computers in the modern sense, but were humans using mechanical calculators, and only late in the project were there mechanical calculators using punched cards. Implosion calculations took months at a time. The transistor was not invented until 1948, and electronic systems in 1945 used vacuum tubes, gas-filled switch tubes, and mechanical relays. Gamma-ray spectroscopy was in its infancy (The Manhattan Project resulted in the invention of the scintillation detector in 1944, by Samuel Curran at Berkeley), and solid-state germanium detectors came along much later. High-speed photography was also developed out of necessity for the project, and high-speed radiography did not exist. Conjectures about the difficulty for small countries or terrorist organizations to stand up a nuclear weapon development program, seventy years later, should consider these changes.

1.2 The Cold War and the Arms Race

While American nuclear experts knew that the Soviet Union would be trying to develop nuclear explosives, it came as a surprise that the first successful Soviet test would happen as soon as 1949, when on August 29 the Soviets detonated a device they referred to as "First Lightning"(nicknamed "Joe-1" in the West, after Joseph Stalin). The test was performed at Semipalatinsk in what is now Kazakhstan. The design was an implosion-type plutonium device with a 22 kiloton yield and was almost identical to Gadget and Fat Man. In retrospect this was not so surprising once the extent of espionage at Los Alamos became known. This test also demonstrated the beginning of airborne radioactivity monitoring to detect nuclear testing, as the United States used a specially fitted B-29 aircraft with radioactivity-sensing equipment, which picked up a plume of radioactivity about a week later when the plume appeared east of the Kamchatka peninsula.

The race was then on to develop a large arsenal of nuclear weapons, and to develop more powerful and more easily deployable designs. Starting with early meetings in Berkeley in 1942, Edward Teller had argued for the development of the "Super", which would exploit nuclear fusion reactions

$$^2_1\mathrm{H} + ^2_1\mathrm{H} \to \mathrm{n} + ^3_2\mathrm{He}$$

$$^2_1\mathrm{H} + ^2_1\mathrm{H} \to \mathrm{p} + ^3_1\mathrm{H}$$

$$^2_1\mathrm{H} + ^3_1\mathrm{H} \to \mathrm{n} + \alpha$$

The last reaction makes 17.6 MeV of energy, much less than the 200 MeV released in a fission event, but with three times the yield per gram of material, and is a net producer of fast neutrons, which can in turn be used to trigger more fission reactions. The two isotopes of hydrogen used, ^{2}H and ^{3}H, known as deuterium and tritium, are easily obtainable: deuterium exists as a minority isotope in ordinary water (fully deuterated water is called heavy water), and tritium can be manufactured in a nuclear reactor by neutron absorption on lithium. (Or the tritium can be created at the time of detonation by introducing lithium deuteride into the device.) While Oppenheimer at Los Alamos did not encourage the development of the Super, renewed interest came after the detonation of Joe-1. After some failed attempts at testing some fusion-boosted designs, a successful (deuterium-only) test was done on November 1, 1952 at the Eniwetok Atoll in the South Pacific. The test, code-named Ivy Mike, produced a little over ten megatons of yield. However, this test involved a device that was far too massive (82 tons) to be used as a weapon.

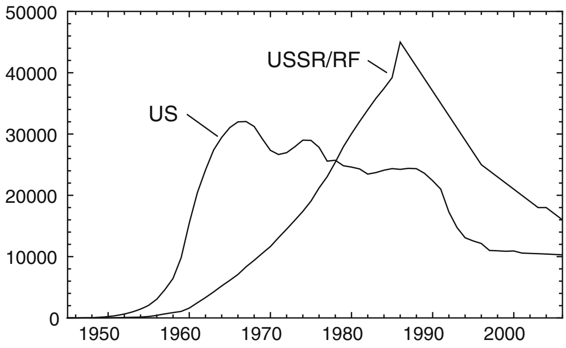

Fig. 1 Stockpile size per year for the United States and Soviet Union/Russian Federation, 1945–2006. Data from [6]

Soviet tests progressed along similar lines, culminating in the first detonation in the megaton range by November 22, 1955. By 1961, the Soviets had assembled a device nicknamed "Tsar Bomba", which was detonated on the remote Arctic island of Novaya Zemlya on October 30, with a yield of 58 megatons.

Meanwhile, the buildup of field-usable nuclear weapons began to grow and become more sophisticated. A typical example was the W-7 device developed in the United States in 1952, which weighed only 400 kg and could be placed on a small short-range missile. As shown in Fig. 1, inventories grew exponentially in the 1950s in the US, with a slower but similar rise in the Soviet Union, continuing upward until the mid-1980s.

Other members were added to the "nuclear club". Great Britain, a partner along with Canada in the U.S. nuclear program during World War II, developed its own arsenal of nuclear weapons starting in 1953. France made its first nuclear test in 1960, and had a nuclear weapon by 1964. China tested in 1964 and started weapon production within the year. While not openly disclosing any details, Israel is believed to have developed nuclear capability, starting in 1967 [10]. In 1974 India tested ("Smiling Buddha") [8] and began putting weapons into stockpile after that time. Pakistan probably started a program shortly after that, and under the leadership of Abdul Qadeer Khan by 1981, and performed cold tests in about 1983. They tested for the first time on 28 May 1998 [1]. A nuclear program was started and later abandoned in South Africa [7]. More recently North Korea has developed a nuclear program, with a low-yield test in 2006 but with substantially higher-yield tests in 2009 and 2013 [2].

1.3 The Fall of the Soviet Union

In 1985, The General Secretary of the Soviet Politburo, Mikhail Gorbachev, announced that the Soviet economic system was not sustainable and called for vast reforms of the Soviet system. Ultimately this led to the breakup of the Soviet Union starting in 1989, followed by complete dissolution of the Soviet Union in 1991. Some of the former Soviet countries possessed nuclear weapons at that time. Of particular interest were Ukraine and Kazakhstan, which had approximately 5000 and 1400 devices respectively in 1991 at the time of the dissolution. All of these weapons were returned to Russia by 1997. However, questions remain about weapons-usable nuclear materials stored (by a DOE estimate in 1998) at over 150 facilities at 53 sites, in Russia and former Soviet republics. Of continuing interest is the former Soviet test site of Semipalatinsk in Kazakhstan, which covers 7000 square miles. The lack of recordkeeping and the lack of site security over this vast area form a risky combination of factors.

2 Device Physics

The treatments given here closely follow the now-unclassified document known as the Los Alamos Primer, distributed at Los Alamos in 1943 as part of an indoctrination course for scientists working on the Manhattan Project [9].

2.1 Critical Mass

The smallest size for a fission explosive is given by neutron transport theory. For a complete derivation of the theory, consult a standard textbook such as Lamarsh [4].

We assume that we have a spherical assembly of pure ^{235}U with radius a. The equation concerning the rate of growth of the fast neutron population is given by:

$$\dot{\mathrm{n}} = \mathrm{D}\Delta\mathrm{n} + \left(\frac{\nu - 1}{\tau}\right)\mathrm{n}. \tag{1}$$

Here n is the number density of neutrons in the assembly, D is the diffusion coefficient and is equal to $(1/3)\lambda_{\mathrm{tr}}\mathrm{v}$, where λ_{tr} is the mean free path for the neutrons, and v is the average speed of the neutrons. The mean free path is given by the number density in the fuel material $\mathrm{n_f}$ and the total cross section $\Sigma_t = \mathrm{n_f}\sigma_{\mathrm{t}}$ as

$$\lambda_{\mathrm{tr}} = \frac{1}{\Sigma_{\mathrm{t}}} = \frac{1}{\mathrm{n_f}\sigma_{\mathrm{t}}} \tag{2}$$

and the quantity ν is the average number of neutrons produced per fission event. The quantity τ is the average time for a neutron to cause another fission event with a fuel nucleus after production and is given by

$$\tau = \frac{1}{\Sigma_{\mathrm{f}}\mathrm{v}}. \tag{3}$$

Here $\Sigma_f = n_f\sigma_f$, with σ_f as the fast fission cross section in the material. The operator Δ is the laplacian operator, sometimes written as ∇^2. We can separate the variables in this equation so that

$$n(\mathbf{r}, t) = T(t)R(r) \tag{4}$$

where we assume spherical symmetry. The time dependence is then given by

$$T(t) = \exp\left(\frac{\nu' t}{\tau}\right) \tag{5}$$

with

$$\Delta R(r) + \frac{-\nu' + \nu - 1}{D\tau} R(r) = 0 \tag{6}$$

If we solve this equation with a boundary condition $n(a) = 0$, we find that the lowest order solution is given by

$$R(r) = n_0 \frac{\sin(\pi r/a)}{\pi r/a}$$

and then the operator Δ is replaced by $-(\pi/a)^2$. However, the choice of boundary condition $n(a) = 0$ isn't quite correct; the actual boundary condition requires a correction to account for the free streaming of neutrons at the boundary, with no returning flux. A simple way to handle this is to add an "extrapolation length" to the actual radius, giving an effective radius as

$$a' = a + \delta \tag{7}$$

for planar geometries, $\delta \approx 0.71\lambda_{tr}$, and we assume that this is approximately correct for the spherical problem. The critical size (for which $\nu' = 0$) is given by

$$(a + \delta)^2 = \frac{\pi^2}{3\Sigma_f \Sigma_t(\nu - 1)} \tag{8}$$

and then the critical mass $M_c = (4/3)\pi\rho a^3$.

We can now calculate the critical mass for ^{235}U as an example. Using modern values for ^{235}U for fast neutrons, $\nu = 2.70$, $\Sigma_f = 0.06192$ cm^{-1}, $\Sigma_t = 0.2160$ cm^{-1}, and $\rho = 18.7$ g cm^{-3} gives

$$M_c = 52 \text{ kg}$$

(The original Los Alamos number was 60 kg, quite close considering the error bars on the data at that time.)

A similar calculation for ^{239}Pu ($\nu = 3.10$, $\Sigma_f = 0.0936$ cm^{-1}, $\Sigma_t = 0.2208$ cm^{-1}, $\rho = 15.92$ g cm^{-3}) gives an much smaller value of $M_c = 11.0$ kg. Note that in general, the critical mass scales as

$$M_c \propto \frac{1}{\rho^2[\sigma_t \sigma_f (1-\nu)]^{3/2}} \tag{9}$$

Note especially the $1/\rho^2$ dependence, showing that significantly less material is required for an implosion-type device.

The above calculations assume that only one species is present. The crude one-speed diffusion theory shown here works fairly well for these examples because the fission cross section is roughly constant over the fast neutron energy spectrum, and the details of more complex scattering physics, such as angular dependence of the scattering and inelastic scattering, are less important. For the case of ^{235}U and ^{238}U at arbitrary enrichment, this is no longer the case, because the neutron-induced fission of ^{238}U is a threshold process with a minimum energy required of about 1 MeV, which is inside the range of energies of neutrons produced in fission. (The neutron energy spectrum from fission is a roughly maxwellian spectrum with a "temperature" of about 1.3 MeV.) Inelastic scattering can lower the fission-produced neutron energy to below the fission energy threshold for ^{238}U in one collision.

For this type of neutronics problem, one is better served by using a Monte Carlo computer code such as MCNP to calculate the critical mass. An example of such a calculation, for uranium spheres at various enrichment levels, is shown as Fig. 2. This calculation shows that the critical mass required goes to very impractical values for enrichments below 15 %, and that no fast assembly (i.e. a bomb) can be made with material at standard power plant nuclear fuel enrichments of 3–4%.

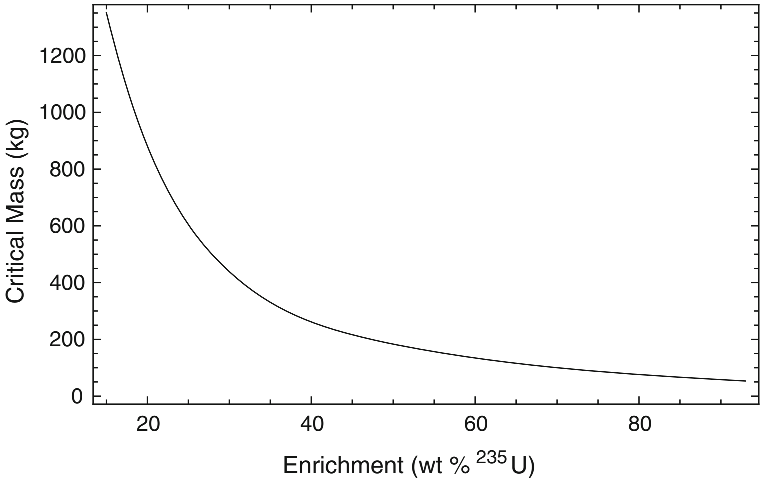

Fig. 2 Critical mass versus enrichment for bare uranium spheres. Data from [3]

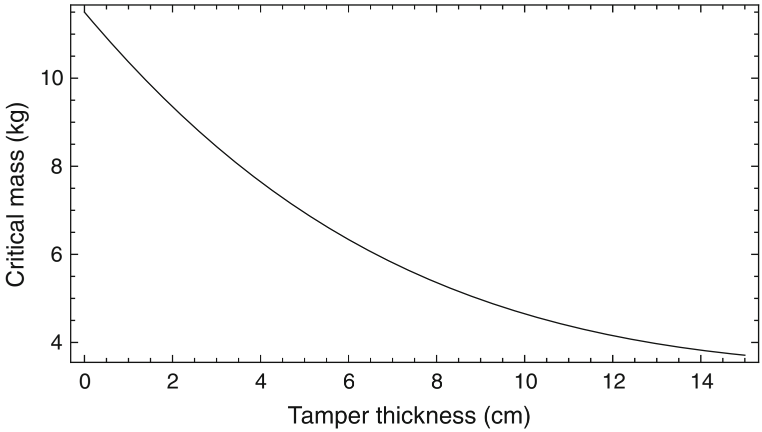

Fig. 3 Critical mass versus Be tamper thickness for weapon-grade Pu. Data from [3]

One further detail of weapon construction needs to be considered as part of a discussion about criticality, however. That is the possibility that a second non-fissile zone may be added to the outside of the fissile material. This is called a "tamper" and it serves two purposes. Firstly, neutrons leaving the fissile zone into the tamper will be scattered and thus some of them will re-enter the fissile zone, or be "reflected" back into the fissile zone. Secondly, by its mere inertia, the tamper slows the expansion of the fissile zone when it is supercritical, thus prolonging the time of exponential growth and increasing the yield. Tamper criticality calculations are also more complex than can be derived accurately with one-speed diffusion theory, but again, Monte Carlo calculations can assist in getting an accurate picture of how the tamper can lower the critical mass required. Figure 3 shows the effect of adding a beryllium tamper to a sphere of weapon-grade plutonium.

2.2 Heat Generation. Neutron Background and Predetonation

Several other details concerning the physics of nuclear weapons must be considered in order to appreciate the risk potential of various fissionable actinide isotopes. The first and simplest topic is the radioactivity of the isotopes involved and their propensity to generate heat. Excessive heat may cause thermal distortions of parts of the device and lead to degradation of the chemical explosive in the device. Table 1 lists the specific heat generation rates for various isotopes of interest. This shows, for example, that while ^{233}U is a usable weapon material, the material must be produced with very tight limits on the presence of ^{232}U, because of its high heat generation rate; the same applies to ^{238}Pu in ^{239}Pu-based assemblies. Also, some of these isotopes generate

Table 1 Properties of various isotopes of interest in fission-based nuclear explosive assemblies

Nuclide	Half-life	Specific activity	Heat Gen.	Spont. fission rate
U-232	6.89E+01 y	8.25E+11 Bq g^{-1}	7.14E-01 W g^{-1}	n/a
U-233	1.59E+05 y	3.57E+08 Bq g^{-1}	2.76E-04 W g^{-1}	2.1E-04 $g^{-1}s^{-1}$
U-234	2.46E+05 y	2.30E+08 Bq g^{-1}	1.79E-04 W g^{-1}	3.98E-03 $g^{-1}s^{-1}$
U-235	7.04E+08 y	8.00E+04 Bq g^{-1}	5.99E-08 W g^{-1}	5.60E-06 $g^{-1}s^{-1}$
U-236	2.34E+07 y	2.39E+06 Bq g^{-1}	1.75E-06 W g^{-1}	2.30E-03 $g^{-1}s^{-1}$
U-238	4.47E+09 y	1.24E+04 Bq g^{-1}	8.50E-09 W g^{-1}	6.78E-03 $g^{-1}s^{-1}$
Np-237	2.14E+06 y	2.61E+07 Bq g^{-1}	2.06E-05 W g^{-1}	5.22E-05 $g^{-1}s^{-1}$
Pu-238	8.78E+01 y	6.34E+11 Bq g^{-1}	5.67E-01 W g^{-1}	1.20E+03 $g^{-1}s^{-1}$
Pu-239	2.41E+04 y	2.30E+09 Bq g^{-1}	1.93E-03 W g^{-1}	7.11E-03 $g^{-1}s^{-1}$
Pu-240	6.57E+03 y	8.39E+09 Bq g^{-1}	7.06E-03 W g^{-1}	4.78E+02 $g^{-1}s^{-1}$
Pu-241	1.44E+01 y	3.82E+12 Bq g^{-1}	3.28E-03 W g^{-1}	9.18E-04 $g^{-1}s^{-1}$
Pu-242	3.74E+05 y	1.46E+08 Bq g^{-1}	1.17E-04 W g^{-1}	8.04E+02 $g^{-1}s^{-1}$
Am-241	4.32E+02 y	1.27E+11 Bq g^{-1}	1.14E-01 W g^{-1}	5.47E-01 $g^{-1}s^{-1}$

Data from [5]

energetic gamma rays in their decay sequence, and the presence of these may make it difficult for workers to assemble these devices or to be near them after they are made.

Also of interest is the rate of neutron emission from these materials. Neutrons can be produced in fissile materials by spontaneous fission. In order for a device to perform with substantial yield, the device must be sufficiently supercritical before neutrons induce a fission chain reaction, which in turn produces enough energy to start the dis-assembly of the device. A predetonation caused by the spurious presence of early neutrons is called a “fizzle”. For the relatively slow assembly afforded by a gun-type process such as used in the Little Boy design, with velocities around 1000 meters per second and distance traveled between exact criticality and supercriticality on the scale of ten centimeters or so, the period when a fizzle is possible by premature neutron-induced fission is on the order of 10^{-4} s. Plutonium, on the other hand, typically gets manufactured in a nuclear reactor by absorption of neutrons on ^{238}U. Further nuclear reactions will turn some of this plutonium into ^{240}Pu, and at least a few percent concentration of ^{240}Pu is unavoidable. This isotope has a high rate of spontaneous fission.

For this reason, even though ^{235}U is a less desirable material than Pu for constructing a nuclear weapon for large programs such as the US and Russian programs, ^{235}U can be considered a greater terrorism/rogue nation threat because the technological barrier is much less for developing a usable weapon, given that sufficient quantity of material is available. On the other hand, kilogram quantities of weapon-grade Pu (usually taken to be $<7\,\%$ ^{240}Pu) is a credible threat in the hands of a somewhat more sophisticated adversary.

The foregoing analysis also points to the types of nuclear reactors that are more of a threat to the production of weapon-usable plutonium. A large power reactor, say an 1100 MWe (3300 MWth) reactor (such as most of the reactors online in the US) typically has very high burnup rates for the fuel, and the fuel elements are in the reactor for years at a time. The plutonium in the spent fuel from these reactors typically has more ^{240}Pu than ^{239}Pu, and is extremely difficult to be used in a nuclear weapon. Small research reactors in the 15–30 MWth class pose more of a risk, as these are more open, accessible systems with lower typical fuel irradiation. CANDU-type reactors, with their ability to be fuel-swapped while they are running, are also more difficult to control from a safeguarding viewpoint.

3 Special Nuclear Material

The purpose of this section is to define the terms that are used to describe materials connected to the development of nuclear weapons.

Special Nuclear Material, or SNM, is a term used by the U. S. Nuclear Regulatory Commission (NRC) to mean uranium enriched in ^{235}U or ^{233}U, ^{233}U, and plutonium of any isotope. This definition is given in Title I of the Atomic Energy Act of 1954. The NRC has the authority to add other materials to the list of SNM materials, but it never has done so.

The NRC has also broken down SNM into three Safeguard Categories of risk. Category I is defined as Strategic Special Nuclear Material, or SSNM, and is defined as material containing:

- 2 kg or more of plutonium; or
- 5 kg or more of U-235 (contained in uranium enriched to 20 % or more in the U-235 isotope); or
- 2 kg or more of U-233; or
- 5 kg or more in any combination computed by the equation grams = (grams contained U-235) + 2.5 (grams U-233 + grams plutonium).

Category II, “Special nuclear material of moderate strategic significance” is defined as

- Less than a formula quantity of strategic special nuclear material but more than 1,000 grams of uranium-235 (contained in uranium enriched to 20 % or more in the U-235 isotope) or more than 500 grams of uranium-233 or plutonium, or in a combined quantity of more than 1,000 grams when computed by the equation grams = (grams contained U-235) + 2 (grams U-233 + grams plutonium); or
- 10,000 grams or more of uranium-235 (contained in uranium enriched to 10 % or more but less than 20 % in the U-235 isotope).

Category III, “Special nuclear material of low strategic significance” is defined as

- Less than an amount of special nuclear material of moderate strategic significance (see category II above) but more than 15 grams of uranium-235 (contained in uranium enriched to 20 % or more in U-235 isotope) or 15 grams of uranium-233 or 15 grams of plutonium or the combination of 15 grams when computed by the equation grams = (grams contained U-235) + (grams plutonium) + (grams U-233); or

- Less than 10,000 grams but more than 1,000 grams of uranium-235 (contained in uranium enriched to 10 % or more but less than 20 % in the U-235 isotope); or
- 10,000 grams or more of uranium-235 (contained in uranium enriched above natural but less than 10 % in the U-235 isotope).

Enriched Uranium means any uranium containing more that 0.71 % ^{235}U. *Highly Enriched Uranium, or HEU*, is defined by the U. S. Department of Energy (DOE) as uranium containing more that 20 % ^{235}U. This is considered the lowest enrichment for which a nuclear explosive is possible. In 1996, the DOE had about 740 metric tons in this category. (Since that time, the inventory has been reduced by downblending and disposal.) The DOE also separates out its inventory of $>$90.0 % enriched uranium, which might be considered "weapon grade", although DOE does not use that terminology specifically, nor does it report its total inventory in that category.

The term *Significant Quantity* is used by the International Atomic Energy Agency (IAEA) to denote "the approximate amount of nuclear material for which the possibility of manufacturing a nuclear explosive device cannot be excluded." The significant quantities are 8 kg of Pu($<$80 % ^{238}Pu), 8 kg ^{233}U, 25 kg HEU, 75 kg enriched U($<$20 % enriched), 10 metric tons natural U, 20 metric tons depleted U, or 20 tons Th. These quantities are used as the trigger points for further action following their detection during inspections.

One can notice some decoupling of these definitions from the actual threat. It is interesting to note that ^{237}Np is not SNM under U.S. guidelines, although it is generally known as a nuclear weapon-usable material. Also, the IAEA would not consider the quantity of plutonium used in the Fat Man Nagasaki weapon to be "significant"!

References

1. Comprehensive Test Ban Treaty Organization: 28 May 1998—Pakistan nuclear tests. https://www.ctbto.org/specials/testing-times/28-may-1998-pakistan-nuclear-tests
2. Comprehensive Test Ban Treaty Organization: On the CTBTO's detection in North Korea (12 Feb 2013). https://www.ctbto.org/press-centre/press-releases/2013/on-the-ctbtos-detection-in-north-korea/
3. Glaser A (2006) On the proliferation potential of Uranium fuel for research reactors at various enrichment levels. Sci Global Secur 14:1–24. doi:10.1080/08929880600620542
4. Lamarsh J (2002) Introduction to Nuclear reactor theory. Am. Nucl. Soc. https://books.google.com/books?id=XGJTAAAAMAAJ
5. Magill J (2003) Nuclides.net—an integrated environment for computations on radionuclides and their radiation. Springer
6. Norris RS, Kristensen HM (2006) Global nuclear stockpiles, 1945–2006. Bull At Sci 62:64–66. doi:10.2968/062004017
7. Nuclear Threat Initiative: South Africa:Nuclear. http://www.nti.org/country-profiles/south-africa/nuclear/

8. Nuclear Weapons Archive: Smiling Buddha: 1974 (2001). http://nuclearweaponarchive.org/India/IndiaSmiling.html
9. Serber RS, Condon EU (1943) The Los Alamos primer. Tech. rep., Los Alamos Laboratory. http://www.fas.org/sgp/othergov/doe/lanl/docs1/00349710.pdf
10. Wisconsin Project on Nuclear Arms Control: Israel's nuclear weapon capability: an overview. Risk Rep 2(4) (July–Aug 1996). http://www.wisconsinproject.org/countries/israel/nuke.html

Signatures and Background

Abstract Models for radiation transport in simple geometries are developed, with an emphasis on self-shielding and distributed sources. Three mechanisms for gamma ray attenuation—photoelectric, Compton, and pair production, are described. Some end-to-end calculations are shown for the estimated count rates with realistic sources and detectors. The impact of background radiation in potentially masking a source from detection is explored. Radiation background sources in the ground and air are described, with particular emphasis on the uranium and thorium decay chains, with tables of the characteristic gamma-ray lines given. Cosmogenic radiation is also explored, along with neutron backgrounds. Next, the impact of naturally occuring radioactive material (NORM) and technologically enhanced NORM (TENORM) are discussed.

1 Simplified Transport Calculations

The modeling of photon and neutron transport in real environments, with real detectors, is the domain of highly sophisticated computer codes. A popular example is MCNPX, a Monte Carlo code package available through the Radiation Safety Information Computational Center (RSICC) in Oak Ridge, TN. (http://www-rsicc.ornl.gov/). This code, originally developed at Los Alamos National Laboratory in the late 1950s, has been refined and thoroughly tested over more than half a century. This approach does have some drawbacks, however. First, users must be aware of the validity of results based on the number of particles used, the correctness of the geometrical model being input to the code, and the quality of the physics approximations being made within the code for those cases where real nuclear and particle data are unavailable. Second, there are export control issues in using this code, and the process of getting set up for a license, even for a single user, may be difficult at times. Thirdly, some decision makers in the various government agencies involved in nuclear security issues are skeptical of code model predictions of the performance of real-world detection systems, having been disappointed in the past.

For these reasons, it is always important to be able to perform simple calculations of the expected behavior of proposed detection schemes based upon the first

E.C. Morse, *Analytical Methods for Nonproliferation*, Advanced Sciences
and Technologies for Security Applications, DOI 10.1007/978-3-319-29731-6_3

principles of radiation transport. While these are not a substitute for the more detailed computations that would be available with MCNPX or other codes, the simple models given here provide insight into the physical processes going on in any detection scheme, and provide a "sanity test" for evaluating code output.

1.1 Gamma Radiation Field from a Point Source

Suppose one has a small gamma-emitting source containing N atoms of a radioactive substance with a half-life $t_{1/2}$. Suppose that the detector is a distance R from the source. The activity

$$\mathscr{A} = -\dot{N} = \lambda N,$$

where λ is the decay constant

$$\lambda = \frac{\ln 2}{t_{1/2}}.$$

The production of a particular gamma ray is given by $-\dot{N}B$, where B is the branching ratio for that gamma ray line.

Consider all gammas being generated out of the source. These gamma rays are uniformly distributed in all directions, i.e. into 4π sterradians of solid angle, and thus uniformly distributed on a surface of area $4\pi R^2$ at a distance R. We define the flux ϕ as being the number of particles passing through a unit area (normal to the source location) per unit time, with units $\mathrm{cm}^{-2}\mathrm{s}^{-1}$. The total flux at the detector is

$$\phi = \frac{-\dot{N}B}{4\pi R^2} = \frac{\ln 2 \cdot BN}{t_{1/2} \cdot 4\pi R^2} \quad \mathrm{cm}^{-2}\mathrm{s}^{-1}. \tag{1}$$

Suppose that the detector has a surface area A_d in the direction facing the source, and the physical dimensions are small compared to R, so that near-field effects can be neglected. Suppose that the efficiency for that detector to report a gamma-ray hit, given that a gamma ray entered the detector, is η_d. Then the total count rate CR for that gamma ray line is given by

$$\mathrm{CR}(\mathrm{s}^{-1}) = \phi A_d \eta_d = \frac{\ln 2 \cdot BNA_d \eta_d}{t_{1/2} \cdot 4\pi R^2}. \tag{2}$$

Count rates are usually reported in counts per minute, however, so it is worth adding this last minor step:

$$\mathrm{CR}(\mathrm{min}^{-1}) = \frac{60 \ln 2 \cdot BNA_d \eta_d}{t_{1/2} \cdot 4\pi R^2}. \tag{3}$$

Another simple task remains. What is N? Often more than one species is present in the source, and the characteristic gamma ray under investigation comes from only one component. For example, suppose that we have a mass m of weapon-grade uranium with an enrichment f, expressed as a weight fraction of the ^{235}U content, with the rest being mostly ^{238}U. Then using Avogadro's constant

$$N_{235} = \frac{fmN_A}{235}. \tag{4}$$

So if we had a (very small!) piece of uranium, the ^{235}U gamma ray signal count rate would be

$$CR(\min^{-1}) = \frac{60 \ln 2 \cdot BfmN_A A_d \eta_d}{235 \cdot t_{1/2} \cdot 4\pi R^2}. \tag{5}$$

1.2 Self-Shielded Disk

The above calculation needs to be modified if the radiation source is large enough to absorb some of its produced gamma photons before they leave the source. This is especially important for low-energy gammas in high-Z elements.

Gamma rays interact with matter by three primary processes. At low energies, the primary process is photoelectric absorption by valence electrons in the atomic structure of the material. At intermediate energies (~1 MeV), gamma-ray photons simply scatter in elastic collisions with the electrons in the material. At high energies, gamma rays in the vicinity of nuclei lose energy by the creation of electron positron pairs. (Details of these reactions are described later in this chapter.) For the present discussion, we are interested in the fraction of the gamma rays surviving at full energy, regardless of whether a secondary, lower-energy photon is produced or not. We use a probability μ to describe the incremental fraction dI per incremental length dx of gamma rays removed from the full-energy channel. The change in the full-energy intensity dI as the photons move through a distance dx is given by:

$$\frac{dI}{I} = -\mu dx. \tag{6}$$

And thus the full-energy intensity of a beam of photons with initial intensity I_0 passing through a distance x is given by:

$$I = I_0 e^{-\mu x}. \tag{7}$$

The quantity μ is called the linear attenuation coefficient and has dimensions of inverse length, i.e. cm^{-1}. Linear attenuation coefficients are proportional to mass density ρ, and thus mass attenuation coefficients are given as μ/ρ, i.e. in units of $cm^2\ g^{-1}$. Tables and graphs of the mass attenuation coefficients for elements and

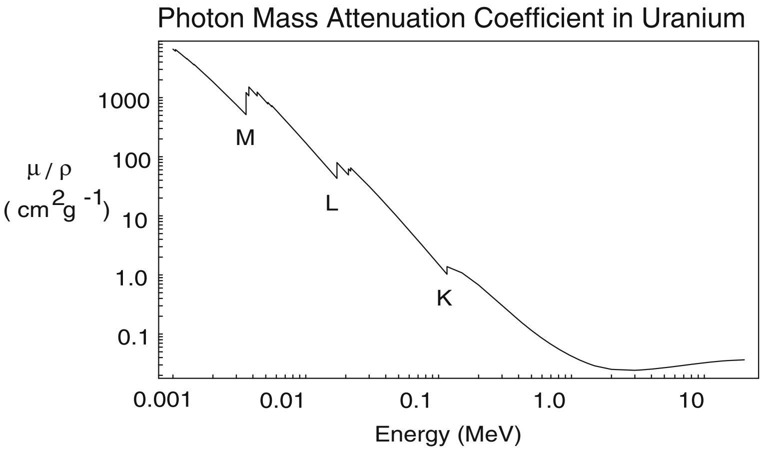

Fig. 1 Mass attenuation coefficient for uranium. Based on the NIST X-ray attenuation data, NIST IR5632, available at http://www.nist.gov/pml/data/xraycoef/

compounds are given at the National Institute for Standards and Technology website www.nist.gov/pml/data/xraycoef/. Figure 1 shows the mass attenuation coefficient μ/ρ for uranium as a function of photon energy. Note that the labels K, L, M refer to the atomic shells, and that the photoelectric effect is responsible for the large attenuation values at energies <1 MeV.

Consider a small disk of area A_s and diameter d which has a thickness $t \gg 1/\mu$, where μ is the removal attenuation coefficient. (The situation where $t \gg 1/\mu$ is called the "optically thick" limit.) Suppose that the detector is a distance $R \gg d$ from the detector. The specific activity is

$$-\dot{n} = \lambda n,$$

where λ is the decay constant as before. The production of a particular gamma ray per unit volume is $-\dot{n}B$, where again B is the branching ratio for that gamma ray line.

Consider all gammas being generated in the forward direction out of the disk. Then the fraction F of those gammas surviving out of the front face of the disk is given by:

$$F = \frac{1}{t}\int_0^t e^{-\mu x}dx = \frac{1}{\mu t}\left(1 - e^{-\mu t}\right) \approx \frac{1}{\mu t}, \tag{8}$$

and then the total flux at the detector is

$$\phi = \frac{-\dot{N}BF}{4\pi R^2} = \frac{-\dot{n}BA_s tF}{4\pi R^2} \approx \frac{\lambda nBA_s(1/\mu)}{4\pi R^2}. \tag{9}$$

This is equivalent to saying that all gammas from a distance $1/\mu$ survive to the surface of the disk and are transported. The effective volume of the source is then only A_s/μ.

The number of counts seen in a detector of area A_d and efficiency η_d is then

$$CR(s^{-1}) = \frac{\lambda nBA_s(1/\mu)A_d\eta_d}{4\pi R^2}. \tag{10}$$

Note that this formula can be re-written to show that the result does not actually depend on density. Noting that

$$n = \frac{f\rho N_A}{M}, \tag{11}$$

where f is the mass fraction of the gamma-emitting component and M is the atomic mass of that component, the above formula can be written as

$$CR(s^{-1}) = \frac{\lambda N_A BfA_s A_d\eta_d}{M \cdot 4\pi R^2 \cdot (\mu/\rho)}, \tag{12}$$

and in a more practical form

$$CR(min^{-1}) = \frac{60 \ln 2N_A BfA_s A_d\eta_d}{t_{1/2} \cdot M \cdot 4\pi R^2 \cdot (\mu/\rho)}, \tag{13}$$

We now show an example calculation. Suppose that a bare spherical solid 10 kg pit of 93 % ^{235}U ($f_{235} = 0.93$) is 10 feet from a detector. ^{235}U has a half-life $t_{1/2} =$ 704 million years, and produces a 185.7 keV gamma ray with branching ratio $B_{185} =$ 0.572. Note that μ/ρ for U at 185 keV is 1.56 cm^{2}g^{-1}. We need to assume a value of the density of the pit to find its radius R_{pit}. The mass m is related to the radius R_{pit} by

$$m = \frac{4}{3}\pi\rho R_{pit}^3 \tag{14}$$

Using density $\rho = 19.1\,g\,cm^{-3}$, this gives $R_{pit} = 5.00\,cm$. Then $A_s = 78\,cm^2$ (note that the area is *not* $4\pi R_{pit}^2$, but rather πR_{pit}^2, because the area seen by the detector is its cross-sectional area, not its total surface area) and $1/\mu = 1/(29.83)$ cm=0.0305 cm = 335 μm. Thus the total equivalent emitting volume is only 2.6 cm^3.

The effective source strength is then

$$\dot{N}_{185} = \frac{f_{235}\rho N_A}{M}(A_s/\mu)\lambda B = 2.13 \times 10^6 \quad s^{-1} \tag{15}$$

A 50 % efficient detector ten feet away with $A_d = 100\,\text{cm}^2$ would see 91 counts per second, or 4700 counts per minute. However, one inch of steel ($\mu/\rho = 0.156\,\text{cm}^2\text{g}^{-1}$, $\rho = 7.8\,\text{g cm}^{-3}$, $L = 2.5$ cm) shielding would take this down by a factor of

$$e^{-(\mu/\rho)\rho L} = e^{-(0.156)(7.8)(2.5)} = 0.045$$

or to 249 counts per minute.

1.3 Intermediate Optical Thickness

If the optical depth parameter μt is of order unity, neither the fully self-shielded case nor the point source case applies, and a more detailed transport calculation must be done. However, for simple geometries such as spheres, hemispheres, spherical shells, cylinders, annular cylinders, cubes, rectangular slabs, and so forth, these calculations are fairly simple to perform. The general form used to quantify these results is to define a shielding factor $F(\mu t)$ such that, for a detector at some distance $R \gg t$, where t is a characteristic dimension of the radiating object, the count rate CR seen is given by

$$CR = F(\mu t) CR(\mu \to 0), \tag{16}$$

i.e. $F(\mu t)$ represents the attenuation factor of the signal at the detector compared to what would be observed for the same source with zero self-attenuation. In general

$$F(\mu t) = \frac{1}{V} \int dV\, e^{-\mu z}, \tag{17}$$

where z is the distance to the surface of the radiating body in the direction of the detector. As an example, consider a sphere of radius R_0. The self-attenuation factor $F(\mu R_0)$ is given by

$$F(\mu R_0) = \frac{3}{4\pi R_0^3} \int_0^{R_0} 2\pi R dR \frac{1 - e^{-2\mu\sqrt{R_0^2 - R^2}}}{\mu}, \tag{18}$$

and this integral is given by (using $x = \mu R_0$):

$$F(x) = \frac{3\left(2x^2 + e^{-2x}(2x+1) - 1\right)}{8x^3}. \tag{19}$$

This function has the asymptotic values $\lim_{x \to 0} F(x) = 1$ and $\lim_{x \to \infty} xF(x) = 3/4$, thus recovering the formulae given above. The optically thin and optically thick approximations are within 10 % for $x < 0.14$ and $x > 2.16$, respectively.

1.4 *Infinite Half-Space Source*

The following is especially useful in evaluating the intensity of background radiation from radioactivity embedded in the earth.

Suppose there is an thick planar source of radiation of infinite extent. A detector is a distance R above this source. The detector sees this source as covering 2π sterradian of solid angle. Each solid angle increment $d\Omega$ intercepts the surface with an equivalent area $R^2 d\Omega$. By the previous rule, we know that a depth $1/\mu$ is the effective radiative depth. Figure 2 illustrates the geometry involved.

If the gamma production rate per unit volume is $-\dot{n}B$, then the total flux to the detector is

$$\phi = \frac{-\dot{n}B}{4\pi R^2 \mu} \cdot R^2 \int d\Omega = \frac{-\dot{n}B}{2\mu}. \tag{20}$$

We can then replace $-\dot{n}$ with $\lambda n = \ln 2n/t_{1/2}$, and substitute $n = f\rho N_A/M$, where again f represents the mass fraction of the emitting isotope of interest. Then we have

$$\phi = \frac{\ln 2 N_A B f}{2 \cdot t_{1/2} \cdot M \cdot (\mu/\rho)}. \tag{21}$$

As before, this can be converted into a detector count rate by multiplying by $\eta_d A_d$ and then

$$CR(\min^{-1}) = \frac{60 \ln 2 N_A B f A_d \eta_d}{2t_{1/2} \cdot \ M \cdot (\mu/\rho)}. \tag{22}$$

Some features of this result are worth noting. Firstly, the count rate does not depend on the height of the detector R above the half-space. (Note that this result ignores the attenuation by air, which has a half-length of about 40 m at 200 keV and 150 m at 3.0 MeV. See Fig. 3.) Secondly, the result does not depend on the mass density of the emitting medium, but only upon the mass fraction of the emitting component. Thirdly, one can estimate the effects of changes in the count rate caused

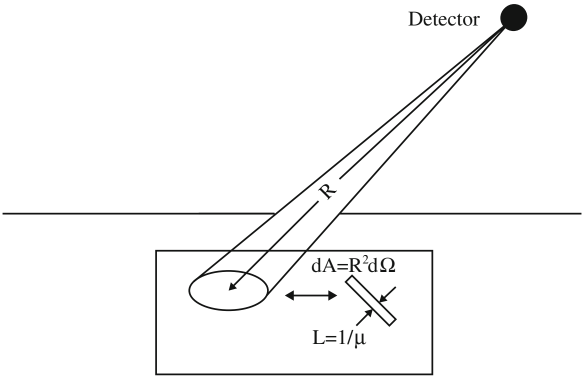

Fig. 2 Detector-source geometry for infinite half-space calculation

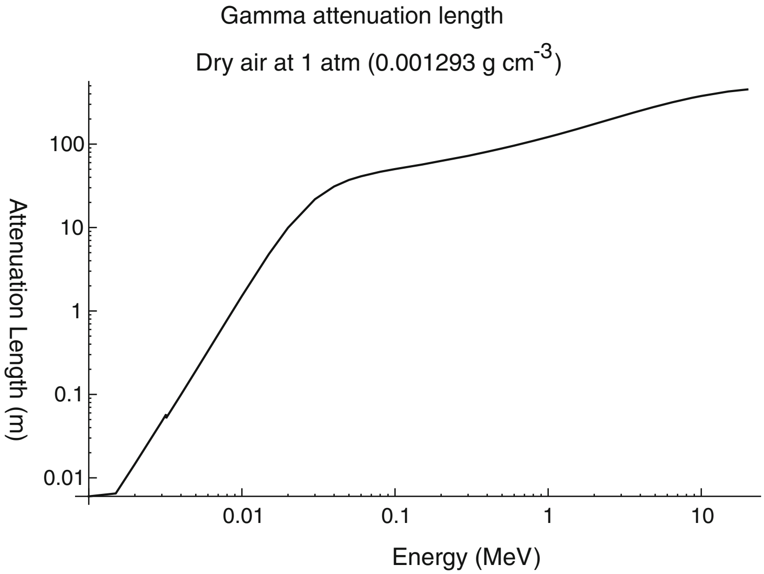

Fig. 3 Attenuation (1/e) length for gamma rays in air

by changes in the emitting medium (such as a measurement on an asphalt roadbed with uncovered soil nearby) by calculating the fraction of the solid angle as seen by the detector from each type of emitting surface. It is important to keep in mind that only a depth of a few times $1/(\mu\cos\theta)$ is involved in transport of photons to the detector, and this is on order of 10–20 cm in soil in the energy range from 150 keV to 3 MeV.

The following calculation illustrates this result. Suppose that a measurement of the 185 keV ^{235}U photon flux is made at a 1 m height above topsoil containing 3 wppm uranium. (This is a typical value in the United States.) The enrichment of natural uranium in ^{235}U (as a mass fraction) is 0.711 % and thus $\mathrm{f} = 2.1 \times 10^{-8}$. The mass attenuation coefficient of soil at 185 keV is about $0.14\,\mathrm{cm}^2\mathrm{g}^{-1}$. Taking $A_d = 100$ cm^2 and $\eta_d = 0.5$ as before then gives a count rate of around 10 counts per minute. This would seem small compared to the 10 kg spherical pit of uranium with one inch of steel shielding mentioned before, with a count rate of 249 counts per minute. But increasing the shielding to just 2.04 inches would make these rates equal.

2 The Radiation Background

2.1 The Primordial Isotopes

The earth's crust contains three elements, in four isotopes, that have sufficiently long half-lives so that they are still present in significant quantities following their primordial synthesis. These elements are uranium, thorium, and potassium. The isotopes are ^{235}U, ^{238}U, ^{232}Th, and ^{40}K. The first three isotopes are actinides and decay primarily by alpha-particle emission. The latter, ^{40}K, decays primarily by a beta emission, with a long half-life because of the large disparity in spin-values between the parent and daughter nucleus, a so-called third-forbidden decay. A table of key properties of these isotopes is given as Table 1.

Average elemental concentrations of these three elements U, Th, and K in the earth's crust are 2.7 ppm, 8.5 ppm, and 2 %, respectively. In the case of ^{238}U and ^{232}Th, no significant gamma rays are emitted during their direct decay, but subsequent decays of the decay products of these isotopes contribute to the natural background radiation field. ^{235}U does produce gamma radiation during its decay, and there are also gamma rays associated with its daughter products as well. The two byproducts of ^{40}K decay, ^{40}Ca and ^{40}Ar, are both stable. One significant radiation is produced by ^{40}K decay: the electron capture channel to ^{40}Ar, which has an 11.0 % branching probability, emits a 1.460 MeV gamma with 100 % probability in that channel. With the photons produced by all members of the decay series taken into consideration, these three elements form roughly equal shares of the natural radiation background.

The three alpha-decaying isotopes, ^{235}U, ^{238}U, and ^{232}Th, have daughter products that decay either by alpha decay or beta decay, hence all elements in the decay chain have masses that are integer multiples 4n smaller than the parent nucleus. Thus ^{235}U is the 4n + 3 series, ^{238}U the 4n + 2 series, and ^{232}Th the 4n series. The end-points of these series are all stable lead isotopes, namely ^{207}Pb, ^{206}Pb, and ^{208}Pb, respectively. The short half-life of ^{233}U (159,000 years) precludes there being a complete 4n + 1 decay chain in natural radioactivity.

Diagrams of the complete 4n + 2, 4n + 3, and 4n decay series are given as Figs. 4, 5 and 6. Tables of the gamma rays produced are shown as Tables 2, 3 and 4. Note that these tables only contain gamma energies above 100 keV and branching ratios above 0.2 %. Also note that there are alternative decay modes in these systems; only the principal ones are given here.

The condition where the parent isotope has a long half-life compared to the daughters, and the daughters remain co-located with the parent, is called secular equilibrium. In this case, the activity of the daughters, if there is total branching to that state, is equal to the activity of the parent. However, with some of the longer-lived isotopes, there can be some migration of the parent and daughter nuclides for both

Table 1 Properties of the primordial isotopes

Nuclide	Z	N	Decay mode	Half life	J^π	Abundance (atom %)
^{235}U	92	143	α, SF, ^{20}Ne	7.038×10^8 y	7/2−	0.7200
^{238}U	92	146	α, SF, $\beta^-\beta^-$	4.468×10^9 y	0+	99.2745
^{232}Th	90	142	α, SF	1.405×10^{10} y	0+	100
^{40}K	19	21	β^-, EC, β^+	1.277×10^9 y	4−	0.0117

Note that SF = spontaneous fission, and EC = electron capture. Abundances are the fraction of the isotope to all isotopes of that element as found in nature

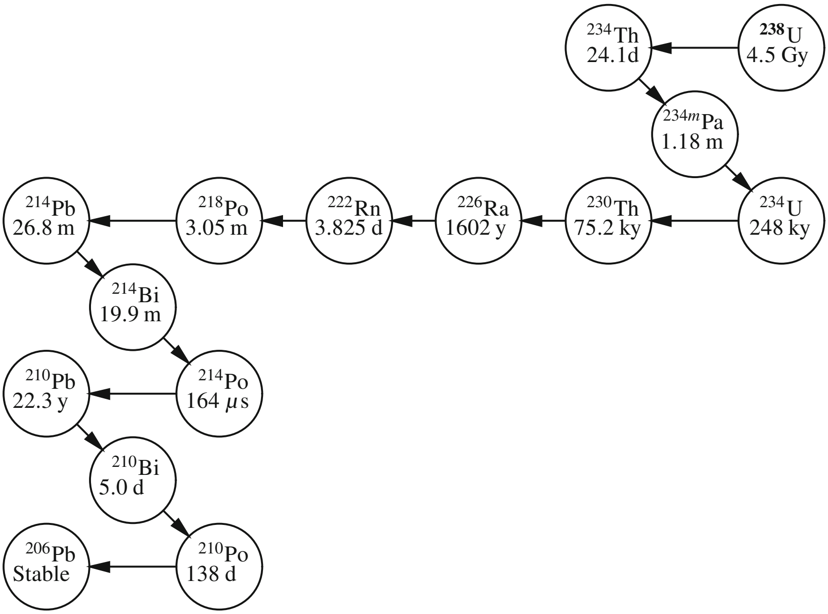

Fig. 4 $4n + 2$ decay chain

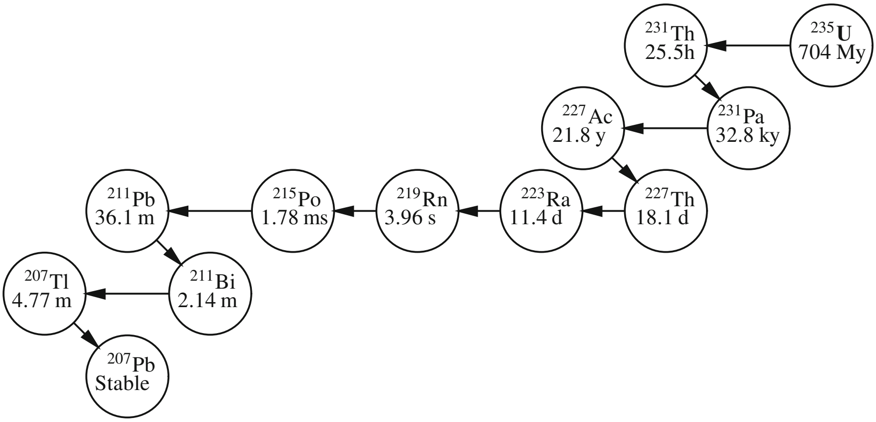

Fig. 5 $4n + 3$ decay chain

chemical and physical reasons–a process called fractionation. For example, ^{222}Rn in the ^{238}U decay chain is a gas and may be released from fractured media. Also, U and Ra are soluble, and Ra with its calcium-like chemistry is a candidate for plant uptake. Thus the U decay series may not be in complete equilibrium. The thorium decay series, with its less-soluble parent and short Rn half-life, is more likely to be in complete equilibrium.

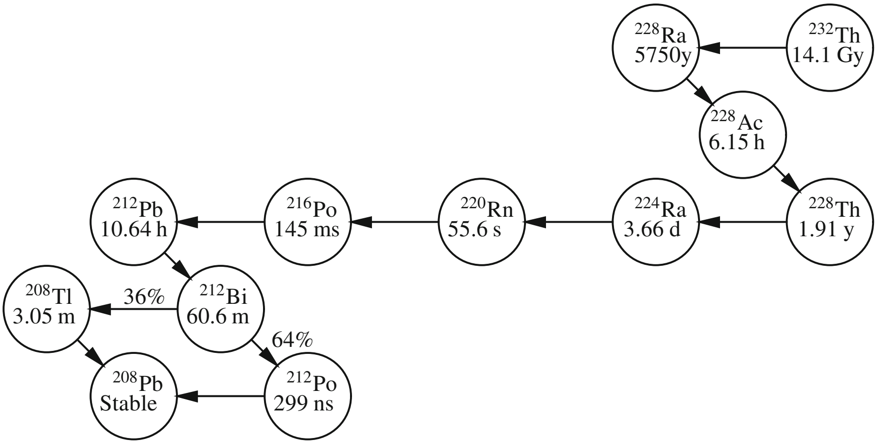

Fig. 6 4*n* decay chain

Table 2 Gamma-ray lines associated with ^{238}U decay

^{234m}Pa		^{234}Th		^{226}Ra	
Energy (keV)	B (%)	Energy (keV)	B (%)	Energy (keV)	B (%)
1001.03	0.837	112.81	0.277	186.211	3.59
766.38	0.294				
^{214}Pb		^{214}Bi		^{214}Bi (contd.)	
Energy (keV)	B (%)	Energy (keV)	B (%)	Energy (keV)	B (%)
351.932	37.6	609.312	46.1	1385.31	0.757
295.224	19.3	1764.494	15.4	1583.22	0.69
241.997	7.43	1120.287	15.1	703.11	0.472
53.2275	1.2	1238.11	5.79	1207.68	0.451
785.96	1.07	2204.21	5.08	719.86	0.379
839.04	0.587	768.356	4.94	1538.5	0.376
258.87	0.524	1377.669	4	388.88	0.37
274.8	0.474	934.061	3.03	964.08	0.362
487.09	0.422	1729.595	2.92	1838.36	0.36
580.13	0.352	1407.98	2.15	1051.96	0.315
480.43	0.32	1509.228	2.11	386.77	0.31
462	0.221	1847.42	2.11	786.1	0.31
533.66	0.186	1155.19	1.63	2293.4	0.305
		2447.86	1.57	454.77	0.3
		665.453	1.46	1069.96	0.275
		1280.96	1.43	1594.73	0.25
		1401.5	1.27	1133.66	0.248
		806.174	1.22	1599.31	0.23
		1661.28	1.15	1873.16	0.219
		2118.55	1.14	1683.99	0.216

Table 3 Gamma-ray lines associated with ^{235}U decay

^{235}U		^{235}U (contd.)		^{231}Th		^{231}Pa	
Energy (keV)	B (%)	Energy (keV)	B (%)	Energy (keV)	B (%)	Energy (keV)	B (%)
185.712	57.2	202.111	1.08	102.268	0.41	300.07	2.46
143.764	10.96	194.94	0.63			302.65	2.2
163.358	5.08	182.52	0.34			283.69	1.7
205.309	5.01	279.5	0.27			283.69	1.396
109.16	1.54	221.399	0.12			302.65	0.68
^{227}Th		^{227}Th (contd.)		^{227}Th (contd.)		^{223}Ra	
Energy (keV)	B (%)	Energy (keV)	B (%)	Energy (keV)	B (%)	Energy (keV)	B (%)
235.971	12.3	334.381	1.05	234.81	0.41	269.459	13.7
256.25	7	254.68	0.7	342.5	0.39	154.21	5.62
329.851	2.7	113.159	0.5	250.35	0.34	323.871	3.93
300	2.32	312.69	0.48	300	0.34	144.232	3.22
286.122	1.54	296.51	0.46	206.11	0.21	338.281	2.79
304.519	1.2	314.78	0.44	204.27	0.2	445.03	1.27
210.65	1.11	314.78	0.44			122.319	1.192
^{223}Ra (contd.)		^{219}Rn		^{211}Pb		^{211}Bi	
Energy (keV)	B (%)	Energy (keV)	B (%)	Energy (keV)	B (%)	Energy (keV)	B (%)
158.633	0.685	271.23	10.8	404.853	3.78	351.059	12.91
371.68	0.480	401.81	6.37	832.01	3.52		
342.90	0.219			427.088	1.76		
328.40	0.206			766.51	0.617		
				704.64	0.462		
^{207}Tl							
Energy (keV)	B (%)						
897.80	0.26						

Some comments regarding the gamma ray data for these isotopes are in order. For the ^{238}U series, the most prominent features are the 351.9 and 609 keV lines from ^{214}Pb and ^{214}Bi. For the ^{235}U series, the most prominent feature is the 185.712 keV line in the ^{235}U decay to ^{231}Th, with $B = 57.2\,\%$. However, there is a coincidental match-up of this line with the 186.211 keV line in the ^{238}U decay chain, in the decay of ^{226}Ra ($B = 3.59\,\%$). Because of the lower abundance of ^{235}U, but taking the shorter half-life of ^{235}U into account, the activity ratio for these lines in natural U (with no fractionation) is almost unity:

$$\frac{\mathscr{A}(186.211)}{\mathscr{A}(185.712)} = \frac{1-\mathrm{f}}{\mathrm{f}} \cdot \frac{\mathrm{B}(186.211)}{\mathrm{B}(185.712)} \cdot \frac{\mathrm{t}_{1/2}\left({}^{235}\mathrm{U}\right)}{\mathrm{t}_{1/2}\left({}^{238}\mathrm{U}\right)} = \frac{0.9928}{0.0072} \cdot \frac{3.59}{57.2} \cdot \frac{7.08 \times 10^{8}}{4.468 \times 10^{9}}$$

$$= 1.36$$

Table 4 Gamma-ray lines associated with ^{232}Th decay

^{228}Ac		^{228}Ac (contd.)		^{228}Ac (contd.)		^{228}Ac (contd.)	
Energy (keV)	B (%)	Energy (keV)	B (%)	Energy (keV)	B (%)	Energy (keV)	B (%)
911.204	25.8	129.065	2.42	1459.138	0.83	1501.57	0.46
968.971	15.8	409.462	1.92	904.19	0.77	508.959	0.45
338.32	11.27	835.71	1.61	153.977	0.722	332.37	0.4
964.766	4.99	1630.627	1.51	726.863	0.62	340.98	0.369
463.004	4.4	772.291	1.49	1580.53	0.6	199.407	0.315
794.947	4.25	99.509	1.26	830.486	0.54	1110.61	0.285
209.253	3.89	755.315	1	1247.08	0.5	958.61	0.28
270.245	3.46	840.377	0.91	782.142	0.485	1625.06	0.255
1588.19	3.22	562.5	0.87	57.766	0.47	321.646	0.226
328	2.95	1495.93	0.86	1638.281	0.47	478.4	0.209
^{228}Th		^{224}Ra		^{212}Pb			
Energy (keV)	B (%)	Energy (keV)	B (%)	Energy (keV)	B (%)		
215.983	0.254	240.986	4.1	238.632	43.34		
				300.087	3.28		
				115.183	0.592		
^{212}Bi		^{208}Tl					
Energy (keV)	B (%)	Energy (keV)	B (%)				
727.33	6.58	2614.533	99				
1620.5	1.49	510.77	22.6				
785.37	1.102	860.564	12.42				
39.858	1.091	277.351	6.31				
1078.62	0.564	763.13	1.81				
893.408	0.378	252.61	0.69				
452.83	0.31	1093.9	0.4				
288.07	0.31	233.36	0.307				
1512.7	0.29	982.7	0.203				
		722.04	0.201				

The close spacing of these lines ≈ 0.5 keV, means that most detectors, including high purity germanium, have difficulty resolving these lines, and this can lead to some confusion. The possibility of fractionation effects, as described above, makes matters even worse.

In the thorium series, the most prominent lines are 238.632 keV in ^{212}Pb, 2614.533 keV in ^{208}Tl, and 911.204 keV in ^{228}Ac. Note the abundance of lines in ^{228}Ac decay: forty lines with $E_\gamma > 100$ keV and $B > 0.2\,\%$. The prominent 2614.533 keV line is usually taken as the upper gamma energy limit for the radiation background due to the primordial isotopes.

There are other primordial isotopes forming a less significant part of the natural radioactive background. These include ^{50}V, ^{87}Rb, ^{113}Cd, ^{115}In, ^{123}Te, ^{138}La, ^{142}Ce, ^{144}Nd, ^{147}Sm, ^{152} Gd, ^{174}Hf, ^{176}Lu, ^{187}Re, ^{190}Pt, ^{192} Pt, and ^{209}Bi.

2.2 Cosmogenic Nuclides

Cosmogenic nuclides are those created by interaction of airborne and surface nuclei with cosmic rays. The primary cosmic rays striking the upper atmosphere are predominantly fast protons, with an energy spectrum peaking at about 300 MeV. A smaller quantity of fast alpha particles are part of the primary cosmic ray flux as well. Spallation-type reactions with the atmosphere result in a good part of the fast protons being converted to fast neutrons impinging on the earth's surface. Some of these neutrons are thermalized in the atmosphere by elastic collisions with atmospheric components, especially H in atmospheric water. As a result, many radioisotopes are produced by (p, n), (n, p), and slow neutron absorption reactions. ^{14}C ($t_{1/2} = 5730\,y$) is the most abundant cosmogenic nuclide and is produced mostly by the $^{14}N(n, p)^{14}C$ reaction with atmospheric nitrogen. Tritium (^{3}H, $t_{1/2} = 12.3\,y$) is produced cosmogenically mostly by the reaction $^{14}N(n,^3 H)^{12}C$. However, neither of these radionuclides have a characteristic gamma ray emission, so they have little effect on nuclear measurements relevant to nonproliferation. On the other hand, $^7Be(t_{1/2} = 53$ d) is a cosmogenic radionuclide that does have a gamma-ray signature: a 477 keV gamma ray is made by the decay of ^{7}Be with 10.5 % branching. Cosmic-ray production of ^{7}Be can be accomplished through the following reactions:

$$\begin{aligned} n + {}^{12}C &\rightarrow {}^7 Be + X \\ p + {}^{12}C &\rightarrow {}^7 Be + X \\ n + {}^{14}N &\rightarrow {}^7 Be + X \\ p + {}^{14}N &\rightarrow {}^7 Be + X, \end{aligned}$$

where X indicates one (or more) reaction products.

Some other cosmogenic radionuclides are ^{10}Be, ^{26}Al, ^{36}Cl, ^{80}Kr, ^{32}Si, ^{39}Ar, ^{22}Na, ^{35}S, ^{37}Ar, ^{33}P, ^{32}P, ^{38}Mg, ^{24}Na, ^{38}S, ^{31}Si, ^{18}F, ^{39}Cl, ^{38}Cl, ^{34m}Cl. Some of these have gamma-ray signatures, but their production rate is much smaller than ^{7}Be.

2.3 The Compton Continuum and Pair Production

The signature gamma rays making up the radiation background for both the primordial and the cosmogenic isotopes can also have elastic collisions with the electrons in materials nearby in a detection system, and also in the detector itself. These collisions are referred to as Compton collisions. Collisions of this type produce a secondary photon that has an energy E'_γ related to the energy of the incident photon E_γ and the angle θ between the incident photon and the scattered photon:

$$E'_\gamma = \frac{E_\gamma}{1 + (E_\gamma/m_e c^2)(1 - \cos\theta)}. \tag{23}$$

Here the rest mass of the electron $m_e c^2 = 0.511\,\mathrm{MeV}$. If $E_\gamma \gg m_e c^2$, the minimum energy of the scattered photon is roughly $m_e c^2/2 \approx 250\,\mathrm{keV}$ for a complete backscatter ($\theta = 180°$). The Compton scattering process can be repeated several times, resulting in a continuum of photon energies being present in the radiation background along with the uncollided, monoenergetic photons.

In a detector, the Compton process can be thought of as having the reverse effect: a monoenergetic photon may enter the detector, interact with the detector material, leaving a recoiling electron in the detector, but producing a scattered photon which exits the detector without further interaction with the detecting material. For $E_\gamma \gg m_e c^2$, this results in the detector reporting an energy deposition ranging from 0 to $E_\gamma - m_e c^2/2$ in energy. For background radiation with many photon energies, the Compton continua for each photon energy are summed together, creating a spectrum that has a general downward trend towards higher energies.

Another process comes into play with very high gamma energies. This is from the possibility that an energetic photon, in the vicinity of a nucleus, especially a heavy nucleus, can create an electron-positron pair and a subsequent photon with an energy less by $2m_e c^2$, or approximately 1.02 MeV. This process can only happen for photon energies $>1.02\,\mathrm{MeV}$, and does not dominate the scattering processes in medium-Z materials (such as rock and soil) unless the photon energies are greater than 10 MeV. The produced positron can be annihilated by a nearby electron, and the result is a pair of 0.511 MeV photons moving in opposite directions. For this reason, 0.511 MeV photons are often present in gamma-ray spectra, but cannot be used to identify the presence of any particular isotope.

Inside the detector, the reverse situation may arise similar to the Compton scattering process above: a monoenergetic photon may enter the detector, undergo a pair production event, leaving an electron-positron pair and a photon with energy $E_\gamma - 2m_e c^2$. The positron annihilation results in two 0.511 MeV photons. One or both of the 0.51 MeV photons may exit the detector without being absorbed, but perhaps the recoil photon following the pair production is absorbed. This results in the detector reporting peaks at E_γ, $E_\gamma - m_e c^2$, and $E_\gamma - 2m_e c^2$. These are the full-energy peak and the so-called single-escape and double-escape peaks. These escape peaks must be carefully accounted for, as they may masquerade as the photopeak of another isotope.

2.4 *Typical Background Spectra*

As an example illustrating the concepts outlined above, Fig. 7 shows a gamma spectrum taken outdoors on the Berkeley campus with a high-purity germanium detector.

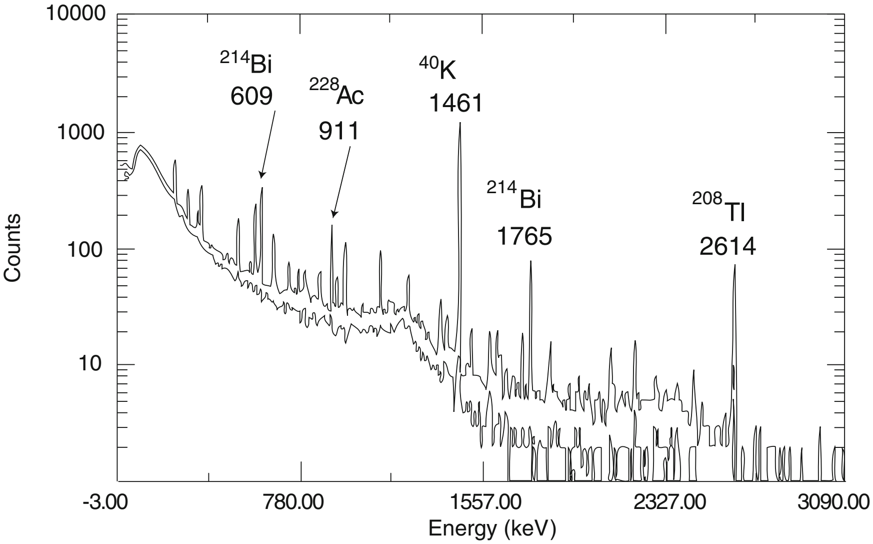

Fig. 7 Gamma spectrum taken with a high-purity germanium detector outdoors on the Berkeley campus. Courtesy of E.B. Norman, UC Berkeley

Note the presence of lines from the primordial isotope ^{40}K and the ^{238}U and ^{232}Th decay chains. Note also the high levels of Compton continuum in the lower channels, which in this case obliterates the 185 keV peak from ^{235}U. The 238 keV peak from ^{212}Pb is visible, however.

There can be quite a variation in background levels from one place to another, and in fact background levels can fluctuate at one point over the course of the day, being sensitive to surface temperature and precipitation. Figure 8 shows the results of a background mapping project carried out at UC Berkeley with a truck outfitted with twenty-four high-purity germanium detectors and a 10 × 10 imaging array of sodium iodide gamma detectors. Note especially the high levels found in industrial areas, and the near-zero levels as the truck crossed over water on a steel drawbridge.

2.5 Man-Made Radioactivity

In addition to natural sources of radioactivity, there can be components to the radioactive background due to human activity. The combustion of coal in power plants can cause release of uranium and thorium isotopes and their radioactive daughter products. Nuclear accidents at both power plants and at fuel reprocessing facilities can result in release of fission products to the atmosphere. Figure 9 shows a part of a background spectrum taken on the Berkeley campus, some months after the Fukushima Dai-Ichi reactor accident in March 2011. The spectrum shows the presence of two

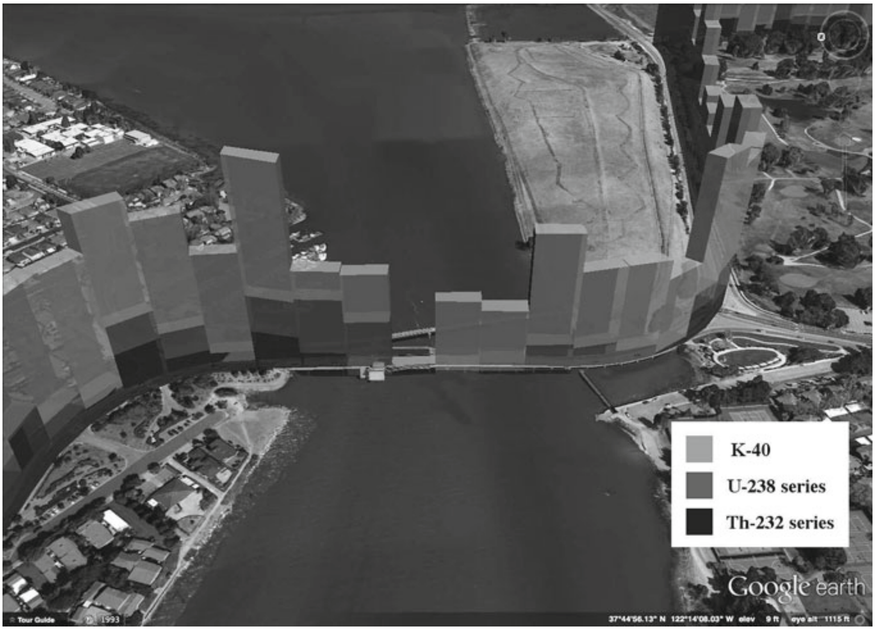

Fig. 8 Map of background radiation variations on a route through the San Francisco Bay area, taken in 30 m increments. Satellite imagery © Google. Adapted from [1]

Cs isotopes, ^{137}Cs ($t_{1/2} = 30.2$y) and ^{134}Cs ($t_{1/2} = 2.06$ y) that were not typically seen in background spectra before that time. There have been occasional reports of other gamma signatures in soil attributed to careless dumping of radioactive material in the past.

2.6 Neutrons

Neutrons are rare in nature. A few isotopes, such as ^{238}U and ^{232}Th, have a spontaneous fission decay channel, with very low branching ratios: ^{238}U is the largest natural spontaneous fission source with $B = 5.45 \times 10^{-5}$. Cosmic rays also provide a source of neutrons. There are fast neutrons produced from spallation by primary cosmic ray protons in the upper atmosphere. The fast neutrons typically have a long interaction length and pass through most detectors without appreciable signal generation. Some of the fast neutrons are thermalized by scattering in the atmosphere, and this results in a thermal neutron flux at sea level (in the middle latitudes) on the order of $4\,\mathrm{cm}^{-2}\mathrm{h}^{-1}$. There can be ($\alpha$, n) reactions in rock: for example, alpha-emitting isotopes in the uranium or thorium decay series can interact with several light elements (Li, Be, B, C, N, O, F) that have substantial (α, n) cross sections. A more energetic

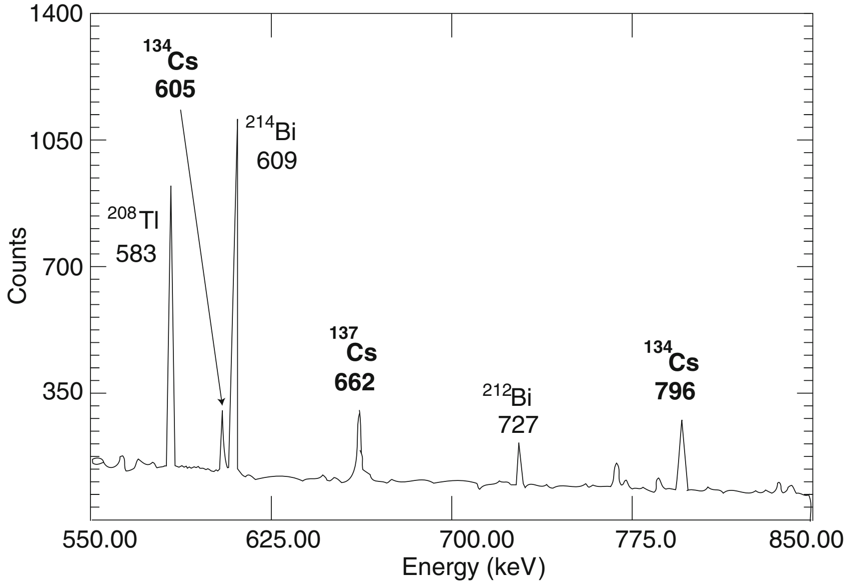

Fig. 9 Part of a gamma background spectrum, taken on the Berkeley campus, showing evidence of fallout from the Fukushima Dai-Ichi accident in 2011. Fallout isotopes are shown in *bold*. Courtesy of E.B. Norman, UC Berkeley

alpha such as the 8.954 MeV ^{212}Po in the Th decay series would be more productive than lower energy alphas, because of the greater range of the alpha in the material and the larger production cross section at higher energies.

2.7 NORM and TENORM

Materials in cargo transport may occasionally be more radioactive than typical radiation background levels. These materials fall into two broad categories: Naturally Occurring Radioactive Materials, or NORM, and Technologically Enhanced Naturally Occuring Radioactive Materials, or TENORM.

Many consumer goods entering commerce are NORM [5]. Among them are smoke detectors (typically containing ^{241}Am), watches and clocks with luminescent dials (the older ones used ^{226}Ra and the newer ones use either ^{3}H or ^{147}Pm), older camera lenses (may contain ^{232}Th), granite monuments and countertops (with varying amounts of natural uranium), ceramic tiles (may contain U, Th, and K), glassware (the older glassware may contain uranium, especially those with a yellowish or greenish tint), ceramic pottery (especially a type known as Fiesta, for which the red color was made with uranium oxide before 1959), fertilizer (the high potassium content includes ^{40}K and phosphate-based fertilizers may contain U), and food (also containing ^{40}K, especially bananas or potatoes). Kitty litter, being a clay product, also contains ^{232}Th. Electric arc welding is sometimes done with welding rods that contain thorium in order to more easily start and stabilize the arc. These are not regulated by law in the U. S., and these can sometimes be detected. In addition, some parts fabricated with these welding rods may also contain enough thorium to be detectable.

TENORM typically involves the waste byproduct of some industrial or mining process. One example is production wastes from geothermal energy power stations, which may contain elevated levels of ^{226}Ra and ^{228}Ra. These, however, are truly waste products, and unlikely to appear in commercial cargo. However, equipment used in these activities may become contaminated and might be detected for high radiation levels when it is transported. An example would be from oil and gas drilling, where the scale on pipes and tanks can reach 100,000 pCi g^{-1} [4]. Before these elevated levels were recognized, many old pieces of drilling equipment were recycled into steel beams, plumbing pipes, and so forth, so that occasionally these ordinary objects in commerce will set off radiation alarms at inspection points.

Recent experience has also shown that there have been a number of nuisance alarms observed for stainless steel items in commerce containing ^{60}Co [3]. Materials with levels up to 600 Bq g^{-1} have been detected. This is usually caused by an "orphaned" ^{60}Co source being mixed with ferrous scrap metal before it is forged into stainless steel. The countries of origin for this contaminated stainless steel have been Canada, China, India, Taiwan, and Zambia. Examples of materials contaminated with ^{60}Co have included eating utensils, elevator buttons, jewelry, and pet dishes, among others. This has led to the rise of radiation portal monitors at the intake of scrap metal yards in some countries, but the practice is hardly universal at this time. Typically, a cargo container showing elevated levels of ^{60}Co must be returned to the country of origin, even if only one item in the container is radioactive. This has created a significant burden for customs clearing points around the world.

2.8 Medical Isotopes

Medical isotopes injected in people also are quite prevalent (about 1 in 2600 Americans has a detectable level at any given time) and can occasionally set off radiation alarms [2]. These represent the largest number of false alarms for passenger vehicles at border crossings with radiation portal monitoring, but also can occur with truck drivers going through container freight cargo monitoring. The most prevalent isotope found is ^{99m}Tc, which is used for diagnostic imaging. Other isotopes which can be seen are ^{57}Co, ^{51}Cr, ^{67}Ga, ^{123}I, ^{131}I, ^{111}In, ^{153}Sm, and ^{201}Tl. Despite the lower number of procedures done with ^{131}I, it is expected to have a high frequency of observation because of its long retention period in the body, coupled with an 8 day physical half-life and the production of two gamma rays in its decay (364.5 keV with BR = 81.7 % and 637 keV with BR = 7.3 %).

Medical isotopes in shipments contain a different suite of isotopes. Some are used for sterilization procedures, such as ^{60}Co, and ^{137}Cs, used in particular for blood transfusions [6]. These probably are a lower risk of a false alarm because they should be called out on a cargo's manifest.

3 Problems

1. A monitoring portal has a paved roadbed that container freight travels on while it is being surveyed for cargo. The paving is a six-inch thick layer of asphalt concrete containing a mixture (by weight) of 5 % asphalt and 95 % limestone. The limestone has a concentration of 2 parts per million (ppm) natural uranium by weight, and the asphalt has 4 ppm U. An overhead detector allows a cargo container to be driven under it, with one foot clearance from the top of the container.
   a. Assuming a detector area of 100 cm^2 and an efficiency at 185 keV of 20 % in the photopeak, find the counts per minute at the 185 keV ^{235}U photopeak in the detector, assuming that the roadbed is an infinite plane.
   b. Assume that when a container is under the detector, the 185 keV photons from the roadbed are completely blocked. Assume that the container has nothing inside except a spherical pit with 90.5 % enrichment in ^{235}U, located mid-center in the 8.5 ft-high container, i.e. 4.25 feet from the floor and directly under the detector. Find the mass of the spherical pit which would give three times the signal in the detector as the asphalt paving would.
   c. Repeat the calculation if the pit is inside a one-inch thick lead pig.
2. ^{233}U can be generated in a thorium breeding zone in a nuclear reactor by neutron capture on ^{232}Th. This is a fissile isotope and can potentially be used in a nuclear explosive. However, small amounts of ^{232}U ($t_{1/2} = 72$ y) will be present due to ^{233}U(n, 2n) reactions in the breeding zone. At the end of the ^{232}U decay chain is ^{208}Tl, with a 36 % branching ratio (see Fig. 6). The characteristic 2614.5 keV gamma is thus seen in 36 % of all ^{232}U decays. Assume secular equilibrium conditions apply and that a 5 kg spherical pit of ^{233}U is in the center of a cargo container (same source and detector conditions as Problem 1). Find the impurity level of ^{232}U in the pit which will result in a threefold increase over background 2614.5 keV gammas from thorium in soil at average concentration (8.5 ppm).
3. Weapon-grade Pu contains up to 7 % of isotope ^{240}Pu. This isotope has a substantial decay channel into spontaneous fission, with 920 neutrons per second per gram of material. Consider a 5 kg spherical pit of Pu ($\rho = 15.8$ g cm^{-3}), 7 % ^{240}Pu by weight, in the same conditions as above but with a neutron detector with 100 cm^2 area and 100 % efficiency at detecting thermal neutrons. Assume that the fast fission neutrons are moderated by material in the container, and the thermal neutron flux at the detector is 0.2 % of what the uncollided (fast) flux would be if all moderating materials were removed. Find the count rate at the detector, and compare this with the thermal neutron count rate that would be seen from cosmic rays. (For these calculations, ignore self-shielding and multiplication in the pit.)

References

1. Aucott TJ, Bandstra MS, Negut V, Chivers DH, Cooper RJ, Vetter K (2013) Routine surveys for gamma-ray background characterization. IEEE Trans Nucl Sci 60:1147–1150. doi:10.1109/TNS.2013.2251355
2. Kouzes RT, Siciliano ER (2006) The response of radiation portal monitors to medical radionuclides at border crossings. Radiat Meas 41(5):499–512. doi:10.1016/j.radmeas.2005.10.005. http://www.sciencedirect.com/science/article/pii/S1350448705002775
3. Sefzig R, Saha B, Stoppa G (2009) Co-60 contaminated stainless steel in Gemany - experiences and first steps. In: International Conference on Control and Management of Inadvertent Radioactive Material in Scrap Metal. http://www-ns.iaea.org/downloads/rw/meetings/tarragona2009/presentations-thursday/b-saha.pdf. Accessed 18 Dec 2014
4. U.S. Environmental Protection Agency: oil and gas production wastes. http://www.epa.gov/radiation/tenorm/oilandgas.html. Accessed 16 Dec 2014
5. U.S. Environmental Protection Agency: what kinds of consumer products contain radioactive materials? http://radiation.supportportal.com/link/portal/23002/23013/Article/23245/What-kinds-of-consumer-products-contain-radioactive-materials. Accessed 16 Dec 2014
6. World Nuclear Association: radioisotopes in medicine. http://www.world-nuclear.org/info/non-power-nuclear-applications/radioisotopes/radioisotopes-in-medicine/. Accessed 16 Dec 2014

Detection Statistics

Abstract Applied probability theory forms the basis for the analysis of signals from nuclear detection equipment. Both classical and Bayesian statistical methods have been applied to nuclear detection problems, and an introduction to the concepts important to these approaches is presented. The statistics of nuclear counting is presented from the classical probability calculations for independent random events, leading to Poisson and Gaussian statistical models. The concept of error propagation, where many concatenated processes produce sources of statistical fluctuations and are convolved together, is presented, and a real-world example is given for a scintillation detector. The use of detector data in decision-making is presented using confusion matrices, and the Bayesian viewpoint is explored here. The concept of the Receiver Operating Characteristic (ROC) is introduced. The use of binary classifiers is explored through the application of various machine learning algorithms to the problem of n/γ pulse-shape discrimination.

1 Classical and Bayesian Statistics

The classical definition of probability arises from the notion of the relative frequency of a certain outcome. The statistics of a coin toss, or the number of counts registered in a certain energy band from a radiation detector, certainly resonates with this basic concept. In classical probability theory, the statistics of prior events gives a number assigned as the probability that a certain event will occur in the future. This method is best served by experiments or processes that have precisely static or repeatable conditions. An alternative viewpoint is that numbers assigned as probabilities are measures of the degree of belief in a certain outcome, i.e. a number between zero and one representing the possibility that a certain hypothesis is correct.

One limitation of classical probability theory is that it loses its meaning when rare events are involved, and another is that it does not lend itself to finding causative effects for a certain outcome. Furthermore, we often desire a way to update a probability distribution as actual data becomes available, perhaps starting with no more than a conjecture about the possible distribution of outcomes.

At the heart of the Bayesian approach is Bayes's theorem. Suppose that we have a hypothesis H which might be used to describe a probability that a certain event E will

E.C. Morse, *Analytical Methods for Nonproliferation*, Advanced Sciences
and Technologies for Security Applications, DOI 10.1007/978-3-319-29731-6_4

happen. This hypothesis is given a priori, i.e. before the experiment is performed. The probability a priori that H is correct is given as P(H). Then experiments are performed. The probability event E happened is given by P(E). This probability is independent of any prior hypotheses, and can be thought of as the sum total response resulting from any of a set of mutually exclusive hypotheses. We can form a conditional probability P(E|H), which is the likelihood that event E would happen if H were true. But we can now look backwards and decide the probability that hypothesis H is true if event E is observed; this conditional probability is written as P(H|E). Because this probability requires that the experiment has already been run, it is called an a posteriori ("looking backward") probability. Bayes's theorem relates these concepts by reversing the order of event and hypothesis:

$$\mathrm{P(H|E)P(E)} = \mathrm{P(E|H)P(H)}. \tag{1}$$

And thus the (unknown a priori) P(H|E) is given by a ratio

$$\mathrm{P(H|E)} = \frac{\mathrm{P(E|H)P(H)}}{\mathrm{P(E)}}. \tag{2}$$

2 Counting Statistics

2.1 Energy Resolution Statistics

The previous chapter showed some energy spectra, taken with a solid state detector, for various background locations. Here we will discuss some of the basic physical and mathematical concepts that determine the properties of these spectra.

Radiation detection generally relies on the energy deposition of some particle in some medium, and the conversion of that energy deposition into a usable signal. A schematic of the general scheme is shown here as Fig. 1. Typically, the radiation

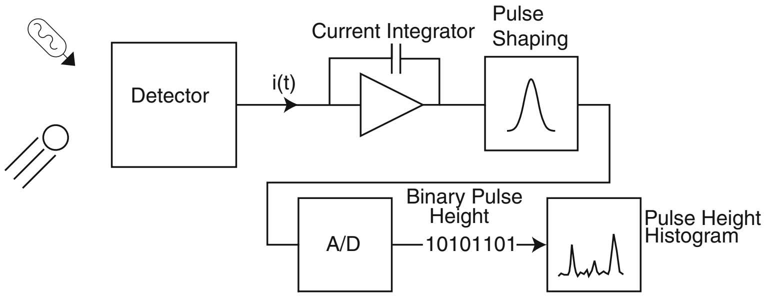

Fig. 1 Generic detector setup

(photons or particles) causes some process, such as light generation in scintillator materials, electron-ion pair production in gases, or electron-hole pair production in solid state materials. In the case of light production in a scintillator, the light is directed to a photomultiplier tube or a solid state photodiode. In the case of a gas-filled detector, electrodes with a an applied electrical potential collect the electron and ion charge. In the case of a solid-state detector such as germanium or silicon, electrodes on the outside of the detector collect electrons and allow for electrons to enter the detector and recombine with the holes. In all of these detector systems, the output signal is a pulse of electrons.

Typically this current signal has a structure in time that depends on where in the detector medium the event occurred, which particular levels in atomic transitions were excited, the direction of the spray of the electrons relative to the crystal structure in semiconductor detectors, and so forth. Because of these uncontrolled variables, it is common to shape this current pulse in such a way that the output analog signal pulse has the same shape every time, varying only in amplitude. These pulses can then be sent though an analog-to-digital converter (A/D), which then outputs a digitized representation of the total signal height, and thus a number associated with the energy deposited in the detector. A histogram can be generated with this digital pulse data, and more sophisticated data processing such as making correlations of this pulse data with coincident reports from other detectors can also be done using computer programs at this stage. Sometimes the raw, unprocessed detector current signal is analyzed as well, and this fast pulse shape information can be used to separate the data into different streams—for example, it is possible to discriminate between neutrons and gamma-ray photons in solid-state detectors using pulse shape information.

Before getting into the intricacies of the detector physics and the downstream electronics, let us look at the statistics applying to the detection process. Typically, many low-energy excitations are caused by the interaction of an energetic particle or high-energy photon in the material. Suppose that the average energy required to produce one electron in the output current pulse is $\varepsilon_{\mathrm{ehp}}$ (where "ehp" stands for "electron-hole pair") in the case of a solid-state detector, or $\varepsilon_{\mathrm{eip}}$ ("eip = "electron-ion pair") in a gaseous detector), or one photon ("hν") in the case of a scintillator, is $\varepsilon_{\mathrm{h}\nu}$. If the incoming particle has an energy E. then the average number $\bar{\mathrm{n}}$ of signal electrons or photons collected is

$$\bar{\mathrm{n}} = \frac{\mathrm{E}}{\varepsilon_{\mathrm{ehp}}} \quad \text{or} \quad \frac{\mathrm{E}}{\varepsilon_{\mathrm{eip}}} \quad \text{or} \quad \frac{\mathrm{E}}{\varepsilon_{\mathrm{h}\nu}}. \tag{3}$$

Suppose that each secondary electron or photon generated by the deposition of energy from the incident particle is independent of all other generated electrons or photons in the detector. We assume that a large number N_0 of sites in the detector could have potentially generated a secondary electron or photon and had that secondary electron or photon be represented in the outgoing current pulse. If the probability of a secondary electron or photon being generated at a single site is r, then the probability of a total of n electrons or photons being collected is

$$P(n) = \binom{N_0}{n} r^n (1-r)^{N_0-n}. \tag{4}$$

Here

$$\binom{N_0}{n} = \frac{N_0!}{n!\,(N_0-n)!} \tag{5}$$

We can take the limit of this expression as N_0 becomes large, noting that the average number of signal photons or electrons is

$$\bar{n} = N_0 r \tag{6}$$

and then

$$P(n) = \lim_{N_0\to\infty} \frac{N_0!}{n!\,(N_0-n)!} r^n (1-r)^{N_0-n} = \frac{\bar{n}^n}{n!} e^{-\bar{n}} \tag{7}$$

This is called the Poisson distribution. It has the property that its mean

$$\sum_{n=0}^{\infty} nP(n) = \bar{n} \tag{8}$$

and its standard deviation σ is given by

$$\sigma^2 = \overline{(n-\bar{n})^2} = \sum_{n=0}^{\infty} (n-\bar{n})^2 P(n) = \bar{n} \tag{9}$$

The Poisson distribution becomes unwieldly to use if $\bar{n} \gg 1$ as is often the case. For large values of $\bar{n}$, the distribution is approximated by a Gaussian distribution:

$$\bar{n} \gg 1 \;\rightarrow\; P(n) \approx \frac{e^{-(n-\bar{n})^2/(2n)}}{\sqrt{2\pi\bar{n}}} \tag{10}$$

Comparison of the Poisson distribution and its Gaussian approximation are shown for two values of $\bar{n}$ as Fig. 2. One can see that the Gaussian distribution is a reasonable substitute for the Poisson distribution with $\bar{n} = 10$, and almost perfect at $\bar{n} = 100$. It is customary in describing counting statistics to quote not the standard deviation σ but rather the “full width at half maximum”, or FWHM, for a distribution. The FWHM is the distance between the points in the distribution that are half the height of the peak, as shown in Fig. 3. These are related by:

$$\text{FWHM} = \sqrt{8\ln 2}\,\sigma = 2.35482\,\sigma. \tag{11}$$

Fig. 2 Comparison of Poisson and Gaussian distributions with $\bar{n} = 10$ and $\bar{n} = 100$

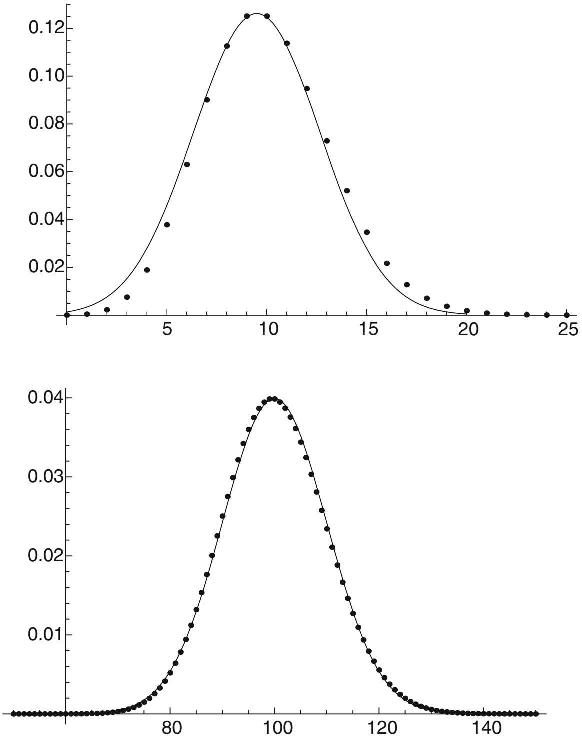

Fig. 3 Gaussian energy histogram, illustrating standard deviation and FWHM

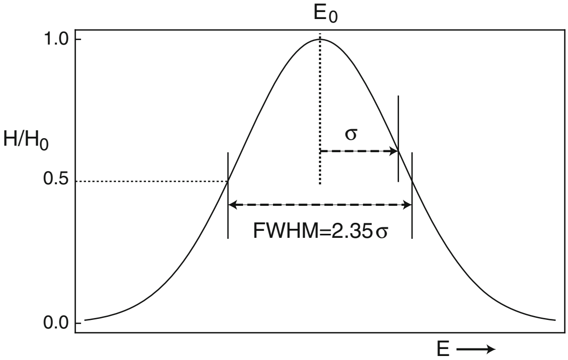

We often quote relative error for the probability distribution for a given measurement, which then produces a unitless result. The relative FWHM error ε (as percent) for a measurement with a mean value M is then

$$\varepsilon(\%) = 100\frac{\mathrm{FWHM}}{\mathrm{M}} \tag{12}$$

For the counting statistics problem discussed earlier, collecting an average of n̄ electrons has a relative error

$$\varepsilon(\%) = 100\frac{\mathrm{FWHM}}{\bar{\mathrm{n}}} = \frac{235}{\sqrt{\bar{\mathrm{n}}}} \tag{13}$$

Often times there are several sequential processes required to obtain a resulting piece of data. Typically each step in the process will introduce some error. Each step in the process can often be modeled as introducing some normally distributed relative error. ("Normally" distributed is a commonly used term for a distribution following Gaussian/Poisson statistics and is an unfortunate term because it implies that most distributions are Gaussian, and many distributions are not Gaussian but also not "abnormal"!) In such a case the final result contains a sum of the errors of each step in the process. If the sources of error are independent of one another, then the total relative error in the measurement with a chain of N steps will be given by

$$\varepsilon_{\mathrm{tot}}^2 = \varepsilon_1^2 + \varepsilon_2^2 + \cdots + \varepsilon_{\mathrm{N}}^2 \tag{14}$$

We now can apply this result to a typical detector. Suppose that we have a thallium-activated sodium iodide NaI(Tl) scintillator detector which has a photomultiplier tube attached to the NaI crystal to collect the incident light. Reference [7] gives some details of performance measurements on this detector system. The scintillator material has an average energy for the production of a scintillation photon $\varepsilon_{\mathrm{h}\nu}$ of 15.0 eV. However, not all photons are collected at the scintillator photocathode and some of these photons do not produce a photoelectron; the authors of [7] found that on average it takes 62.5 eV of deposited energy to produce one photoelectron. Consider detection of a 662 keV gamma ray from the decay of ^{137}Cs, a commonly used standard laboratory source. Using the results above, a 662 keV gamma ray would produce $\bar{n} = 662{,}000/62.5 = 10{,}592$ photoelectrons on average; this would produce a relative energy resolution given by

$$\%\mathrm{FWHM}_{\mathrm{pe}} = \frac{235}{\sqrt{10592}} = 2.28\,\% \tag{15}$$

However, as Ref. [7] shows, the Poisson statistics of the produced photoelectrons do not tell the entire story. There are other sources of random error in play as well. In addition to the Poisson statistical variation, the system has a source of electronic noise due to thermal effects on the photocathode, noise in the resistors in the biasing string, in the dynodes, and in subsequent amplification stages. State-of-the-art systems have an electronic noise equivalent to 470 electrons at 662 keV and this results in an electronic noise relative energy spread of $\%\mathrm{FWHM}_{\mathrm{en}} = 470/10592 = 4.43\,\%$, almost twice as large as the Poisson statistical variation. Additionally, electrons produced by Compton scattering or by the photoelectric effect by the primary gamma ray in the scintillating medium may not produce scintillation photons in a directly linear way, and this produces another error term (called the "intrinsic resolution due to nonlinear electron response") $\%\mathrm{FWHM}_{\mathrm{in}} = 3.6\,\%$. Also, the efficiency of light collection into the photomultiplier photocathode varies depending upon where the primary photon deposited its energy and this produces a "collection loss" variation $\%\mathrm{FWHM}_{\mathrm{cl}} = 4.5\,\%$. The variances in these error terms, presumed to be independent, add linearly:

$$\sigma^2 = \sigma_{\mathrm{pe}}^2 + \sigma_{\mathrm{en}}^2 + \sigma_{\mathrm{in}}^2 + \sigma_{\mathrm{cl}}^2 \tag{16}$$

or equivalently

$$(\%\mathrm{FWHM})^2 = \left(\%\mathrm{FWHM}_{\mathrm{pe}}\right)^2 + (\%\mathrm{FWHM}_{\mathrm{en}})^2 + (\%\mathrm{FWHM}_{\mathrm{in}})^2 + (\%\mathrm{FWHM}_{\mathrm{cl}})^2 \tag{17}$$

which for this example gives a %FWHM of $\sqrt{2.28^2 + 4.4^2 + 3.6^2 + 4.5^2} = 7.6\,\%$ at 662 keV for a state-of-the-art NaI scintillator, or an energy resolution of about 50 keV FWHM. Actual measurements confirm a resolution only slightly worse than this at around 7.7 % [7].

However, even this lackluster energy resolution may compare favorably to actual field conditions using this type of detector. Sodium iodide has a substantial drift in scintillation photons produced per incident photon as a function of temperature, and field conditions may range from below freezing to above 40 °C. Vibration may be present, which can cause variation in the photomultiplier's dynode amplification and thus decrease the energy resolution. Purely random electronic noise can be augmented by unwanted interference from strong radiofrequency signals or low-frequency magnetic fields due to power transformers or electric motors. Over time, even well-sealed NaI crystals, the material being an inorganic salt and very hygroscopic, can pick up moisture causing a gradual decrease in light output.

The statistical story with solid-state detectors has a happier chapter. Charge collection efficiency is very high for a solid-state detector. The electron-hole pair energy is also much lower than the photon production energy in a scintillator. But also significantly, the generation of electron-hole pairs has some aspects of being a correlative and collective process, i.e. not being governed by the Poisson statistics of multiple independent processes. The energy level that one valence electron gets "promoted" to affects where another promoted electron might go, resulting in a less-than-random process in the generation of a number of electron-hole pairs. The so-called Fano factor gives a quantitative figure for this as a ratio of observed variance in electron hole pairs to that predicted from Poisson statistics with the same average number of electron-hole pairs. Thus:

$$\mathrm{F} = \frac{\sigma_{\mathrm{obs}}^2}{\sigma_{\mathrm{pred}}^2} = \frac{\sigma_{\mathrm{obs}}^2}{\bar{\mathrm{n}}_{\mathrm{ehp}}} \tag{18}$$

Since the energy resolution $\Delta\mathrm{E(FWHM)/E} = 2.35\sigma/\bar{\mathrm{n}}_{\mathrm{ehp}}$, we have

$$\Delta\mathrm{E} = 2.35\sqrt{\mathrm{E}_\gamma \varepsilon_{\mathrm{ehp}}\mathrm{F}}. \tag{19}$$

Fano factors in germanium at 77 °K have been reported to be lower than 0.08 [6]. For example, in [6], the authors show the results for a Ge detector with a resolution ΔE of 1.30 keV FWHM at the 1.333 MeV line in ^{60}Co, or better than 0.1 % energy resolution. The resolution of the test pulser (an indication of electronic noise) $\Delta \mathrm{E}_{\mathrm{en}}$ was around 140 eV. Since the observed width includes the electronic noise, which adds in quadrature to the total width as before, the derived statistical width would be $\Delta \mathrm{E}_{\mathrm{stst}} = \sqrt{\Delta \mathrm{E}_{\mathrm{obs}}^2 - \Delta \mathrm{E}_{\mathrm{en}}^2} = 1292\,\mathrm{eV}$. This gives a Fano factor equivalent to (using an electron hole pair energy of 2.96 eV for Ge)

$$\mathrm{F} = \frac{(\Delta \mathrm{E}_{\mathrm{stst}})^2}{\mathrm{E}_{\gamma}\varepsilon_{\mathrm{ehp}} 8 \ln 2} = 0.0763. \tag{20}$$

Note that electronic noise can also be lower in solid state detectors than in scintillator/photomultiplier detectors, because the high electron yield from the detector competes favorably with the equivalent electrons of noise in the preamplifier, and also because the first stage of the electronic amplification is usually cooled by the liquid nitrogen bath provided for the Ge crystal.

2.2 *More on Error Propagation Statistics*

Frequently operations are done on statistical data to arrive at a final result. As mentioned in the previous section, if each step is a sequential part of the data processing, then in general the relative errors add in quadrature. Another interesting application is the error estimation for spectra which have been manipulated by background subtraction. Figure 4 shows the results of a computer simulation, where a 662 keV gamma line is shown in a background radiation continuum. Here a random normal distribution containing a random number of counts (with a mean number of 1000 and a standard deviation of $\sqrt{1000}$), with a mean of 662 keV and a standard deviation of 0.9 keV was combined with a random gamma distribution (in the mathematical sense, not the physics sense of gamma) representing a Compton continuum. (For the simulation, a random number (normally distributed with a mean of 1,000,000 and a standard deviation of $\sqrt{1{,}000{,}000}$) of counts were generated with energies upto about 7.0 MeV.) The background subtraction was done by summing the adjacent channels labeled “A” and “B” on the spectrum and subtracting that number, scaled by the ratio of the number of peak channels to the number of background channels, from the total raw counts in the peak channels. The experiment was repeated 100 times, and a histogram of the calculated background subtracted counts is shown. The standard deviation of this calculated result was 65.56, in good agreement with the square root of the average total counts in the peak channel (≈64.76). This shows that the masking of the background-subtracted counts by the background is real. If we had naively calculated the standard deviation in the counts by taking the square root of the background-subtracted count only, we would be deluding ourselves. As

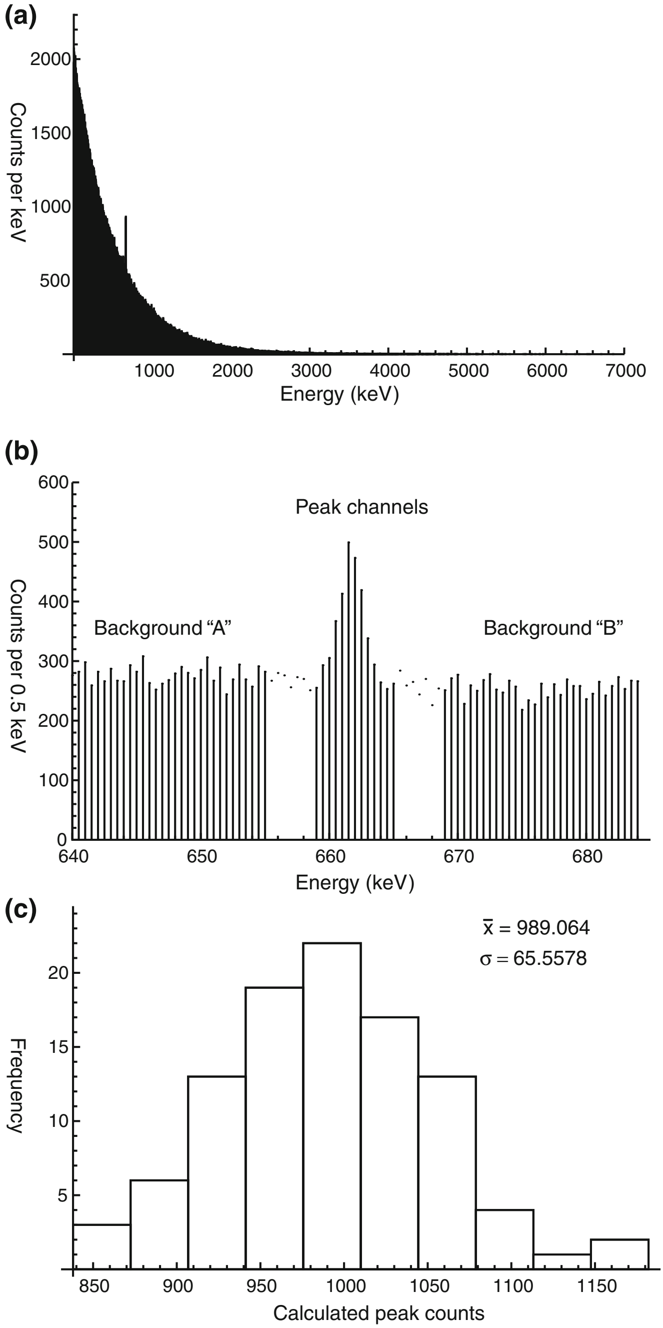

Fig. 4 Simulated spectrum for a 662 keV gamma ray line with background. **a** Simulated spectrum containing a 662 keV line and background continuum. **b** Close-up of count histogram around the line. Channels used for background subtraction are shown. **c** Histogram of calculated counts in photopeak from 100 trials with random data

an example, one of the 100 trials gave a result of 845 counts after background subtraction. Since $\sqrt{845} = 29.07$ and had we quoted our result as $\bar{n} \pm \sigma = 845 \pm 29$, we might have thought that the correct answer for the average (1000 counts) was different from our experiment by more than five standard deviations and dismissed this (the true average) as being virtually impossible.

More sophisticated peak-fitting algorithms exist than the simple-minded procedure given here, but the important point is that the statistics of background subtraction process are heavily weighted towards the background when it is larger than the signal involved. No algorithm exists that can make the statistical uncertainty due to the background go away.

Finally, we note that if there is a quantity $f(x, y)$ derived from two uncorrelated experimental measurements x and y, with errors Δx and Δy following a normal distribution of error, then the error Δf is given by

$$\Delta f = \sqrt{\left(\frac{\partial f}{\partial x}\right)^2 \Delta x^2 + \left(\frac{\partial f}{\partial y}\right)^2 \Delta y^2} \tag{21}$$

As a simple example, if a ratio between two counts are required, i.e. $f = x/y$, then the result given earlier for relative error reappears:

$$\frac{\Delta f}{f} = \sqrt{\left(\frac{\Delta x}{x}\right)^2 + \left(\frac{\Delta y}{y}\right)^2} \tag{22}$$

The key requirement, however, is that in order to use the general expression for error propagation, the quantities x and y as they appear here must be truly uncorrelated. As an example, suppose that x represented the total counts in a spectrum between 295 and 305 keV and y represented the total counts between 300 and 310 keV. The overlap of the data ranges shows that the two measurements would be correlated and the error analysis given for the ratio, or any other algebraic combination of these results, would be wrong.

3 Confusion Matrices

We now turn our attention to what to do with detection data once we obtain it from a detection system. Suppose that we are screening cargo containers for nuclear or radioactive material. We may set a limit so that if the counts obtained from the detection in certain channels, or some combination of signals from several detection systems, exceeds that limit, then further action should be taken. That action can include a re-trial of the detection process with a longer counting time, subjecting the load to a more revealing test such as some active detection process (i.e. using a source of neutrons or photons to generate a return signal from inside the cargo), impounding the container for a physical inspection at some other location, or sending in a haz-mat

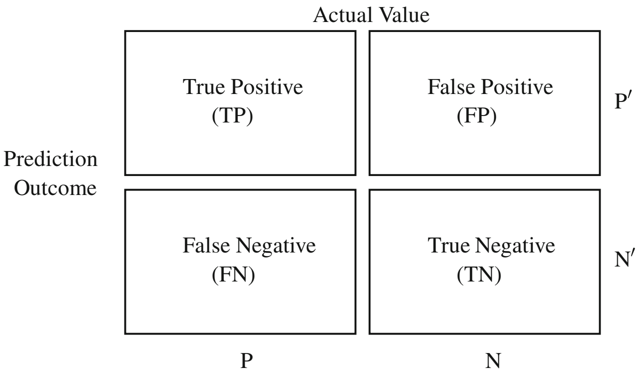

Fig. 5 The confusion matrix

team if it is truly hazardous. While the point of the detection process is the beneficial interdicting of nuclear or radioactive material, possible false alarms could slow the movement of cargo. The negative effect on commerce of a substantial impediment to cargo movement would be very serious. In other words, while failure to detect special nuclear material (SNM) in cargo can have an obvious negative consequence, generating many false alarms can be devastating in another way.

The function of detection systems (also called classifiers) was formalized during World War II with the development of radar systems. We create a simple construct called a “confusion matrix” [3, 8]. We take the simplest possible system where the actual status of an object under test is either positive (P) or negative (N). The test system is used on the object and returns a result P′ if the object tests positive and N′ if the object tests negative. Figure 5 shows the layout of the confusion matrix.

We note four possible outcomes for the test: a true positive (TP), also called a a “hit”, a true negative (TN), also called “correct rejection”, false positive (FP), also called a a “false alarm” or a “Type I error”, a false negative (FN), also called a “miss” or a ’Type II error”.

We then assume that a number of tests have been carried out and we can make various ratios of the number of outcomes for TP, FP, FN, and TN. The “Accuracy” is defined as the ratio of total correct tests to the total tests performed, or

$$\mathrm{ACC} = \frac{\mathrm{TP} + \mathrm{TN}}{\mathrm{P} + \mathrm{N}}. \tag{23}$$

The “Sensitivity”, or the “True Positive Rate” (TPR), or the “Hit Rate”, or the “Recall” is given by

$$\mathrm{TPR} = \frac{\mathrm{TP}}{\mathrm{P}} = \frac{\mathrm{TP}}{\mathrm{TP} + \mathrm{FN}}. \tag{24}$$

The “False Positive Rate” (FPR), also called the “Fall-out”, is given by

$$\mathrm{FPR} = \frac{\mathrm{FP}}{\mathrm{N}} = \frac{\mathrm{FP}}{\mathrm{FP} + \mathrm{TN}}. \tag{25}$$

The “False Negative Rate” (FNR), is given by

$$\mathrm{FNR} = \frac{\mathrm{FN}}{\mathrm{P}} = \frac{\mathrm{FN}}{\mathrm{FN} + \mathrm{TP}}. \tag{26}$$

The “Specificity” (SPC) or “True Negative Rate” (TNR) is given by

$$\mathrm{SPC} = \mathrm{TNR} = \frac{\mathrm{TN}}{\mathrm{N}} = \frac{\mathrm{TN}}{\mathrm{FP} + \mathrm{TN}} = 1 - \mathrm{FPR}. \tag{27}$$

The “Positive Predictive Value” (PPV) or “Precision” is given by

$$\mathrm{PPV} = \frac{\mathrm{TP}}{\mathrm{TP} + \mathrm{FP}}. \tag{28}$$

The “Negative Predictive Value” (NPV) is given by

$$\mathrm{NPV} = \frac{\mathrm{TN}}{\mathrm{TN} + \mathrm{FN}}. \tag{29}$$

The “False Discovery Rate” (FDR) is given by

$$\mathrm{FDR} = \frac{\mathrm{FP}}{\mathrm{FP} + \mathrm{TP}}. \tag{30}$$

Figure 6 shows four examples of confusion matrices with different results. Example A shows the results for a detection system with fair utility, but far from perfect. Example B has the same TPR and FPR, which implies that there is no correlation between the measured outcome and the actual data and therefore the test would be equivalent to performing a (weighted) coin toss to obtain an outcome, and is therefore useless. Example C shows a worse-than-random outcome: the system reliably gets the wrong answer. However, this test passes information, and therefore the output could be differently interpreted. By inverting the definitions of the test’s outcome, we arrive at test D (which we might call $\bar{\mathrm{C}}$), which is better in all respects (higher TPR and TNR, lower FPR and FNR) than test A.

An additional test metric can be employed which is a bit more descriptive when there are unmatched numbers in each classification, e.g. if there are more actual negatives than positives. This is called the Matthews correlation coefficient [5], or MCC, and is given by

$$\mathrm{MCC} = \frac{\mathrm{TP} \cdot \mathrm{TN} - \mathrm{FP} \cdot \mathrm{FN}}{\sqrt{\mathrm{P} \cdot \mathrm{N} \cdot \mathrm{P}' \cdot \mathrm{N}'}} = \frac{\mathrm{TP} \cdot \mathrm{TN} - \mathrm{FP} \cdot \mathrm{FN}}{\sqrt{(\mathrm{TP} + \mathrm{FN})(\mathrm{FP} + \mathrm{TN})(\mathrm{TP} + \mathrm{FP})(\mathrm{FN} + \mathrm{TN})}}. \tag{31}$$

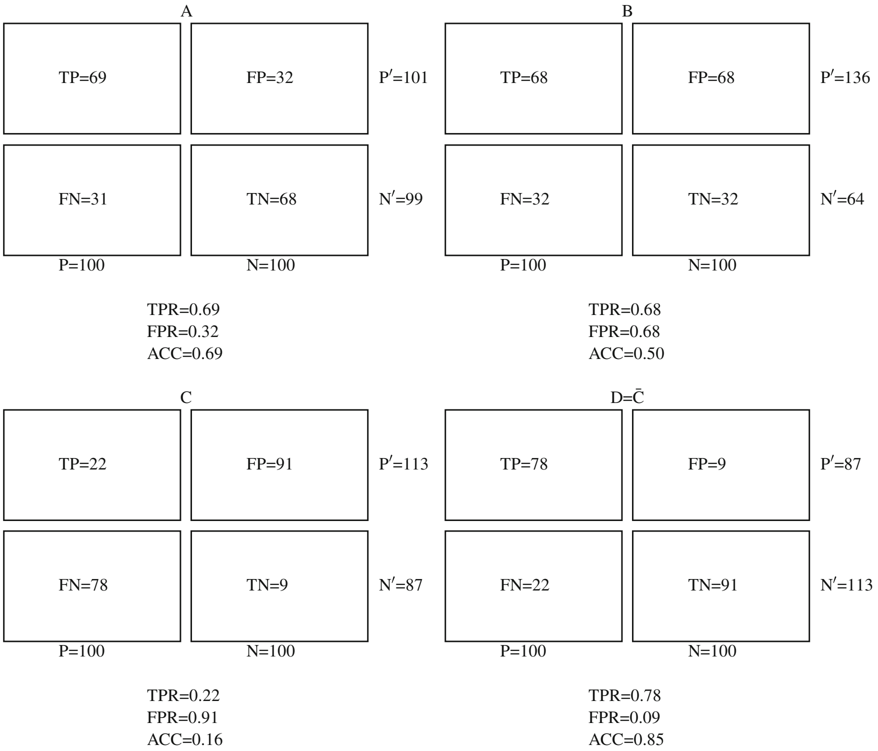

Fig. 6 Confusion matrices for four test algorithms

The MCC is always between -1 and $+1$. An MCC of zero means that the test is no better than random, and a negative MCC is a “worse than random” result, as in Example C in Fig. 6. The MCC is symmetrical in that if the outcomes are reversed in interpretation, the MCC is reversed in sign. For the examples given in Fig. 6, the MCC values are MCC{A, B, C, D} $= \{0.370, 0.0, -0.696, +0.696\}$.

Not all of these simple performance metrics given above do a good job at representing the quality of the test when the positives are a rare event. For example, suppose that nuclear material is in a cargo container with a one-in-a-million chance, but is never detected. The detector, however, clears clean cargo with a 99 % rate, getting a false positive rate of 1 %. Then we have (normalized to one) FN $= 10^{-6}$, TP $= 0$, FP $= 0.999999 \cdot 0.01 = 0.00999999$, and TN $= 0.999999 \cdot 0.99 = 0.989999$. The accuracy (ACC) is $(0 + 0.98999)/1 = 0.9899999$, which we might describe as “99 % accurate”, even though the test is useless! The MCC for this test is -0.0001, showing that the test is worse than random, although this result fails to display the true nature of the test’s inadequacy.

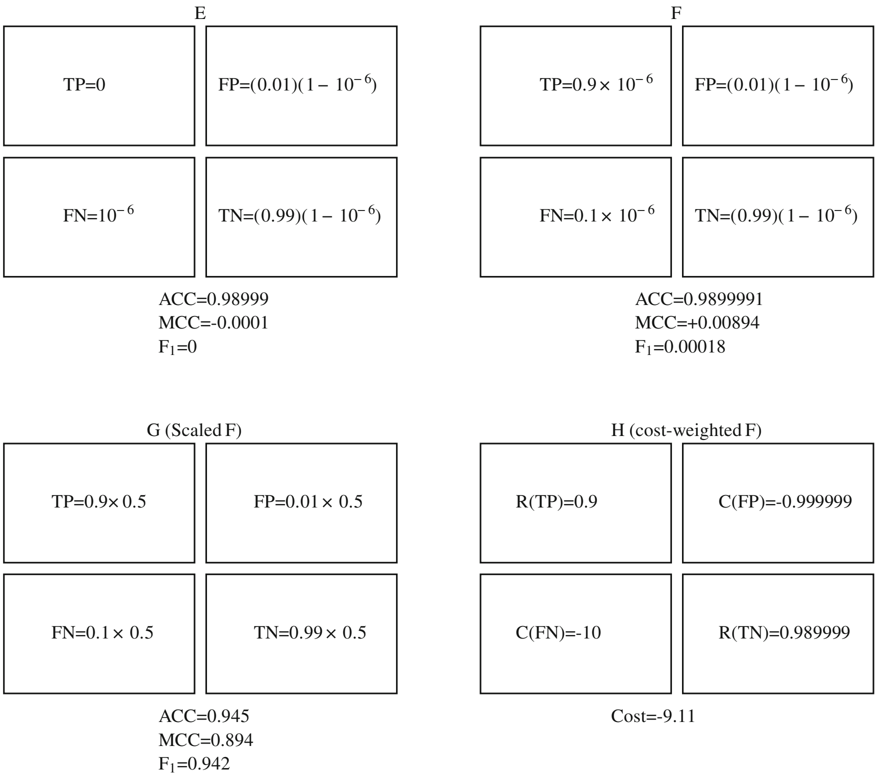

E

TP=0	FP=(0.01)$(1-10^{-6})$
FN=10^{-6}	TN=(0.99)$(1-10^{-6})$

ACC=0.98999
MCC=-0.0001
F_1=0

F

TP=0.9×10^{-6}	FP=(0.01)$(1-10^{-6})$
FN=0.1×10^{-6}	TN=(0.99)$(1-10^{-6})$

ACC=0.9899991
MCC=+0.00894
F_1=0.00018

G (Scaled F)

TP=0.9×0.5	FP=0.01×0.5
FN=0.1×0.5	TN=0.99×0.5

ACC=0.945
MCC=0.894
F_1=0.942

H (cost-weighted F)

R(TP)=0.9	C(FP)=-0.999999
C(FN)=-10	R(TN)=0.989999

Cost=-9.11

Fig. 7 Confusion matrices for four rare-event tests

A performance metric with some merit for rare event detection is called the F_1 test [4]. It is given by

$$F_1 = 2 \cdot \frac{\text{Recall} \cdot \text{Precision}}{\text{Recall} + \text{Precision}} = \frac{2\,\text{TP}}{\text{FN} + \text{FP} + 2\,\text{TP}}. \tag{32}$$

In order to test the properties of these performance metrics, a set of possible rare-event matrices were constructed. These are shown as Fig. 7. Figure 7 shows case E as the example given above, the “useless” test. For case F in this figure, we suppose that the detection system can detect true positives 90 % of the time. For this case, the figure of merit ACC only moves in the sixth decimal place, but the MCC and F_1 test show some movement, albeit only in the third or fourth digit. In order to highlight the need to detect true positives, another test was developed, where the number of true positives was made equal to the number of true negatives, i.e. the true positive number was increased by a factor of one million. This would be typical of a “red/blue” exercise by professionals in the nuclear security business, where they might plant cargo with SNM to see if another group could detect it, and not in one-in-a-million ratios during their tests. All three of the indices ACC, MCC, and F_1 then report high values. We then try another figure of merit: what if we try to multiply the outcomes by a cost/reward function germane to the process? For test H in Fig. 7, we look at the rewards (R) and costs (C) associated with the detection outcomes. Here a reward of 10^6 (e.g. dollars) is assumed for detection of SNM. The cost of not finding true SNM (the FN outcome) is assumed to be 10^8, i.e. the cost of a nuclear detonation in a city divided by the number of clandestine shipments required for a terrorist group to make a bomb. The cost of a false positive is assumed to be 100, on the order of the extra hours of paid time for the transporter involved in the interrogation. The reward for a true negative was placed at $+1.0$, an arbitrarily small value for business as usual, reflecting public opinion for support of the detection process. The result of this weighting scheme gives a "cost" for the test of -9.11, which would indicate that any improvement in the system would be beneficial in toto.

4 Receiver Operating Characteristics

We can apply the concepts of the confusion matrix to a graphical interpretation known as the Receiver Operating Characteristic, or ROC. This is a plot of the true positive rate (TPR) on the y axis versus the false positive rate (FPR) on the x axis. For the single-valued results as in examples A, B, C and D give above, this gives a plot of the four points. Figure 8 gives this plot for these four cases. In this figure, note that the line TPR = FPR is also drawn. This line is the result equivalent to random guessing as a detection test, and we note that case B was such a result and thus is on

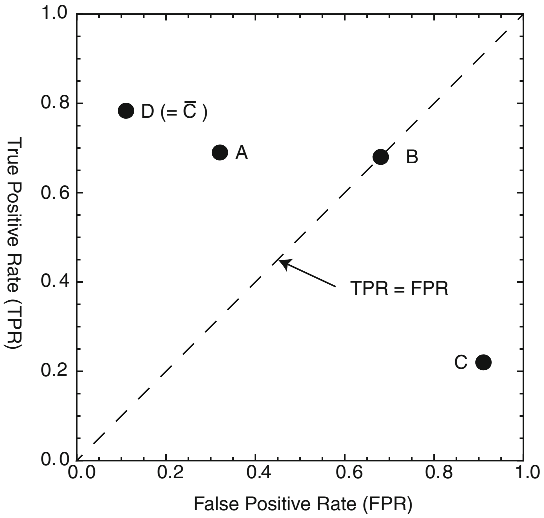

Fig. 8 Receiver Operating Characteristic (ROC) for Examples A, B, C, D

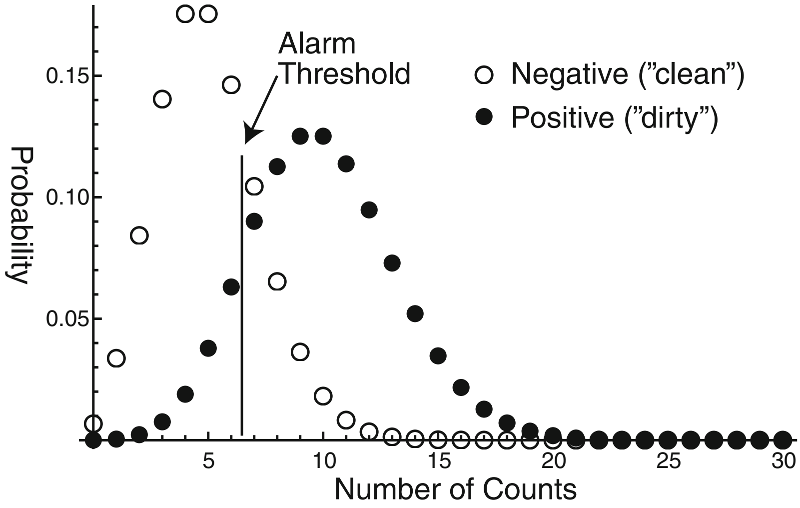

Fig. 9 Probability distributions for a negative ("clean") and a positive ("dirty") cargo used to calculate a receiver operating characteristic (ROC) for a detection system

this line. Also note that Case D, resulting form an inversion of the outcomes of case C, is mirrored about this line. In general, a measure of the test's quality is how close the point is to the ROC graph's upper left corner.

Frequently there can be a variable parameter involved in the binary classification process leading to a decision on whether a particular sample is considered to be a positive or a negative. In the context of nuclear counting, this is often done by setting a threshold value for the total counts in some energy range to be considered a positive. Figure 9 shows an example of this. Here a Poisson distribution of counts for a "clean" cargo with $\bar{n} = 5$ is shown along with a "dirty" cargo with $\bar{n} = 10$. Here the sum of the probabilities for the open circles to the right of the alarm threshold is the false positive rate and the sum of the probabilities for the filled circles to the left of the alarm threshold is the false negative rate (equal to 1-TPR). As the threshold is adjusted upwards or downwards, the FNR and FPR show a tradeoff effect. The effect of running the threshold from zero to infinity then results in a plot of TPR versus FPR as shown in Fig. 10. Notice in this ROC chart that there is a staircase effect caused by the integer nature of the count. The plot is extended horizontally to the right from the TPR of the last integer value until the next (FPR, TPR) ordered pair applies at the next integer number of counts. (In this case, the threshold is decreasing as the TPR and FPR increase.) Representing the ROC this way is the conservative approach to estimating the system performance.

As mentioned earlier, the ideal test in ROC space is close to the point (0,1), i.e. the upper left corner of the plot. As a method of describing the overall system performance, the notion of the "area under the (ROC) curve", or AUC, is often used as a performance metric for the detection system. Thus a system that produces

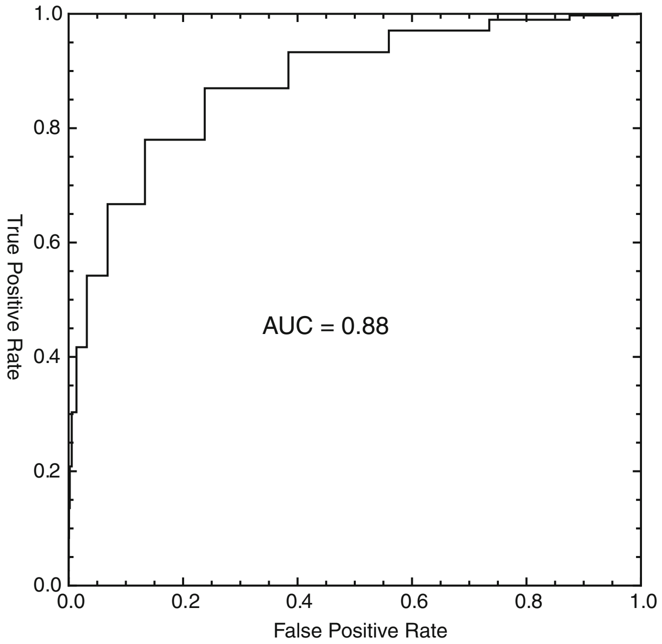

Fig. 10 Receiver Operating Characteristic (ROC) for the data in Fig. 9

identical FPR and TPR, but with both varying according to the threshold, would have an ROC curve that is a diagonal from (0,0) to (1,1), and the AUC would be 0.5. The AUC for the example given here is 0.88, showing a system with some merit, though hardly foolproof. If the individual ROC data points were connected by straight lines or spline curves, the AUC would be slightly higher at about 0.90, but that is not the usual conservative way that this figure is determined.

We now turn our attention to ROC curves generated by test systems that generate continuous data rather than discrete points. It is useful to imagine a system where the clean versus dirty responses are modeled by two normal distributions, for example. Figure 11 shows a model detection scheme where the negative and positive response signals are both normally distributed as

$$\begin{aligned} P_N(x) &= \frac{1}{\sqrt{2\pi}\sigma} \exp\left(-\frac{(x - \mu_N)^2}{2\sigma_N^2}\right) \\ P_P(x) &= \frac{1}{\sqrt{2\pi}\sigma} \exp\left(-\frac{(x - \mu_P)^2}{2\sigma_P^2}\right) \end{aligned} \tag{33}$$

with different values of μ (and possibly also σ) for the negative and positive distributions. The false positive signal is given by the fraction of the N distribution above the alarm point x_A; this is expressed as

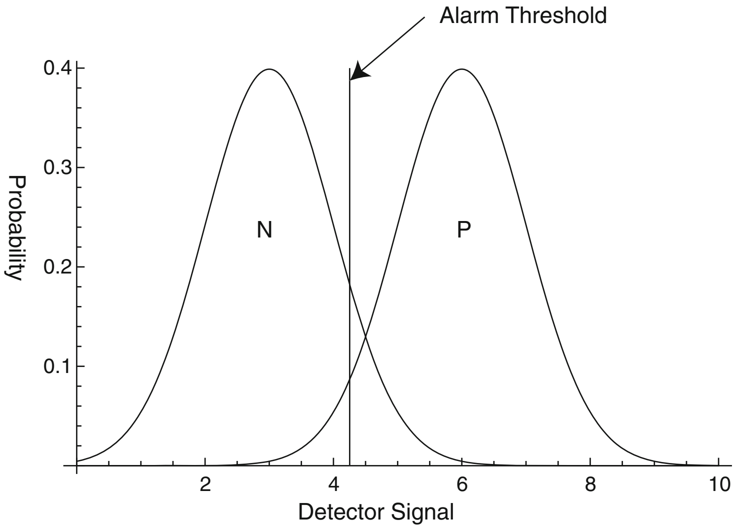

Fig. 11 Two-gaussian model for Receiver Operator Characteristic (ROC) data

$$\mathrm{FP}(\mathrm{x_A}) = \int_{\mathrm{x_A}}^{\infty} \mathrm{P_N}(\mathrm{x})\mathrm{dx} = \frac{1}{2}\mathrm{erfc}\left(\frac{\mathrm{x_A} - \mu_{\mathrm{N}}}{\sqrt{2}\sigma_N}\right), \tag{34}$$

where erfc(x) is the complementary error function, defined by

$$\mathrm{erfc}(\mathrm{x}) = 1 - \mathrm{erf}(\mathrm{x}) = 1 - \frac{2}{\sqrt{\pi}}\int_0^{\mathrm{x}} \exp\left(-\mathrm{t}^2\right)\mathrm{dt}. \tag{35}$$

Figure 12 shows ROC curves for four different two-gaussian probability distributions which differ by the distance between the normalized means z, given by:

$$\mathrm{z} = \frac{\mu_{\mathrm{P}} - \mu_{\mathrm{N}}}{\sqrt{\sigma_{\mathrm{P}}^2 + \sigma_{\mathrm{N}}^2}} \tag{36}$$

A simple expression for the area under the ROC curve, or AUC can be obtained:

$$\mathrm{AUC} = \frac{1}{2}\mathrm{erfc}\left(-\frac{\mathrm{z}}{\sqrt{2}}\right) = \frac{1}{2}\mathrm{erfc}\left(-\frac{\mu_1 - \mu_2}{\sqrt{2}\sqrt{\sigma_1^2 + \sigma_2^2}}\right) \tag{37}$$

The derivation of this result is somewhat lengthy and is given in Appendix B. Table 1 gives the ROC area for integer values of z for the two-gaussian model.

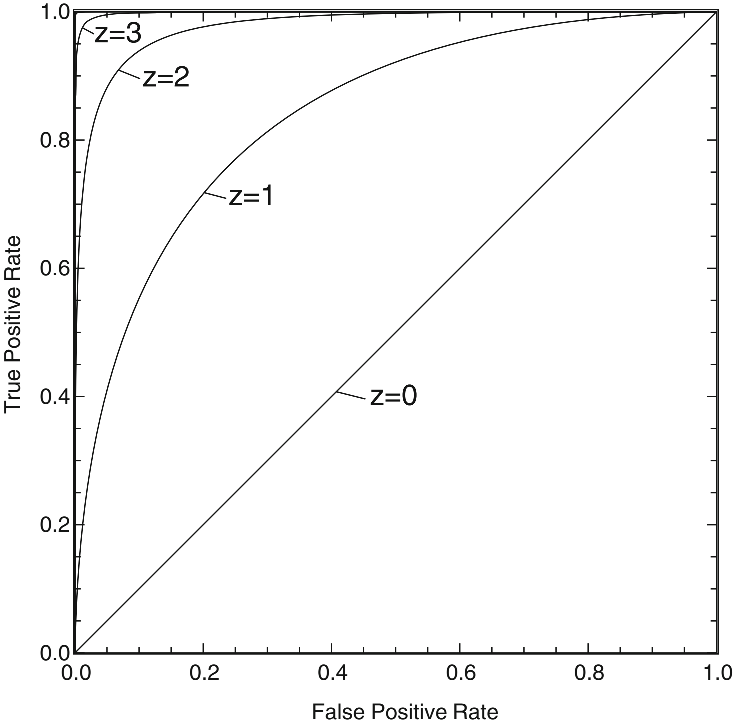

Fig. 12 Receiver Operating Characteristic (ROC) plot for two-gaussian model as a function of peak separation parameter z

Table 1 Table of AUC for integer values of z

z	AUC
0	0.5
1	0.84135
2	0.97725
3	0.99865
4	0.999968

5 Application of Bayesian Statistical Methods

We can apply Bayes's theorem to the confusion matrix concepts that started this chapter. Suppose that 0.1 % of cargo is loaded with SNM. The testing system has a probability of 95 % of detecting the SNM. The testing system has a false positive rate of 1 % for clean cargo. So what is the probability that a positive test result is a false positive? We let E be the outcome (a positive test) and H be the hypothesis (the cargo contains SNM). We know that $P(H) = 0.001$. The probability P(E) is given by

	Actual Value		
Prediction Outcome	TP=0.0095	FP=0.0099	P'
	FN=0.00005	TN=0.98901	N'
	P=0.001	N=0.999	

Fig. 13 Confusion matrix as an example of Bayes's theorem

$$\mathrm{P(E)} = \mathrm{P(E|H)P(H)} + \mathrm{P(E|\bar{H})} = 0.95 \cdot 0.001 + 0.01 \cdot 0.999 = 0.01094 \tag{38}$$

and then

$$\mathrm{P(H|E)} = \frac{\mathrm{P(E|H)P(H)}}{\mathrm{P(E)}} = \frac{0.95 \cdot 0.001}{0.01094} = 0.0868. \tag{39}$$

and thus the probability that a positive test is a false positive is $1 - 0.0868 = 0.913$, or 91.3 % of positive test results are false positives.

However, we don't have to use the Bayesian nomenclature to get this result. If we create the confusion matrix for this system, we get the following: $\mathrm{TP} = 0.001 \cdot 0.95 = 0.00095$, $\mathrm{FP} = 0.01 \cdot 0.999 = 0.0099$, $\mathrm{TN} = 0.99 \cdot 0.999 = 0.98901$, $\mathrm{FN} = 0.001 \cdot 0.05 = 0.00005$. The confusion matrix is shown as Fig. 13. The total positives are $\mathrm{P}' = \mathrm{TP} + \mathrm{FP} = 0.01094$ and the fraction of these that are false positives is $\mathrm{FP/(TP + FP)} = 0.9131$. Thus the confusion matrix "knows Bayes's theorem".

We can also use a set of confusion matrices to illustrate the automatic application of Bayes's theorem. Suppose that we have a detection system for cargo inspection with a neutron detector as well as several gamma-spectroscopy instruments. Because of the high spontaneous fission rate in plutonium as opposed to uranium, the confusion matrices for these systems are different. Suppose that we have the two confusion matrices as shown in Fig. 14. If we suppose that 50 % of weapon materials are uranium and 50 % are plutonium, and weapon material gets through, what is the a posteriorii probability that the weapon was plutonium? Let E be the event that nuclear material has evaded detection and H be the hypothesis that the material is plutonium. Using Bayes's theorem, P(Pu is undetected) = P(H|E) =1/12 and P(SNM is Pu) = P(H) = 1/2. Also we know that P(SNM is undetected) = P(B) = 3/24. Then P(SNM going undetected is Pu) = P(H|E)

Uranium

TP=10	FP=500
FN=2	TN=9500

Plutonium

TP=11	FP=500
FN=1	TN=9500

Fig. 14 Confusion matrices as an example of Bayes's theorem

$$= \frac{(1/12)(1/2)}{(3/24)} = \frac{1}{3} \tag{40}$$

But this result is obvious from reading the separate confusion matrices, since P(undetected SNM is Pu)

$$= \frac{\mathrm{FN(Pu)}}{\mathrm{FN(Pu)} + \mathrm{FN(U)}} = \frac{1}{1+2} = \frac{1}{3}. \tag{41}$$

Extensions of Bayesian methods can be made to more sophisticated prediction and decisionmaking alogorithms. For example, a classification scheme such as deciding whether a cargo is "clean" or "dirty" may be based on the inputs of many sensors. "Machine Learning" algorithms have been constructed whereby a set of measurements are obtained for known conditions, e.g. "clean" containers with various cargo including some with NORM or TENORM material, and HEU and Pu-containing cargo also with various other loads, and the measured signals coupled with the actual classification form the "training data" [2]. There are a number of different ways that these algorithms can be constructed, but a consistent feature is that the decision function can be iteratively modified, both to optimize its performance on the training data, but also in response to new data as it is introduced.

Non-Bayesian classifiers exist as well. One popular algorithm of this type, known as "Random Forest" [1], takes a set of decision "trees" (operators on the data yielding the predictor) generated with random weights and sensitivities, and scores each for its predictive performance. The algorithm tends to converge on an optimum score after many iterations. Other algorithms are based on forming surfaces in the multidimensional space formed by the data components, and classifying the sample data by its relation to these surfaces using various weighting schemes. The MATHEMATICA computer program, for example, has a function called "Classify", and has as options different classifiers, including "RandomForest", "LogisticRegression", "NearestNeighbor", "NaiveBayes", and "SupportVectorMachine".

6 Pulse Shape Discrimination as an Example of Binary Classification

A simple and practical example of a binary classification scheme arises from a technique sometimes employed with organic scintillators and BaF_2 scintillators as radiation detectors. In these detectors, the light response as a function of time depends on the type of particle involved. In the case of a plastic scintillator, gamma rays undergo Compton scattering of electrons, creating a cascade of electrons from subsequent electron-electron collisions as well as subsequent electron cascades from subsequent Compton-scattered gammas. The ranges of the electrons and scattered gammas are large enough so that the excited molecular sites are isolated from one another and the excitation involves largely singlet states. Neutrons, however, undergo proton recoil reactions, and the energy loss per unit length dE/dx for the recoil proton is much higher. This results in nearby molecules being excited, and this leads to the production of triplet molecular excitations, which decay by light emission more slowly. Thus the electronic pulses produced in the photomultiplier or photodiode downstream from the detector tend to be longer, and this can be exploited to discriminate neutrons (rare in cargo and potentially a sign of spontaneous fission of ^{240}Pu in plutonium, among other things) from gamma radiation (relatively common and causing more false positive alarms.) A typical method for separating the neutron and gamma signals is to take time integrations of the electronic pulse $V_s(t)$ with different lengths τ_1 and τ_2 (e.g. $\tau_1 = 100$ ns and $\tau_2 = 20$ ns for a typical plastic scintillator) and then compare the result:

$$V_1 = \int_0^{\tau_1} V_s(t)dt; \qquad V_2 = \int_0^{\tau_2} V_s(t)dt. \tag{42}$$

Figure 15 shows the typical output characteristics. (For this study, results of this type were generated with simulated data so that many trials could be performed.) Training data was generated by the same algorithm as shown in Fig. 15, but with N = 10,000. A set of test data with N = 10,000 was also generated. Then classification was done with the available 32-bit MATHEMATICA classifiers “LogisticRegression”, “NearestNeighbor”, “NaiveBayes”, and “SupportVectorMachine”. Table 2 shows the results for the classifiers available in 32-bit MATHEMATICA.

Notice the especially poor performance of the NaiveBayes classifier for the numerical test performed, with very high FNR and FPR statistics. This is due to the nature of the Bayesian algorithm when the two components of the test data are highly correlated—in this case, both data sets have the same basic shape, with the gamma data resembling a multiple of the neutron data. In order to study this, a training data set was prepared by removing a function representing an average of these two data sets:

$$\hat{V}_2 = V_2 - 0.9V_1^{0.8}, \tag{43}$$

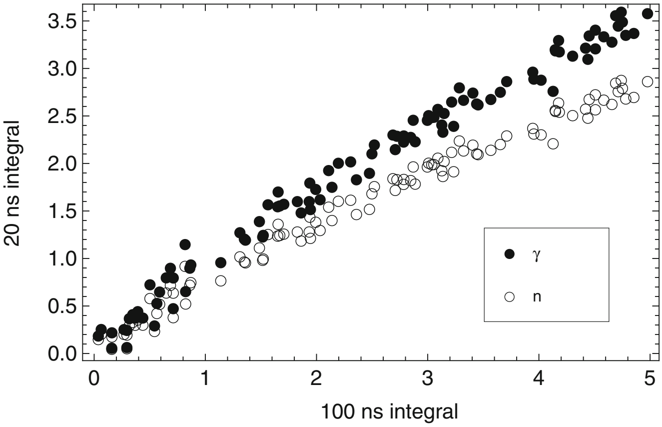

Fig. 15 Typical output from two-component analysis of scintillator pulses with gamma and neutron signals

Table 2 Performance of classifiers on γ/n pulse-shape discrimination data

Method	TPR	TNR	FPR	FNR
NaiveBayes	0.875	0.363	0.637	0.125
LogisticRegression	0.916	0.923	0.077	0.084
NearestNeighbor	0.923	0.945	0.055	0.055
SupportVectorMachine	0.912	0.954	0.046	0.088
not-so NaiveBayes	0.904	0.958	0.042	0.096

and the test data was treated similarly. This simple pre-conditioning of the data (labeled "not-so NaiveBayes" in the table) now had the lowest FNR of all of the tests. The other methods did not show significant improvement with a similar pre-conditioning, evidencing their ability to cope with highly correlated datasets.

Another feature available for these classifier methods is the ability to select data that is so close to the bounding surface that the data point can be labeled as "Indeterminate". While this feature might not be useful for an overall decision method (such as whether to accept or reject a cargo), it is a reasonable feature to consider when there are a multitude of counts to classify. For example, a run with N $=$ 2000 was performed with the SupportVectorMachine classifier with an IndeterminateThreshold of 0.999, i.e. only events with $p \geq 0.999$ were included; this resulted in TPR $=$ 1. FPR $=$ 0. FNR $=$ 0.0014, and TNR $=$ 0.9986—an almost perfect result, with a rejection rate (fraction of indeterminate findings) of 0.28. This can be thought of as trading a detection system with a 5–10 % inaccuracy for one with 70 % of the old system's efficiency, but deadly accurate—a trade that most detector designers would gladly make.

	Actual Value		
Measurement Outcome	5	595	P′
	51	5999	N′
	P=56	N=6594	

Fig. 16 Confusion matrix for Problem 1

As a final note, a user could identify (in this case, by eye) where the classification trouble will appear in the data. In this case, it is fairly obvious that the lower values of V_1 and V_2 tend to be within statistical noise. For the numerical experiment performed here, with $N = 2000$ and an IndeterminateThreshold of 0.995, giving a minimum threshold of $V_1 = 1.0$ resulted in six out of ten trials having FNR and FPR both zero, and the worst case had $\text{FNR} = 0.002$ and $\text{FPR} = 0.007$.

Clearly these algorithms can be "tailored" for an optimum performance based on sensitivity and acceptable error. In fact, one vendor of an electronic pulse shape discrimination device allows the customer a place to program a "bespoke" algorithm for this purpose, borrowing this term for custom tailoring of a suit.

7 Problems

1. A "confusion matrix" for a detection system tested in the field gives the following values (Fig. 16):
   a. Find the false positive rate and the false negative rate for this test.
   b. Find the Matthews correlation coefficient for this system.
2. Suppose that one in 10,000 cargo containers contains a kilogram quantity of plutonium. A passive neutron detection system is used to look for spontaneous fission neutrons from the container. The detector will sense the presence of the plutonium in a plutonium-bearing container with 99 % probability. A container with no plutonium will test positive using this system 2 % of the time. Given that a particular container tests positive, what is the Bayesian probability that this test is a false positive? Given that the test returns a negative, what is the probability that the test is a false negative?

3. A detection system has a one-minute counting time. It is known that the negative counts are distributed according to Poisson statistics with an average number of counts $\langle n \rangle = 10$. The positives have counts that also are distributed according to Poisson statistics with an average number of counts $\langle n \rangle = 20$. Draw a receiver operating characteristic (ROC) for this system. Use only discrtete values of n for this ROC, i.e. it should be a scatter plot of points.
4. Now replace the discrete Poisson statistics with Gaussian statistics, with distributions having $\mu_1 = 10$ and $\sigma_1 = \sqrt{10}$, and $\mu_2 = 20$ and $\sigma_2 = \sqrt{20}$. Draw the ROC for this with the results of Problem 3 superimposed. Find the area under the curve (AUC) for the Gaussian case and compare this a discrete integration of the above case using Simpson's rule.

References

1. Breiman L (2001) Random forests. Mach Learn 45(1):5–32. doi:10.1023/A:1010933404324
2. Dalal SR, Han B (2010) Detection of radioactive material entering national ports: a Bayesian approach to radiation portal data. Ann Appl Stat 4(3):1256–1271. http://www.jstor.org/stable/29765553
3. Fawcett T (2006) An introduction to ROC analysis. Pattern Recognit Lett 27(8):861–874. doi:10.1016/j.patrec.2005.10.010, http://www.sciencedirect.com/science/article/pii/S016786550500303X
4. Goutte C, Gaussier E (2005) A probabilistic interpretation of precision, recall and f-score, with implication for evaluation. In: Proceedings of the 27th European conference on advances in information retrieval research, ECIR'05. Springer, Berlin, pp 345–359. doi:10.1007/978-3-540-31865-1_25
5. Matthews B (1975) Comparison of the predicted and observed secondary structure of T4 phage lysozyme. Biochim et Biophys Acta (BBA): Protein Struct 405(2):442–451. doi:10.1016/0005-2795(75)90109-9, http://www.sciencedirect.com/science/article/pii/0005279575901099
6. Pehl R, Goulding F (1970) Recent observations on the fano factor in germanium. Nucl Instrum Methods 81(2):329–330. doi:10.1016/0029-554X(70)90569-0, http://www.sciencedirect.com/science/article/pii/0029554X70905690
7. Sasaki S (2006) Average energies required per scintillation photon and energy resolutions in NaI(Tl) and CsI(Tl) crystals for gamma rays. Jpn J Appl Phys 45:6420–6430. doi:10.1143/JJAP.45.6420
8. Wikipedia (2014) Receiver operating characteristic. http://en.wikipedia.org/wiki/Receiver_operating_characteristic. Accessed 14 Nov 2014

The Nuclear Fuel Cycle

Abstract Vast amounts of ore are mined to produce usable stocks of uranium due to the low concentration of uranium in the ores. The worldwide distribution of uranium ore is discussed. Next, the steps in preparing this material for processing in enrichment plants are described. Enrichment technologies, including gaseous diffusion, centrifuges, electromagnetic separation, and laser isotope separation, are described. The concept of the Separative Work Unit, or SWU, is introduced, and the mass balance calculations for an enrichment cascade are given. The proliferation potential for each of these schemes is described. Reactors are used to make plutonium, and the features making reactor types attractive or unattractive for weapon-grade plutonium production are described. Conversion of military material to civilian use is discussed, and proliferation risks in the waste stream are assessed.

1 Mining and Chemical Processing of Uranium

The first step is taking uranium ore out of the ground. Uranium ores vary widely in uranium content. The U concentration (by weight) for usable ore varies from just under 1 % down to about 0.05 %. This relatively low concentration means that shipping this material to some remote location for refining is not economical. Consequently, the refining process is typically co-located with the mining operation, and the uranium is extracted near the mining site in the chemically stable form U_3O_8, known as “yellowcake”. This also produces a waste stream at the refining site, known as “tailings”, which can be an important signature of U mining activity. In short, U mining is difficult to hide.

Table 1 shows the reserves of uranium by country. The data shown here from [7] are for recoverable resources with an extraction cost below USD 130/kg. Australia has not only the world’s largest supply, but also has U reserves in relatively high quality ore (about 0.13 % for most of its mines), making extraction costs low. Interestingly, the largest U mining operation in the world, at Olympic Dam in Australia, has ore with only 0.05 % U content, but the ore also contains gold, silver and copper, so that the U process stream is a “co-product” which makes the overall mining enterprise quite profitable. Australia has no commercial nuclear power plants, so

E.C. Morse, *Analytical Methods for Nonproliferation*, Advanced Sciences and Technologies for Security Applications, DOI 10.1007/978-3-319-29731-6_5

Table 1 World uranium reserves as of 2009

Known Recoverable Resources of Uranium (2009)		
Country	Tonnes U	Percentage of world (%)
Australia	1,673,000	31
Kazakhstan	652,000	12
Canada	485,000	9
Russia	480,000	9
South Africa	295,000	5
Namibia	284,000	5
Brazil	279,000	5
Niger	273,000	5
USA	207,000	4
China	171,000	3
Jordan	112,000	2
Uzbekistan	111,000	2
Ukraine	105,000	2
India	80,000	1.5
Mongolia	49,000	1
Other	150,000	3
World total	5,404,000	

Data from [7], Table 2

the extracted uranium oxide is almost certainly headed elsewhere. (Naturally, the Australian government monitors these movements very carefully.) At the other end of the spectrum, one should note that India has remarkably low available U reserves, and this has driven India's decision to develop a fuel cycle based on thorium as a fertile breeding material, which in turn generates fissile ^{233}U, causing a rather different proliferation scenario, since no isotope separation is required.

2 UF_6 Conversion and Enrichment

The next step in the fuel cycle is the conversion of U_3O_8 into uranium hexafluoride gas, UF_6. UF_6 is stable but highly corrosive, and must be handled in containers, valves, and piping that are chemically compatible. The reason for conversion to UF_6 is that this gaseous form lends itself to every type of isotope production process for the next step.

Natural U has an enrichment (^{235}U/total U by weight) of 0.71 %. With a few exceptions (such as heavy-water moderated reactors such as CANDU), most nuclear power plants require fuel with an initial enrichment of between 3 and 5 %. Thus an enrichment step is required. The details of the enrichment technologies will be discussed later. The most common enrichment process today is the gas centrifuge, but other options include gaseous diffusion, electromagnetic separation, and laser separation. A typical throughput to support a 1000 megawatt electric (MWe) power plant is on the order of 200 tonnes U per year, or about 290 tonnes of UF_6. Each type of U enrichment results in enriched product (the "heads") and a depleted uranium stream (the "tails").

Following the enrichment process, the enriched UF_6 is converted into the particular fuel format desired at a fabrication facility. The most common fuel type is uranium dioxide (UO_2) fuel, typically as small cylindrical pellets of ten to twelve mm diameter and a similar length. These pellets are loaded into fuel pins, typically about three meters in length, and made of a chemically compatible alloy such as the zirconium alloy Zircaloy. These pins are then bundled together into square or round units containing anywhere from thirty to almost three hundred pins. Alternative fuel formats are under development. One example is a spherical "pebble" made of uranium carbide and coated with silicon carbide, for use in a gas-cooled pebble bed modular reactor (PBMR).

The tailings are depleted uranium (called DU), typically 0.2–0.4 % enriched. This material has certain non-nuclear applications, such as aircraft counterweights and as a replacement for lead in ammunition. It is considered to be of little strategic value. However, it can be used to fabricate so-called mixed oxide, or MOX, fuel made of DU and recycled plutonium bred in prior batches of nuclear fuel. At this point the quantities of material are much smaller, since a 1000 MWe reactor need only consume about 24 tonnes of uranium (or about 27 MT of UO_2) per year. On the other hand, the tailings represent the rest of the process stream, or about 250 MT of UF_6 per thousand MWe-years. As a result, for example, there is now over a billion pounds of DU in the American stockpile.

3 Post-reactor

At the back end of the fuel cycle, the fuel becomes spent nuclear fuel. Because of its high radioactivity, it is usually stored in a spent fuel pool near the reactor, sometimes even in the same building, for at least several years. Many reactors in the United States have all of the spent fuel still on site since the reactor was started up. Because of the fertile conversion of the ^{238}U into ^{239}Pu and then into higher isotopes of Pu, Np, Am, Cm, and Cf, some of which have large fission cross sections, this material is considered to be a risk for proliferation, and these materials are carefully inventoried and monitored. The very high radiation levels associated with spent fuel, however, make it a very risky target for a small-scale operator to handle.

Some countries (France, Russia, Japan, among others) are now reprocessing spent nuclear fuel in order to provide fresh fuel for nuclear power plants. The general objective is to combine the Pu isotopes produced by fertile conversion in the spent fuel with recycled uranium in MOX form. Typically the reprocessing is done by chemically separating the transuranic (TRU) elements (Pu, Np, Am, Cm, and Cf) from the spent fuel. Eventually a fairly pure stream of Pu can be obtained through a long set of solvent extraction processes. In one of the oldest and most well-known processes, “PUREX” (for “Plutonium Uranium Redox EXtraction”), spent fuel rods are first cut up with a chop saw and then dissolved in a $\approx$7 M nitric acid solution. After some solids are removed, the solution is treated with an organic solvent such as kerosene combined with tributyl phosphate (TBP). This causes the U and Pu complexes, which become nitrate-TBP compounds that are soluble in the organic solvent, to separate from the fission products and other TRU in complexes that are water-soluble. Then the U and Pu-bearing organic phase is treated with ferrous sulphamate, changing the Pu compound into a water-soluble compound, thus separating the U from Pu in another solvent extraction step. Other steps are required to separate the other TRU from fission products, and to separate other useful isotopes such as technetium from the process.

While the PUREX process is fairly well-understood, it is not without its risks. The process involves highly corrosive materials combined with organic solvents that pose a combustion risk, and huge amounts of radioactivity are to be found in the fission product stream. From the standpoint of nuclear proliferation, a group wishing to steal spent nuclear fuel and then to reprocess this spent fuel with a process such as PUREX stand a good chance of killing or injuring themselves unless they had the in-depth skill and experience required.

It is also important to note that spent nuclear fuel from power reactors typically has seen very high values of neutron fluence. A standard metric for describing burnup of the fuel is the number of megawatt-days of power produced per tonne of U and Pu (“heavy metal”), or MWd/THM. Modern reactors run with fuel burnup of up to 60,000 MWd/THM. At this level of total neutron fluence, the amount of ^{240}Pu exceeds the amount of ^{239}Pu in the fuel. Since ^{240}Pu has a substantial spontaneous fission rate, this makes generating a workable nuclear weapon very difficult. However, there is a caveat: every fuel pin has a top and a bottom, and the flux is generally lower at the top and bottom of the reactor core. The lower-burnup pellets within the fuel pin have a lower ^{240}Pu/ ^{239}Pu ratio, and pose more of a proliferation risk. Therefore special attention should be paid to the physical handling of the spent fuel prior to the dissolution phase to avoid a diversion risk at this step.

4 Conversion of Military Materials

Today there is another source for enriched U and Pu for nuclear fuel. That is weapon-grade U and Pu from disassembled nuclear weapons. As the US and Russia gradually reduce the size of their weapon stockpiles, substantial quantities of material is available for “downblending” to make low-enriched U nuclear fuel or MOX fuel. The “Megatons to Megawatts” program, running from 1993 to 2013, was a successful program to provide nuclear fuel fabricated in this way. Under this program, over 500 tonnes of weapon-grade U was converted into low enrichment uranium (LEU) for use in reactors, supplying up to 10 % of the electricity in the US at certain times. If we assume an average U pit mass of 25 kg, this represents the destruction of 20,000 nuclear weapons. An agreement for continuation of this program after 2013 has not been reached as of this writing, but it will be likely in the future if energy prices rise, nuclear power demand increases, and arms reduction efforts are successful.

From a proliferation standpoint, downblending is of limited risk if the physical process occurs at a secure site co-located with the weapon-grade materials. If additional transportation is required for these weapon-grade materials to travel from military stockpiles to commercial fuel fabrication facilities, there is an element of risk. The 20-year example of Megatons to Megawatts shows that this option can be made practical and safe.

5 Waste Management

Some details of nuclear waste management are important to understand from a proliferation risk viewpoint. First, were the actinides in the spent fuel left in the waste product, or were they removed? Second, what is the format of the waste material? The waste can be vitrified, for example, before placing it in a canister. That adds a difficult reprocessing step to someone trying to reclaim the fissionable material in the future. Another question is the type of monitoring to be used at the waste repository. While above-ground cask storage has the obvious need for continuous surveillance, in-ground storage may not be designed with much surveillance in mind, and it might be possible for someone to attempt some "nuclear archeology" after tens or hundreds of years have passed.

6 Enrichment Technologies

Enrichment technologies for uranium isotope separation include gaseous diffusion, centrifuge, electromagnetic separation, and laser separation (AVLIS and MLIS). These will be discussed in order.

6.1 Gaseous Diffusion

A description of the first gaseous diffusion plant for enrichment of uranium built in Oak Ridge, Tennessee for the Manhattan Project was given in the famous Smyth Report [11]. The general idea behind gaseous diffusion separation is that the coefficient D that appears in Fick's law for permeation of a fluid species μ through a porous media

$$\mathrm{J}_{\mu} = -\mathrm{D}_{\mu}\,\nabla \mathrm{c}_{\mu}, \tag{1}$$

where J is the flux of the fluid particles and c is the concentration, is inversely proportional to the square root molecular weight of the fluid substance:

$$D_\mu \propto \sqrt{\frac{1}{M_\mu}}. \qquad (2)$$

For the case of $^{235}UF_6$ (species 1) and $^{238}UF_6$ (species 2), we have

$$\alpha \equiv \frac{D_1}{D_2} = \sqrt{\frac{352}{349}} = 1.00429. \qquad (3)$$

One important aspect of choosing fluorine to make the gaseous uranium compound is that there is only one stable isotope of fluorine with mass nineteen. The amount of enriched product is optimized when half of the gas introduced in the cell has passed through the barrier, producing a 50–50 split between the enriched part ("heads") and the depleted part ("tails"). Let n_1 be the number of ^{235}U atoms and n_2 be the number of ^{238}U atoms at the input to the cell and n_1' and n_2' be the numbers at the heads output. For one diffusion cell the ratio of the isotope ratios of the output compared to the input (known as the separation factor) is

$$r = \left(\frac{n_1'}{n_2'}\right) \bigg/ \left(\frac{n_1}{n_2}\right). \qquad (4)$$

Because the separation factor is close to one for a single gaseous diffusion stage, it is more convenient to work with the quantity $\varepsilon = r - 1$, known as the enrichment factor.

For maximum throughput of enriched material, a cascade is formed where the enriched "heads" are sent to the input of the next stage and the "tails" are sent to the input of the previous stage. The "cut" is the fraction of the input diffusing through the barrier, i.e. the fraction of heads to the input. Figure 1 shows the arrangement of the cells in the cascade. (This is the simplest cascade topology and is called the symmetric cascade. Other arrangements are possible, such as a "two up, one down" configuration, but not useful for low separative power processes such as gaseous diffusion.) Typically, each stage in the process is formed of many units operating in parallel. The number of separating units for each stage drops in either direction from the feed point.

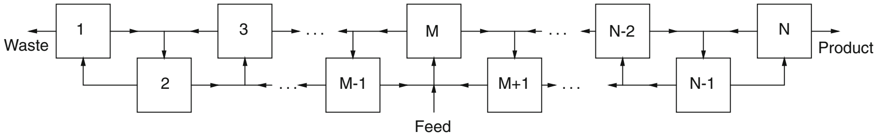

Fig. 1 Cascade arrangement for uranium isotope separation

For a cut of 1/2, the ideal separation factor is

$$\mathrm{r} - 1 = (\alpha - 1)\ln 2 = 0.69(\alpha - 1), \tag{5}$$

and thus one might expect that $\mathrm{r} = 1.0030$ would be the ideal limit for each stage. However, the effects, such as imperfections in the barrier material and effects of finite pressure drop cause the maximum achievable value of ε to be less than half that, $\varepsilon \approx 0.0014$.

We now consider the mass balance in the cascade. Call P the amount of product ("heads") and W the amount of waste ("tails"), and F the amount of feed material. Then $\mathrm{F} = \mathrm{P} + \mathrm{W}$. The enrichments of the feed, product and waste are $\mathrm{x_F}$, $\mathrm{x_P}$, and $\mathrm{x_W}$. Conservation of one isotope gives the relation

$$\mathrm{Fx_F} = \mathrm{Px_P} + \mathrm{Wx_W}, \tag{6}$$

and from these equations we obtain

$$\mathrm{F} = \mathrm{P}(\mathrm{x_P} - \mathrm{x_W})/(\mathrm{x_F} - \mathrm{x_W}) \tag{7}$$

and

$$\mathrm{W} = \mathrm{P}(\mathrm{x_P} - \mathrm{x_F})/(\mathrm{x_F} - \mathrm{x_W}). \tag{8}$$

Equation 7 shows why the cascade must be continued downward some length for the feed point where natural U enters the cascade: If the enrichment difference $\mathrm{x_F} - \mathrm{x_W}$ were due to just one stage, the feed rate to produce even a small amount of product would be impractically large. Typically, $\mathrm{x_W} \approx 0.003$–$0.004$. Then the total number of stages N required for $\mathrm{x_P} = 0.93$ and $\mathrm{x_W} = 0.004$ is on the order of

$$\mathrm{N} = \ln(\mathrm{x_P}/\mathrm{x_W})/\ln \mathrm{r} \approx 4,000, \tag{9}$$

whereas, in order to produce 3 % enriched reactor fuel, "only" about 1,400 stages are needed. Gaseous diffusion plants are huge. One in Paducah, Kentucky intended for reactor uranium enrichment covers 3,425 acres, with more than a square mile (750 acres) of enrichment plant. The site has a design electrical demand of 3,040 megawatts—equal to the output of three standard size nuclear power plants! It is unlikely that any new enrichment plants based on gaseous diffusion will be built.

6.1.1 Separative Work

The performance of an individual component in an enrichment cascade is quantified by the separative work unit (SWU). SWU takes into account the change in entropy required to turn the feed into separate product and waste streams. A "Value Function" is defined by the enrichment x at any point in the process, and is given by:

$$V(x) = (2x - 1) \ln \left(\frac{x}{1 - x} \right). \tag{10}$$

The total SWU for the enrichment process is given by the weighted sums of the feed, waste, and product mass produced (typically as kilograms of uranium) with their respective value functions:

$$SWU = \Delta U = PV(x_P) + WV(x_W) - FV(x_F).$$

If the feed, product, and waste stream flowrates F′, P′, and W′ are given in units of milligrams of UF_6 per second, rather than kg-U per year, a conversion factor can be added:

$$kg - SWUy^{-1} = \Delta U = 21.2 \left(P'V(x_P) + W'V(x_W) - F'V(x_F) \right).$$

6.2 *Centrifuge Separation*

6.2.1 History

Centrifuge separation technology is mentioned in the Smyth report [11] and in fact a centrifuge pilot plant was operated during the early 1940s in the U.S. However, the technology required for large-scale production was thought to be too risky a path to take. In the spring of 1945, as the Russians occupied parts of Germany, a group of German and Austrian scientists were taken to Russia, where they worked on developing isotope separation technology including the gaseous centrifuge as well as electromagnetic separation and gaseous diffusion. Some of the principals involved were Manfred von Ardenne, Max von Steenbeck, Gustav Hertz, and Gernot Zippe [13]. Much progress came about, especially for the centrifuge, and Zippe returned to Germany in 1956. Zippe made a trip to the United States after that time, and was in communication with U.S. scientists at the University of Virginia [6]. This was the beginning of what are now termed “Zippe centrifuges” in the West. Zippe also was a consultant in Germany for a company named Degussa, which eventually merged with several other companies to form an international conglomerate known as Urenco. An employee of Urenco named Abdul Qadeer Khan, a Pakistani native fluent in German and Dutch, was charged with translating the German centrifuge documents into Dutch for use at a facility in Almelo in the Netherlands. As such he became familiar with centrifuge technology, and returned to Pakistan after a call from then president Zulfikar Ali Bhutto for nuclear-trained citizens to return home. Later, however, A.Q. Khan seems to have shared some of this technology with other countries, including North Korea, Libya, and Iran [2]. The widespread dissemination of centrifuge technology poses one of the biggest risks to nuclear proliferation today.

6.2.2 Centrifuge Separation Physics

Figure 2 shows the salient features of the Zippe-type centrifuge design. Reference [8] gives a thorough review of the theoretical aspects of centrifuge performance. The centrifuge involves a carefully controlled interplay between the forces set up by centrifugal force, coriolis forces, and pressure gradient forces caused by an externally imposed temperature gradient. As can be seen from Fig. 2, an interior rotating canister is contained within an evacuated casing. Uranium hexafluoride gas (UF_6) is fed into the center of the assembly from the middle of three concentric tubes. The

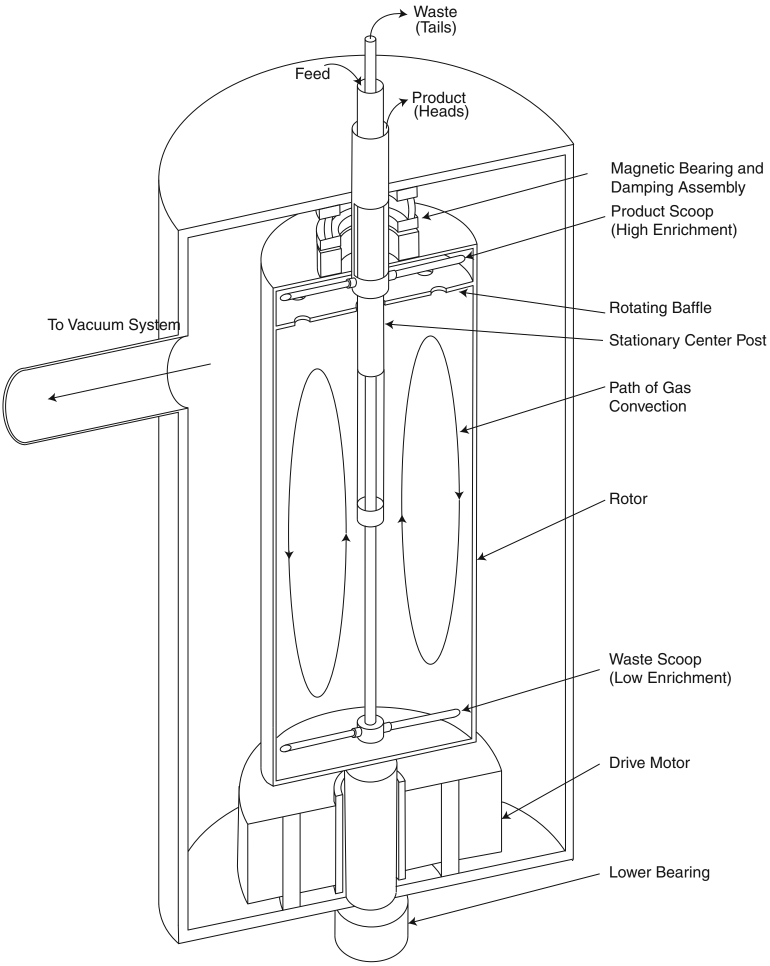

Fig. 2 Internal components of the gaseous centrifuge for isotope separation. From [8]

combined effects of the rotation and a temperature gradient (top-to-bottom) produce a convection cell. The normalized velocity of the rotor wall is given by dividing by the one-dimensional RMS speed of the gas molecules as:

$$M = \left(\frac{m\Omega^2 a^2}{2kT}\right)^{1/2}. \tag{11}$$

Here Ω is the rotation rate, T is the temperature of the UF_6 gas, k is Boltzmann's constant, and a is the radius of the rotor. M is closely related to the Mach number of the gas. A very high M is required: typically the M number is in the 5–6 range and wall velocities are on the order of 500 m/s. For a 9 cm radius rotor, this implies rotational speeds on the order of 75,000 rpm. While in gaseous diffusion, the separative power is governed by a square-root-of-mass law, that is not the case in the centrifuge: the separative power due to the coriolis and centrifugal effects scale linearly with the mass ratio.

The theoretical separation factor α for an infinitely long cylindrical rotor is obtained by comparing the pressure distribution for each species i as a function of radius given by the Boltzmann law:

$$p_i(r) = p_i(0)\exp\left(\frac{m_i\Omega^2 r^2}{2kT}\right). \tag{12}$$

Then, for low enrichment, the separation factor α is given approximately by the ratio

$$\frac{p_1(r)}{p_2(r)} \approx \exp\left(\frac{(m_1 - m_2)\Omega^2 r^2}{2kT}\right). \tag{13}$$

Taking the position of the exhaust to be at radius $r = a$ and using $e^x \approx 1 + x$ then gives an expression for α in this simple one-dimensional, no-flow model:

$$\alpha \approx 1 + \left(\frac{m_1}{m_2} - 1\right)M^2. \tag{14}$$

For $M = 5.5$, this gives a separation constant $\alpha = 1.24$. While this would still require a cascade in order to enrich materials to reactor grade (and a longer one for weapons-grade), this is obviously an improvement over the performance of the gaseous diffusion process.

However, other effects make this analysis rather simplistic. Firstly, finite length of the rotor needs to be accounted for, and the centrifuge is not an equilibrium environment as the gas molecules do not have an infinite residence time. Equation 14 thus is an overestimate considering the non-equilibrium effects. However, this loss in separative power is compensated by the effects of a convection cell due to thermal and coriolis forces in the cell. The overall theory of the fluid model is somewhat complex and involves a sixth-order partial differential equation in two dimensions. Reference [6] gives some details of the more physically refined treatments. This reference also gives an overall rule-of-thumb for the separative work that a centrifuge can achieve. In terms of kg-SWU per year,

$$\delta \mathrm{U} = \frac{\mathrm{V}^2 \mathrm{Z}}{33{,}000} \mathrm{e_E}. \tag{15}$$

Here $\mathrm{V} = \Omega \mathrm{a}$ is the velocity of the rotor wall, Z is the length of the rotor, and $\mathrm{e_E}$ is an overall "experimental efficiency" which is between 0.8 and 1.14 for modern designs.

6.2.3 A Sample Cascade Design

Here is an example of a cascade of gas centrifuges designed to produce one significant quantity (25 kg) of uranium enriched to at least 93 % in 1 year. We assume parameters in the range similar to those studied studied in Ref. [8]. We will take a feed rate of 40 mg/s and assume that $\alpha = 1.21239$. We also require that the waste enrichment at the bottom of the cascade be around 0.4 %. (As stated before, this is required in order to keep the overall feed rate to a reasonable value.) We will assume that the cut θ can be adjusted so that the waste isotope ratio $\beta = \alpha$, as this results in no loss of separative work when the $\mathrm{n}-1$ product and $\mathrm{n}+1$ waste streams are combined at feedpoint n. This is called an "ideal cascade". Conservation of mass then requires that

$$\theta = \frac{1 + (\alpha - 1)\mathrm{x_F}}{1 + \alpha} \tag{16}$$

for each stage, i.e. the cut depends on the feed enrichment. Since

$$\alpha = \frac{\mathrm{x_P}(1 - \mathrm{x_F})}{(1 - \mathrm{x_P})\mathrm{x_F}}, \tag{17}$$

we can then determine the feed, waste, and product enrichment at each stage. Here we number the stages with $\mathrm{n} = 0$ at the natural U feed point and negative numbers for the stages below the feedpoint. This gives

$$\mathrm{x_W}(\mathrm{n}) = \frac{\mathrm{x_F}(0)\alpha^{\mathrm{n}-1}}{1 - \mathrm{x_F}(0) + \alpha^{\mathrm{n}-1}\mathrm{x_F}(0)}, \tag{18}$$

$$\mathrm{x_F}(\mathrm{n}) = \frac{\mathrm{x_F}(0)\alpha^{\mathrm{n}}}{1 - \mathrm{x_F}(0) + \alpha^{\mathrm{n}}\mathrm{x_F}(0)}, \tag{19}$$

and

$$\mathrm{x_P}(\mathrm{n}) = \frac{\mathrm{x_F}(0)\alpha^{\mathrm{n}+1}}{1 - \mathrm{x_F}(0) + \alpha^{\mathrm{n}+1}\mathrm{x_F}(0)}. \tag{20}$$

Using $x_F(0) = 0.0072$, we find that n must range from −2 to 39 in order to satisfy the enrichment requirements. Thus a total of 42 stages are required, and two are below the feed point. We can then calculate the overall F, P, and W from the enrichments. We find that $x_P = 0.941437$ at the output of stage 39 and $x_W = 0.00405$ at the tail end of stage $n = -2$. The design requires that we have 25 kg of WGU at the P end after 1 year; using the factor given earlier, this translates to 1.17866 mg s^{-1} UF_6. The other two are calculated from the known P and the mass balance:

$$\begin{aligned} F &= P(x_P(39) - x_W(-2)/(x_F(0) - x_W(-2)) = 351.085\,\text{mg s}^{-1} \\ W &= P(x_P(39) - x_F(0)/(x_F(0) - x_W(-2)) = 349.906\,\text{mg s}^{-1}. \end{aligned} \tag{21}$$

Now the mass balances can be constructed. First we calculate the special cases at the ends of the cascade, where there is no P input from a lower stage at $n = -2$ and no W input at $n = 39$. Then, at the bottom of the cascade:

$$F(-2) = W/(1 - \theta(-2)), \tag{22}$$

$$F(-1) = F(-2)/(1 - \theta(-1)), \tag{23}$$

and

$$F(0) = (F(-1) - F(-2)\theta(-2))/(1 - \theta(0)). \tag{24}$$

The feedpoint for the natural UF_6 (at $n = 0$) is also a special case, and this shows up in the mass balance for stage $n = 1$:

$$F(1) = (-F(-1)\theta(-1) + F(0) - F)/(1 - \theta(1)). \tag{25}$$

At the top of the cascade:

$$F(39) = P/(1 - \theta(39)) \tag{26}$$

and

$$F(38) = F(39)/(1 - \theta(38)). \tag{27}$$

The rest of the mass flows can then be calculated iteratively:

$$F(n+1) = (-F(n-1)\theta(n-2) + F(n))/(1 - \theta(n+1)). \tag{28}$$

(It is interesting to note that these difference equations are a stable set of leapfrog steps in one direction but unstable in the other direction, in which the errors grow exponentially.) The complete set of mass flows into the each stage sets the number of centrifuges. The number of centrifuges is taken by dividing the feed rate by the design standard (in this example, 40 mg s^{-1}), and rounding up to the next integer. In practice, one could find some method of load sharing for the higher stages, where the feed rate is less than the design rate for a single centrifuge. Table 2 shows the overall

Table 2 Spreadsheet of parameters for cascade design

Stage No.	Tail enrichment	Feed enrichment	Head enrichment	Feed	No. of centrifuges	SWU
1	0.00405303	0.00490963	0.00594618	639.064	16	250.492
2	0.00490963	0.00594618	0.0072	1167.39	30	457.579
Feed Point → 3	0.00594618	0.0072	0.00871588	1604.64	41	628.966
4	0.0072	0.00871588	0.0105475	1325.43	34	519.526
5	0.00871588	0.0105475	0.0127591	1095.13	28	429.257
6	0.0105475	0.0127591	0.0154272	905.181	23	354.802
7	0.0127591	0.0154272	0.0186427	748.504	19	293.389
8	0.0154272	0.0186427	0.0225131	619.274	16	242.735
9	0.0186427	0.0225131	0.0271648	512.681	13	200.954
10	0.0225131	0.0271648	0.0327454	424.761	11	166.492
11	0.0271648	0.0327454	0.039426	352.241	9	138.067
12	0.0327454	0.039426	0.0474027	292.424	8	114.621
13	0.039426	0.0474027	0.0568978	243.084	7	95.2809
14	0.0474027	0.0568978	0.0681586	202.385	6	79.3282
15	0.0568978	0.0681586	0.0814557	168.812	5	66.169
16	0.0681586	0.0814557	0.0970766	141.118	4	55.3136
17	0.0814557	0.0970766	0.115317	118.271	3	46.3582
18	0.0970766	0.115317	0.136467	99.4206	3	38.9696
19	0.115317	0.136467	0.160791	83.8664	3	32.8729
20	0.136467	0.160791	0.188504	71.0293	2	27.8412
21	0.160791	0.188504	0.219742	60.4317	2	23.6873
22	0.188504	0.219742	0.254534	51.6793	2	20.2566
23	0.219742	0.254534	0.292767	44.4464	2	17.4215
24	0.254534	0.292767	0.334169	38.4639	1	15.0766
25	0.292767	0.334169	0.378294	33.5092	1	13.1345
26	0.334169	0.378294	0.424531	29.398	1	11.5231
27	0.378294	0.424531	0.472127	25.9773	1	10.1823
28	0.424531	0.472127	0.520235	23.1199	1	9.06225
29	0.472127	0.520235	0.567971	20.7193	1	8.12131
30	0.520235	0.567971	0.614478	18.6864	1	7.32446
31	0.567971	0.614478	0.658983	16.9454	1	6.64205
32	0.614478	0.658983	0.700852	15.4316	1	6.04869
33	0.658983	0.700852	0.739612	14.0887	1	5.5223
34	0.700852	0.739612	0.774962	12.8666	1	5.04329
35	0.739612	0.774962	0.806767	11.7199	1	4.59384
36	0.774962	0.806767	0.835034	10.6061	1	4.15723
37	0.806767	0.835034	0.859884	9.48348	1	3.71722

(continued)

Table 2 (continued)

Stage No.	Tail enrichment	Feed enrichment	Head enrichment	Feed	No. of centrifuges	SWU
38	0.835034	0.859884	0.881522	8.31044	1	3.25742
39	0.859884	0.881522	0.900206	7.0433	1	2.76075
40	0.881522	0.900206	0.916224	5.63492	1	2.2087
41	0.900206	0.916224	0.929871	4.03288	1	1.58076
42	0.916224	0.929871	0.941437	2.17758	1	0.853542
Total					306	4419.12

parameters for this design. (Note that the stage number has been shifted here, so that the numbering starts with one rather than −2.)

This design thus calls for a total of 306 centrifuges and has a total feed for 1 year's operation of about 5000 kg of natural U. The efficiency of the design can be determined by looking at the total SWU produced divided by the design SWU for each centrifuge. We can see that the total SWU generated is 4419.12 kg-SWU per year, and that each centrifuge has a SWU generating capacity of

$$\mathrm{SWU\ yr^{-1}} = 21.2\dot{\mathrm{M}}\left((1-\theta)\mathrm{V}(\mathrm{x_W}) + \theta\mathrm{V}(\mathrm{x_P}) - \mathrm{V}(\mathrm{x_F})\right). \tag{29}$$

This gives 15.6787 SWU per year per centrifuge, showing that the utilization factor is

$$\frac{4419.12}{306 \times 15.6786} = 92.1\,\%.$$

6.2.4 Applications of Centrifuge Estimates

The preceding analysis can be modified to suit different scenarios for HEU production with centrifuges. Firstly, the feedrate and specific SWU depend on the centrifuges involved: for example, the IR-1 model centrifuge available in Iran is thought to have a production rate of about 0.9 SWU per year. This increases the estimate of the number of units involved, but not exactly linearly because of the need to have as many centrifuges at each stage as an integer greater than the total feed to the stage divided by the design feedrate of each unit. (Also, the performance of centrifuges drops when they are not fed at their ideal design feedrate.) So a cascade with units producing 0.9 SWU per year gives an estimate of around 12,500 IR-1 units. A newer IR-2 model has an estimated output of 3–5 SWU y^{-1}. This would require 2200–3700 units for production of 1 SQ WGU per year.

Another scenario, however, is the possibility that a country can produce a supply of material at just below 20 % enrichment, with the justification that this material is suitable nuclear fuel for power reactors and medical isotope production reactors. From the previous example, we can see that this is roughly halfway up the enrichment cascade to weapon-grade material. If a large amount of, say, 19.8 % enriched UF_6 is stockpiled, then the same set of centrifuges could be fed with the LEU material and taken up to high enrichment in less time. The time that this would take is called the "breakout time" and could be as low as a few months with a few thousand-SWU system available. While a re-optimization of the cascade would be required from running the plant for natural-to-LEU enrichment, the valving and piping requirements for this type of flexibility probably would not contribute very much to the total cost of the facility. Without vigilant monitoring and inspection, a "breakout" could happen in a very compressed time frame.

6.2.5 Export Control Issues

Modern centrifuges for isotope separation use a variety of fairly advanced technology. While the older designs tended to use aluminum or maraging steel for the rotors, the newer machines typically use carbon fiber composite materials. Shipment of this material from western countries into countries attempting a centrifuge program are prohibited. Similarly, the drive motor power supplies, which are variable frequency inverters, are also carefully monitored. Process control computers are also controlled. Since UF_6 gas is corrosive, piping and valves are typically fabricated with corrosion-resistant alloys such as Inconel 625. In fact, a recent (2013) seizure of forty-four Inconel valves happened in Spain's Basque country. These valves were being illegally transported to Iran [4, 10].

6.3 Electromagnetic Separation

6.3.1 History and Basic Concept

Electromagnetic separation was developed for the Manhattan Project in 1942 [9, 12]. The concept is based on the dependence of the trajectory of an ion in a magnetic field as a function of the ion mass. An ion with mass m and charge q with energy E in a constant magnetic field B has a radius of gyration r given by

$$r = \frac{mv}{qB} = \frac{\sqrt{2mE}}{qB}. \tag{30}$$

A schematic of the concept is shown in Fig. 3. It was called the "calutron" because of its provenance from the Berkeley laboratory. While this relation gives only a square-root-of mass dependence, the ability to produce tightly focussed beams allowed ^{238}U and ^{235}U to be separated in only a few passes through the machine. The Manhattan Project electromagnetic separation program started at Berkeley and used the newly constructed 184-inch cyclotron as a source for the magnetic field. After

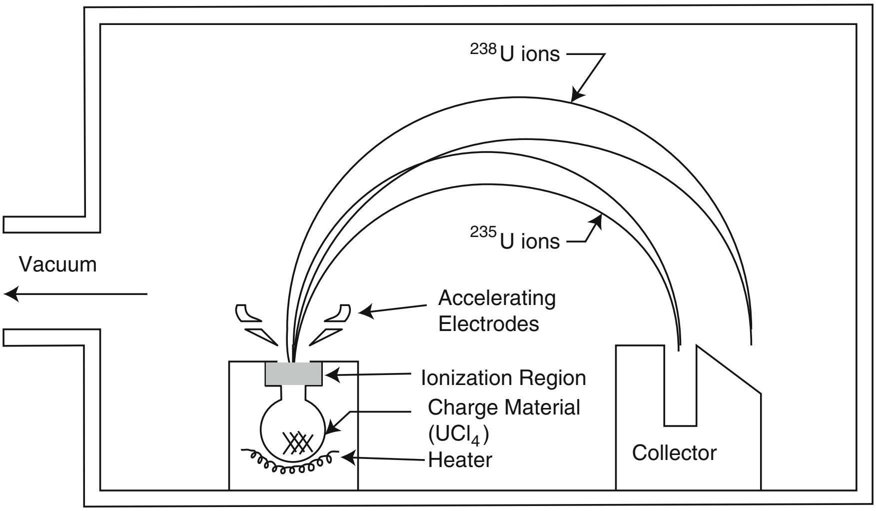

Fig. 3 Schematic for calutron. Note that the difference in orbital paths is exaggerated. From [11]

proving the concept, a full-scale effort was mounted at Oak Ridge, Tennessee to provide sufficient units to develop enough capacity to produce tens of kilograms of 90 % enriched U. At its peak, the Oak Ridge facility known as Y-12 had 1152 calutrons, each with a large racetrack magnet weighing ten to twenty tons. The diameter of the uranium ion orbit was approximately four feet. Much of the electrical conductor was pure silver, some 395 million Troy ounces, because copper was scarce during the war and a loan of the silver was obtained from the U.S. Treasury. This silver would be worth USD ten billion today, and virtually all of it made its way back to the treasury's repository after the war. Each device had either two or four sources in the tank, each source typically running at around 100 mA beam current. A set of calutrons known as the Alphas would enrich either natural U (0.711 % enriched) or output from the nascent gaseous diffusion plant, which produced some material at 0.89 % enrichment. The Alpha machines would provide a product at around 15 % enrichment, which would be fed into the Beta machines, yielding a product at 90 % enrichment.

It took much trial and error to obtain satisfactory results in the early stages of the project. First an appropriate source material for the ionization step had to be found: it was found that uranium tetrachloride, or UF_4, was the most suitable choice as it had a low sublimation temperature and was less corrosive than other metal halides. Second, much of the uranium from stray ions would end up on the walls and would also form deposits on the accelerating electrodes. This forced an assembly line type of design where a tank could be removed from the electromagnet via a rail system, where it would be stripped of uranium "gunk" and "crud", as well as product, as the next tank was rolled into place. There was also a problem with secondary electrons, which would be accelerated back towards the ion source through the accelerating structure, wasting power. An especially interesting problem was that the device needed to be operated at many times the Child-Langmuir limit for the stable operation of a focussed beam in the presence of space charges [9]. This had a fortuitous solution, because the lack of high-quality vacuum (typically around 2×10^{-5} torr) provided some charge neutralization through the background gas. Fine-tuning the device was more art than science, and a group of local Tennessee women then proved to be much better operators than the physicists from Berkeley. The square-root-of mass dependence resulted in only a $\sqrt{238/235} - 1 \approx 0.6\,\%$ difference between the strike location, or about 0.3 in., and ion optics were also very challenging. It was found that accelerating the ions up to 60 keV, and then decelerating them back down to around 35 keV, gave better ion optics. Having more than one beam in the tank meant that there were points of intersection of the beam paths, and special steps had to be taken to avoid electrostatic beam blow-up.

The calutrons provided virtually all of the WgU for the Little Boy device deployed on August 6, 1945. After that time, there were improvements in the performance of the gaseous diffusion plant (K-25) at Oak Ridge. The gaseous diffusion process ultimately won out over the calutron. A major problem with the calutron was that it had to be operated as a batch process because of the short maintenance interval for removal of product and cleaning. Although huge and expensive, the gaseous diffusion process had an economic advantage over the calutron in the end. The calutron isotope uranium isotope separation program was ended in 1946; however, the calutron device was still being used decades later for the production of other isotopes at Oak Ridge. There are calutrons at Oak Ridge that could be up and running again, especially if the supplies of medical isotopes are threatened.

6.3.2 More Recent Usage

Calutrons re-emerged in Iraq during the time of Saddam Hussein [12]. Iraq operated an experimental calutron-type isotope separator at the Tuwaitha Nuclear Research Center, 16 km SSE of Baghdad. The first unit was installed in 1986, with that number growing to two by 1987. By 1991, there were as many as ten calutrons operating there [5]. In 1991, during the Gulf War, many of these machines were destroyed. A second facility was being readied in Tarmiya, about 40 km north of Baghdad. It was designed with enough electrical supply for 100 calutrons, but when it was inspected in 1991, it was the IAEA's expert opinion that no calutrons ever operated there. After that time, Iraq apparently abandoned its nuclear program.

One might wonder why the Iraqi nuclear scientists were interested in the calutron as an isotope separation process, when it had been abandoned in the West. One speculation is that because the calutron does not demand any exotic parts or materials, the effort could have been easier to keep secret. In the end one of the biggest give-aways to its existence was the large electrical capacity installed—hundreds of megawatts at each site. One site identified for magnet fabrication was identified by what was not there: the Iraqis claimed that the building was for transformer fabrication, but there were no metal-stamping or coil-forming equipment present.

6.4 *Laser Isotope Separation*

6.4.1 History and Basic Concept

There are two types of laser-based isotope separation: atomic vapor laser isotope separation (AVLIS) and molecular laser isotope separation (MLIS). We will discuss AVLIS first.

AVLIS

During the Manhattan project there was some research into the atomic properties of uranium, including detailed studies of the difference in absorption spectra due to isotopic effects [1]. The hyperfine structure of ^{235}U is very different from the behavior of ^{238}U owing to nuclear spin. Whereas ^{238}U has a nuclear spin of zero, as all even-Z, even-N nuclei do, the nuclear spin of ^{235}U is 7/2, allowing for some lines in the absorption spectrum to be broken into a group of lines separated by small differences in energy (and thus wavenumber, spectroscopically speaking). The overall group of hyperfine lines in ^{235}U has a centroid which is shifted by an overall isotope shift wavenumber δT. Figure 4 shows the results of the Los Alamos work, published in 1947. The authors of this work indicated that the line(s) around 5027 Å showed a large isotope shift of about 0.426 cm^{-1}, or about 0.108 Å, for this line group.

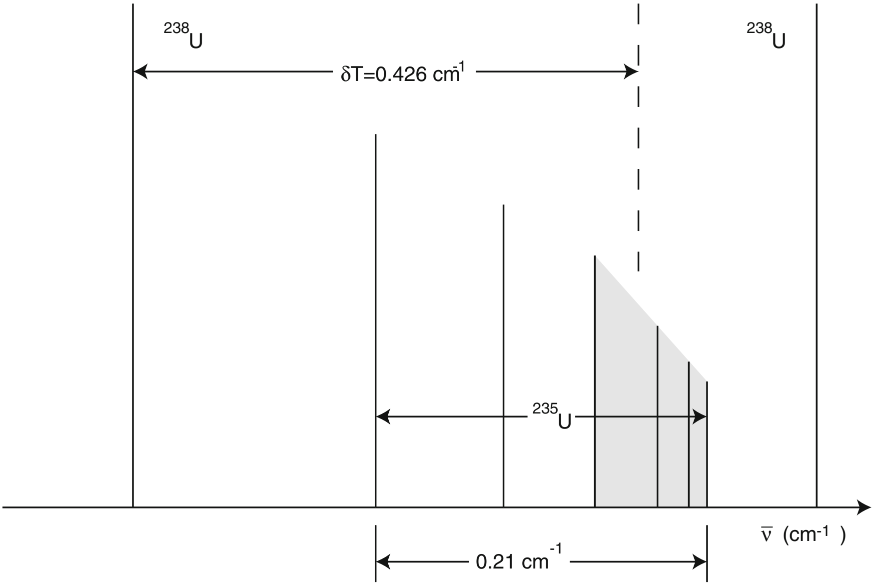

Fig. 4 Intensity versus wavenumber $\bar{\nu}$ (in cm^{-1}) for ^{238}U and ^{235}U in the vicinity of $\lambda = 5027$ Å. From [1]

While the prospect of using this information for isotope separation probably did not get much discussion in 1947 because the laser had not yet been invented, by the mid-1970s it became apparent that the isotope effect and the hyperfine structure could be exploited for isotope separation with the advent of tunable dye lasers. A program at Lawrence Livermore National Laboratory was launched in 1973, in partnership with Martin Marietta Energy Systems, to explore the possibilities. By 1992, tonne quantities of uranium had been processed through a pilot plant system, and a technology transfer program was put in place to commercialize the process through a company called U.S. Enrichment Corporation (USEC). However, in 1999, USEC announced that it was closing down the AVLIS program, taking a USD 100 million loss.

MLIS

Molecular laser isotope separation (MLIS) exploits a different optical property with isotope-specific energy levels than AVLIS. That is the vibrational energies associated with molecules of the actinide. The most commonly studied uranium compound used is uranium hexafluoride or UF_6. UF_6 in gaseous form is exposed to laser light tuned to vibrational levels in $^{235}UF_6$ which are at energies corresponding to the infrared range of frequencies. Typically the UF_6 is chilled and used with a carrier gas to provide less Doppler broadening of the vibrational lines. After several photon absorptions (using more than one laser wavelength), the UF_6 molecule undergoes dissociation to UF_5 and a fluorine atom. UF_5 is less volatile than UF_6 and tends to nucleate into fine particulate and is removed from the gaseous stream as enriched $^{235}UF_5$.

While MLIS was dropped in favor of AVLIS in the US in the 1980s, it is still being explored by other countries and commercially. The largest-scale R&D program is at an Australian company called Silex, which has partnered with General Electric in the US, Hitachi in Japan, and Cameco of Canada (the world's largest publicly traded uranium company). The high level of investment by some of the largest corporations in the nuclear energy business suggests that this technology will eventually mature and might replace centrifuge technology for isotope separation in the future.

6.4.2 Proliferation Risk

AVLIS and MLIS both pose interesting challenges for nonproliferation. While both have been researched mostly for the production of LEU at 3–5 % enrichment for power reactors, there have been reports of small quantities (milligrams) of material enriched to as high as 77 % [3]. Advances in technology might lead to weapon-usable material from a small system which might go undetected because of its small size and lower power consumption compared to centrifuges, calutrons, or gaseous diffusion.

A further risk for laser isotope separation is that a system capable of large separative work might also tempt a country or some individuals to try plutonium isotope separation on plutonium extracted from spent nuclear fuel. While this material typically contains enough ^{240}Pu and other isotopes to render it more difficult to use in a weapon, an efficient AVLIS or MLIS setup might make kilogram quantities of WgPu become available in a short period of time.

The technological sophistication of these systems is quite high. Hundreds of millions have been spent on the development of these systems, so far providing no practical, industrial-scale enrichment plants. This has to be weighed against a key advantage for a would-be weapon developer to try this route, which is that the equipment demands are not unique to this technology. Lasers of all wavelengths are commonly used in research and industry, and the chemicals, vacuum, and refrigeration demands for AVLIS and MLIS are not out of the ordinary.

7 Reactors and Proliferation

The interplay of nuclear power with proliferation has several facets. Firstly, if an outside provider sells fresh nuclear fuel at standard enrichment (say, 3–5 %) to a country with an agenda for creating a uranium nuclear weapon, then that material could be used as feedstock in an enrichment cascade to produce HEU with far fewer centrifuges (or other enrichment machines) than if they started with natural uranium. For example, the same enrichment cascade calculation shown before with 40 mg s^{-1} feed enriched to 3 % would only require eighty-nine centrifuges, rather than the 306 needed with natural U feed. This could reduce the breakout time to a period much shorter than the interval between IAEA inspections (assuming that the country in question has remained as a NPT signee and has any inspections at all).

Reactors can be fueled with uranium enriched to up to 20 % and still be considered to be LEU-fueled. This reduces the cascade size considerably if a breakout move is started with 20 % enriched fuel on hand. For the same cascade parameters as before, with two stages below the feedpoint stage, only twenty-six centrifuges would be required for twenty-four total stages. If we shorten the period of time to deliver 25 kg of uranium enriched to more than 93 % to 3 months, the number of centrifuges of the type described before, starting with 20 % enriched material, only climbs to sixty. This makes the breakout scenario truly frightening.

To date, however, civilian nuclear power has not been a route for the development of nuclear weapons (with the possible exception of South Africa, which has since dropped its weapons program [15]). Research reactors, however, are another matter. To date nine countries outside of the original "nuclear club" have built research reactors in the 5–100 MW class with suspected use for plutonium production: Burma/Myanmar, India, Iran, Iraq, Israel, Libya, North Korea, Pakistan, and Syria [14]. The lighter irradiation of the fuel in these reactors makes them ideal for the production of plutonium with relatively small ^{240}Pu buildup.

Although there is no evidence that it has happened so far, many are concerned about the proliferation risk of the CANDU-type reactor. A schematic of this reactor is shown as Fig. 5. This reactor type can be refueled while operating. This may allow for a covert refueling schedule, with some channels being shuffled through with relatively low burnup. The potential for this to happen creates a symbiotic relationship between

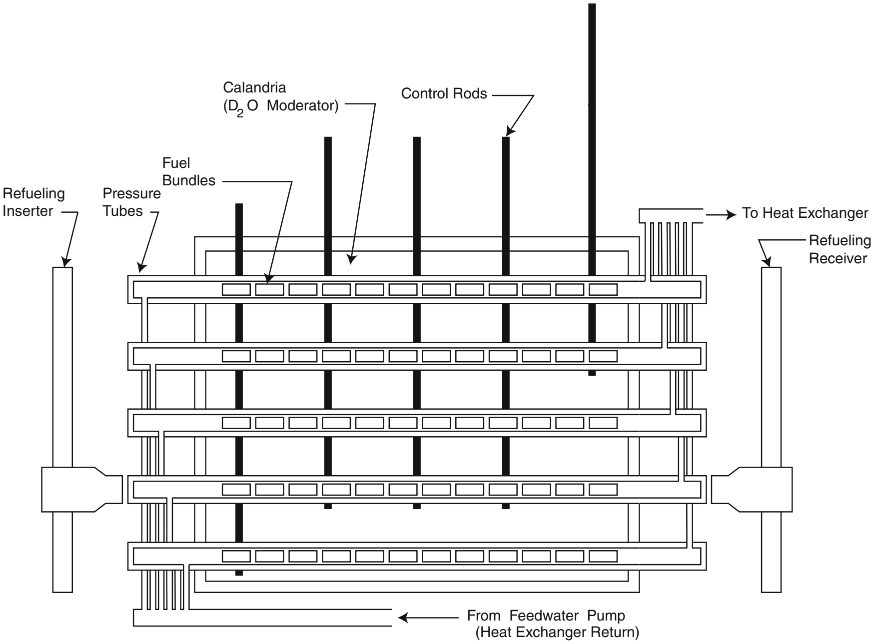

Fig. 5 Schematic of CANDU reactor

a military plutonium program and civilian electric power generation. Also, the lower enrichment required for a heavy water-moderated reactor allows the use of natural U or a combination of Pu with thorium breeding of ^{233}U, where the Pu can eventually be replaced with ^{233}U produced by the thorium [16]. While ^{233}U has been successfully used as a nuclear weapon material, the presence of ^{232}U makes it more difficult to utilize because of its high gamma radiation.

8 Problems

1. A gaseous centrifuge isotope separation plant has an entry point of natural uranium at Stage 7 and exit points for heads at Stage 21 and tails at Stage 1. The exiting enrichment at Stage 21 is 4.0 %.
    a. Find the separation coefficient α for each stage.
    b. Find the enrichment of the tails.
    c. If feedstock of the maximum enrichment to still be called LEU, i.e. 19.9 % enriched, were fed into the same entry point as before, i.e. Stage 7, then what would the output enrichment be at Stage 21?

References

1. Anderson OE, White HE (1947) Hyperfine structure and the nuclear spin of U^{235}. Phys Rev 71:911–911. doi:10.1103/PhysRev.71.911
2. Bernstein J (2007) Where Those Reactors and Centrifuges Came From. The New York Times. http://www.nytimes.com/2007/03/10/opinion/10bernstein.html?pagewanted=print
3. Director General I (2004) Implementation of the NPT Safeguards Agreement in the Republic of Korea. https://www.iaea.org/Publications/Documents/Board/2004/gov2004-84.pdf also at http://www.globalsecurity.org/wmd/library/report/2004/rok-gov-2004-84_iaea_11nov04.pdf
4. Dowsett S (2013) Spain seizes valves bound for iran's nuclear program: ministry. Reuters. http://www.reuters.com/article/2013/01/11/us-spain-iran-idUSBRE90A11A20130111
5. International Atomic Energy Agency (1991) Consolidatad report on the first two IAEA inspections under Security Council Resolution 687 (1991) of Iraqi nuclear capabilities. http://www.iaea.org/OurWork/SV/Invo/reports/s_22788.pdf
6. Kemp RS (2009) Gas centrifuge theory and development: a review of U.S. programs. Sci Global Secur 17:119. doi:10.1080/08929880802335816
7. OECD (2010) Uranium 2009 Resources, Production and Demand. OECD NEA Publication 6891
8. Olander DR (1981) The theory of uranium enrichment bythe gas centrifuge. Progr Nucl Energy 8:1–33
9. Parkins WE (2005) The uranium bomb, the calutron, and the space-charge problem. Phys Today 58. doi:10.1063/1.1995747
10. Project Alpha, Centre for Science and Security Studies at King's College London: Fluval Spain S. L. (March 2–13). https://www.acsss.info/news/item/198-fluval-spain-s-l
11. Smyth HD (1945) Atomic energy for military purposes 17(4), 351–471. doi:10.1103/RevModPhys.17.351. http://rmp.aps.org/abstract/RMP/v17/i4/p351_1
12. U.S. Nuclear Regulatory Commission (2008) Uranium enrichment processes directed self-study course module 5.0: Electromagnetic separation (calutron) and thermal diffusion. http://pbadupws.nrc.gov/docs/ML1204/ML12045A056.pdf
13. U.S. Central Intelligence Agency (1955) Information Report: The Development of an Ultra-Centrifuge at the Nuclear Institute of Manfred von Ardenne in Sinop. https://www.documentcloud.org/documents/399990-doc-1-crest.html. Accessed 01 Nov 2015
14. World Nuclear Association (2014) Nuclear Proliferation Case Studies. http://www.worldnuclear.org/info/SafetyandSecurity/NonProliferation/Appendices/NuclearProliferationCaseStudies/
15. World Nuclear Association (2014) Safeguards to Prevent Nuclear Proliferation. http://www.world-nuclear.org/info/Safety-and-Security/Non-Proliferation/Safeguards-to-Prevent-Nuclear-Proliferation/
16. World Nuclear Association (2014) Thorium. http://www.world-nuclear.org/info/Current-and-Future-Generation/Thorium/

Nuclear Forensics

Abstract The two types of nuclear forensics, pre-detonation and post-detonation, are differentiated, and the types of information to be gathered are identified. Methods to provide attribution are explored, including isotope chronometers on the actinide decays, oxygen, lead, and strontium isotope identification, material characteristics such as morphology and structure, and in the case of nuclear reactor fuel, the dimensions of the pellets. Plutonium is discussed from the standpoint of gallium alloying and from the microstructure, revealing heat treatments being used. Next, there is a discussion about the tools used in nuclear forensic analysis, including alpha, beta, and gamma spectroscopy, neutron counting, and various types of mass spectrometry.

1 Introduction

The term "forensics" is today equivalent to "forensic science". The original meaning of the Latin-derived word was to prepare an argument for public discourse and debate; this later morphed into the preparation of scientific evidence to present before a court of law. As the term "nuclear forensics" has become common usage, perhaps we must revert to the original Latin meaning, since often the outcome of nuclear forensic efforts will be to force international public debate rather than to convict a small group of individuals before a court of law.

A division of the field of nuclear forensics into two quite different branches is also worth noting. One branch deals with using scientific information, working with law enforcement and intelligence sources, to identify answers to questions raised by a found object, a signal detected, an intercepted communication, or some other event indicating nuclear activity. This is often called "pre-detonation forensics" and can involve evidence quite removed from an imminent threat of a nuclear detonation. The complement to this type of nuclear forensics is referred to as "post-detonation nuclear forensics" and differs from pre-detonation forensics in the broader scope of professionals immediately involved, including all levels of government and the public from heads of state to eyes on the street. It is important to point out that post-detonation forensics is not a theoretical construct, as Hiroshima and Nagasaki

E.C. Morse, *Analytical Methods for Nonproliferation*, Advanced Sciences
and Technologies for Security Applications, DOI 10.1007/978-3-319-29731-6_6

are examples where the harsh reality of understanding and coping with a nuclear detonation in a populated area had to happen.

For pre-detonation nuclear forensics, the “questions” alluded to in the previous paragraph include all of the usual ones in typical law enforcement. What individuals are involved in the activity that triggered this investigation, and where are they from? If nuclear material is involved, can it be tracked back to where it was produced? What route might the material have traveled along? Were the individuals acting as part of a larger group? How might the individuals involved have communicated with one another? If material has been interdicted, is it likely that it is part of a larger supply? How long might the individuals involved been in possession of the material, and how long ago was it made? What other physical evidence of a conventional nature, such as fingerprints, fibers, hair, DNA, and so forth, might give more information?

Post-detonation nuclear forensics has all of these questions plus a few more. What can we tell about the size and sophistication of the device? Was the weapon uranium or plutonium, and are there signs of boosting? How widespread is the fallout? What are the health implications of the blast radiation on the survivors? What can be done to mitigate further loss of life? An organization behind a nuclear attack might have additional devices ready to be used. If that were the case, where would the next target be?

Nuclear forensic studies can result in a wide range of outcomes including legal prosecution and possibly even military retaliation. For this reason, these studies should be carried out in a careful and well-documented way invoking the best practices of criminology work. This includes careful chain-of-custody logging, contamination control with samples, cross-calibration of analysis equipment with laboratory standards, and in some cases, independent review of methods and procedures by outside authorities. Because nuclear forensics capabilities naturally tend to gravitate towards nuclear weapons laboratories in the nuclear weapon states, there can be information barriers in place which might prevent the development of global standards for nuclear forensic evaluations.

A good part of nuclear material interdictions in the past have involved hoaxes and spoofs–benign materials such as depleted or natural uranium, and even materials that had no connection to anything remotely “nuclear” in the first place. For this reason nuclear forensic experts need to be trained to recognize all manner of non-nuclear materials as well. A classic example was the “red mercury” spoof some years ago [4]. This material, while touted to be able to replace the fission trigger in a thermonuclear weapon without the need for a U or Pu primary, actually turned out to be Hg, HgO, or HgI in every case and not a particularly interesting chemical compound. Another spoof involved Osmium-187, which was touted as having special application for nuclear weapons construction but is simply a stable isotope of osmium with no particular utility in weapons [16]. This material was offered for sale in 2002 for USD 30,000 for a 1.33 g quantity. The accomplice to the seller was also trying to sell a large quantity of Iraqi dinar currency.

2 Attribution Methods

2.1 Chronometers

Assigning a date to initial fabrication of a piece of nuclear material is a very important first step towards attribution of the material's origin [21]. Since nuclear fabrication facilities often do not operate full time, the time since separation/purification may be used to suggest or rule out places of manufacture. Since there are no stable isotopes of U and Pu, a "clean" separation of plutonium will, for example, pick up ^{235}U through the decay of ^{239}Pu to ^{235}U due to the 24,110 y half-life of ^{239}Pu. The long half-life of ^{235}U, 704×10^6 y, means that subsequent decay of ^{235}U can be ignored. Assuming that the separation of Pu from U was very complete (typically this is done to the part per million level), then

$$\frac{\mathrm{N}\left({}^{235}\mathrm{U}\right)}{\mathrm{N}\left({}^{239}\mathrm{Pu}\right)} \approx \lambda_{239}\mathrm{t} \tag{1}$$

This then gives a time since separation given by

$$t \approx \frac{t_{1/2}}{\ln 2}\frac{\mathrm{N}\left({}^{235}\mathrm{U}\right)}{\mathrm{N}\left({}^{239}\mathrm{Pu}\right)} = 3.478 \times 10^4 \frac{\mathrm{N}\left({}^{235}\mathrm{U}\right)}{\mathrm{N}\left({}^{239}\mathrm{Pu}\right)} \tag{2}$$

Other useful isotope chronometers include the ^{235}U/^{231}Pa ratio and the ^{234}U/^{230}Th ratio for uranium materials. The long half-life of ^{235}U (704 My) is a disadvantage because the Pa/U fraction is very small for the range of age since fabrication (0–65 y). Also, there are no other suitable Pa isotopes that are alpha-emitting which could be used as a "spike" to calibrate the efficiency of the chemical separation and subsequent analysis [25]. Thus ^{234}U/^{230}Th is the preferred chronometer, but it suffers in the case of LEU samples from the small abundance of ^{234}U (55 ppm in natural U). For thorium-bred uranium, isotopes ^{233}U and ^{232}U will be present, and the appropriate chronometers are ^{232}U/^{228}Th and ^{233}/U^{229}Th. In addition to ^{239}Pu/^{235}U outlined above for plutonium materials, other chronometers include ^{238}Pu/^{234}U, ^{240}Pu/^{236}U, and ^{241}Pu/^{241}Am [12]. Since all of the daughter isotopes listed here are radioactive as are the parents, in some cases with relatively short daughter half-lives, even grandaughter isotopes can be detected. As an example, ^{234}U decays to ^{230}Th, which has a half-life of 7.538×10^4 y. The decay product of this reaction, ^{226}Ra, can then be compared back to the ^{234}U inventory:

$$\frac{\mathrm{N}\left({}^{226}\mathrm{Ra}\right)}{\mathrm{N}\left({}^{234}\mathrm{U}\right)} \approx \lambda_{234}\lambda_{230}\frac{t^2}{2} \tag{3}$$

The more complete chain makes it much more difficult to fake the age of the material by adding, say, extra ^{226}Ra to the material to make it look older [15].

The determination of these ratios analytically typically has a chemical separation as a first step and then can be followed with alpha emission spectroscopy coupled with mass spectrometry. There are exceptions to this destructive assay process, however. In some cases characteristic gamma ray lines from both parent and daughter can be seen with a high-purity germanium detector. In general, one cannot obtain isotope ratios from lines at different energies because of the self-shielding of the source and possible inaccuracy in determining the relative efficiency of the detector as a function of gamma energy. However, sometimes two lines from parent and daughter will be close in energy by some lucky accident, and line pair ratios can be reliably calculated. An example of this is the ^{241}Am/^{241}Pu chronometer, where both emit gammas a few keV apart in energy at around 300 keV. This gives rise to the well-known "Pu-300" method which will be described in Chap. Arms Control and Treaty Verification.

An unlucky coincidence with plutonium isotopes involves the alpha decay energies of ^{239}Pu (5244.50 keV) and ^{240}Pu (5255.78 keV). These energies are too close together to resolve the ^{240}Pu/^{239}Pu ratio using standard surface-barrier semiconductor diode detectors. This can cause problems in applying the ^{240}Pu/^{236}U and ^{239}Pu/^{235}U simultaneously; however, the alpha energies of the U daughters differ by more than 100 keV, easily outside the $\approx$20 keV resolution of a typical surface barrier detector. The three parameters obtained (the sum of the two Pu activities and the individual activities for ^{235}U and ^{236}U can be used for an age determination, with confirming measurements with mass spectrometry.

2.2 Calculation of Initial Enrichment

An example of a sample of nuclear material interdicted at the Bulgarian border is given in [15], Chap. 20. In this case it was determined that the glass ampoule contained material that was largely U_3O_8 powder with an unusual isotopic mixture: ^{234}U:^{235}U:^{236}U:^{238}U ratios were 1.1:72.7:11.9:13.9. The presence of substantial ^{236}U immediately stands out, as this is produced by neutron absorption on ^{235}U, indicating that this material was probably initially very highly enriched U that had been used in a reactor and exposed to a rather high burnup rate. The sample contained only trace quantities of Pu isotopes and fission products, which probably indicates that the material was run through a separation step such as PUREX (see Chap. "The Nuclear Fuel Cycle"). The isotopics of the uranium begs the question of what the initial enrichment might have been. This can be determined with extreme certainty only if the energy spectrum of the neutrons in the reactor was known, and then a burnup calculation using ORIGEN or some other code can be performed. If the neutron spectrum is well-moderated, such as in a graphite-moderated reactor, one can analyze the coupled set of rate equations in a simplified way using thermal neutron cross sections and ignoring (n, 2n) and (n, α) reactions requiring fast neutrons. We can assume that absorption on ^{238}U immediately takes the produced ^{239}U out of the uranium cohort, since it has a 23 min half-life by beta decay to ^{239}Np (also with a short 2.36 day half-life, decaying to ^{239}Pu, but the isotope purification would have removed either of these). Similarly, absorption of a neutron by ^{236}U also almost immediately takes this nucleus out of the uranium cohort because of the 6.75 day half-life of ^{237}U. We can also ignore ^{234}U in the rate equations because the quantities involved are small and the rate of ^{235}U production by this isotope is about 500 times smaller than the destruction of the majority isotope ^{235}U by fission and capture. Then the rate equations for the inventories of ^{235}U, ^{236}U, and ^{238}U are given by:

$$\begin{aligned}
&\mathrm{N}_{238}{}'(\mathrm{t}) = \Phi \mathrm{N}_{238}(\mathrm{t})(-\sigma_{\mathrm{c}}^{238})\\
&\mathrm{N}_{235}{}'(t) = \Phi \mathrm{N}_{235}(\mathrm{t})(-\sigma_{\mathrm{c}}^{235} - \sigma_{\mathrm{f}}^{235})\\
&\mathrm{N}_{236}{}'(\mathrm{t}) = \Phi \sigma_{\mathrm{c}}^{235}\mathrm{N}_{235}(\mathrm{t}) - \Phi \sigma_{\mathrm{c}}^{236}\mathrm{N}_{236}(\mathrm{t})\\
&\mathrm{N}_{236}(0) = 0\\
&\mathrm{N}_{235}(0) = \mathrm{f}\\
&\mathrm{N}_{238}(0) = 1 - \mathrm{f}
\end{aligned} \tag{4}$$

The thermal neutron cross sections are: $\sigma_{\mathrm{f}}^{235} = 584\mathrm{b}$, $\sigma_{\mathrm{c}}^{235} = 97\mathrm{b}$, $\sigma_{\mathrm{c}}^{236} = 24\mathrm{b}$, and $\sigma_{\mathrm{c}}^{238} = 2.683\mathrm{b}$.

$$\begin{aligned}
&\mathrm{N}_{235}(t) = \mathrm{f}\mathrm{e}^{-\Phi \mathrm{t}(\sigma_{\mathrm{c}}^{235}+\sigma_{\mathrm{f}}^{235})}\\
&\mathrm{N}_{236}(\mathrm{t}) = \left\{-\frac{\mathrm{f}\sigma_{\mathrm{c}}^{235}\left(\mathrm{e}^{-\Phi \mathrm{t}(\sigma_{\mathrm{c}}^{235}+\sigma_{\mathrm{f}}^{235})} - \mathrm{e}^{-\Phi \mathrm{t}\sigma_{\mathrm{c}}^{236}}\right)}{\sigma_{\mathrm{c}}^{235} - \sigma_{\mathrm{c}}^{236} + \sigma_{\mathrm{f}}^{235}}\right\}\\
&\mathrm{N}_{238}(\mathrm{t}) = (1 - \mathrm{f})\left(e^{-\Phi \mathrm{t}\sigma_{\mathrm{c}}^{238}}\right)
\end{aligned} \tag{5}$$

The solutions for an initial enrichment of $\mathrm{f} = 0.905$ (standard Russian WGU) and $\mathrm{f} = 0.93$ (US WGU) is shown as Fig. 1. (Note that these curves are for the fractional quantities, not the absolute quantities, as this is the only way the data is available.) A fluence Φt can be determined that is the bast match for the three isotopes, and then these numbers can be "diluted" by adding the assayed ^{234}U content into the mixture. As can be seen, the match is more consistent with Russian WGU at a fluence of around 0.0012 inverse barns, and at this fluence, the ^{236}U:^{238}U ratio is very different between these initial assumed enrichments.

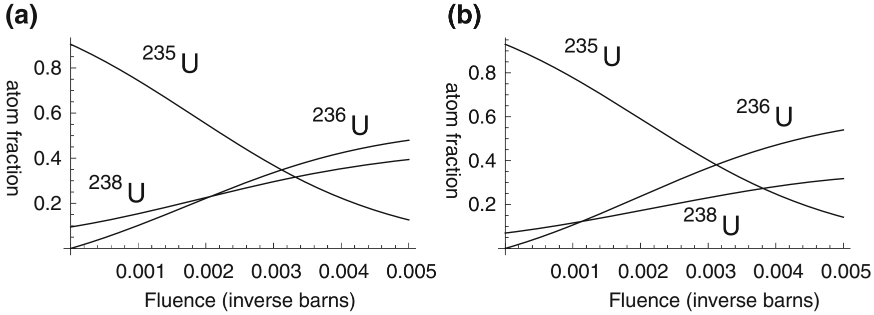

Fig. 1 Solution to rate equations for **a** f = 0.905 and **b** f = 0.93

2.3 Other Nuclear Signatures

Since forensic analysis of nuclear materials obviously takes place in a laboratory setting with isotope measurement capability, other non-actinide signatures can be observed as well. As an example, nuclear fuel, either U or Pu, is usually fabricated as UO_2/PuO_2. The relatively rare stable isotope ^{18}O has a worldwide average abundance of 2.0052×10^{-3} (this is the "Standard Mean Ocean Water", or SMOW value), and an average U.S. value of 1.950×10^{-3}. Studies have been made of the variation of ^{18}O content of UO_2 as a function of its place of origin [17]. In general, colder climates have lower ^{18}O in precipitated water and rivers. In addition to UO_2, U_3O_8 (yellowcake) has been studied in this regard as well.

Frequently nuclear materials are transported in lead pigs. Lead is also interesting from an isotopics viewpoint. Since the stable isotopes of lead ^{206}Pb and ^{207}Pb arise at least in part from the decay of U isotopes ^{238}U and ^{235}U, whereas ^{208}Pb comes about partially because of ^{232}Th, the differing amounts of U and Th deposits worldwide results in a significant variation in the isotope ratios in Pb depending on where it was mined [20]. Lead is also present in other items such as paper and other shipping materials because of its use in gasoline, which causes Pb to be an atmospheric pollutant. While the isotopic variation is distinct and easily measurable, the worldwide trade in Pb (and the reduction of Pb mining activities in the US and western Europe), coupled with the recycling of Pb-bearing materials such as batteries, has blurred the isotopic fingerprint in some cases.

Similarly, the two stable isotopes of strontium, ^{86}Sr and ^{87}Sr, have been studied from the perspective of mine-to-mine variations in the ^{86}Sr/^{87}Sr ratio. This has been found to vary between 0.70785 and 0.76063 from one place to another [13, 23]. One application of using this signature is described in Ref. [24], where some yellowcake was found in a shipment of scrap metal in Rotterdam in 2003. There was suspicion that the material originated in Iraq. Subsequent analysis showed that the Sr ratios were consistent with uranium ore concentrates found in phosphorite rock formations, which are found to represent Iraqi uranium ore deposits. While these formations are also found in other places, the combination of this result with the Pb isotope results and other rare-earth markers, forms a more compelling case.

2.4 Morphology and Structure

Uranium and plutonium can have variations in their physical characteristics, depending on where they were manufactured, and why. A variety of different interdicted nuclear materials has been described in [18]. For example, a sample seized at Munich airport, inbound from Moscow, contained a mixture of UO_2 and PuO_2 oxides in powder form. The particle shapes and sizes revealed two distinctly different particle types for the Pu and for the U material. While it was not possible to point to a single source for the material, it was possible to rule out any manufacture in western Europe. A sample of HEU interdicted at the Bulgarian border is described in [15]. This also consisted of a powdery substance, mostly U_3O_8, with a very small grain size, averaging just 0.16 μm. The authors point out that this practically rules out the material being of US origin, because these facilities only operate with much larger grain size to avoid respiratory hazards. In this case, the small grain size probably meant that the material was to be used in a powder metallurgy process at a nuclear fuel facility.

Bulk properties of interdicted fuel can lead to some clues about the type of reactor the material was intended for. Most BWR and PWR fuel is in the form of cylindrical UO_2 pellets, with lengths of around 1 cm and diameters between 7 and 12 mm. Some have a central hole and others do not. Of more interest is fuel for submarines and icebreakers, because many of the propulsion reactors for these run on HEU fuel at 90 % enrichment or higher. While most of the parameters of the fuel for submarine reactors is classified, there is an example where some of the details of a Russian icebreaker reactor design for the nuclear-powered *Sevmorput* were disclosed to the Norwegian government prior to its visit to Tromsø in 1990 [2]. From the data given, one can surmise that the fuel pellets were annular cylinders of $\approx$2.3 mm in diameter and fabricated as a U-Zr alloy. In general, one expects submarine reactors to use fuel on this diameter scale in order to deliver more power for a fixed volume. (Fuel rods of different diameters all have roughly the same linear heat rate for the same maximum internal temperature.)

A great deal of information about plutonium metallurgy has been published [3, 5–8, 14, 22]. A good bit of this information is applicable to nuclear forensic science involving this material. Reference [8] gives some information regarding determination of the age of a Pu sample since manufacture from the formation of He gas bubbles in the material due to alpha decay.

Let's consider a fifty-year-long debate about the phase diagrams of the plutonium-gallium system used in the United States, France, and the United Kingdom as opposed to Russia [9]. Early in 1945 at Los Alamos it was realized that the δ-phase of plutonium was desirable from a workability viewpoint, and it was found that alloying the material with either aluminum or gallium would allow this phase to remain at room temperature. Ga won out over Al as the alloy of choice because it does not have significant (α, n) reactions whereas Al does have these. Typically gallium metal is alloyed with plutonium to around 0.5–1.0 wt% in order to make a stable, crack-free weapon component. Figure 2 shows the microstructure of a Pu-Ga alloy after casting. This material has a two-component structure; however after annealing, the material becomes a uniform δ-phase with a density of $15.8\,\mathrm{g\,cm^{-3}}$, as shown in Fig. 3. Annealing for hundreds of hours allows for the Ga to diffuse through the material until it is uniformly distributed. Experience has shown that this alloy, now known to be a metastable state, does not decompose into an α+Pu_3Ga eutectoid, which would cause mechanical problems. In fact, the 70-year old US plutonium stockpile has been described as "aging gracefully" [10].

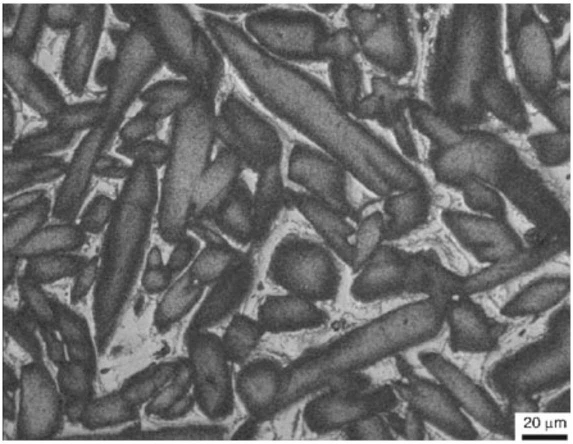

Fig. 2 Micrograph of an as-cast Pu-0.6 wt% Ga sample. The lath-like objects are δ-phase Pu in an α-phase matrix. From [14]

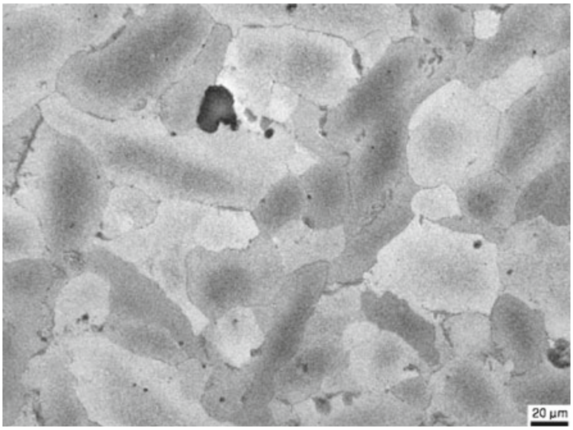

Fig. 3 Micrograph of a Pu-0.6 wt% Ga sample after 50 h annealing at 420 °C. The δ-phase Pu grains have varying amounts of Ga. Longer annealing times tend to equalize the Ga content grain-to-grain. From [14]

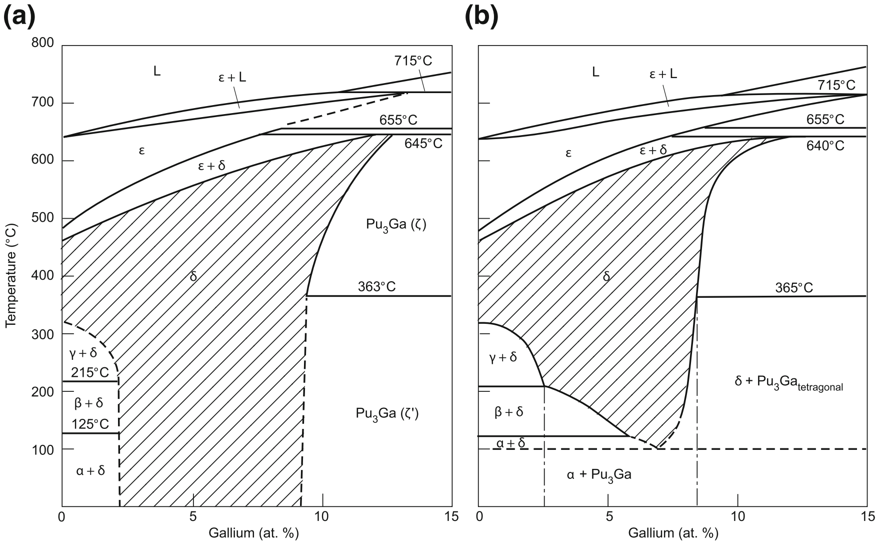

Fig. 4 Phase diagrams for the Pu-Ga system: **a** US version, **b** Russian version. From [9]

The Russian viewpoint was somewhat different. Their version of the Pu-Ga phase diagram was substantially different than the one used in the West. This is illustrated in Fig. 4. In order to speed up the transformation of δ-phase to an α-Pu$_3$Ga eutectoid, they added a plastic deformation step in their experiments and then annealed for long periods. They could then see the transformation of the material over thousands of hours. This knowledge may have led to different process steps than the path taken for WgPu production in the West.

Another variable worth noting in Pu samples is the impact of process purity on the grain structure. Common process impurities are nickel and iron. These materials, if present, accumulate at grain boundaries and can form eutectoid inclusions in the material.

However, interdicted weapon-grade Pu is more likely to have its origin in an analytical plutonium metallurgy laboratory than from a weapon-ready component stockpile, as these assets are considerably more secure. An analysis laboratory is more likely to make or possess Pu samples with parameters varying widely from production Pu, for scientific or process reasons. Therefore the above information cannot be applied directly to make rigid attribution findings based on microstructure or Ga content, but can be used in context with other findings.

3 Analysis Tools

Here some of the analysis tools used in nuclear forensic science are described. While none of the equipment and techniques described here are unique to nuclear forensic science, their basic function and relevance to nuclear forensics are explored.

3.1 Radiation Detection Equipment

The overall subject of radiation detection and measurement is covered in depth in the textbook by Knoll [11]. The most common radiation detection equipment involves α, β, γ, and neutron counting.

The most relied-upon instrument in nuclear forensic radiation detection laboratories is the high purity Ge detector for gamma radiation. Embellishments on the basic HPGe detector include fitting them with a low resolution outer detection medium (such as a plastic scintillator) to veto Compton scattering events in the main detector, to reduce the background for low-energy gamma detection, and linear (as opposed to coaxial) geometry Be-window low energy photon spectrometers (LEPS) for measurement of gamma and X-ray energies below 100 keV with good efficiency.

It is important to have contamination-free, low-activity counting areas for detecting trace amounts of radioactivity. Contamination control is accomplished by a combination of factors including filtered room air, locating the facility underground (to reduce the cosmic ray background), gloves, booties, and clean lab coats, oil-free vacuum lines, avoidance of post-WWII lead and steel (^{60}Co contamination), and adequate ventilation to avoid radon gas. Automated operation allows less exposure of personnel to the sample, and vice versa.

Beta counting is less important because almost all β^- emitters with short half-lives emit a characteristic and well-identifiable gamma. The exception would be if tritium or ^{14}C contamination is suspected on a sample, or certain fission products such as ^{90}Sr with no gamma emission. These are best measured by liquid scintillation counting (LSC). Automated LSC systems are typically maintained in laboratories with health physics requirements to look for these isotopes.

Alpha spectroscopy is an important component of nuclear forensic analysis because of the characteristic alphas for the U, Pu and Th isotopes. Alpha spectroscopy is routinely done with silicon surface-barrier detectors mounted inside a vacuum vessel with a door. The sample is inserted, the door is closed, and the system is pumped down to rough vacuum ($\approx 10^{-3}$ mbar), sufficient to prevent the slowing-down of the alphas, which have a short range in atmospheric air. Alternatively, an alpha-emitting material can be electrodeposited on a metallic disk used in a Frisch-grid ionization ion chamber, designed to be insensitive to the location of the disintegration in the chamber. While energy resolution is not as good as the semiconductor diode (50 keV vs. $<$20 keV), the efficiency is quite high, virtually all of the alphas exiting the sample (i.e. about half of the total disintegrations) are counted.

Neutron detection is generally done in nuclear forensic laboratories only to protect people and HPGE detectors from dangerously high radiation levels. It is important to look for neutrons at the intake of a suspicious sample. There have been several incidents involving a stolen or misplaced radium-beryllium or plutonium-beryllium neutron source, and radiation levels a few feet from the source can be quite high ($\approx$20 mSv/h).

3.2 Mass Spectrometry

Mass spectrometry is an indispensible tool for isotope identification of actinides and identification by elemental analysis. The common theme in mass spectrometry is that an ion beam is sent through a set of magnetic/electric fields and the individual charge-to mass ratios are differentiated by their dynamics in these fields. Isotope differentiation and quantitative assay to high precision (parts per million) are hallmarks of MS specifications. Some systems, such as accelerator mass spectrometry, can work with extremely small samples.

3.2.1 Thermal Ion Mass Spectrometry (TIMS)

Thermal ion mass spectrometery can achieve high-precision isotope ratio measurement ($<$10 ppm) in U and Pu isotopes. Reference [19] describes the state of the art for U isotope discrimination a decade ago. These systems use a heated filament, typically tungsten or rhenium, which has been coated with a solution containing the material to be analyzed. Typically another heated filament is used for ionization. An extracted beam is then sent through a series of analyzing magnetic sectors and $\mathbf{E} \times \mathbf{B}$ filters, with electrostatic filters as well, with the result that the individual isotope components are well separated with known isotopic efficiency variation. Some systems have several Faraday cups arranged so the individual ionic isotopic components are available in real time. Some fractionation effects are inevitable; however, Ref. [19] points out that if the process is run to extinction of the test material on the filament, and the currents are integrated, the accuracy in the isotope ratios is much improved.

3.2.2 Inductively Coupled Plasma Mass Spectrometry (ICPMS)

Inductively coupled ion mass spectrometry [1] is a newer competitor to the TIMS process and differs mostly in the way that the ions to be sent through the mass analyzer are made. In ICPMS, the test material is dissolved in an acid and is then sent through a nebulizer into a cover gas, typically argon. The Ar/sample gas is then ionized using radiofrequency energy and an ion beam is extracted from this plasma region. From that point on, the analysis section is essentially equivalent to that in the TIMS apparatus.

4 Problems

1. An interdicted sample of material contains the following isotopic mix: 1.13 wt% ^{234}U, 74.7405 wt% ^{235}U, 13.458 wt% ^{236}U, 10.8015 wt% ^{238}U.
   a. Assume that the ^{234}U inventory is unchanged from initial separation. Find the thermal fluence ϕt that the material was exposed to, in neutrons cm^{-2} assuming that it was in a thermal reactor and subsequently reprocessed. Use the following method: (1) Ignore the ^{234}U presence. (2) Calculate the fluence ϕt by taking the ratio of the ^{235}U to ^{236}U (In the ratio, notice that the enrichment f drops out).
   b. Compute the initial enrichment in ^{235}U of this material, by the ratio of ^{235}U to ^{238}U (which results in an equation in $f/(1-f)$), using the value of ϕt calculated above.
2. Repeat the exercise above, but now solve for the enrichment and the fluence simultaneously by doing a least-square fit to the data.
3. A sample which is presumed to be reprocessed spent uranium fuel contains a ^{231}Pa-to-^{235}U ratio of 3.2495×10^{-9} and a ^{230}Th-to-^{234}U ratio of 9.2076×10^{-6}. Calculate the age since reprocessing. Assume that the decay constants are known to $\pm 0.5\,\%$ accuracy and that the measured ratios are known to $\pm 0.1\,\%$ accuracy, find the error estimate on the age. (Note that all errors are $1-\sigma$ values.)

References

1. Becker JS, Dietze HJ (2000) Inorganic mass spectrometric methods for trace, ultratrace, isotope, and surface analysis. Int J Mass Spectrom 197(1–3):1–35. doi:10.1016/S1387-3806(99)00246-8. http://www.sciencedirect.com/science/article/pii/S1387380699002468
2. Diakov AC, Dmitriev AM, Kang J, Shuvayev AM, von Hippel FN (2006) Feasibility of converting russian icebreaker reactors from HEU to LEU fuel. Sci Global Secur 14:33–48
3. Freibert FJ Presentation: “Plutonium Metallurgy". Los Alamos Laboratory Unclassified Report LA-UR-12-23982
4. Grant PM, Moody KJ, Hutcheon ID, Phinney DL, Haas JS, Volpe AM, Oldani JJ, Whipple RE, Stoyer N, Alcaraz A, Andrews JE, Russo RE, Klunder GL, Andresen BD, Cantlin S (1998) Forensic analyses of suspect illicit nuclear material. J Forensic Sci 43(3):680–688
5. Hammel EF (1943–1945) Plutonium metallurgy at Los Alamos
6. Hecker S (2000) Plutonium an its alloys: from atoms to microstructure. Los Alamos Sci 26:290–335
7. Hecker S (2001) MRS Bull 26:672–678
8. Hecker S, Martz JC (2000) Aging of plutonium and its alloys. Los Alamos Sci 26:238–243
9. Hecker S, Timofeeva LF A tale of two diagrams. Los Alamos Sci 244–251 (Number 26 2000)
10. Heller A (2012) Plutonium at 150 years: going strong and aging gracefully. Sci Technol Rev. https://str.llnl.gov/Dec12/chung.html. Accessed 26 Mar 2015
11. Knoll G (2000) Radiation detection and measurement. Wiley. http://books.google.com/books?id=HKBVAAAAMAAJ
12. Mayer K, Wallenius M, Ray I (2005) Nuclear forensicsa methodology providing clues on the origin of illicitly trafficked nuclear materials. Analyst 130:433–441. doi:10.1039/b412922a

13. Mayer K, Wallenius M, Varga Z (2013) Nuclear forensic science: correlating measurable material parameters to the history of nuclear material. Chem Rev 113(2):884–900 (2013). doi:10.1021/cr300273f. PMID: 23194287
14. Mitchell JN, Stan MD, Schwartz S, Boehert CJ (2004) Metall Mater Trans A 35A:2267–2278
15. Moody KJ, Hutcheon ID, Grant PM (2005) Nuclear forensic analysis. CRC Press-Taylor& Francis
16. Nuclear Threat Initiative: Osmium-187 Seized in Omsk, Russia (March 2, 2003). http://www.nti.org/analysis/articles/osmium-187-seized-omsk-russia/
17. Pajo L UO_2 fuel pellet impurities, pellet surface roughness and $n(^{18}O)/n(^{16}O)$ ratios applied to nuclear forensic science. PhD thesis, University of Helsinki. http://ethesis.helsinki.fi/julkaisut/mat/kemia/vk/pajo/. Accessed 24 Mar 2015
18. Ray I, Schubert A, Schenkel R, Koch L (2001) Nuclear forensic science - case histories and investigation methods at the institute for transuranium elements. IAEA Report IAEA-CN-86-82P
19. Richter S, Goldberg S (2003) Improved techniques for high accuracy isotope ratio measurements of nuclear materials using thermal ionization mass spectrometry. Int J Mass Spectrom 229(3):181–197. doi:10.1016/S1387-3806(03)00338-5. http://www.sciencedirect.com/science/article/pii/S1387380603003385
20. Sangster DF, Outridge PM, Davis WJ (2000) Stable lead isotope characteristics of lead ore deposits of environmental significance. Environ Rev 8(2):115–147. doi:10.1139/a00-008. http://www.nrcresearchpress.com/doi/abs/10.1139/a00-008
21. Stanley FE, Stalcup AM, Spitz HB (2013) A brief introduction to analytical methods in nuclear forensics. J Radioanal Nucl Chem 293:1385–1393. doi:10.1007/s10967-012-1927-3
22. Valone SM, Baskes MI, Rudin SP (2012) J Nucl Mat 422:20–26
23. Varga Z, Wallenius M, Mayer K, Keegan E, Millet S (2009) Application of lead and strontium isotope ratio measurements for the origin assessment of uranium ore concentrates. Anal Chem 81(20):8327–8334. doi:10.1021/ac901100e. http://dx.doi.org/10.1021/ac901100e. PMID: 19824713
24. Varga Z, Wallenius M, Mayer K, Meppen M (2011) Analysis of uranium ore concentrates for origin assessment. Proc Radiochim Acta 1:1–4. doi:10.1524/rcpr.2011.0004
25. Wallenius M, Morgenstern A, Nicholl A, Fiedler R, Apostolidis C, Mayer K (2001) Age determination of highly enriched uranium. In: IAEA symposium on international safeguards: verification and nuclear material security, Vienna, Austria IAEA-SM-367/5/07. http://www-pub.iaea.org/MTCD/publications/PDF/ss-2001/PDF%20files/Session%205/Paper%205-07.pdf. Accessed 24 Mar 2015

Nuclear Testing

Abstract The early history of above-ground nuclear testing is discussed, along with the formation of treaties to limit and later to ban nuclear testing. The structure of the Comprehensive Test Ban Treaty Organization (CTBTO) is outlined, along with its International Monitoring System (IMS). The physics and technology of each type of nuclear test monitoring is discussed, starting with the general nature of fission product distributions and the relationship with the isotope undergoing fission and the neutron energies involved. The fission product signatures for xenon, cesium, krypton, and argon are discussed, their atmospheric transport is studied, and the three technologies used at IMS radioxenon stations are explored. Next seismic waves are discussed, along with some historical examples of nuclear detection with seismic signals. Hydroacoustic signals are also discussed, and finally infrasound signals in the atmosphere.

1 Introduction and History

The first nuclear test was performed by the United States at the White Sands Missile Range near Alamogordo, New Mexico on July 16, 1945. The test was an above-ground detonation of an implosion-type plutonium device with a yield of around twenty kilotons. Since that time over 2000 nuclear weapons tests have been performed by (in order by date of first test) the United States, the Soviet Union, the United Kingdom, France, China, India, Pakistan, and North Korea. Figure 1 shows the chronology of these tests by the countries indicated. Over 200 of these tests have been above-ground and have resulted in significant exposure to the public in some cases [34]. One of the most notorious cases was the Castle Bravo test at the Bikini Atoll, which resulted in many cases of radiation sickness and death, especially impacting the island of Rongelap (see Fig. 2 for a map of the fallout zone.) The Limited Test Ban Treaty was signed by the United States, the former Soviet Union, and the United Kingdom on 5 August 1963 and this ended above-ground nuclear testing by the three countries. However, France and China did not sign the treaty and above-ground testing continued for many years afterward [38].

E.C. Morse, *Analytical Methods for Nonproliferation*, Advanced Sciences
and Technologies for Security Applications, DOI 10.1007/978-3-319-29731-6_7

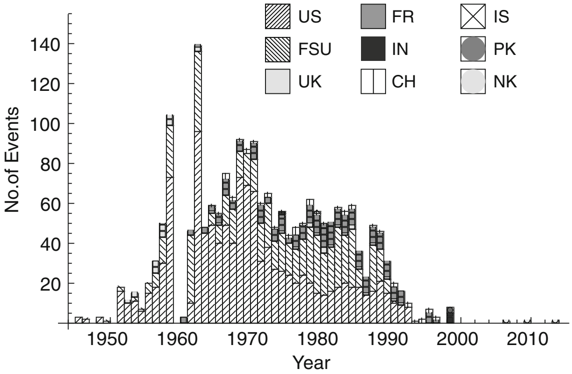

Fig. 1 Nuclear explosions worldwide, 1945–2013

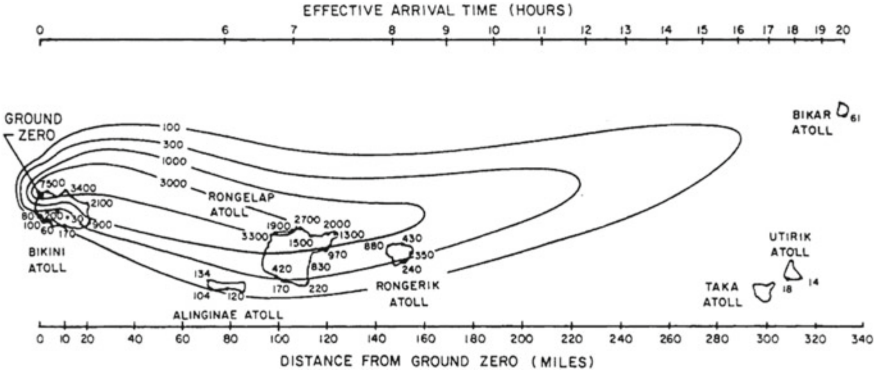

Fig. 2 Fallout from the Castle Bravo test, 1954. Dose contours in roentgens for 96 h of exposure after the detonation. *Source* U.S. Department of Energy

2 The Comprehensive Test Ban Treaty and the International Monitoring System

The idea of a total ban on nuclear weapons testing is almost as old as the idea of building nuclear weapons. Starting in the 1950s, critics of nuclear weapons began calling for a ban on nuclear testing, citing concerns over fallout as well as testing's effect on aiding the development of more lethal nuclear explosives. The Limited Test Ban Treaty mentioned above banned nuclear testing in the atmosphere, underwater, at the ground's surface, or in outer space. This treaty did not cover underground nuclear testing, however. Eventually the "nuclear club" grew in size, and sentiment for a world-wide ban on nuclear testing began to grow. On 10 September 1996, the United Nations passed a resolution calling for a ban on all nuclear testing, and sent it to the member states two weeks later for signature and ratification. (In this context, "signature" means the signing of a treaty by the foreign minister or secretary of state indicating that the government of that state has the intention of entering it into the law of that country. "Ratification" is the actual vote on the treaty by the legislature of that country, making it legally binding.) As of this writing, 164 states have signed and ratified the Comprehensive Test Ban Treaty, and nineteen have either not signed or signed but not ratified the treaty, and thus the treaty is not in force at the time of this writing.

Although the Comprehensive Test Ban Treaty has not been ratified by several states known to have conducted nuclear weapons tests (including China, India, Pakistan, and the United States), nuclear testing has stopped for at least a decade in all of these listed. North Korea has tested more recently—as of this writing, the most recent test was in 2016. There are other countries that might try to develop nuclear weapons in the future, and some of the aforementioned countries could resume testing if they decided that there might be some strategic advantage to doing so. Therefore the ability to detect nuclear explosions, monitor radioactive releases from them, and to develop forensic methods that could give information about the type of device, its yield, and details about the test environment can be regarded as useful capabilities to have. While the large nuclear-capable states have these capabilities on a stand-alone basis, it has been realized that there will need to be a coordinated, world-wide monitoring capability integrated into the United Nations to allow for enforcement of the treaty when it is finally ratified by all parties and passed into law. To this end, a Preparatory Commission for the Comprehensive Test Ban Treaty Organization (CTBTO) has been set up and tasked with the establishment of a world-wide International Monitoring System (IMS) for nuclear test detection.

The IMS is a network of 321 measurement stations and sixteen laboratories. The goal of the IMS system is to be able to detect a nuclear detonation with a yield of one kiloton or more anywhere on the planet. Four technologies are employed for detection: seismic, hydroacoustic, infrasound, and radionuclide monitoring. The IMS consists of 50 primary and 120 auxiliary seismic stations, 80 radionuclide stations, 11 hydroacoustic/T-phase stations, and 60 infrasound stations. Figure 3 shows the worldwide deployment of this system. Reference [20] gives some details of the seismic stations for this network. The science and technology for each of these detection methods will now be discussed in detail.

3 Radionuclide Monitoring

3.1 Fission Product Distributions

The detection of fission products is a powerful tool for the analysis of nuclear tests that have either been carried out above-ground or have released fission products from below the ground. The latter case can be further divided into those shots that have had catastrophic venting due to failure to recognize geological factors such as faults at the site, and those which seep radioactive noble gases through small cracks. The

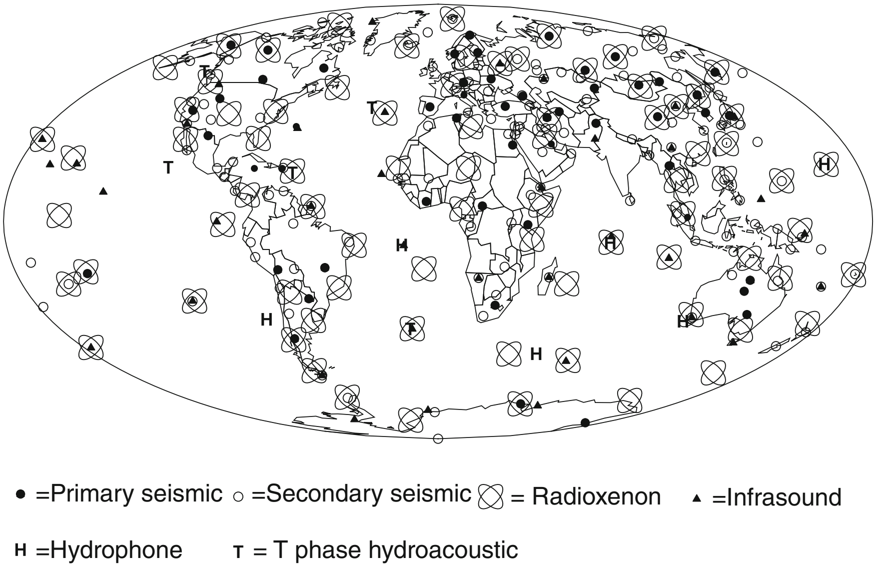

Fig. 3 Map showing locations of IMS stations. From [20]

fission product mass distributions are a function of the fissile isotope involved and the neutron spectrum involved. Figures 4 and 5 show the variations in the fission product mass distributions with these two parameters. In Fig. 4, three energy spectra are used: a thermal spectrum appropriate for a well-moderated (such as graphite) reactor, a fast spectrum typical of an un-boosted nuclear weapon, and a "high energy" spectrum typical of a device with a 14 MeV neutron component due to D-T fusion reactions. Of particular interest is that the double-humped fission product mass distribution is somewhat more filled in between the two peaks as the neutron energy is raised. In Fig. 5, one can see the difference in the mass yield curves between ^{235}U and ^{239}Pu. The noteworthy feature here is that the change in the fission product distribution

Fig. 4 Fission product mass distribution for ^{235}U with different energy spectra. Data from [9]

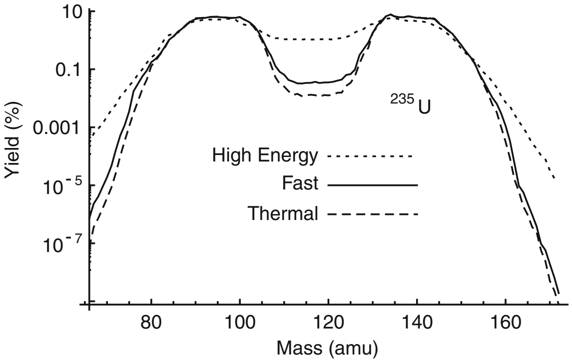

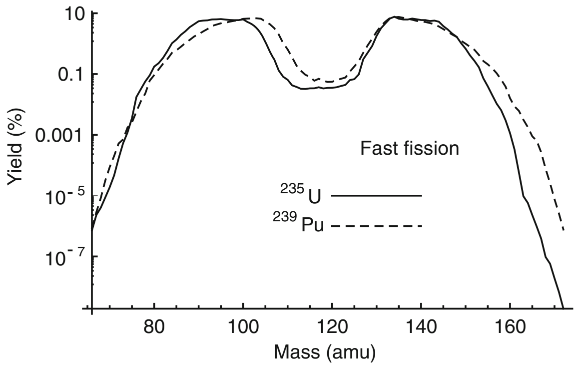

Fig. 5 Fission product yields for ^{239}Pu and ^{235}U. Fast spectrum. Data from [9]

between these isotopes (which must move the ^{239}Pu distribution three or four mass units up from the ^{235}U distribution) takes place by an increase in the centroid of the lower-mass part of the curve and not the upper-mass part of the curve.

3.2 Xenon and Cesium Signatures

The fission product distributions around mass numbers 133 through 135 have a number of interesting features. First, at mass 134, the yield, both independent and cumulative, for the production of ^{134}Cs is essentially zero. This is because ^{134}Cs is an odd-odd nuclide and also far from the average proton-to-neutron ratio for fission products. Also, ^{134}Xe is stable, so there is no decay from the chain of mass 134 isotopes into ^{134}Cs from beta decays. ^{134}Cs is, however, quite common in fission-induced radioactivity in nuclear reactors, because it can be produced by neutron capture on ^{133}Cs. ^{133}Cs has a large cumulative yield of 6.79 %, mostly from the decay of ^{133}Xe with a 5.24 d half-life. The instantaneous nature of nuclear explosions rules out these long-term production steps, so nuclear weapon tests produce virtually no ^{134}Cs, whereas nuclear reactor accidental releases show this isotope prominently. Figure 3.9 shows an example of this after the Fukushima incident. The half-life of ^{134}Cs is 2.06 y and there are strong gamma lines at 604.7 and 795.8 keV, and a weaker line at 801.953 keV.

The four noble gas isotopes ^{133m} Xe, ^{133}Xe, ^{135}Xe, and ^{131m}Xe also give a detailed story about the origin of these fission products. Table 1 gives the relevant radiation data. In fact measurement of these four isotopes form the basis of the International Monitoring Station (IMS) system maintained by the Comprehensive Test Ban Treaty Organization (CTBTO) [18]. As a result of the creation and destruction of these isotopes in the presence of neutrons in a reactor on a timescale similar to or greater than the half-lives involved, the ratios of these isotopes present in a discharge from a reactor are very different from that of a nuclear explosion, as shown in Fig. 6. The dashed "Kalinowski Line" shows the demarcation in the Xe ratio space. While

Table 1 Radiation characteristics of xenon isotopes suitable for atmospheric detection

	Nuclide			
Radiation type	^{131m}Xe	^{133m}Xe	^{133}Xe	^{135}Xe
$t_{1/2}$	11.97 d	2.19 d	5.25 d	9.09 h
γ rays				
Energy, keV	163.9	233.2	81.0[a]	249.8
Absolute intensity, %	1.92	10.0	36.3	90.1
X rays				
Energy, keV	30.0	30.0	31.0	31.0
Absolute intensity, %	54.7	56.6	47.5	4.2
β particles				
Maximum energy, keV			346[b]	905[c]
Absolute intensity, %			99.1	96.0
Conversion electrons				
Energy, keV	129.0	199.0	45.0	214.0
Absolute intensity, %	61.5	63.7	54.0	5.6

From [29]

[a] One more γ ray line with an energy of 769.62 keV and a yield of 0.29 ± 0.07 % is observed

[b] There are two more groups of β particles with end-point energies of 43 and 266 keV and a total yield of 0.897 ± 0.22 %

[c] Two additional groups of lower energy β particles with a total yield of 3.80 ± 0.019 % are observed

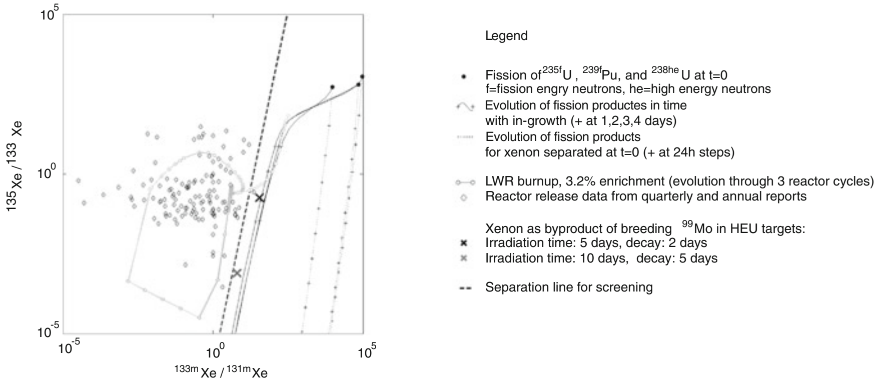

Fig. 6 Isotope ratio plots for Xe isotopes for both nuclear explosives and reactor releases, showing the dashed "Kalinowski line" as a demarcation between reactor-produced xenon (calculated and as reported) and weapon test-produced xenon (calculated). From [18]. Used with permission, Springer

nuclear explosive tests are ruled out by any point to the left of this line, the converse is not necessarily true; however, all reported Xe releases from reactors have fallen to the left of the line. The most difficult case is where the medical isotope ^{99m}Mo is produced in small HEU targets in reactors with short irradiation times; emissions from these facilities can be confused with continuously venting nuclear tests.

3.3 Krypton Signatures

The xenon isotopes fall in the middle of the upper peak in the fission mass distribution, whereas ^{85}Kr falls toward the left side of the lower peak. As a result, the production of the radioactive noble gas ^{135}Xe is similar between fast fission in ^{235}U and ^{239}Pu (within 20 %), but the production of ^{85}Kr differs by more than a factor of two. This may have been exploited to determine that the 2006 North Korean nuclear test was based on a plutonium design rather than uranium by sampling these two gases [33, 35].

A complicating factor in using fission product signatures is that the fission product isotopes are typically produced both directly from a fission event and also from the decay of other fission products. In general, fission products are neutron-rich and decay by beta emission. The half-lives of the precursor isotopes can range from less than a second to several days, and the precursors have widely varying chemistry and thus quite different transport properties through the ground. Reference [9] quotes both cumulative and independent yields for the production of these isotopes. Furthermore, a long-lived noble gas isotope such as ^{85}Kr (10.73 y) may be in the atmosphere downstream from the test site in significant quantities before the test, due to fuel reprocessing, releases from nuclear power plants, or prior nuclear testing [19].

3.4 Argon-37

While ^{37}Ar is not a fission product, it is produced in underground nuclear tests, especially in devices with D-T fusion boosting. This is because almost every type of rock in the earth has some calcium content, and there is a threshold reaction ^{40}Ca(n, α)^{37}Ar. While the energy threshold for this reaction is 1.75 MeV, The cross section is relatively low below about 3 MeV but rises to substantial levels ($>$100 mb) in the range from 4 to 15 MeV. Thus the fast fission neutron spectrum does not create large quantities of ^{37}Ar, but fusion neutrons can cause substantial ^{37}Ar production. Some cross section measurements at energies around 14 MeV were performed at UC Berkeley (with Livermore technical support) in 1999. The cross section data from these measurements is shown as Fig. 7. ^{37}Ar has a 35 d half-life and decays through electron capture. Low-background gas proportional counters are used to detect ^{37}Ar, which forms a 2.822 keV K-shell energy peak in the counting medium.

While the venting of large quantities of ^{37}Ar may indicate that a fusion-boosted weapon has been detonated, there can be some interfering factors to consider in making this determination. Firstly, there is some overlap of the fast fission neutron spectrum with the ^{40}Ca(n, α)^{37}Ar production cross section. Secondly, there is a neutron capture reaction on the stable isotope ^{36}Ar, which has an abundance of 0.337 % in argon, and argon is present in air at around 0.98 %. The cross section for thermal neutrons (0.0253 eV) for $^{36}\mathrm{Ar}(n,\gamma)^{37}\mathrm{Ar}$ is $\sigma_c(0.0253\,\mathrm{eV}) = 5.3$ b. So a "decoupled" device with a fair amount of air in the chamber may produce a negligible contribution

Fig. 7 ^{40}Ca(n, α)^{37}Ar cross sections. From [2]

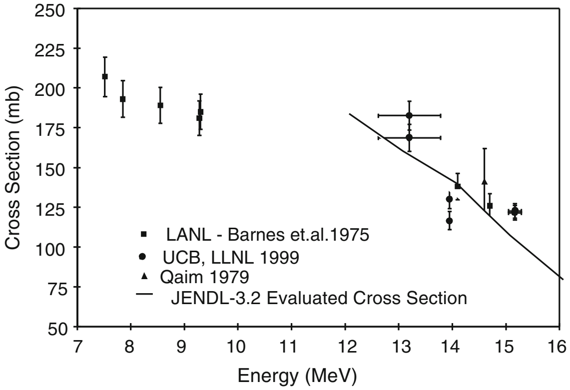

from this side reaction. Thirdly, there is another stable argon isotope present in air, ^{38}Ar, natural abundance 0.063 %, which has an (n, 2n) reaction with high energy neutrons to produce ^{37}Ar. The ^{38}Ar(n, 2n)^{37}Ar reaction cross section also measured at UCB [2].

3.5 *Atmospheric Transport of Radionuclides*

Volatile radionuclides such as Cs and I isotopes that emerge with vent gases from an underground nuclear test are typically attached to dust particles and are considered aerosols. Particle sizes $>5\,\mu$m have enough gravity that they do not travel far from the production site [27]. Smaller particles form a plume which is transported by the local wind and generally is mixed into the air mass up to an altitude of about 2 km. The degree of mixing is controlled by the local air turbulence and the terrain over which the plume is traveling. Precipitation along the plume path can cause rain-out of these radioactive particles. Often detection consists of finding these isotopes as contaminants on the ground in rainwater or soil.

In some cases, however, some of the radionuclide-bearing aerosol can be transported through the mixing layer and be transported to the bottom of the stratosphere through a type of "conveyor belt" convection process. Aircraft fitted with special filtering equipment can detect this radioactivity. Because the winds aloft at the higher altitudes are typically at higher velocity and more consistently in one direction, this can result in earlier detection of a nuclear test from some distance away. Atmospheric nuclear testing, however, creates an initial column of radioactivity extending upwards to the stratosphere without any special weather conditions required. In fact the first nuclear test by the Soviet Union, called RDS-1 by the Soviets and nicknamed "Joe-1" in the West, was detected by WB-29 aircraft flying missions over the Pacific Ocean, Alaska, and Canada at a pressure altitude of 500 mbar (about 18,000 feet). The aircraft were fitted with an air sampling system where outside air was drawn

Fig. 8 Map of radioactive contamination at 500 mb pressure altitude, approximately ten days after the first Soviet nuclear test in 1949. (National Weather Service, see Ref. [21])

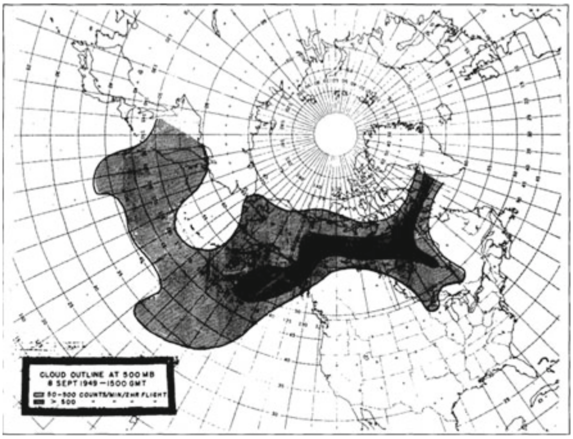

through filter papers, which were analyzed at the air base after the planes returned. Radioactivity was detected off of the Kamchatka peninsula four days after the test. In less than ten days after the detonation, the plume had reached as far as the western side of Greenland [21]. Figure 8 shows a map of the plume at that time.

Noble gases, on the other hand, do not have the chemical affinity for colloidal dust particles and simply travel as an inert component of the atmosphere. There is no dry deposition and limited rainout with these isotopes. Thus, they can remain in the atmosphere for a long time. For the North Korean nuclear test in 2013, xenon was finally detected in Takasaki, Japan 55 days later [5, 32].

Codes have been developed for detailed atmospheric modeling of radionuclide releases, and these have been exploited for predictive modeling of radionuclide concentrations following a known nuclear test. A good example is the FLEXPART code [36], a Lagrangian fluid model code with adjustable particle mass parameters, vegetation accumulation factors, and a library of radionuclide species with their half-lives.

3.6 Radionuclide Monitoring Technology

As discussed earlier, noble gas isotopes tend to stay in the atmosphere for a long time and are the basic atmospheric radionuclide signatures used at IMS stations. Equipment used for detecting radioxenon must have a very high sensitivity to allow for potentially very high dispersal factors in the atmosphere. In order to obtain these high sensitivities, xenon must be extracted from rather large quantities of air. Since the concentration of natural xenon in the atmosphere is 0.087 parts per million, separation factors $>10^6$ are required before counting, and suppression of radon gas in the sample is especially important. The separation technology at IMS comes from three different approaches: the Swedish-built SAUNA system, the French-built SPALAX system, and the Russian-made ARIX [32].

The SAUNA system [31] uses a three-step process to isolate the Xe component in air. A 7 m^3 volume of air is drawn through the system in a 12 h sampling interval. In this time period, about 0.5 cm^3 of Xe is extracted. This is accomplished by first passing the air over a thermoelectrically cooled heat exchanger at a temperature of -5 °C to remove most of the water vapor. Then the air sample is run through a molecular sieve, which removes the residual water. From there, the sample is injected through four consecutive activated charcoal columns at a pressure of 2.4 bar. After a 6 h period, the charcoal filter is taken off-line and the process air is redirected to a tandem unit. The unit is evacuated and heated to 300 °C and helium carrier gas is introduced. The exhausted gas is then passed through a gas chromatography (GC) unit, which separates radon from the xenon, an important step because of the interference of the radon radioactivity with the sensitive xenon counting to be performed later. The xenon portion of the GC output is then re-absorbed on carbogenic molecular sieve material (6.4 cm^3) to reduce its volume for the counting step. The sample is inserted into a $\beta - \gamma$ coincidence counter with 4π geometry. The system consists of two NaI scintillators with holes through the middle. The sample is placed in the middle of the tunnel and two plastic scintillators are butted against the sample. Standard signal processing downstream yields measurement of the four xenon isotopes potentially present in the sample. Threshold sensitivity is better than 1 mBq m^{-3} for all four isotopes (^{133m}Xe, ^{133}Xe, ^{135}Xe, and ^{131m}Xe) for this system.

The SPALAX system [11] (acronym, in French, for Système de Prélèvement Automatique en Ligne avec l'Analyse du Xénon) first pressurizes the air and passes it through a drying membrane followed by a microporous polymetric membrane. This membrane has the property that oxygen, carcon dioxide, and water vapor pass more easily than nitrogen and xenon, resulting in a 12x increase in xenon concentration (from 0.087 to 1.0 ppm). Then the gas, which is now 99.99 % nitrogen, is sent through a series of activated charcoal columns, similar to the SAUNA system described above. These are then put into a desorption cycle at a temperature of 250 °C. This temperature is chosen so that the Xe desorbs more readily than the radon, resulting in a Rn decontamination factor of 10^5. From there another sorption/desorption cycle is done using a molecular sieve with a desorption temperature of 320 °C, which then results in an overall Xe concentration factor of 3×10^6. The overall system processes 80 m^3 of air per day, resulting a total of 7.5 cm^3 of Xe per day for analysis. Unlike the SAUNA system described above, counting is done with a high purity germanium (HPGe) detector, which allows for higher resolution detection of gamma signals from the Xe at the expense of somewhat lower sensitivity than $\beta - \gamma$ coincidence counting. Overall detection thresholds are 1.5, 0.15, 0.65, and 4.05 mBqm^{-3} for ^{133m}Xe, ^{133}Xe, ^{135}Xe, and ^{131m}Xe, respectively.

The ARIX-1 system, developed in Russia, uses cryogenic methods [7]. A schematic of the xenon trapping system is shown as Fig. 9. In this system, the air is compressed and a 1 m^3h^{-1} feed rate is maintained. The air is pre-cooled to eliminate most of the water and then passed through NaA and CaA zeolite filters, cooled to 80 °K, to remove all water and carbon dioxide. The process gas is then sent to an activated charcoal adsorption column cooled to 100 °K. The column is then slowly warmed to –20 °C over a period of 1 h, and then vented to the atmosphere.

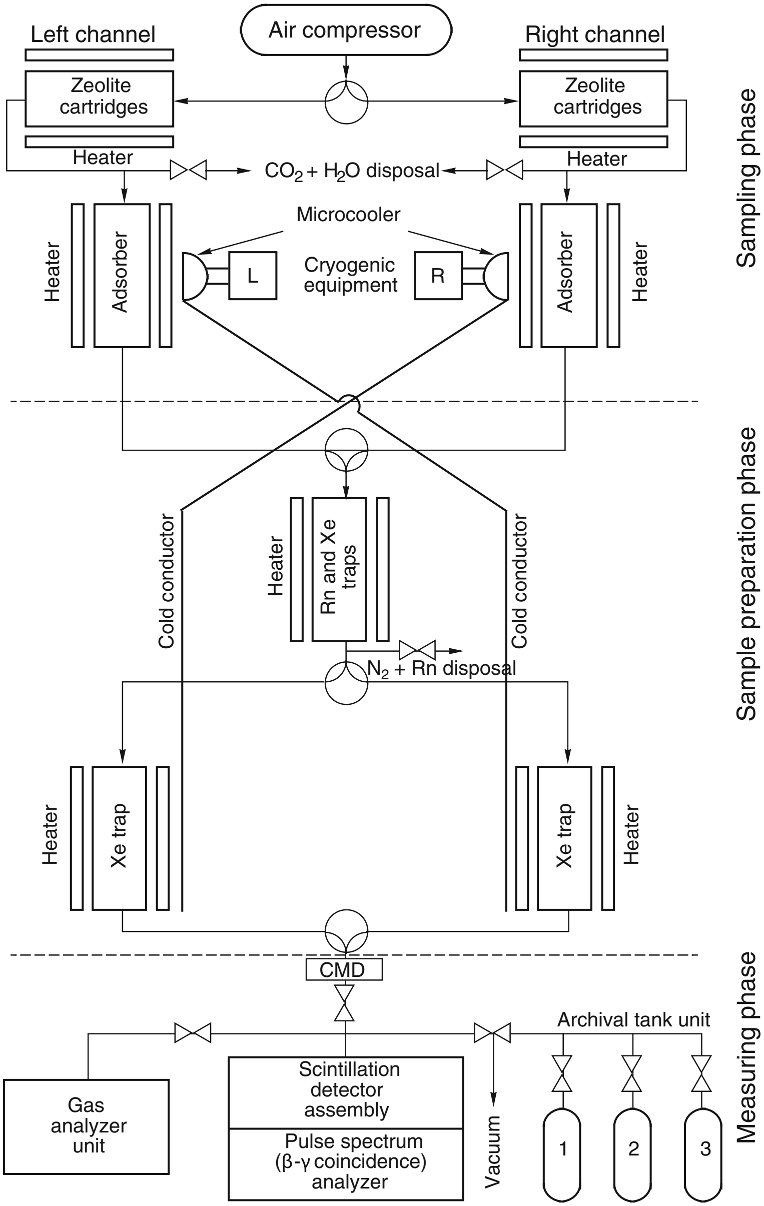

Fig. 9 Schematic of xenon separation system for the ARIX-1 xenon air monitoring system. From [7]. Used with permission, Springer

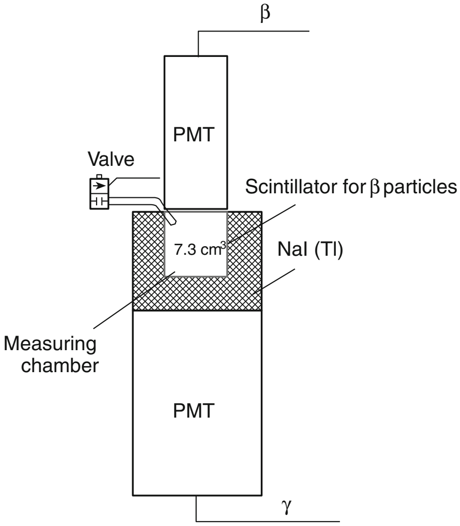

Fig. 10 $\beta - \gamma$ coincidence detection system for ARIX-1 xenon detection. From [29]. Used with permission, Springer

The trap is then heated to 200 °C, and then the effluent (with a helium cover gas) is fed into a series of two traps at room temperature. The first accumulates the radon and nitrogen and the second traps the xenon. Finally, the second trap is heated to 200 °C and then re-adsorbed in a small volume (0.2 cm^3) charcoal trap at 140 °K. a mechanical piston is then used upon regeneration to compress the gas sample into a small volume (6–8 cm^3) for introduction into the test chamber. The counter is a NaI well detector, and the walls of the test chamber are coated with polystyrene, which provides a scintillation medium for $\beta - \gamma$ coincidence counting. Details of the test cell are shown in Fig. 10. The details of the counting system are given in [29]. Overall sensitivities (with uncertainty) for a 10 h collection time for $^{131\text{m}}$Xe, $^{133\text{m}}$Xe, ^{133}Xe, and ^{135}Xe isotopes are 0.62 ± 0.18, 0.66 ± 0.18, 0.48 ± 0.14, and 0.77 ± 0.21 mBq m^{-3}, respectively.

The ARIX-1 system is relatively heavy and consumes a fairly large amount of electrical power. For this and other reasons, it is not portable. Since the design of the ARIX-1, the Russian designers have produced a xenon monitor design with slightly higher minimum detectable activity (by a factor ≈2), but lighter and with lower electrical demand so that it can be transported on a truck. The tradeoff in efficiency is well balanced against this portability, because seismic analysis coupled with atmospheric modeling could yield a good prediction of where the xenon plume will be detectable. The design of this system, called ARIX-3, is described in [30].

The choice of detector type in the three systems mentioned (HPGe or NaI) shows strengths and weaknesses. For the HPGe approach, energy resolution is good, but the system is relatively insensitive to $^{131\text{m}}$Xe, because there is only one gamma in its decay with a branching ratio of only 2 %. On the other hand, the $\beta - \gamma$ coincidence counter requires intimate contact of the gas with the scintillator material. Because some absorption of the Xe gas into the plastic can take place, a detector system exposed to elevated levels of xenon may exhibit a "memory effect", where the detection threshold for subsequent test samples is elevated because of the higher background caused by Xe retention. It might be possible to alleviate this by some very thin coating of a metal such as aluminum on the scintillator, or perhaps switching to an inorganic scintillator, but each of these has an efficiency drawback. The HPGe system does not suffer from this effect.

4 Seismic Signals

Seismic signals add a vital component to nuclear weapon test detection. Since most nuclear tests are performed underground, there is frequently a seismic signal that is easily identifiable as an explosion underground as opposed to an earthquake. Furthermore, there are several different wave propagation velocities connected with the different modes of propagation, and this allows ranging from each seismic monitoring point. Combining the distance-to-event data from several monitoring points then allows one to determine the location of the event, sometimes with great accuracy. Finally, the magnitude to the seismic signal allows an estimate of the yield of the device. While the field of seismology requires a great deal of experience and expertise, the detection of underground nuclear tests has become well-developed by specialists in this area. The information given here should provide a brief introduction.

4.1 Seismic Wave Types

Seismic waves are classified into two broad areas: body waves and surface waves. Body waves involve bulk motion through the medium, whereas surface waves are attenuated exponentially away from the surface. Body waves tend to have higher propagation velocities than surface waves. if we consider a seismic wave with a propagation path $\mathbf{r}$, Then the body wave's displacement vector $\boldsymbol{\xi}$ will have a functional dependence

$$\boldsymbol{\xi}(\mathbf{r}, \mathrm{t}) = \boldsymbol{\xi}_0 \exp\left(\imath\left(\mathbf{k} \cdot \mathbf{r} - \omega \mathrm{t}\right)\right). \tag{1}$$

Here $\mathbf{r}$ can be a travel path with any possible alignment with respect to the local direction away from the center of the earth $\mathbf{z}$. The case where $\boldsymbol{\xi} \parallel \mathbf{k}$ is called the P wave, or primary wave. It is a longitudinal wave similar to an acoustic wave in a fluid, and it is the one that travels the fastest. The case where $\xi \perp \mathbf{k}$ is called the S wave, or secondary wave. It is a shear wave, similar to the motion of a rod (such as a tuning fork) when it is struck.

The most important surface waves are the Rayleigh wave and the Love wave. These have a functional form

$$\boldsymbol{\xi}\,(\mathbf{r},\mathrm{t}) = \exp(-\lambda|z|)\boldsymbol{\xi}_0 \exp\left(1\,(\mathbf{k}\cdot\mathbf{r} - \omega \mathrm{t})\right). \tag{2}$$

For these waves, **k** and **r** are presumed to be in the plane of the earth's surface. For the Rayleigh wave, $\xi \sim \mathbf{r} + \mathrm{i}\mathbf{z}$, and for the Love wave, $\xi \perp \mathbf{r}$, $\xi \perp \mathbf{z}$ and $\xi \perp \mathbf{k}$. Thus the Rayleigh wave represents a rolling motion similar to a water wave, whereas the Love wave is a side-thrusting wave moving along the surface. The displacement vectors for each type of wave are shown in Fig. 11. The propagation velocities for the P, S, and Rayleigh wave are

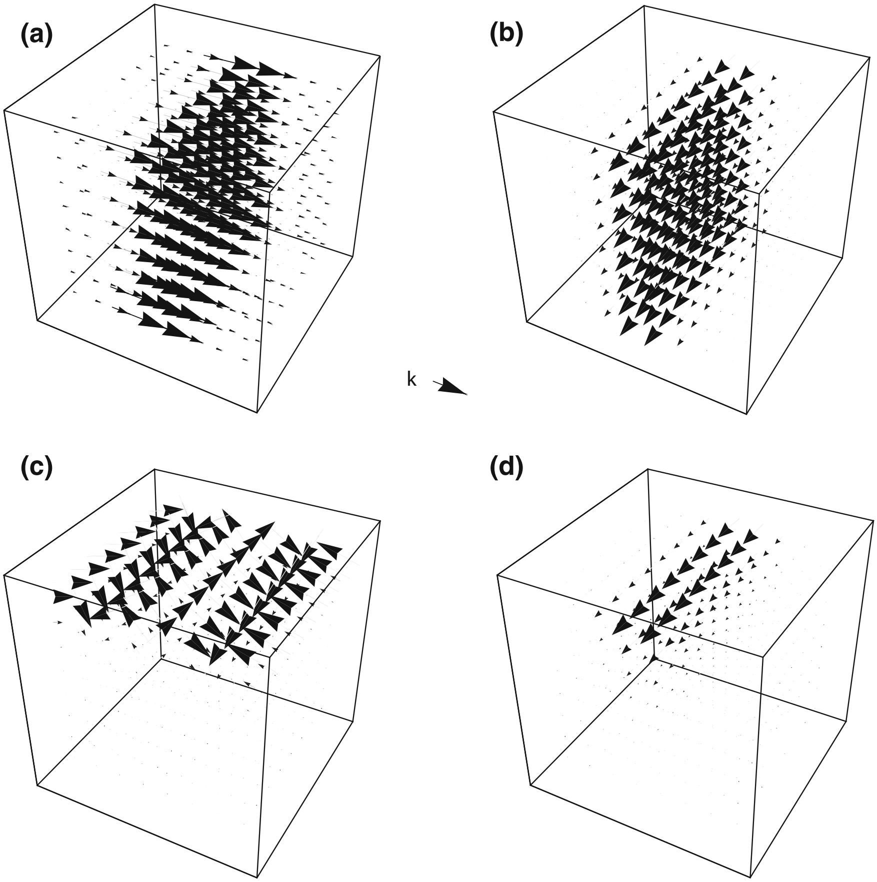

Fig. 11 Displacement vectors for **a** P, **b** S, **c** Rayleigh, and **d** Love waves. Direction of propagation is the same for all four waves

$$\mathrm{V_P} = \sqrt{\frac{\kappa+(4/3)\mu}{\rho}}$$

$$\mathrm{V_S} = \sqrt{\frac{\mu}{\rho}}$$

$$\mathrm{V_R} = \sqrt{\frac{\mathrm{E}}{\rho}}$$

Here ρ is the density, κ is the bulk modulus, μ is the shear modulus, and E is Young's modulus. The Love wave has a more complex velocity of propagation expression, and it is dispersive, i.e. frequency dependent.

The physical constants E, ρ, Y, and μ are all functions of depth, generally resulting in increased velocities for the S and P waves with depth. The path for propagation is the one that will transmit the signal to the observer in the minimum time. (This is known as Fermat's principle.) For relatively short paths (<2000 km, known as "regional" vs. "teleseismic"), the seismic wave will bend down and then resurface at the observer, but staying in the earth's crust during transit without encountering the mantle. This propagation trajectory is labeled with a trailing lower case "g" (for "granite"), and thus Pg and Sg waves [37]. The Rayleigh and Love waves stay on the surface, so these are labeled Rg and Qg (the "Q" is for "Querwellen", German for "sideways"). The mixture of S and P waves, staying near the surface and at low frequencies, are called Lg waves. (Here, the "L" is for "Long".) Another set of regional phases travel down to the outer mantle, then along the top of the upper mantle and then back up to the observer. These are called Sn and Pn waves (here the "n" stands for "normal"). Since P and S velocities are higher in the mantle (by about 1 km $\mathrm{s^{-1}}$ for the P wave), and the mantle is typically 30–40 km under the continents, the Pn and Sn waves are the first to arrive at intermediate distances (a few hundred km) from the event.

4.2 Distance-to-Event Determination

The distance from the source to the observer L can be determined by the difference in arrival time between the P and S wave. This can be written as

$$\Delta \mathrm{t_{P-S}} = \mathrm{t_S} - \mathrm{t_P} = \frac{\mathrm{L}}{\mathrm{V_P}} - \frac{\mathrm{L}}{V_\mathrm{S}} \equiv \frac{\mathrm{L}}{\mathrm{V'}}, \tag{3}$$

with

$$\mathrm{V'} = \frac{\mathrm{V_P V_S}}{\mathrm{V_P - V_S}}. \tag{4}$$

Thus the distance L between the observer and the event is simply $\mathrm{V'}\Delta \mathrm{t_{P-S}}$. While both the P and S wave velocities vary with depth (as well as location), the effective velocity V′ is fairly consistent at around 8 km $\mathrm{s^{-1}}$. Thus one can obtain a quick estimate of the distance to the event fairly easily. Propagation characteristics for most areas of the world are known very accurately, and improved estimates based on the P-S arrival time typically result in location estimates with <10 km error.

4.3 Seismic Signatures of Nuclear Explosive Tests

A nuclear detonation represents a radially symmetric pulse followed by some relaxation movement. As such, the coupling is particularly strong to the P waves. The fast nature of the pulse compared to normal geological events also causes much greater high frequency content in the seismic signal, which is typically analyzed by its Fourier transform. Figure 12 shows the difference in the seismograms of the 1998 India nuclear test and an earthquake from the same area. Figure 13 shows the P-to-S

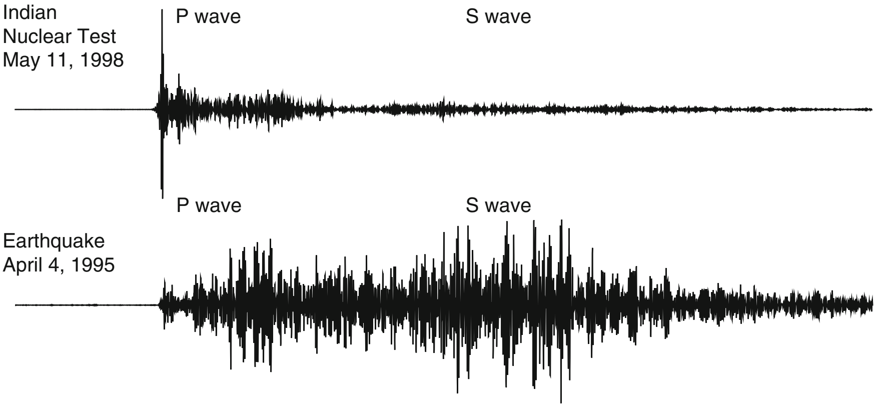

Fig. 12 Seismograms for the 1998 India nuclear test and an earthquake in the same area. Data from monitoring station NIL in Pakistan. From [17]. Lawrence Livermore National Laboratory

Fig. 13 Ratio of P-to-S wave intensity by frequency groups. From [17]. Lawrence Livermore National Laboratory

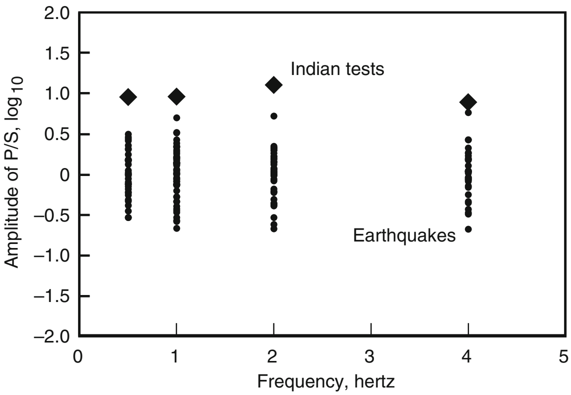

amplitude ratio by frequency groups. The range from 1.5 to 3.0 Hz generally shows the most clear separation between underground explosions and earthquakes.

The yield of a nuclear detonation can also be correlated with the seismic signature. This is usually based on the high-frequency body wave magnitude m_b. The coupling of the device to deeper rock is dependent on the type of media present at the test site. Figure 14, with data from [23], shows an example of the range of m_b measurements for nuclear tests in various media. In the case of volcanic tuff (material covering large areas of the Nevada Test Site), the coupling also depends on the water content, with saturated tuff coupling with an m_b about 0.5 units higher than dry tuff, and similar to granite. In a subsequent publication [23], the same author gives a range of values:

$$m_b = (3.75\text{–}4.45) + 0.75 \log_{10} W, \tag{5}$$

where W is the yield in kilotons.

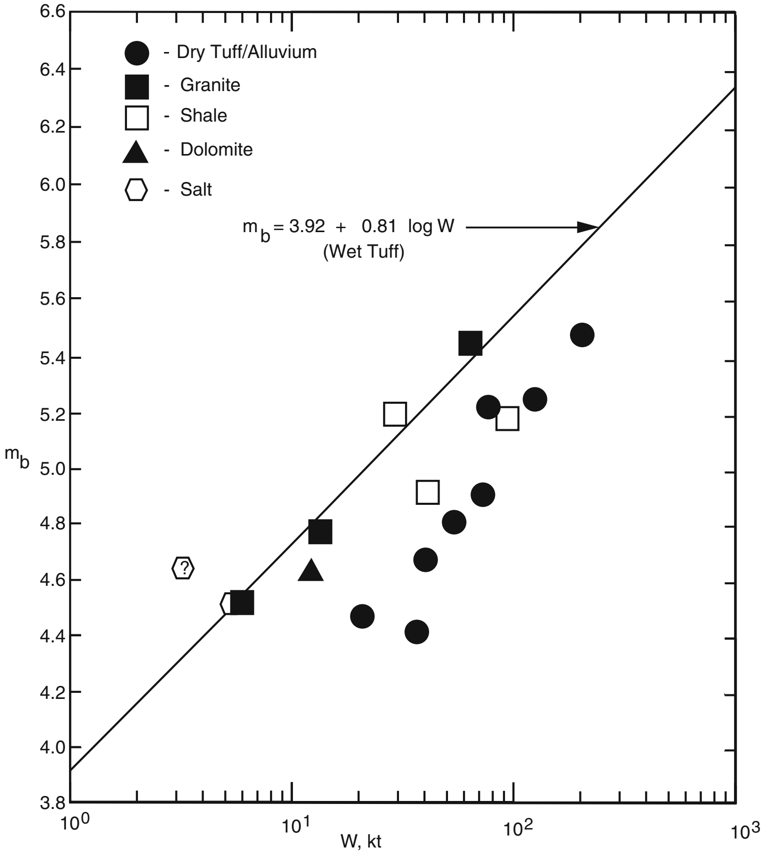

Fig. 14 Relationship between body-wave magnitude m_b and yield for nuclear explosions in various media. From [22]. Used with permission, Springer

It is also worth noting that seismic m_b measurements are a function of the location of the monitoring station and its system response. The International Seismological Centre, located in the U.K., receives data from most seismic monitoring locations on the planet, and has attempted to correlate multiple reports of seismic signals from different stations. They find that the standard deviation for the "raw" seismic data is around 0.3 m_b units, but by assigning response adjustments for each station, the standard deviation drops to around 0.1–0.3 m_b units. Thus the variation seen in Fig. 14 is much wider than the instrument error.

4.4 Limitations of Seismic Monitoring

Seismic monitoring for nuclear tests can help identify the location of a test and give rough estimates of the yield of the test. There have been some examples where the accuracies of these measurements have not always been sufficient to support definite conclusions.

One example would be early experiences with the Soviet nuclear tests at Semipalatinsk in Kazakhstan. The Threshold Test Ban treaty between the Former Soviet Union (FSU) and the United States was signed in 1974, and it was an agreement between the two countries to not test nuclear weapons with a yield greater than 150 kT. However, after that time, seismic signals from FSU tests, especially at certain sites at the Semipalatinsk test site in Kazakhstan [24], showed m_b values up to 6.2, outside the range of the correlations given earlier for yields of <150 kT. While this created some controversy at the time, it was eventually determined that certain geologic areas at the test site were exceptionally well coupled to the surrounding deep rock media. Collaboration between US and FSU geologists, including participation at the US and FSU test sites by both sides during some tests, convinced the US that if treaty violations had occurred, they were of limited importance and accidental. Because of these technical issues, the treaty, although signed in 1974, did not come into force until 1990.

Another example is the detection of a seismic event near the Arctic island of Novaya Zemlya on 16 August 1997 at 0211Z. The large ARCESS array in Norway was down at this time, and the seismic signals from relatively far-away stations FINES in southern Finland (about 1800 km from the event) and NORES in Norway (2300 km away) were used for preliminary analysis of this event. Data from the monitoring station KEV in Kevo, Finland was not used since this station was not part of the US-certified monitoring stations, nor was it included as an International Monitoring System (IMS) station at that time. Station KEV was 1126 Km from the event. (See Figs. 15 and 16 for maps of this area.) As a result, the probability ellipse for this event included the nuclear test site at Novaya Zemlya. The U.S. Secretary of State, Madeleine Albright, issued a *démarche* to the Russian government, claiming that a nuclear test had been performed at Novaya Zemlya [16, 39]. If the data from other stations in the area had been included, especially KEV and station KBS on Spitsbergen island, the event would never have been taken that seriously [16].

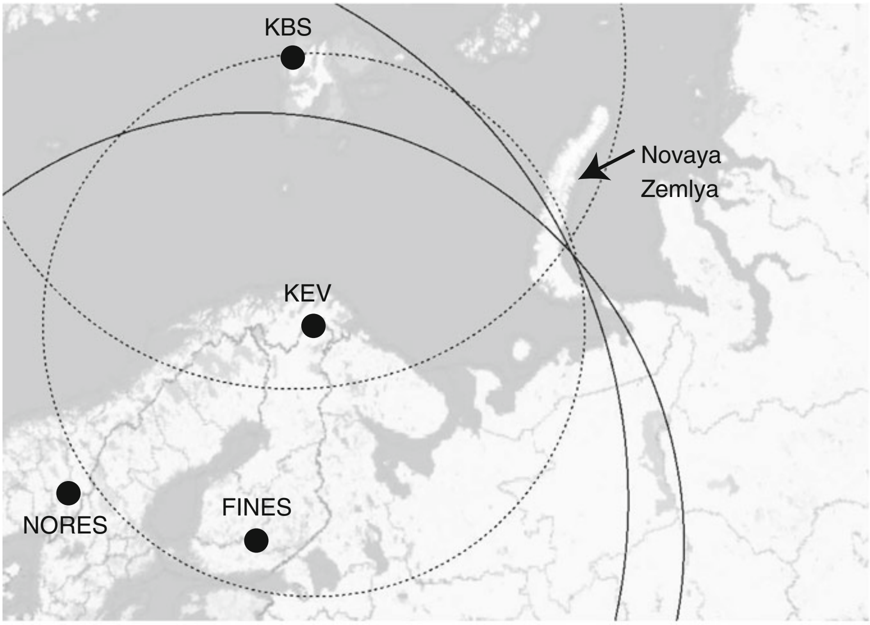

Fig. 15 Distance-to-event estimates from stations NORES and FINES (*solid lines*) and KEV and KBS (*dashed lines*) for the event on 16 August 1997. Data from [39]

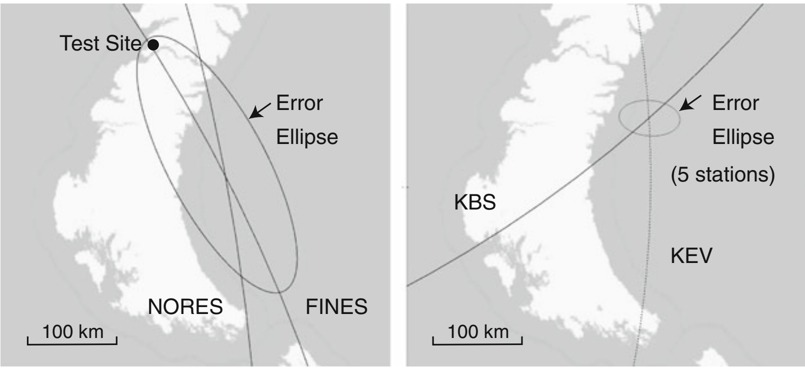

Fig. 16 Close-up of seismic event on 16 August 1997, showing data from both the IMS stations and other, non-IMS stations. Data from [39]

Figure 16 shows a close-up of the distance-to-event estimates, showing that with the additional stations a very small probability ellipse could have been drawn, and the event would have been in the ocean floor and 150 km from the test site. Furthermore, the signal at KEV showed an S/P ratio consistent with an earthquake and not a nuclear test, whereas the lack of high frequency response for the more distant stations such as FINES and NORES stations showed signals which the intelligence community concluded were consistent with a weapon test because they resembled seismographs from known nuclear tests at Novaya Zemlya which had been recorded earlier at those stations. Also, the magnitude of this event, $m_b = 3.25$, was not at all consistent with earlier Russian nuclear tests at Novaya Zemlya—this would have meant a yield of around 0.2 kT.

5 Hydroacoustic Monitoring

Sound waves propagate very easily in water. The attenuation factors are small enough that signals from events such as nuclear tests can be received from hydroacoustic stations all over the planet. This allows for hydroacoustic monitoring of nuclear tests with a very limited number of stations.

If one examines the data for sound speeds in water at a certain point as a function of depth, such as shown in Fig. 17, a persistent feature emerges and that is a minimum in the sound speed at around 500–1000 m. The actual sound speeds may vary from location to location because they are functions of density, pressure, and salinity, but the variation retains the basic structure as seen in Fig. 17. Because of Fermat's

Fig. 17 Two measurements of the speed of sound in ocean water. Showing SOFAR region around 500–1000 m depth. From [15]

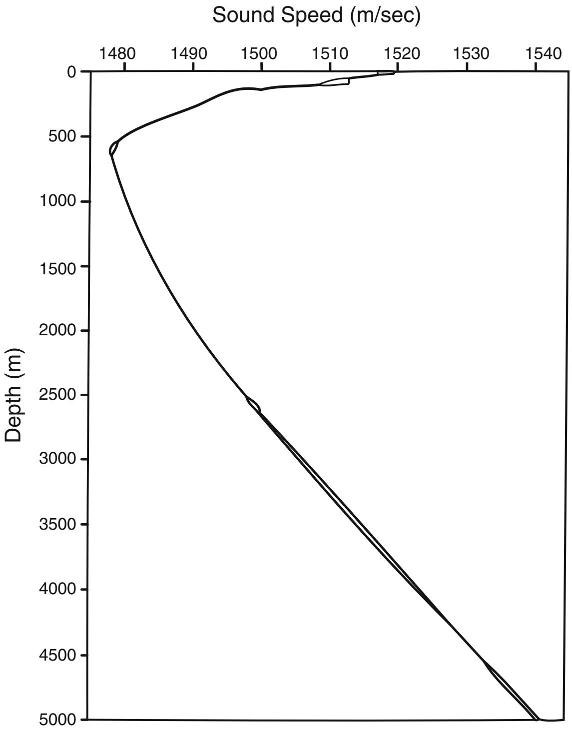

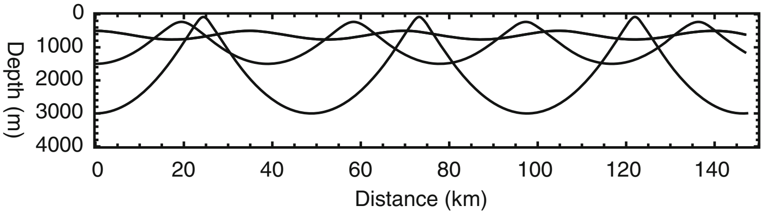

Fig. 18 Ray tracing simulation of sound waves in the ocean near the SOFAR channel

principle mentioned earlier, this causes sound waves launched at a small angle in the 500–1000 m depth zone to be refracted back through the original depth at launch and then to oscillate inside this channel, which acts as an acoustic waveguide. One can easily construct a ray-tracing code to model the behavior of sound waves, which was done to produce Fig. 18. (This code uses the eikonal limit, which requires that $k_z L \gg 1$, where k_z is the wavenumber in the z-direction and L is the gradient length for the sound speed variation, which holds in the high-frequency limit.) Typically, the sound waves propagate at small angles with respect to the horizontal, and in no case greater than a 12° angle to the horizontal. Also, if the wave is launched from a depth where the sound speed is greater than at the ocean surface, a reflection will occur, but with some dispersal and attenuation of the wave's energy. Waves launched at large angles and large depth may also encounter the sea bottom, and will be similarly dispersed and attenuated.

The sound channel at 500–1000 m depth is called the SOFAR channel, standing for SOund Fixing and Ranging. It has been theoretically and experimentally understood since the mid-1940s by Leonid Brekhovskikh [8] and Maurice Ewing [6], working independently. It has been exploited by various submarine communication and stealth strategies since that time, and has thus been heavily researched by military organizations.

One can monitor for nuclear testing using the direct measurement of sound waves in the SOFAR channel. A typical hydroacoustic monitoring station has a set of three tethered buoys at a depth of 800 m. Data from the horizontal triangular arrangement can be used to determine the direction that a particular sound wave came from. An underwater cable takes the telemetry from all three sensors back to a land-based station for recording and analysis. Because of the construction cost of placing the buoys in deep water and the long undersea cable required, hydroacoustic monitoring stations are more expensive than seismic and isotope monitoring systems, but fortunately, only a few are required.

Another signal path for the SOFAR channel exists, however, and that is when there is a sloping sea floor that passes through SOFAR depth and then converts the hydroacoustic wave into P and S seismic waves, which then can propagate to a monitoring station on land. This converted hydroacoustic wave is called a T-phase seismic wave, and is best observed in places not on a continental shelf, such as an island or atoll with a sharply sloping sea floor. (The designation "T" stands for

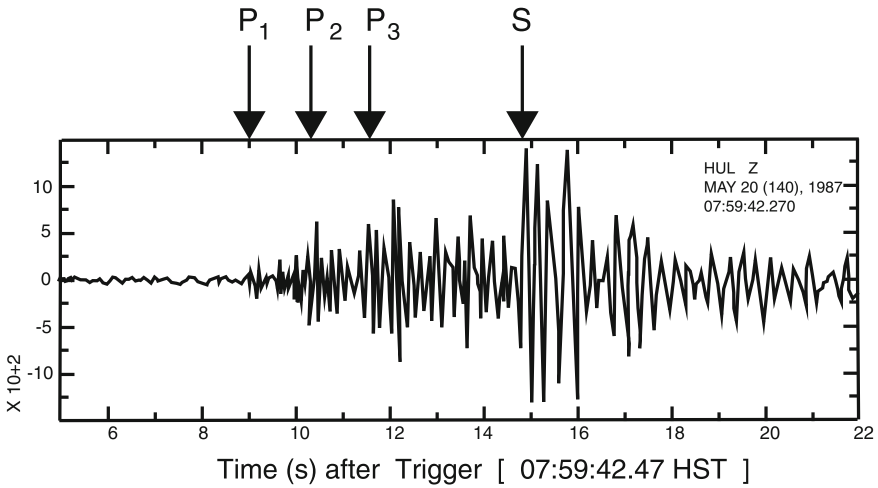

Fig. 19 T-phase seismograph recorded at station HUL at Heiheihulu, Hawaii on 20 March 1987 at 17:59:42.3 Z. The event recorded was the French nuclear test "Lycomède", detonated at Mururoa at 17:05:00.1 Z. From [26]

"tertiary" and is used in cases when an earthquake or nuclear test from a device embedded in the earth is the originating source, so that the overall signal path is P/S-hydroacoustic-P/S. The case where an explosion happened in the water is called an H phase, and it does not necessarily travel in the SOFAR channel, but may be picked up by either hydroacoustic or land-based seismic monitors.) Classic examples of T-phase monitoring include the observation of signals at T-phase stations in Hawaii from French nuclear tests in the Tahitian atoll, almost 5000 km away. Figure 19 shows an example of the monitoring of the French nuclear test on 20 May 1987, which had a yield of 30 kT. The arrival time was 54.8578 min after detonation, giving an apparent velocity of around 1486 m s^{-1}, indicating that there was some travel distance through rock before and after the wave went through water at about 1480 m s^{-1}. (This is also seen from the S-P separation, as there is no S wave in water.)

The advantage of the T-phase monitoring stations is their low cost compared to hydroacoustic monitoring. A disadvantage is that since these stations are located within a few km of shorelines and beaches, there can be an elevated noise floor due to human activity nearby.

6 Infrasonic Signatures

Airborne infrasonic waves of interest for nuclear test detection span the range of frequencies from about 0.002 Hz up to 20 Hz. Low-frequency infrasonic waves have very low loss at lower frequencies, and thus can be detected from great distances.

However, turbulence, meteor penetration, lightning strikes, and other meteorological phenomena can mask or confuse the detection of a nuclear event. First the science of atmospheric waves will be discussed, and then some of the engineering techniques behind ultrasonic monitoring will be presented.

6.1 Waves in the Atmosphere

At high frequencies (in this context, above 1 Hz), the equation relating frequency and wavenumber, known as the dispersion relation, is straightforward:

$$\omega = \mathrm{c_s k} + \mathbf{k} \cdot \mathbf{U}. \tag{6}$$

Here $\mathrm{c_s}$ is the sound speed, $\mathbf{k}$ is the wavenumber vector, $\mathbf{U}$ is the vector wind velocity, and $\mathrm{k} = |\mathbf{k}|$. The speed of sound is a function of temperature and the mix of gases present in the atmosphere. The lower atmosphere has a rather constant average molecular weight, and thus the speed of sound is a function of temperature only and is given by

$$\mathrm{c_s} = \sqrt{\gamma \mathrm{RT}} = \sqrt{402.8\mathrm{T}(^\circ\mathrm{K})}\ \mathrm{ms}^{-1}. \tag{7}$$

Here γ is the ratio of specific heats (around 1.4 for air), R is the gas constant (the ratio of pressure/temperature to mass density) and the temperature is in Kelvin ($\mathrm{T}(^\circ\mathrm{K}) = \mathrm{T}(^\circ\mathrm{C}) + 273.16$). At 20 °C, this gives a sound speed of $343.65\,\mathrm{m\ s}^{-1}$. The temperature of the atmosphere is not constant and is subject to weather conditions, pollution, and other variables. There is, however a "standard atmosphere" that can represent average conditions. The U.S. Standard Atmosphere serves as the basis of the temperature distribution in the atmosphere shown as Fig. 20. Similar to the case with hydroacoustic waves, the two minima shown for temperature, one in the stratosphere at 30–40 km and another in the thermosphere at around 90–100 km, can serve as acoustic waveguides for long-range travel of acoustical energy. These are sometimes referred to as "S" and "T" waves, an unfortunate coincidence with the same letters being associated with seismic waves!

At very low frequencies, the influence of gravity, the earth's rotation, and the pressure and density variation must be included in the momentum equation for the air motion during acoustical excitation. The resulting dispersion relation is given by [13]:

$$\mathrm{n}^2 = \frac{(\mathrm{N}^2 - \omega^2)\mathrm{m}^2}{\omega^2 - 4\Omega_\mathrm{z}^2} + \frac{\omega^2}{\mathrm{c_s^2}} - \frac{\mathrm{N}^2 + \mathrm{c_s^2}\Gamma^2}{\mathrm{c_s^2}} \tag{8}$$

Here N is the Brunt-Väisälä frequency given by

$$\mathrm{N}^2 = -g\left\{\frac{\mathrm{g}}{\mathrm{c_s^2}}(1-\gamma) - \frac{2}{\mathrm{c_s}}\frac{\partial \mathrm{c_s}}{\partial \mathrm{z}}\right\} \tag{9}$$

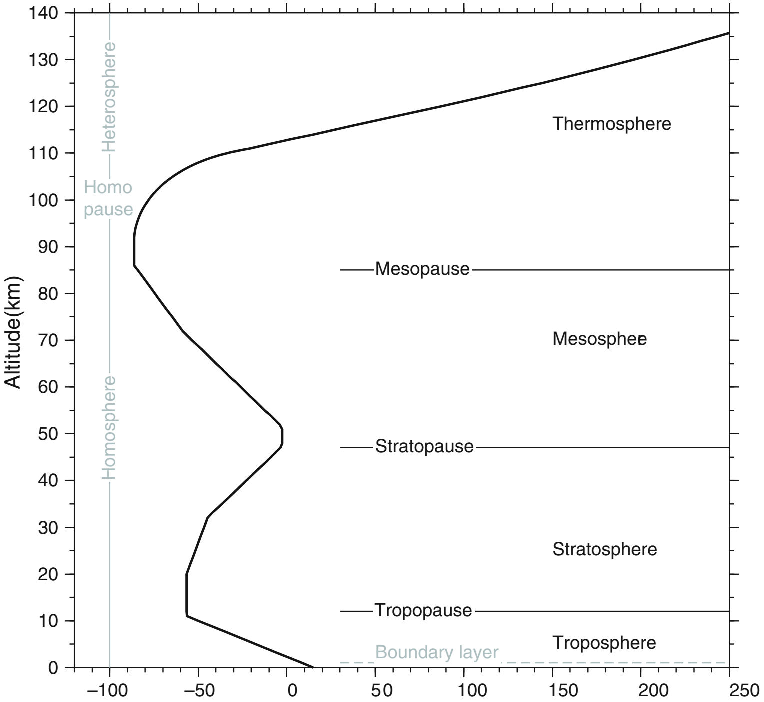

Fig. 20 Temperature distribution in the atmosphere from the U.S. Standard Atmosphere, From [10]. Used with permission, Springer

with g being the gravity constant, Γ is Eckart's constant:

$$\Gamma = \frac{1}{2\rho_0}\frac{\partial \rho_0}{\partial \mathrm{z}} + \frac{\mathrm{g}}{\mathrm{c}_\mathrm{s}^2}, \tag{10}$$

Ω_z is the component of the earth's rotation vector in the direction of the local zenith, i.e. $\Omega \sin \phi$, where ϕ is the latitude and Ω is the earth's rotation rate. The wave is presumed to have a structure $\exp(\mathrm{i}(\omega t - (\mathrm{kx} + \mathrm{ly} + \mathrm{nz})))$, and the total horizontal wavenumber $\mathrm{m} = \sqrt{\mathrm{k}^2 + \mathrm{l}^2}$.

Roots to the low-frequency dispersion equation are shown as Fig. 21. The two solutions spanning a finite range of frequencies are taken as purely horizontal waves, i.e. n = 0. These are separated by a gap in frequency between the Brunt-Väisälä frequency N and the acoustic cutoff frequency $\mathrm{N_A}$. The acoustic cutoff frequency is given by

$$\mathrm{N}_\mathrm{A}^2 = \mathrm{N}^2 + \mathrm{c}_\mathrm{s}^2 \Gamma^2 \tag{11}$$

The upper root in frequency of the dispersion relation asymptotically becomes the simple dispersion relation given earlier, $\omega = \mathrm{c_s k}$, at high frequencies. (Here

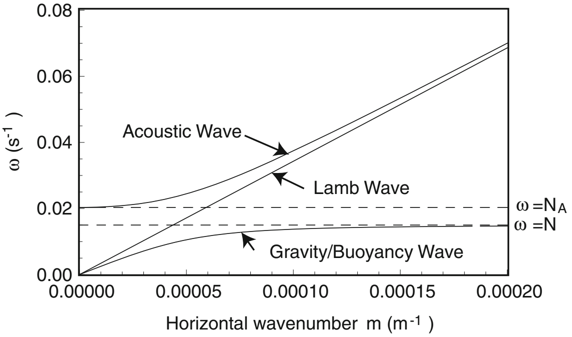

Fig. 21 Infrasound wave modes. From [13]

the Doppler term has been suppressed and the solution can be thought of as the Lagrangian frequency in the comoving frame of the air mass). The lower root has $m \to \infty$ as ω approaches the Brunt-Väisälä frequency N from below. This wave is called the buoyancy wave or sometimes the "gravity wave", a confusing name given the use of the term "gravitational waves" in general relativity. Another type of wave does not have a frequency gap. This wave is called the Lamb wave and it has no z-component of motion. This wave is evanescent in the z-direction so that the wavenumber in the z direction n is imaginary. Using a normalized pressure $P = p(\rho/\rho_s)^{1/2}$, where ρ_s is the mass density at the earth's surface, the z-dependence of the normalized pressure is given by

$$\frac{dP}{dz} + \Gamma P = 0, \tag{12}$$

and taking Γ to be roughly constant (within a factor of two up to 90 Km for the standard atmosphere) gives $P = P_0 \exp(-\Gamma z)$ and thus $n^2 = -\Gamma^2$. This solution to the dispersion relation is shown on Fig. 21 as well. At ultra-low frequencies, another cut-off is seen at the Coriolis frequency $2|\Omega_z|$. A close-up of the dispersion diagram at ultra-low frequencies shows the effect of the earth's rotation. Figure 22 shows this for a middle latitude where $\Omega_z = 10^{-4}$.

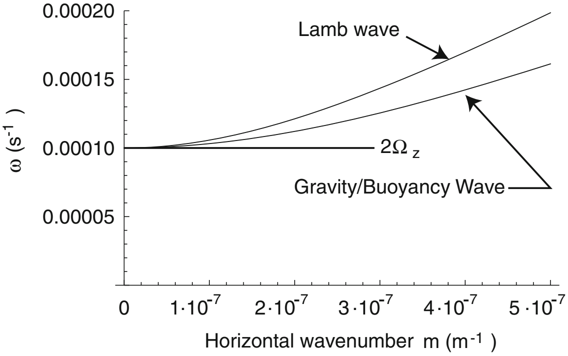

Fig. 22 Ultra-low frequency dispersion diagram, showing the cutoff at the Coriolis frequency $2\Omega_z$ for approximately 45° latitude. From [13]

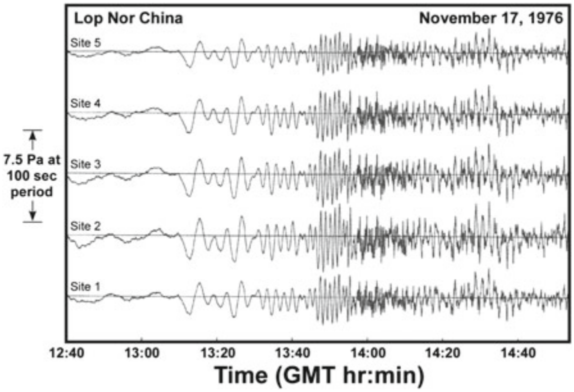

Fig. 23 "Infrasonic signals recorded at WRAI (Warramunga, Northern Territory, Australia) from the thermonuclear test carried out at Lop Nor, China, on November 17, 1976, at a distance of 8,370 km. Yield is estimated to be 4,000 kT. The first arrival is dominated by very low frequencies and is very likely a Lamb wave. The dispersion of all of the higher frequency modal components is clearly visible. Note that the signal extends over a period of several hours. The data shown in this diagram have not been filtered." From [3]. Used with permission, Springer

6.2 Infrasound Signatures for Atmospheric Nuclear Testing

A classic example of an infrasound detection of a nuclear event at Lop Nor, China in 1976 is shown in Fig. 23. This event was recorded in Warramunga, Australia, at a distance more than 8000 km away. Several features of this signal are interesting. The first arrival signal has a period of around 370 s, or a radian frequency of $\omega = 1.7 \times 10^{-3}\ \mathrm{s}^{-1}$. If this were below the acoustic cutoff frequency, but still the fastest-traveling part of the signal, then it was probably a Lamb wave. A much shorter-period group (period 60–70 s) arrives about 2000 s later, indicating a longer path length by about 700 km. This could be explained by multiple bounces between the earth's surface and acoustic waveguides at around 30 and 100 km height, although the later-arriving signals are more likely to have been affected by the wind speed in the trajectory path. The extremely long coda for this event illustrates the relatively loss-free zone of travel for this signal.

In general, the coupling of the blast pressure of a nuclear detonation into the atmospheric waves is a convolution of the initial pressure waveform near the blast with the propagation characteristics of the atmospheric wave medium. The initial pressure pulse at ≈1 km from the blast has been modeled by [12] as

$$\mathrm{p_B(t) = (p_A/r)(1 - t/\tau)u(t)\exp(-t/\tau)} \tag{13}$$

This is plotted as Fig. 24. Analysis with ray tracing can give a fairly detailed picture of the expected pressure signal at a distant observation point. Figure 25 shows an example of ray trajectory calculations using an eikonal approximation. This assumes that

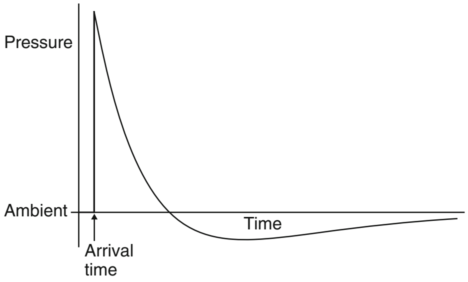

Fig. 24 Model of pressure pulse from above-ground nuclear blast. From [12]

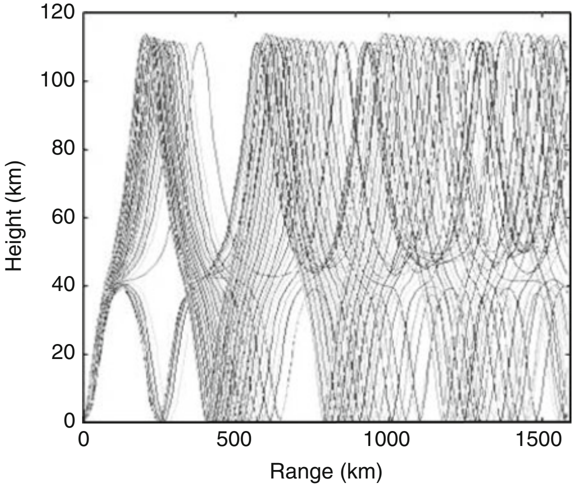

Fig. 25 Example of a ray tracing calculation showing the bounces at 40 and 110 km. From [25]. Used with permission, Springer

the length scale for the variation of the sound speed is large compared to the acoustic wavelength. This example clearly shows the ducting caused by the sound speed minima at around 40 and 110 km. The ray tracing calculations can be extended to include absorption within the atmosphere. Absorption of sound wave energy comes about because of classical effects such as diffusion and viscosity and from excitation of rotational and vibrational states in the molecules. A chart showing the components to the atmospheric absorption as a function of frequency and height is shown as Fig. 26. This frequency-dependent loss also leads to an imaginary part to the wavenumber that is frequency-dependent, and this in turn leads to dispersion, i.e. a change in the sound speed as a function of frequency. This is shown in Fig. 27.

There are many sources of infrasonic background noise that could potentially mask or confuse the detection of a nuclear detonation. Reference [4] gives a ranked list of these noise sources as follows. First and foremost, wind-generated noise caused by turbulent eddies in the boundary layer of the atmosphere dominates the noise spectrum most of the time at all frequencies. Secondly, infrasonic waves caused by air fluctuations associated with large oceanic storm systems ("microbaroms") can occur in the frequency range from 0.12 to 0.35 Hz. Next, noise from surf, usually

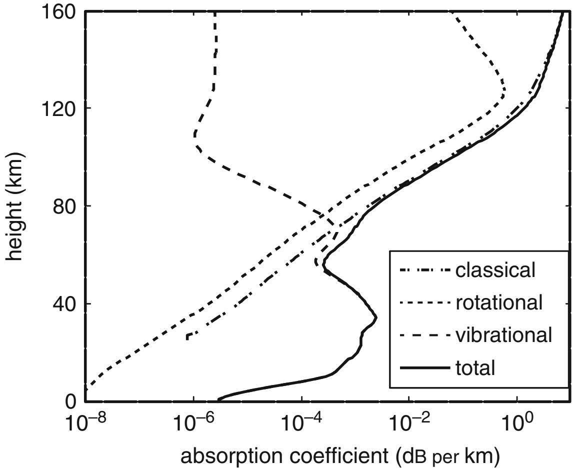

Fig. 26 Infrasound absorption versus frequency and atmospheric height. From [25]. Used with pemission, Springer

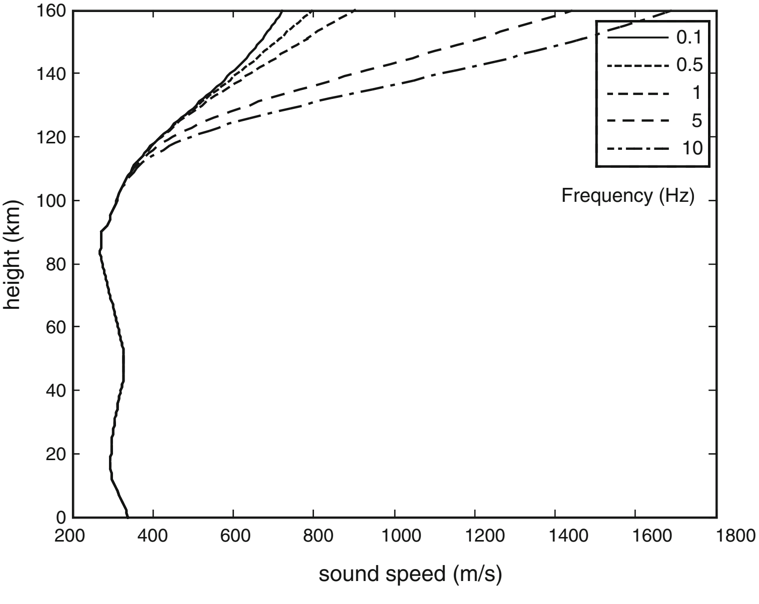

Fig. 27 Speed of sound as a function of frequency and atmospheric height, showing dispersive characteristic above 110 km. From [25], modified from [1]. Used with permission, Springer

above 1.0 Hz, can be present. After that, noise due to man-made sources such as traffic, trains and aircraft, and industry, called cultural noise sources, can occur towards the high end of the infrasound spectrum. Next there is the noise from oil and gas refinery flares, hydroelectric plants, and wind turbines, all at the high end of the band as well. Then there is noise associated with the aurora, usually below 0.1 Hz. After that, infrasonic noise from volcanoes, forest fires, and waterfalls can occur in the higher frequency band. Mountains with wind currents coursing around them can act as a sort of paddle and create infrasonic noise below 0.1 Hz. Next, very low frequency fluctuations can be caused by mesoscale (tens to hundreds of km horizontally) density currents. Then there can be fluctuations associated with nonlinear solitary buoyancy waves and bore waves. Finally, shear instabilities at the boundary of the jet stream and at the top of the troposphere can generate infrasonic noise at low frequencies.

Because of these sources of noise, the preferred channel for nuclear test detection, at least in the sub-kiloton range, is the channel from 0.4 to 1.2 Hz [4]. The signals in this channel at intermediate distance from the event are mostly stratospheric bounces. Corroboration with other frequencies in the spectrum, however, is most likely necessary to avoid a false report. Thermospheric signals are typically at lower frequencies, 0.04 –0.1 Hz, on the other side of the microbarom noise spectrum given earlier. In the infrasonic observation of 183 U.S. nuclear tests, stratospheric signals are seen about 95 % of the time and thermospheric signals about 52 % of the time [14].

6.3 Instruments for Infrasonic Detection

Infrasonic waves can be measured by devices that resemble either aneroid barometers or microphones. The microbarometer design in use at IMS stations was designed by the Laboratoire de Geophysique at the Commissariat à l'Énergie Atomique (CEA) in Bruyères-le-Châtel [4, 28]. This design features an evacuated stainless steel bellows connected to a linear variable differential transformer (LVDT) position sensor. The stainless steel alloy chosen for the bellows features very small displacement as a function of temperature. This is an absolute pressure measuring instrument, however it is electronically filtered to give a passband down to 0.01 Hz and up to 27 Hz to avoid large noise components in the output signal. Another type of infrasonic detector in use in the IMS monitoring stations is based on a differential capacitance microphone. This instrument has been developed by Chaparral Physics, now a part of the Geophysical Institute at the University of Alaska at Fairbanks. This instrument uses a diaphragm with one side exposed to the atmosphere through direct coupling, with the other side backed with a chamber with a small air leak. This mechanical arrangement allows for a very low cutoff frequency of 0.02 Hz, with a high-frequency roll-off at 50 Hz. This instrument has an extremely low intrinsic noise of below 10^{-10} $\mathrm{Pa}^2\ \mathrm{Hz}^{-1}$, as compared to 4×10^{-7} $\mathrm{Pa}^2\ \mathrm{Hz}^{-1}$ for the CEA instrument.

Wind-induced noise is a problem with any infrasonic measuring site. It can be a primary decisive factor in locating the site. For example, the IMS station in Qaanaaq, Greenland was located there in part because it has significantly lower winds than other parts of the Arctic. Wind noise can be reduced by designing a "rosette" of sound-carrying tubes from all directions to connect to the transducer. Arrays of infrasound transducers can also be built, allowing some local noise cancellation but also allowing some directional measurements for high frequency arrivals. It has also been found that microporous tubes (such as "soaker hoses" normally used for lawn and garden irrigation) have excellent wind-noise reduction capability, and in fact the tubing fittings on the manifold for the transducer are the common garden-hose type.

7 Concluding Remarks

While the frequency of nuclear testing has seen a precipitous drop since peaking in the 1960s and 1970s, there will probably be more tests in the future, and despite the high costs and personnel demands, the "nuclear-have" countries are still willing to support the International Monitoring System within the framework of the IAEA. The multifaceted approach, including xenon, seismic, hydroacoustic, and infrasound monitoring should give some confidence that a nuclear test anywhere on the planet has a high probability of detection. The wide breadth of the underlying science for these detection systems is quite impressive, but it is also important to review the mistaken identification episodes that have happened in the past.

8 Problems

1. Three reactors at Fukushima Dai-Ichi were vented. Reactor 1F1 ran on uranium and had a power output of 460 MWe. Reactor 1F2 ran on uranium and had a power output of 784 MWe. Reactor 1F3 ran with 5 % MOX (50 % uranium, 50 % plutonium) and had a power output of 784 MWe. All thermal-to electrical efficiencies were 0.33. Assume that 10 % of xenon inventory was exhausted during the controlled vents, which all happened after all ^{135}I had decayed to ^{135}Xe. The ^{133}Xe production rates are (in percent):

Fig. 28 North Korean nuclear test, 2013

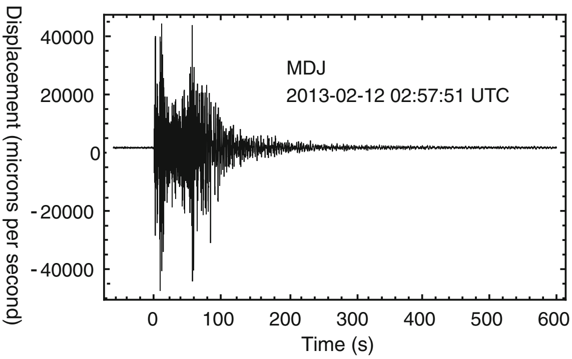

Isotope	Thermal	Fast Fission
^{235}U	6.70	6.72
^{239}Pu	7.02	6.97

Similarly, the ^{135} I production rates are:

^{235}U	6.28	6.30
^{239}Pu	6.54	6.08

a. ^{135}Xe ($t_{1/2} = 9.1$ h) is produced from the decay of ^{135}I ($t_{1/2} = 6.57$ h, thermal fission yield = 6.28 %). Assume that all ^{135}Xe is consumed immediately when the reactors are running, because of the very large (2×10^6 b) capture cross section. Assume that the parent isotope ^{135}I has zero capture cross section. ^{133}Xe decays with a 5.24 day half-life, and has a small (assume zero) capture cross section. Find the concentration of these isotopes six days after shutdown, if they are uniformly dispersed in a 200 Km diameter cylindrical cloud at sea level density (1.293 kg m^{-3}) with a height of 7.5 km. Give your answer in Bq m^{-3}.
b. Find the percentage change in the ^{133}Xe/^{135}Xe ratio if 1F3 were run with 100 % MOX fuel and the other reactors had not vented, i.e. fifty atomic percent of the fuel fissile atoms were plutonium. (Note the different thermal fission cross sections for ^{235}U fission and ^{239}Pu fission.)
c. What signature(s) would you use to determine that measurement was from a reactor accident and not from nuclear weapon testing, say in nearby North Korea?

2. Assume that a 20 kT nuclear device has been detonated at zero altitude and that all noble gases have been released. Assume that the ^{135}Xe and ^{88}Kr isotopes released travel through the atmosphere with no fractionation. Find the ratios between activities for these two isotopes, for the case of ^{235}U fission and ^{239}Pu fission. (Note: use the "fast, pooled" data in the England and Rider tables [9].)
3. A North Korean nuclear test was performed on 2013-02-12 at 02:58:44 (UTC). The test had a seismic magnitude m_b of 5.1. Shown here as Fig. 28 is the seismic signal recorded at monitoring station MDJ in Mudanjiang, China, 372 km away.

   a. What features of this waveform show that this is a nuclear test and not an earthquake?
   b. Identify the S-wave onset and calculate the P-to-S dispersion time V'.
   c. Find a range of values for the yield for this test.

References

1. Bass H, Hetzer C (2006) An overview of absorption and dispersion of infrasound in the upper atmosphere. Inframatics 15:1–5
2. Belian AP (2000) Measurement of the ^{38}Ar(n,2n)^{37}Ar and ^{40}Ca(n,α)^{37}Ar cross sections, and National Ignition Facility concrete activation using the Rotating Target Neutron Source. The design of an experiment to measure the ^{9}Be(n,γ)^{10}Be cross section at 14 MeV. Ph.D. thesis, U C Berkeley. http://search.proquest.com/docview/304590923?accountid=14496
3. Campus P, Christie D (2009) Worldwide observations of infrasonic waves. In Le Pichon A, Blanc E, Hauchecorne A (eds) Infrasound monitoring for atmospheric studies. Springer, Netherlands, pp 184–234. doi:10.1007/978-1-4020-9508-5_6
4. Christie D, Campus P (2009) The ims infrasound network: design and establishment of infrasound stations. In: Le Pichon A, Blanc E, Hauchecorne A (eds) Infrasound monitoring for atmospheric studies. Springer, Netherlands, pp 29–75. doi:10.1007/978-1-4020-9508-5_2
5. Comprehensive Nuclear Test Ban Treaty Organization: CTBTO detects radioactivity consistent with 12 February announced North Korean nuclear test (2013). http://www.ctbto.org/press-centre/press-releases/2013/ctbto-detects-radioactivity-consistent-with-12-february-announced-north-korean-nuclear-test/. Accessed 28 May 2015
6. Drake CL (1974) Maurice Ewing. Physics Today, p 59. http://dx.doi.org/10.1063/1.3128712. http://scitation.aip.org/content/aip/magazine/physicstoday/article/27/7/10.1063/1.3128712
7. Dubasov Y, Popov YS, Prelovskii V, Donets A, Kazarinov N, Mishurinskii V, Popov VY, Rykov YM, Skirda N (2005) The ARIX-01 automatic facility for measuring concentrations of radioactive xenon isotopes in the atmosphere. Instrum Exp Tech 48(3):373–379. doi:10.1007/s10786-005-0065-3
8. Dubrovsky N (2007) The phenomenon of L.M. Brekhovskikh-man and scientist. Acoust Phys 53(3):250–256. doi:10.1134/S1063771007030025
9. England T, Rider B Evaluation and compilation of fission yields. LA-UR-94-3106 ENDF-349. http://ie.lbl.gov/fission.html
10. Evers L, Haak H (2009) The characteristics of infrasound, its propagation and some early history. In: Le Pichon, A, Blanc E, Hauchecorne A (eds) Infrasound monitoring for atmospheric studies. Springer, Netherlands, pp 3–27. doi:10.1007/978-1-4020-9508-5_1
11. Fontaine JP, Pointurier F, Blanchard X, Taffary T (2004) Atmospheric xenon radioactive isotope monitoring. J Environ Radioact 72(1–2):129–135. doi:10.1016/S0265-931X(03)00194-2. http://www.scopus.com/inward/record.url?eid=2-s2.0-0346734303&partnerID=40&md5=20bf1492b730cbaffcdf1bea0ec648f3. Cited By 78
12. Glasstone SE (1962) The effects of nuclear weapons. U.S. Atomic Energy Commission, U. S. Government Printing Office, Washington, D.C
13. Gossard E, Hooke W (1975) Waves in the atmosphere: atmospheric infrasound and gravity waves: their generation and propagation. Developments in atmospheric science. Elsevier Scientific Pub. Co. https://books.google.com/books?id=pydRAAAAMAAJ
14. Green DN, Pichon AL, Ceranna L, Evers L (2009) Ground truth events: assessing the capability of infrasound networks using high resolution data analyses. In: Le Pichon A, Blanc E, Hauchecorne A (eds) Infrasound monitoring for atmospheric studies. Springer, Netherlands, pp 599–625. doi:10.1007/978-1-4020-9508-5_6
15. Hanson J, Bras R, Brumbaugh D, Guern J, Dysart P, Gault A (2001) Operational processing of hydroacoustics at the prototype international data center. In: deGroot Hedlin C, Orcutt J (eds) Monitoring the comprehensive nuclear-test-ban treaty: hydroacoustics, Pageoph Topical Volumes. Birkhäuser, Basel, pp 425–456. doi:10.1007/978-3-0348-8270-5_2
16. Hartse HE (1998) The 16 august 1997 Novaya Zemlya seismic event as viewed from GSN stations KEV and KBS. Seismol Res Lett 69(3):206–215. http://srl.geoscienceworld.org/content/69/3/206.full.pdf
17. Heller A (1999) Seismic monitoring techniques put to a test. Sci Technol Rev. https://str.llnl.gov/str/pdfs/04_99.3.pdf

18. Kalinowski MB, Axelsson A, Bean M, Blanchard X, Bowyer TW, Brachet G, Hebel S, McIntyre JI, Peters J, Pistner C, Raith M, Ringbom A, Saey PRJ, Schlosser C, Stocki TJ, Taffary T, Ungar KR (2010) Discrimination of nuclear explosions against civilian sources based on atmospheric xenon isotopic activity ratios. Pure Appl Geophys 167(4–5):517–539. doi:10.1007/s00024-009-0032-1
19. Kang J, von Hippel FN, Zhang H (2007) Letter to the Editor: The North Korean Test and the Limits of Nuclear Forensics. Arms Control Today. http://www.armscontrol.org/act/2007_01-02/LettertoEditor
20. Kebeasy R (2008) The ctbto international monitoring system and global seismicity. In: Husebye E (ed) Earthquake monitoring and seismic hazard mitigation in Balkan countries, NATO Science Series: IV: Earth and Environmental Sciences, vol 81. Springer, Netherlands, pp 113–120. doi:10.1007/978-1-4020-6815-7_7
21. Machta L (1992) Finding the site of the first Soviet nuclear test in 1949. Bull. Amer. Meteor. Soc. 73:17971806. http://dx.doi.org/10.1175/1520-0477(1992)073(1797:FTSOTF)2.0.CO;2
22. Murphy JR (1981) P wave coupling of underground explosions in various geologic media. In: Husebye ES, Mykkeltveit S (eds) Identification of seismic sources—earthquake or underground explosion, NATO Advanced Study Institutes Series, vol 74. Springer, Netherlands, pp 201–205. doi:10.1007/978-94-009-8531-5_6
23. Murphy JR (2012) Types of seismic events and their source descriptions. In: Husebye E, Dainty A (eds) Monitoring a comprehensive test ban treaty, Nato Science Series E. Springer, Netherlands, pp 225–246. https://books.google.com/books?id=HfrwCAAAQBAJ
24. Murphy JR, Barker BW (2001) Application of network-averaged teleseismic p-wave spectra to seismic yield estimation of underground nuclear explosions. Pure Appl Geophys 158:2123–2171
25. Norris D, Gibson R, Bongiovanni K (2009) Numerical methods to model infrasonic propagation through realistic specifications of the atmosphere. In Le Pichon A, Blanc E, Hauchecorne A (eds) Infrasound monitoring for atmospheric studies. Springer, Netherlands, pp 541–573. doi:10.1007/978-1-4020-9508-5_17
26. Okal E (2001) Converted T phases recorded on Hawaii from polynesian nuclear tests: a preliminary report. In: deGroot Hedlin C, Orcutt J (eds) Monitoring the comprehensive nuclear-test-ban treaty: hydroacoustics, Pageoph Topical Volumes. Birkhäuser, Basel, pp 457–474. doi:10.1007/978-3-0348-8270-5_3
27. Persson C, Rodhe H, De Geer LE (1987) The Chernobyl accident: a meteorological analysis of how radionuclides reached and were deposited in Sweden. Ambio 16(1):20–31. http://www.jstor.org/stable/4313314
28. Ponceau D, Bosca L (2009) Low-noise broadband microbarometers. In Le Pichon A, Blanc E, Hauchecorne A (eds) Infrasound monitoring for atmospheric studies. Springer, Netherlands, pp 119–140. doi:10.1007/978-1-4020-9508-5_6
29. Popov YS, Kazarinov N, Popov VY, Rykov YM, Skirda N (2005) Measuring low activities of fission-product xenon isotopes using the $\beta - \gamma$ coincidence method. Instrum Exp Tech 48(3):380–386. doi:10.1007/s10786-005-0066-2
30. Prelovskii V, Kazarinov N, Donets A, Popov V, Popov I, Skirda N (2007) The ARIX-03F mobile semiautomatic facility for measuring low concentrations of radioactive xenon isotopes in air and subsoil gas. Instrum Exp Tech 50(3):393–397. doi:10.1134/S0020441207030165
31. Ringbom A, Larson T, Axelsson A, Elmgren K, Johansson C (2003) SAUNA—a system for automatic sampling, processing, and analysis of radioactive xenon. Nucl Instrum Methods Phys Res Sect A: Accel Spectrom Detect Assoc Equip 508(3):542–553. doi:10.1016/S0168-9002(03)01657-7. http://www.scopus.com/inward/record.url?eid=2-s2.0-0041743907&partnerID=40&md5=f7754ed87b917e4d449dcfacc4a61cc5. Cited By 97
32. Ringbom A, Axelsson A, Aldener M, Auer M, Bowyer T, Fritioff T, Hoffman I, Khrustalev K, Nikkinen M, Popov V, Popov Y, Ungar K, Wotawa G (2014) Radioxenon detections in the CTBT international monitoring system likely related to the announced nuclear test in North Korea on February 12, 2013. J Environ Radioact 128:47–63. doi:10.1016/j.jenvrad.2013.10.027

33. Shanker T, Sanger DE (2006) North Korean fuel identified as plutonium. New York Times. http://www.nytimes.com/2006/10/17/world/asia/17diplo.html?_r=0
34. Shapiro CS (ed) Atmospheric nuclear tests: environmental and human consequences, NATO ASI series, vol 35. Springer (1998)
35. Smith HP (2006) Nuclear Forensics and the North Korean Test. Arms Control Today. http://legacy.armscontrol.org/node/2391
36. Stohl A, Forster C, Frank A, Seibert P, Wotawa G (2005) Technical note: The lagrangian particle dispersion model flexpart version 6.2. Atmos Chem Phys 5(9):2461–2474. doi:10.5194/acp-5-2461-2005. http://www.atmos-chem-phys.net/5/2461/2005/
37. Storchak D, Schweitzer J, Bormann P (2003) The IASPEI standard seismic phase list. Seismol Res Lett 74:761–772. ftp://isc-mirror.iris.washington.edu/pub/docs/srl_sspl.pdf
38. U.S. Department of State: Treaty banning nuclear weapon tests in the atmosphere, in outer space and under water. http://www.state.gov/t/isn/4797.htm
39. van der Vink G, Park J, Allen R, Hennet C (1998) False accusations, undetected tests and implications for the CTB treaty. Arms Control Today 7–13. http://seismo.berkeley.edu/~rallen/pub/1998arms/ACT1998.pdf

Active Interrogation

Abstract Active interrogation is defined and general properties of active interrogation systems are described for various applications. Active interrogation with fast neutron sources are detailed, including differential die-away analysis, delayed neutrons from fission, and delayed gammas from fission. Next a treatment of neutron transport for fast neutrons is given, along with concepts from age theory and methods to treat hydrogenous media. Next photofission active interrogation is explored. Then nuclear resonance fluorescence (NRF) is studied from the nuclear physics involved, and from potential practical implementations. Photon sources for NRF are studied, including bremsstrahlung, laser Compton upshift, and laser wakefield acceleration combined with Compton upshift. Lastly, the health physics aspects applicable to these systems are presented, with some examples of radiation dose calculations for neutron-based and photon-based systems.

1 Introduction

Active interrogation in the field of nuclear detection means sending an external source of energy into a sealed object and detecting material inside by its reaction to the external source. The most common source examples are neutron and photon (X-ray and gamma) sources and neutron and gamma return signals. (One can consider interaction with cosmic rays as a special case.) Typical objects include sea-going and aircraft cargo containers, luggage, packaged mail, trains, ships, trucks, automobiles, aircraft, and all manner of objects found in ordinary commerce. Another important class of sealed objects are missile warheads and storage containers for weapon parts, where the goal is verification of a declared inventory for treaty verification without being able to actually see the nuclear material inside the object. Active interrogation systems typically must conform to many performance conditions, including low false positive and false negative rates, short interrogation times, minimal radiation exposure to the operators and nearby people, and non-lethal exposure rates to potential stowaways. Some systems must be made portable and battery-operated. Environmental factors are often a consideration, since some outdoor systems might operate in rain, snow, extreme heat or cold, with high levels of vibration, radiofrequency

E.C. Morse, *Analytical Methods for Nonproliferation*, Advanced Sciences
and Technologies for Security Applications, DOI 10.1007/978-3-319-29731-6_8

noise, and so forth. In addition, systems intended for large-scale deployment such as cargo screening at thousands of entry points must be inexpensive to fabricate and to operate, and must not require highly skilled operators. Active interrogation systems for arms control purposes may also require "information barriers", i.e. they must not give away weapon design details by way of the output signals received.

Another active interrogation division is made between those systems where intimate positioning (within a few meters) of the source and detector with the object is possible, and those situations where longer distances (up to 1 km) might be required. An example of the latter is where military aircraft are trying to determine whether an enemy ship is carrying nuclear-tipped missiles. Typically source strengths can be quite high in these scenarios. Technology for this type of active interrogation uses the word "standoff".

First various types of active interrogation with a neutron source will be described. These are characterized by the energy and intensity of the source, and whether the source is pulsed or "cw" (continuously operated, borrowing an old term from radio technology). Then methods using a photon source will be described. Some practical health physics will be applied to assess the radiological risk of these methods.

2 Neutron Active Interrogation

As indicated in Chap. "Signatures and Background", neutrons are relatively rare in nature. Therefore background signals on a neutron detector (with high gamma-ray rejection) will be very low. So if one were to imagine a detection scheme where a short pulse of neutrons were sent in to the inspection object containing SNM, the fission induced in the SNM will also produce neutrons. If these excess neutrons can be detected over the decaying number of neutrons which would be present if no SNM were in the object, then a detection would be made.

2.1 Differential Die-Away Analysis

One scheme exploiting this concept is called "differential die-away analysis", or DDAA [7, 11, 26–28, 52]. In this method, a high energy neutron source, such as an accelerator producing neutrons by means of either the D-D or D-T reaction, or with an electron accelerator producing photoneutrons from bremsstrahlung, is pulsed on for a 1 ms pulse length or less. The high-energy neutrons are moderated in the sample to thermal energies in a relatively short time frame, on the order of $100\,\mu s$. (This characteristic time τ is determined by $\tau = 1/(\Sigma_s v)\ln(E_0/E_{th})/\xi$, where Σ_s is the macroscopic cross section for scattering, v is the speed of the fast neutron, E_0 is the initial neutron energy, E_{th} is the thermal energy (0.025 eV), and ξ is the average logarithmic energy loss per collision.) Once thermalized, the neutrons have a longer lifetime, typically with an e-folding time of order 0.5 ms. This time depends on the absorption cross section at thermal energies, and can be much shorter if a large quantity of neutron-absorbing materials such as hydrogenous materials or boron-loaded shielding is present.) If fissile material is present in the test sample, then fast neutrons are generated, and this fast neutron signature has a time dependence similar to the thermal neutron die-away time, rather than the time dependence for the initial fast neutrons from the source. If some of these fission-generated neutrons leak out before complete moderation, they form a detectable signal in a neutron detector which is made insensitive to thermal neutrons. Typically the detector is a ^{3}He detector shielded with cadmium, which has a very large capture cross section for neutrons below 0.5 eV. Figure 1 shows a typical result of a DDAA analysis, showing the marked difference in fast neutron count rates in the period from 100 μs to 3 ms after the source is turned off. (Typically, the time histogram is built up over many pulses, with the accelerator delivering pulses at a repetition rate of a few hundred pulses per second for periods of time from minutes to hours.)

Several alternative versions of the basic concept also exist. One interesting application [50] is for confirmation of the plutonium inventory in spent nuclear fuel assemblies. Spent nuclear fuel typically has a fairly substantial level of spontaneous fission, mostly due to ^{244}Cm for high burnup and relatively short cooling times and mostly from ^{240}Pu for lighter burnup and longer cooling times. (The half-lives are 18.1 y and 6563 y, respectively, and ^{240}Pu is generated after the absorption of two neutrons from ^{238}U, whereas ^{244}Cm requires six.) Spontaneous fission neutrons also multiply in these assemblies, with multiplication factors between 1.2 and 2.0. (Multiplication is defined as the total flux in the object divided by the flux that would be there from the source, without any neutron-induced fissions occurring. See [45].) These spontaneous fission neutrons, along with neutrons from prompt fissions induced by them, can be thought of as a neutron interrogation pulse. A "clump" of neutrons closely spaced in time, known as neutron multiplicity, is a sign of a fission event, rather than a (α, n) event, also common in spent fuel. Other late-arriving fast neutrons can be counted in a longer tail for the reasons outlined above, i.e. fissions from thermalized neutrons in the assembly. This scheme is called a "self-interrogating" DDAA

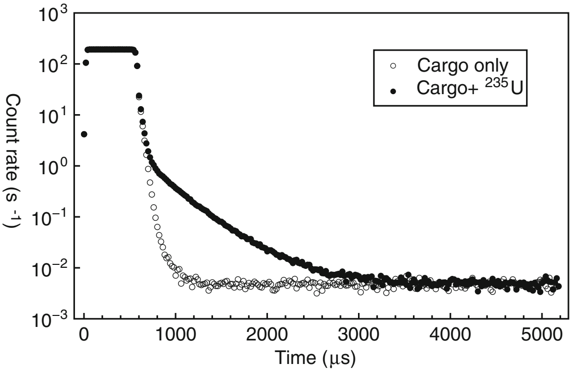

Fig. 1 Fast neutron count rate versus time for a typical differential die-away analysis. After [52]

process, and it requires no accelerator. In other words, this is a passive technique for Pu assay masquerading as an active technique.

For the “real” DDAA systems, the high energy neutrons for interrogation can also be used to determine other properties of the object under test if its makeup is unknown, which can be exploited to sharpen the DDAA analysis. For example, systems employing a D-T neutron source with its 14 MeV neutrons will typically produce large quantities of prompt gammas from $(n, n'\gamma)$ reactions in the light elements such as C, N, and O. The 4.43 MeV carbon inelastic gamma and the 6.13 MeV oxygen gamma are especially prominent. The thermalized neutrons will be absorbed in hydrogen if it is present, producing a 2.2 MeV capture gamma. (In fact the previous three sentences sum up the science of oil exploration.) Reference [52] describes a system where these gamma signatures are used to make some rough cuts into different types of cargo, and then using this information, make corresponding changes to the thresholds and time dependence for the DDAA signal.

2.2 Delayed Neutrons

Since the fission products from induced fission contain isotopes which undergo a beta-decay followed by a neutron emission, these β-delayed neutrons form a longer tail on the neutron count rate versus time [1]. The yield of delayed neutrons is rather small: for ^{235}U, the yields are 0.0158 an 0.0165 for thermal and fast neutrons, respectively, and for ^{239}Pu, they are 0.0063 and 0.0061 [29]. The delayed neutrons are emitted from isotopes with differing half-lives, so the timescale for emission is over a range from a fraction of a second to minutes (see Fig. 2). The delayed neutrons have energies in the range from 200 $\rightarrow$ 500 keV, which is lower than the energy of prompt fission neutrons, and this implies that they are more readily absorbed in other material possibly present in the object. This is especially troublesome if hydrogenous media such as wood, cardboard, or fresh food is present, because hydrogen tends to moderate neutrons to thermal energies very easily, and absorbs thermal neutrons. Also fast neutrons can cause reactions in substances other than U or Pu that also produce delayed neutrons. Among the more troublesome are ^{17}O which can have an (n,p) reaction producing ^{17}N, a beta-delayed neutron emitter with a 4.17 s half-life. (^{17}O has a natural abundance of 0.0373 %.) Also, thorium has a fast fission cross section, but no thermal fission cross section. It will make beta-delayed neutrons on exposure to fast neutrons.

As a forensic application, delayed neutron activation analysis is well suited to use with a nuclear reactor. Research reactors such as the one at he NIST facility in Gaithersburg, MD have a low ratio of fast-to-thermal neutron flux (2×10^{-3}), and this minimizes the interferences from ^{17}O and Th. Trace quantities of U or Pu left behind on packaging materials, wipes, booties, and so forth can be picked up with measurable quantities of ^{235}U down to 200 picograms, for example [16]. Typically

Fig. 2 Fraction of total delayed neutrons released by fast fission of ^{235}U versus time for fast fission. Data from [29]

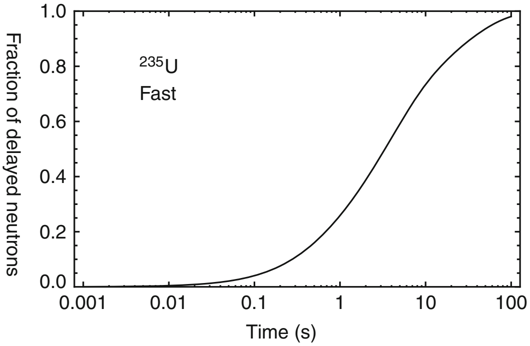

Fig. 3 NIST delayed neutron calibration, with 17 measurements of 15 standards. One second counting time. From [16]. Used with permission, Springer

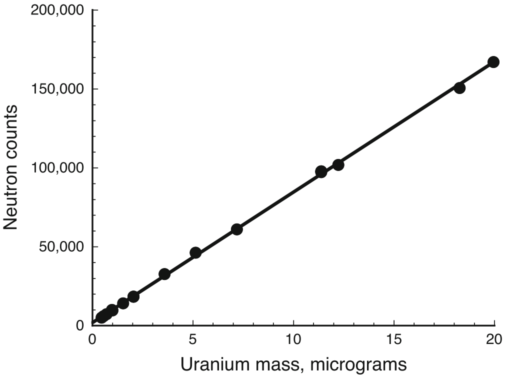

the sample is irradiated for 1 min or less and transferred out of the reactor into a counting cell within a few seconds using a pneumatic transfer tube. The counting cell is typically a polyethylene well moderator with embedded ^{3}He tubes. A 1 s counting time is sufficient to detect the delayed neutrons. Figure 3 shows the performance of the NIST delayed neutron detection system, which shows excellent linearity over many orders of magnitude.

Reference [8] gives a design for a dual-mode system, where both DDAA and delayed neutron assay can be done with the same basic components.

2.3 *Delayed Gammas from Fission Products*

In addition to delayed neutrons, the beta disintegration process in fission products also creates delayed gamma rays. Since the energy of these gamma rays can range above the energies found in natural radioactive decay, it is possible to make a threshold window for gamma energies above the endpoint of the natural background radiation (usually taken to be the 2.614 MeV line in ^{208}Tl, at the end of the ^{232}Th decay series). Reference [19] gives some details about the total number of gammas above a 3 MeV

Table 1 Properties of fission-delayed neutrons and gammas for three important fissile isotopes

	^{235}U thermal fission	^{239}Pu thermal fission	^{238}U fast fission
Delayed neutrons	0.015	0.0061	0.044
γ-rays at $E_\gamma > 3$ MeV	0.127	0.065	0.11
γ-rays at $E_\gamma > 4$ MeV	0.046	0.017	0.03

From [19]

threshold and a 4 MeV threshold for isotopes of interest. Table 1 shows the data for delayed gammas in three fissile isotopes. One notes that there are many more delayed gammas above 3 MeV than delayed neutrons for ^{235}U. Figure 4 shows the time dependence for the production of delayed gammas in ^{235}U for fast fission.

While the natural background radiation has a practical endpoint at 2.6 MeV, there can be interference from induced activity from the neutron source. An example is a 14 MeV accelerator-based neutron source using the D-T reaction. There is a reaction in oxygen, ^{16}O(n,p)^{16}N, which produces a 6.13 MeV gamma ray, with a 7.13 s half-life for the ^{16}N, and 67 % branching to the gamma. The activation of the air around and possibly inside the test object can present a huge signal from ^{16}N. Perhaps even more importantly, most neutron generators have water-cooled targets, and thus oxygen is present within millimeters of the neutron production site. The production of ^{16}N may make the delayed gamma signal unrecognizable, especially if the detector is a low-resolution type such as a high-volume water or plastic scintillator. Therefore it is desirable to use neutrons of energy less than the threshold for this reaction, which is around 10.5 MeV [37]. However, there is a minority stable isotope of nitrogen, ^{15}N, with an abundance of 0.366 %. This has a positive Q for the reaction ^{15}N(n, γ)^{16}N and thus there is a neutron capture cross section down to thermal energies, with a thermal cross section of 79 mb. Thus the ^{16}N signal cannot be completely eliminated for any source energy.

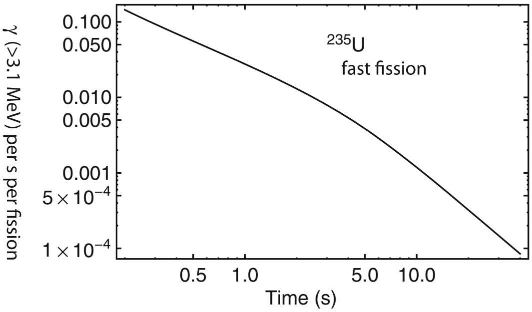

Fig. 4 Delayed gammas with $E_\gamma > 3.1$ MeV from fission of ^{235}U (fast spectrum). Data from [15]

2.4 Neutron Transport

The general theory of neutron transport in matter is framed by the Boltzmann transport equation. The equation is

$$\begin{aligned}&\frac{1}{\mathrm{v(E)}}\frac{\partial\varphi(\mathbf{r},\mathrm{E},\hat{\Omega},\mathrm{t})}{\partial \mathrm{t}}+\hat{\Omega}\cdot\nabla\varphi(\mathbf{r},\mathrm{E},\hat{\Omega},\mathrm{t})+\Sigma_{\mathrm{t}}(\mathbf{r},\mathrm{E},\mathrm{t})\,\varphi(\mathbf{r},\mathrm{E},\hat{\Omega},\mathrm{t})\\&=\int_{4\pi}\mathrm{d}\Omega'\int_0^\infty \mathrm{dE}'\,\Sigma_{\mathrm{s}}(\mathbf{r},\mathrm{E}'\to\mathrm{E},\hat{\Omega}'\to\hat{\Omega},\mathrm{t})\varphi(\mathbf{r},\mathrm{E}',\hat{\Omega}',\mathrm{t})+\mathrm{s}(\mathbf{r},\mathrm{E},\hat{\Omega},\mathrm{t})\end{aligned}\tag{1}$$

Here $\mathrm{E}=\frac{1}{2}\mathrm{mv}^2$ is the energy of the neutron, E' is the energy before a collision resulting in the neutron having energy E afterward, $\hat{\Omega}'$ and $\hat{\Omega}$ are the direction of motion for the neutron before and after a collision, φ is the neutron flux per unit energy and solid angle at time t, Σ_{t} is the total removal cross section, Σ_{s} is the scattering cross section taking neutrons from energy and angle E' and $\hat{\Omega}'$ to energy E and angle $\hat{\Omega}$, and s is a source term for neutrons at energy and angle E and angle $\hat{\Omega}$. The full seven-dimensional neutron transport problem with realistic geometry and source term is usually not solvable analytically, but can be solved numerically with either Monte Carlo or discrete ordinate methods.

However, there are some simplifying concepts that can be used to get the general nature of the neutron population in a particular application such as active interrogation with neutrons. For fast neutrons, one would like to know the rate at which the neutrons thermalize, and how quickly they leave the test object.

Transport is rather different in hydrogenous media than high-Z media. This is because of large differences in the rate of thermalization of high-energy neutrons depending on the atomic weight of the moderating media. The mean logarithmic energy loss ξ is given by

$$\xi\equiv\frac{\Delta\mathrm{E}}{\mathrm{E}}=1+\frac{(\mathrm{A}-1)^2}{2\mathrm{A}}\ln\left(\frac{\mathrm{A}-1}{\mathrm{A}+1}\right)\approx\frac{2}{\mathrm{A}+2/3}\tag{2}$$

Here the last approximation holds for $\mathrm{A}>10$. Thus the average number of collisions for neutrons to thermalize is $\mathrm{N}=\ln(\mathrm{E}_0/\mathrm{E}_{\mathrm{th}})/\xi$, or a time to thermalization $\tau=1/(\Sigma_{\mathrm{s}}\mathrm{v})\ln(\mathrm{E}_0/\mathrm{E}_{\mathrm{th}})/\xi$ as given earlier. For hydrogen, $\xi=1$, whereas for iron, $\xi\approx1/28$. In applications such as cargo inspection, there is a constraint on the average density due to weight limitations for the container. For container cargo, dividing the maximum net weight by the cargo volume gives a maximum density of around 0.6 g cm^{-3}. Then the macroscopic scattering cross section is $\mathrm{n}\sigma$, where the number density $\mathrm{n}=(\rho/\mathrm{M})\mathrm{N}_{\mathrm{A}}$, where A is Avogadro's number, ρ is the mass density, and M is the average atomic mass. Figure 5 shows the macroscopic scattering cross sections for wood (modeled as cellulose, $C_6H_{10}O_5$) and steel (modeled as iron with 1 % carbon by weight) cargo, with each taken to have an average density of 0.6 g cm^{-3}. One can see from the figure that steel has a complex resonant structure above 10 keV, with a large "window" at 27 keV due to the ^{56}Fe cross section approaching zero at this energy.

Fig. 5 Macroscopic cross sections for wood ($C_6H_{10}O_5$) and steel (Fe + 1 wt% C) for densities of 0.6 g cm^{-3}. Data from [10]

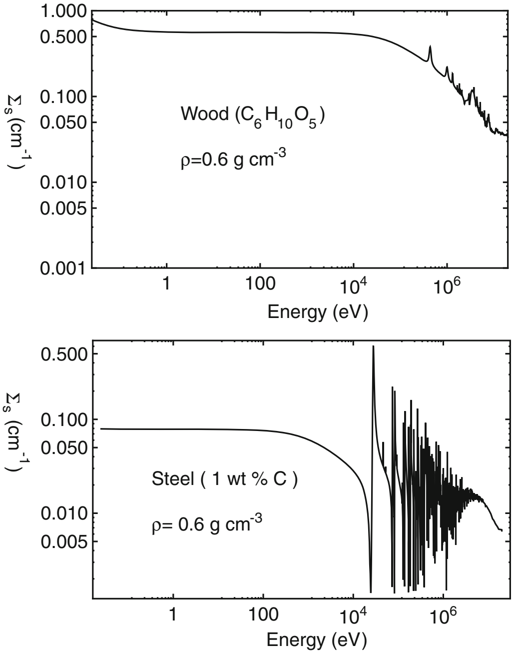

Although the nuclear structure for iron and thus steel is quite complex, we can see that outside of some narrow resonances, the mean free path $1/\Sigma$ is rather long in the high energy region, with an average value of around 30 cm. If we take the mean free path $\lambda = 1/\Sigma$ to be roughly constant in the high energy region for neutrons in the moderating medium, then

$$\langle r^2 \rangle = \frac{1}{\Sigma} \int_0^\infty r^2 e^{-\Sigma r} dr = \frac{2}{\Sigma^2} = 2\lambda^2 \tag{3}$$

Since the individual slowing-down steps add in quadrature, then the mean-square slowing-down length $L_{E_0 \to E_1}$ is given by

$$L^2_{E_0 \to E_1} = 2N\langle r^2 \rangle = 2N\lambda^2 = \frac{2\ln(E_0/E_1)}{\xi}\lambda^2 \tag{4}$$

If we use $E_0 = 10$ MeV and $E_1 = 50$ keV, with $\langle \lambda \rangle = 30$ cm, this gives $\langle r^2 \rangle \approx 3.5 \times 10^5$ cm^2, and thus $\langle r^2 \rangle^{1/2} \approx 6$ m, larger that the container. This means that most fast neutrons will be scattered out of the container before thermalizing.

For hydrogenous targets, the number of collisions to thermalization is much smaller, and one expects to see a cloud of thermal neutrons around the source. Here it is useful to apply the Fermi age model to describe the energy- and spatiallydependent flux. If we take $\phi \mathrm{dE} = (\int \varphi \mathrm{d}\Omega)\mathrm{dE}$ to be the total flux of neutrons with energy between E and E+ dE, then we have a rate of neutrons moving down through the logarithmic energy space (called the lethargy) given by

$$\mathrm{q} = \xi \Sigma_{\mathrm{s}} \mathrm{E} \frac{\mathrm{d}\phi}{\mathrm{dE}}, \tag{5}$$

where Σ_{s} is the scattering cross section as used previously. If we re-write the neutron diffusion equation, $\mathrm{D}\nabla^2\phi - \Sigma_{\mathrm{s}}\phi = 0$ (where $\mathrm{D} = 1/(3\Sigma_{\mathrm{tr}})$, with $\Sigma_{\mathrm{tr}} = \Sigma_{\mathrm{s}}(1 - 2/(3\mathrm{A}))$ in terms of the new variable q and a "time-like" quantity τ (called the "Fermi age") defined by

$$\tau = \int_{\mathrm{E}}^{\mathrm{E}_0} \frac{\mathrm{D}}{\xi \Sigma_{\mathrm{s}} \mathrm{E}} \tag{6}$$

we then have a simple parabolic equation

$$\nabla^2 \mathrm{q}(\mathbf{r}, \tau) = \frac{\partial}{\partial \tau} \mathrm{q}(\mathbf{r}, \tau). \tag{7}$$

In an infinite medium with a source $\mathrm{q}(\mathbf{r}, 0) = \delta(\mathbf{r})$, Eq. (7) has a solution

$$\mathrm{q}(\tau, \mathbf{r}) = \frac{\exp(-\mathrm{r}^2/(4\tau))}{(4\pi\tau)^{3/2}}. \tag{8}$$

The Fermi age τ actually has units of square centimeters, rather than time, and is associated with the mean square distance traveled by the neutron from its birthplace, given by:

$$\langle \mathrm{r}^2 \rangle = \frac{\int_0^\infty \mathrm{r}^2 \mathrm{q}(\mathrm{E}, \mathrm{r}) 4\pi \mathrm{r}^2 \mathrm{dr}}{\int_0^\infty \mathrm{q}(\mathrm{E}, \mathrm{r}) 4\pi \mathrm{r}^2 \mathrm{dr}} = 6\tau \tag{9}$$

For a wood cargo at a density of 0.6 g cm^{-3}, Ref. [41] gives a Fermi age from an initial energy of 10 MeV down to thermal energy (0.025 eV) of 700 cm^2. It is empirically found that the Fermi age solution given above (Eq. 8) does not work well for hydrogenous media. Reference [2] gives an alternative expression for the slowing-down density $\mathrm{q}(\mathrm{r}, \tau)$, given by

$$\mathrm{q}(\mathrm{r}, \tau) = \frac{\exp(-\mathrm{r}/\sqrt{\tau})}{4\pi \mathrm{r} \tau} \tag{10}$$

This is the so-called Yukawa kernel. The slowing down density at $\mathrm{E} = \mathrm{E}_{\mathrm{th}}$ becomes the source term for the thermal neutron diffusion equation:

$$-\mathrm{D}\nabla^2\phi + \Sigma_{\mathrm{a}}\phi = \mathrm{q}(\mathrm{E}_{\mathrm{th}}) \tag{11}$$

Convolving the source term $q(E_{th})$ with the Green's function kernel for Eq. (11), such that $\phi(\mathbf{r}) = \int G(\mathbf{r}, \mathbf{r}')q(E_{th})d\mathbf{r}'$ gives the thermal flux:

$$G(\mathbf{r}, \mathbf{r}') = \frac{\exp\left(-\Sigma_a|\mathbf{r} - \mathbf{r}'|\right)}{4\pi D|\mathbf{r} - \mathbf{r}'|} \tag{12}$$

$$\phi_{th} = \frac{1}{4\pi D}\left(\frac{1}{1/\tau - k^2}\right)\left(\frac{1}{r}\right)\exp(-kr)\left[1 - \exp(r(k - \tau^{-1/2}))\right] \tag{13}$$

Here $\kappa = \sqrt{\Sigma_a/D}$.

However, this flux expression can only be applied for distances on the order of the rms distance scale $\langle r^2\rangle^{1/2} = \sqrt{6\tau}$ given earlier, and for larger distances, another approach can be used. Fermi age theory is not valid at large distances [3]. Experimental data using high energy neutrons in water reveals a different radial dependence and exponential factor at large distances. Figure 6 illustrates the actual situation. At larger distances, the source of neutrons entering the slowing-down process are the neutrons encountering their first scatter. The uncollided flux (per source neutron per second) at some distant point r is given by

$$\phi_u = \frac{\exp\left(-\Sigma_s(E_0)r\right)}{4\pi r^2} \tag{14}$$

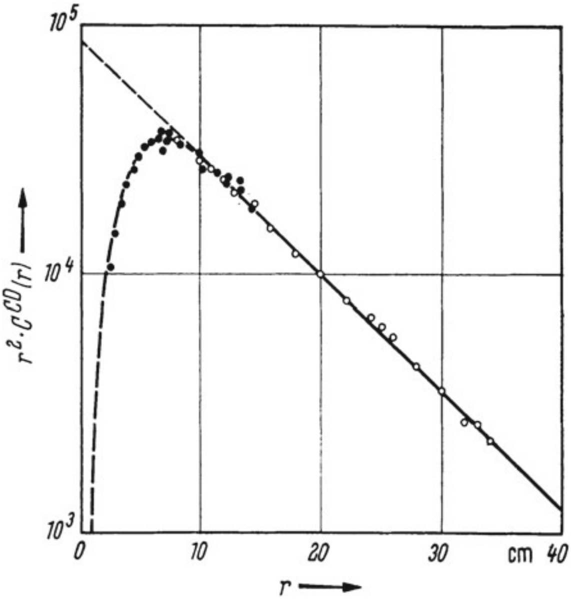

Fig. 6 Neutron flux (at indium resonance energy, 1.46 eV) in water as a function of distance from a radium-beryllium source (3–5 MeV neutrons), showing the $\exp(-\Sigma_s r)/r^2$ dependence. From [3]. Used with permission, Springer

which results in a local slowing down density given by $q(E_0) = \xi \phi_u \Sigma_s$. At large distances, the operator ∇^2 in Eq. (7) is small, as is the ∇^2 term in Eq. (11). Then the thermal flux $\phi_{th} = q(E_{th})/\Sigma_a$. If we ignore absorption at intermediate energies, then

$$\phi_{th} = \frac{\exp(-\Sigma_s(E_0)r)\xi\,\Sigma_s(E_0)}{4\pi r^2 \Sigma_a(E_{th})} \tag{15}$$

Applying this to the case of a 10 MeV neutron source at the bottom of a cargo container filled with wood at a density of 0.6 g cm^{-3}, this gives a thermal flux at the center of the container of about 0.036 times the fast flux that would be there from a point source at the bottom of an empty container.

As an example of a system of cargo container size and its neutron transport properties, Ref. [12] gives an example of a neutron interrogation experiment using a 7 MeV neutron source (based on a 4 MeV radio-frequency quadrupole deuteron accelerator with a deuterium gas target) that was directed at either a stack of plywood or a structure made out of steel tubes. For the plywood case, the density was 0.55 g cm^{-3}, which results in a macroscopic scattering cross section of 0.0409 cm^{-1} at 7 MeV. Two different size targets of highly enriched U_3O_8 were used, one containing 221.1 g ^{235}U and the other 376.5 g ^{235}U. Gamma rays with energy above 3 MeV were collected in large plastic scintillators. By assuming that the delayed fission gamma signal was proportional to the surface area of the HEU targets (because of the very short mean free path for thermal neutrons, the HEU targets appear "black"), and assuming constant efficiency versus target position for collection of gamma rays, one can draw a graph of the count rate times the square of the distance from the source to the HEU target. (The source was approximately 70.9 cm below the plywood stack,

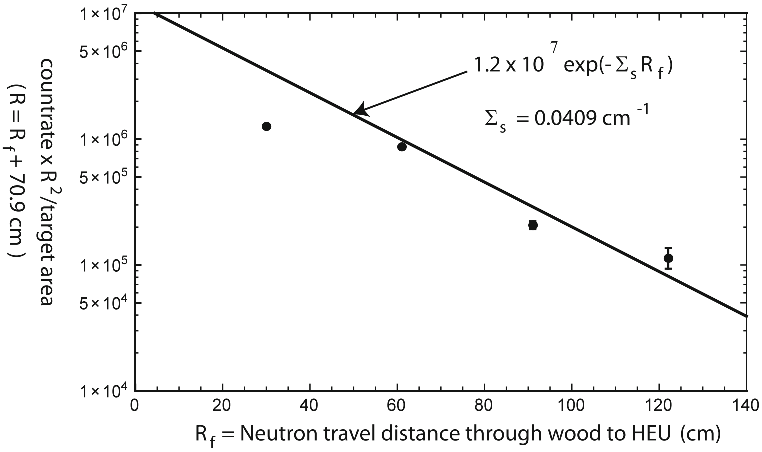

Fig. 7 Plot of $R^2 \times$ counts in a 100 s counting interval for beta-delayed photons from fission with $E_\gamma > 3$ MeV. Counts are normalized to target area. Data from [12]

with a polyethylene collimator allowing a 15° angle of neutrons into the cargo.) This graph is shown as Fig. 7. Note the resemblance of this data to the data for thermal neutron production in water from an MeV-range neutron source shown in Fig. 6.

3 Photofission

Photofission or (γ, f) reactions are threshold processes with typical energy thresholds between 5 and 7 MeV for isotopes of interest [60]. Photofission cross sections for three isotopes of interest are shown as Fig. 8. Typically, there are also (γ, n) reactions in these isotopes with similar thresholds, and there are many non-actinide (γ, n) with even lower thresholds. Reference [53] cites the deuteron photodisintegration threshold of 2.23 MeV and ^{182}W at 6.0 MeV. Other examples include ^{9}Be at 1.67 MeV, and ^{6}Li at 3.6 MeV, although the latter has a cross section in the millibarn range [13]. As a result of possible interferences by these nuclides in objects under inspection, photofission interrogation systems usually focus on the production of delayed neutrons, similar to the differential die-away technique discussed for active neutron interrogation.

In most cases the photon source for photofission active interrogation is a bremsstrahlung source with an electron accelerator producing energies between 8 and 15 MeV and a target of a high-Z material such as tungsten or rhenium [25, 38]. Because the energy spectrum of the bremsstrahlung photons peaks at a rather low energy and tapers off to zero at the electron energy, there are few photons available for photofission if the accelerator's voltage is near the photofission threshold. Reference [60] gives an example of unshielded HEU showing a response of delayed neutrons approximately ten times stronger at 11 MeV electron energy than at 8 MeV. The response ratios were different in HEU from depleted uranium (DU) and thorium, but relatively independent of the presence of shield material. Thus the technique showed some promise for an isotope-sensitive detection scheme.

Fig. 8 Photofission cross sections versus photon energy for ^{235}U, ^{238}U, and ^{239}Pu. Data from [10]

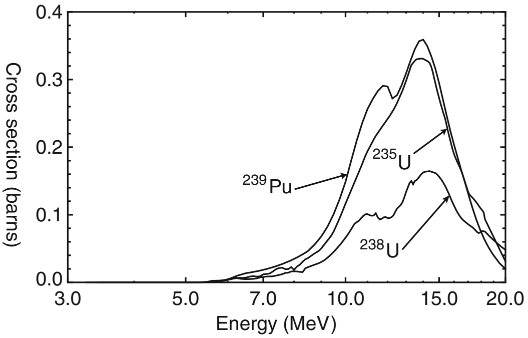

4 Nuclear Resonance Fluorescence

Nuclear resonance fluorescence (NRF) is a process by which a nucleus is energized to an excited state by the absorption of a photon, followed by de-excitation, either directly or through a cascade of other excited states before returning to the ground state. These processes have been well-studied in the past [31, 35]. The prospect of NRF as a detection tool was suggested by Bertozzi et al. [6]. Key cross section data for NRF in ^{235}U and ^{239}Pu at energies sufficiently high to allow penetration of the interrogation beam ($E > 2$ MeV) were carried out shortly after that time [5]. Prior data on the even-even actinides ^{232}Th and ^{238}U have existed for some time [22], and more recent experiments have been performed showing the transport properties in realistic configurations [36, 43]. More recently NRF cross section data for ^{240}Pu has become available [44].

4.1 NRF Physics

The nuclear excitation involved in NRF is typically one of two modes. The first is a "scissors" type of excitation, as shown in Fig. 9. Here the proton and neutron collective population can be thought of as somewhat elongated and rotating through each other, creating a type of excitation with a $J^{\pi} = 1^{+}$ mode, which would be excited from a 0^{+} ground state nucleus (such as ^{232}Th, ^{238}U, and ^{240}Pu) by an M1 photon coupling channel. The second mode is a mixture of quadrupole and quadrupole excitation, which can couple from the ground state with an E1 photon coupling scheme. The excited spin and parity states for the nuclei not in a 0^{+} ground state, including ^{235}U and ^{239}Pu, are a bit less clear, but $\Delta J = \pm 1$ or 0 would tend to be the most likely for strong observed NRF lines. At the present time there is very little information available on the spins and parities of excited states involved in resonance fluorescence.

Fig. 9 "Scissors"-type of nuclear excitation, $J^{\pi} = 1^{+}$

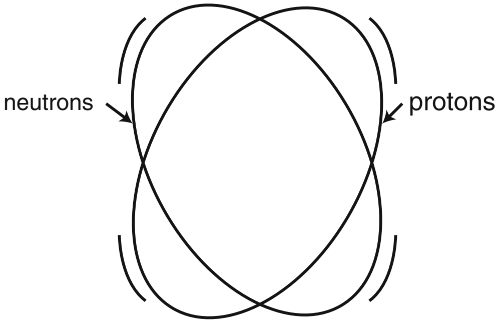

Before discussing the cross sections for NRF processes, it is necessary to look at the kinematics of photon absorption. Since a photon of energy E_γ has a momentum $p = E\gamma/c$, and that momentum is imparted to the excited nucleus, the total energy of that nucleus after the photon absorption is given by

$$E_{nuc} = E_{ex} + E_k = E_{ex} + \frac{P^2}{2M} = E_{ex} + \frac{E_\gamma^2}{2Mc^2} \tag{16}$$

This (typically small) recoil energy allows the use of non-relativistic mechanics to calculate the nucleus kinetic energy after the photon absorption. We can then apply a Breit-Wigner form for the cross section, assuming a resonance at excitation energy E_{ex}:

$$\sigma(E_\gamma) = \frac{4\pi}{k^2}\frac{2J+1}{(2J_0+1)g_\gamma}\frac{(\Gamma_f\Gamma_0/4)}{(E_\gamma^2 - E_{nuc}^2) + (\Gamma/2)^2}. \tag{17}$$

Here J and J_0 are the angular momenta of the excited and initial states of the nucleus, and g_γ is the statistical factor for the photon. The energy width of the state Γ is given by the Heisenberg relation for the lifetime of the excited state by $\Gamma = \hbar/\tau$. There may be more than one decay mode for the excited state, and Γ_0 represents the partial width for direct decay to the ground state; in general Γ is the sum of the partial widths for all decay channels. Figure 10 shows the details and nomenclature. Since $g_\gamma = 2$ for a photon, we can write this expression in terms of photon energy as [31]

$$\sigma(E_\gamma) = \frac{2\pi}{k^2}\frac{2J+1}{2J_0+1}\frac{(\Gamma_f\Gamma_0/4)}{(E_\gamma^2 - E_{nuc}^2) + (\Gamma/2)^2}. \tag{18}$$

The above equation assumes that the nucleus is at rest before the encounter with the photon. In actuality there is some finite velocity spread of the nuclei caused by thermal motion. If the nucleus is part of a gas (such as UF_6), then the velocity spectrum

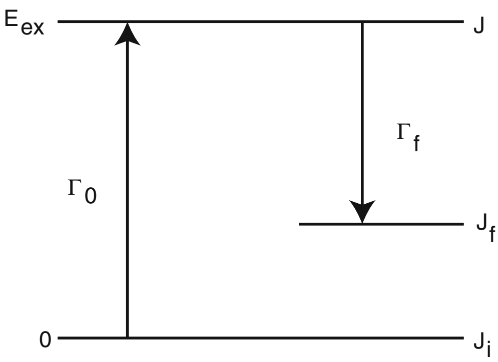

Fig. 10 Level diagram for nuclear resonance fluorescence excitation and emission. After [31]

of the nuclei is given by a Maxwell-Boltzmann distribution (in one dimension), which can be given (on a distribution normalized to one) by:

$$f(v) = \left(\frac{M}{2\pi T}\right)^{1/2} \exp\left(-\frac{Mv^2}{2T}\right) \tag{19}$$

Here T is the temperature (in units of energy). Note that $\int fd^3v = 1$. In crystalline materials the assumption of a maxwellian velocity distribution is not bad as long as the material has a temperature on the order of the Debye temperature or greater [32], which holds for U and Pu, for example [42]. We then observe that the moving nucleus sees a frequency ω' given by a Doppler shift, $\omega' = \omega - \mathbf{k} \cdot \mathbf{v}$. We then can make a normalized form factor $F(\omega)$ for the cross section by taking

$$\sigma(E) = \sigma_0 \frac{\Gamma_0 \Gamma_f \pi}{2\hbar\Gamma} F(\omega) \tag{20}$$

with

$$F(\omega) = \int_{-\infty}^{+\infty} \frac{\Gamma/(2\pi\hbar) f(v)}{(\omega - \omega_* - kv)^2 + (\Gamma/(2\hbar))^2} dv \tag{21}$$

and

$$\sigma_0 = \frac{2\pi}{k^2} \frac{2J+1}{2J_i+1}. \tag{22}$$

Note that $\int F(\omega)d\omega = 1$. We then have a solution

$$F(\omega) = \frac{1}{\sqrt{2\pi} kv_{th}} e^{\frac{\Gamma_\omega^2 - 4(\omega-\omega_*)^2}{8k^2v_{th}^2}} \Re\left(e^{-\frac{i(\omega-\omega_*)\Gamma_\omega}{2k^2v_{th}^2}} \operatorname{erfc}\left(\frac{\Gamma_\omega - 2i(\omega - \omega_*)}{2\sqrt{2}kv_{th}}\right)\right) \tag{23}$$

Here $\hbar\omega_* = E_{ex} + E_\gamma^2/(2Mc^2)$ is the photon excitation energy adjusted for the recoil energy, and $\Gamma_\omega = \Gamma/\hbar$ is the line width in units of frequency, and $v_{th} = (T/M)^{1/2}$ is the one-dimensional rms thermal velocity. (For gases, M is the molecular weight; for solid crystalline materials, M is the effective nuclear mass.)

(In the literature [20], this form factor has also been given in dimensionless form by assigning dimensionless units

$$x = \frac{E - E_{nuc}}{\Gamma/2} \quad \text{and} \quad t = \left(\frac{\Delta}{\Gamma}\right)^2 \tag{24}$$

with $\Delta = E\sqrt{2T/Mc^2}$. Then the cross section is given by $\sigma(E) = \sigma_0 \psi(x, t)$, with:

$$\psi(x,t) = \frac{1}{2\sqrt{\pi t}} \int_0^{\infty} \frac{\exp(-\left((x-y)^2/(4t)\right)}{1+y^2} dy = \frac{\sqrt{t}e^{-\frac{1}{4}t\left(x^2-1\right)} \Re\left(e^{-\frac{1}{2}itx} \mathrm{erfc}\left(\frac{1}{2}\sqrt{t}(1-ix)\right)\right)}{\sqrt{\pi}} \tag{25}$$

Tables of this function have also been published [47].)

The usual situation is that $E_{\mathrm{recoil}} \gg Mv_{\mathrm{th}}^2/2 \gg \Gamma$, so that the form factor $F(\omega)$ given above becomes

$$F(\omega) \approx \frac{1}{\sqrt{2\pi} k v_{\mathrm{th}}} e^{\frac{-(\omega-\omega_*)^2}{2k^2 v_{\mathrm{th}}^2}} \tag{26}$$

Typically, the width of the line Γ is not known, nor is the spin J_f of the excited state. What is actually known is the integral $\int \sigma dE$ of the resonant cross section. The basic cross section σ_0 is quite large:

$$\sigma_0 \approx \left(\frac{2J+1}{2J_0+1}\right)\left(\frac{2500\ \mathrm{b}}{E_{\mathrm{MeV}}^2}\right), \tag{27}$$

but typical widths Γ are on the order of milli-electron volts (meV), so that the integrated cross sections for the larger NRF lines are on the order of tens of barn-eV. The thermal Doppler broadening width ΔE can be estimated from (26) as

$$\frac{\Delta E(\mathrm{FWHM})}{E} = \sqrt{8 \ln 2} \frac{v_{\mathrm{th}}}{c} \approx 10^{-6}. \tag{28}$$

for $A \approx 240$ and $T \approx 300$ °K. Thus MeV-range NRF lines have a thermal Doppler linewidth ΔE of a few eV. The maximum Doppler-broadened cross section is given by

$$\sigma_{\max} = \frac{\int \sigma dE}{\sqrt{2\pi} E} \cdot \frac{c}{v_{\mathrm{th}}} = 2\sqrt{\frac{\ln 2}{\pi}} \frac{\int \sigma dE}{\Delta E(\mathrm{FWHM})}. \tag{29}$$

Thermal Doppler broadening has no effect on the integrated cross section:

$$\int \sigma dE = \left(\frac{2J+1}{2J_i+1}\right) \sigma_0 \frac{\Gamma_0 \Gamma_f \pi}{2\Gamma}, \tag{30}$$

and the spectral peaks with eV-range widths from the decay of NRF-excited levels appear as discrete lines on high-resolution detectors such as germanium solid-state detectors. The maximum cross section is then on the order of a few 1000 b $\cdot$ $(\Gamma/\Delta E)$ = tens of barns.

As an example, the most prominent NRF line in ^{235}U is at 1.733 MeV and has an integrated cross section $\int \sigma dE$ of 13.1 eVb [59]. At normal metallic density (19 g cm^{-3}), this gives a characteristic e-folding length of 3.5 cm for 93 % enriched material. The gamma-ray mass attenuation at this energy has an e-folding length of 1.0 cm, so that about one-quarter of all photon interactions in the material at this energy will be NRF interactions resulting in the release of a 1.733 MeV photon. Since the photon source will usually be in the form of a beam, the fluorescence photons generated at some large angle to the beam can be detected with relatively low background. (The spin statistics for photon emission from an excited state to a ground state for an even-odd nucleus such as ^{235}U, with $J^{\pi} = 7/2^{-}$, are such that there is very little angular dependence for the re-emitted photon.)

Because of the relatively large NRF cross section, another option is available for detection of nuclear material using NRF and that is to reverse the detection process and look for a “notch” in the photon spectrum from the source as it leaves the inspection object. Since the notch is only an electron-volt wide, it cannot be observed directly on a photon detector. But if a target is made of the isotope under study, it will have NRF interactions when there is no notch in the spectrum, but they will be attenuated by NRF absorption if the object under test contains the material. Reference [42] gives an example. The advantage of this scheme is that the detectors required do not have to have high resolution, since they are comparing relative count rates only. Thus the detectors can be very large scintillators, either water-filled or plastic, and thus high efficiency and low cost. This system is also ideal for a photon source with a narrow energy spectrum around the NRF line, with narrow beam angle as well, i.e. a beam-transmission test setup.

4.2 Photon Sources for NRF

4.2.1 Bremsstrahlung

The most common source for MeV-range NRF photons of relevance for most inspection scenarios are bremsstrahlung sources. These sources use an accelerated beam of electrons which then interacts with some target material. The photons produced have a spectrum with an end-point at the energy of the electron and a peak production rate dN_{γ}/dE at around 20 or 30 % of the endpoint energy. Photon production increases rapidly with increasing electron energy. Production also depends on the target thickness. This thickness is usually given in “radiation lengths”, where radiation length is defined as the distance through the target for a high energy electron ($E_{e^-} \gg m_e c^2/(\alpha Z^{1/3})$, with $\alpha = 1/137.04$ and Z the atomic number of the target material) to have its energy reduced by a factor of e. The radiation length (in units of g cm^{-2}) is given approximately by:

$$\rho X_0 \approx \frac{716.4\,A}{Z(Z+1)\log\left(287/\sqrt{Z}\right)}. \qquad (31)$$

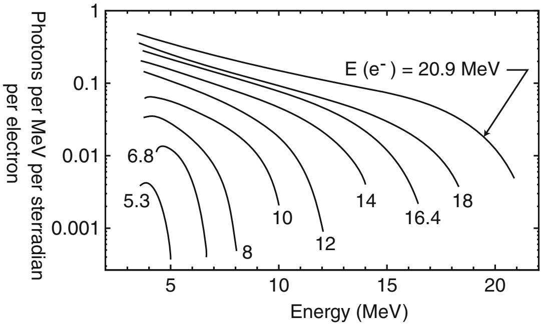

Fig. 11 Bremsstrahlung from a thick (0.2 radiation length) W-Au target. Yields measured by deuteron photodissociation. Data from [39]

(Online tables of radiation lengths for elements and compounds are available at [40].) Optimized targets for bremsstrahlung photon production typically have areal densities of around $0.2\rho X_0$. An example of production as a function of electron energy is shown in Fig. 11.

At higher beam energies, (γ, n) reactions in the target can cause interference in identifying NRF resonant lines. For this reason, sometimes targets are selected to have high neutron separation energies. An example would be aluminum, with only one stable isotope (^{27}Al) with a neutron separation energy above 13 MeV. This was the target material selected for the recent Darmstadt NRF experiment on ^{235}U [59].

Bremsstrahlung sources have peak production in the forward direction, and typically have an angular spread localized to a cone half-angle of $\approx 1/\gamma$, where $\gamma = 1 + E_k/m_e c^2$. This is somewhat helpful in shielding the beam at large angles from the beam. However, high-MeV bremsstrahlung sources are prodigious producers of photons, and careful shielding and interlock controls are necessary to avoid potentially lethal doses from these machines on a timescale of seconds.

4.2.2 Laser Compton Upshift

An interesting alternative to bremsstrahlung excitation has emerged in recent years and that involves using a short-pulse laser and a relativistic electron beam to create a narrow-band photon source by virtue of relativistic Compton scattering. The basic concept is relatively simple: a photon with a frequency ω in the lab frame is "seen" by an electron moving in the opposite direction as having a frequency given by the relativistic Doppler formula:

$$\frac{\omega'}{\omega} = \left(\frac{c + v}{c - v}\right)^{1/2} = \gamma + \sqrt{\gamma^2 - 1}. \tag{32}$$

Here γ is the relativistic factor $\left(\sqrt{1 - v^2/c^2}\right)^{-1}$. The electron can then re-radiate at the frequency ω' in its frame of reference. If it does this in the direction it is traveling in the laboratory frame, then the re-radiated photon is seen in the laboratory frame with this same Doppler factor applied again, i.e.

$$\frac{\omega_{\mathrm{X}}}{\omega_{\mathrm{L}}} = \left(\gamma + \sqrt{\gamma^2 - 1}\right)^2 \approx 4\gamma^2 (\gamma \gg 1), \tag{33}$$

where the "X" and "L" subscripts denote the produced X-ray and the initial laser frequency, respectively. If the X-ray photon is launched at a small angle θ with respect to the electron beam, this formula is modified to read

$$\frac{\omega_{\mathrm{X}}}{\omega_{\mathrm{L}}} \approx \frac{4\gamma^2}{1 + \gamma^2\theta^2} \tag{34}$$

As an example, Ref. [42] considers a system with a 236 MeV electron beam with laser scattering from a frequency-doubled Nd:YAG (yttrium aluminum garnet) laser emitting light at 0.53 μ wavelength ($\hbar\omega = 2.33$ eV). The relativistic factor $\gamma = 436$ here, so that the scattered X-ray photons have energies near 2 MeV, where NRF lines for U and Pu isotopes are known to exist.

The interaction rate is given by the product of the photon flux and the electron density and the interaction volume:

$$\dot{\mathrm{N}}_{\mathrm{X}} \approx \mathrm{n_e}\phi_\gamma \sigma_{\mathrm{T}} \mathrm{V}, \tag{35}$$

where σ_{T} is the Thomson cross section

$$\sigma_{\mathrm{T}} = \frac{8\pi}{3}\mathrm{r_e^2}, \tag{36}$$

where $\mathrm{r_e}$ is the electron classical radius $\mathrm{e^2/m_ec^2} = 2.8$ fm. Thus the Thomson cross section is about 0.665 b. This small cross section shows the need for highly focussed electron beams with minimal angular divergence, and similarly tight tolerances on the laser beam. The emergence of chirped pulse amplification (CPA) lasers has been very helpful in this regard. In the CPA scheme [9], a short-pulse seed laser is sent into a diffraction grating that acts as a pulse stretcher, which allows further amplification of the laser light without the effects of nonlinearity that would take place if the laser pulse was at very high power. Following amplification, the laser energy is sent through a second grating which re-constitutes the laser pulse into a very short (femtosecond range) pulse with very high power. A schematic is shown in Fig. 12. Some of the short-pulse laser energy can be split from the main beam and directed to a photocathode, thus producing a precisely timed burst of electrons for the electron accelerator. Reference [42] gives a prototype design with laser and electron spot sizes on the order of 6 μ m and 22 μ m respectively, with pulse widths of 1.25 ps and 3 ps, respectively. This design would produce 4.5×10^8 X-ray photons per pulse at a 1 KHz repetition rate. The rms energy spread of the X-ray photons would be about 0.5 %. While this energy spread is much greater than the NRF Doppler-broadened width, it is certainly much more narrow-band than a bremsstrahlung source.

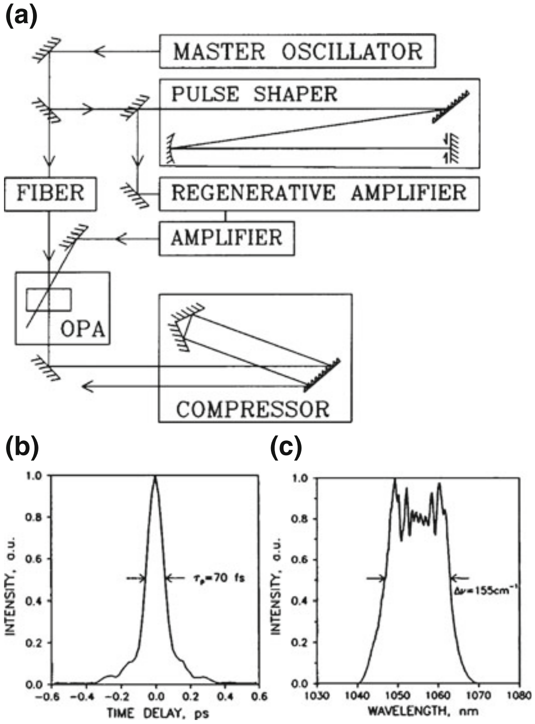

Fig. 12 **a** Schematic of the first demonstration of chirped pulse amplification. **b** Time and wavelength dependence of the output pulse. From [9]. Used with permission, Springer

An inspection tool based on a device of this type is impractical if the electron accelerator cannot be made small enough to be portable, and this is a challenge for, say, an rf-driven linac delivering electrons at hundreds of MeV at average current of 1 μA. However, there may be another alternative and that is to produce the electrons using a laser wakefield acceleration process [18, 21]. In a laser wakefield accelerator, a short pulse laser interacts with a plasma generated by an electric discharge, typically in a capillary tube [33] or a gas jet, self-ionized by the laser. The nonlinear wave coupling mechanism causes extremely high electric fields to build up, which in turn accelerate electrons at energies up to the mid-GeV range. The short-pulse laser for the wakefield acceleration process can also be utilized for the Compton upshift, resulting in MeV-range photons [49], or a separate scattering laser can be employed.

Another possibility exists for Compton upshift NRF sources that exploits the polarized nature of the produced X-ray photons. Since the original ultraviolet photons from the laser are typically linearly polarized, the polarization characteristic is retained in the upshifted X-ray photons. For NRF interaction in the even-even 0+ nuclides, this creates strong angular dependence for the NRF-scattered photons. This strong angular dependence is a unique feature, and it may be sufficient to detect the presence of the isotope under investigation, without the need for energy resolution. Thus high-volume, inexpensive detectors at different scattering angles may show the presence of the isotope, perhaps running in current-mode in real time [51].

5 Dose Considerations

Active interrogation systems for nuclear material detection carry the risk of exposure to both personnel operating the equipment and to stowaways that might be present inside the object under test. For this reason it is worth presenting some basic information about health risks from radiation exposure, and quantitative methods for assessing the risks associated with various active interrogation schemes.

5.1 *Radiation Exposure*

Neutron and gamma radiation are considered to be forms of ionizing radiation. This means that the interaction of these particles with matter causes the release of enough localized energy to create an ionized molecule in tissue. At low doses, this can cause cell-changing reactions to occur, particularly changes to cellular DNA information. While most organisms have the ability to perform a sort of error-correcting function on these DNA upsets, the capacity to repair simultaneous upsets in nearby DNA sites is more limited. Natural factors cause there to be huge numbers of DNA modifications. For example, there are approximately 55,000 single-strand DNA breaks *per cell* per day in humans [4, 55]. Double-strand breaks are much more rare but also are less likely to get a full repair. Exposure to radiation can increase the number of DNA damage events and tax the natural repair system, with the result that certain types of cancer may be more likely.

The possibility of DNA upsets at nearby molecular sites also exists with radiation. It becomes progressively more likely that no repair mechanism can reverse the damage to DNA when there are closely spaced DNA breaks. For this reason, there is an elevated risk of cancer upon exposure to radiation with a high energy deposition per unit length. The so called “LET”, or linear energy transfer, distinguishes those radiations with a high value of $\mathrm{dE/dx}$ along the ray path from those with less, and an additional factor is added to form the equivalent dose compared to the same amount of energy deposited in the low-LET case. The dividing line between low-LET and high-LET is about $\mathrm{dE/dx} = 10$ keV per micron.

The internationally recognized absorbed dose unit is the Gray (Gy) and is equivalent to 1 J/kg of tissue. The Sievert (Sv) is the internationally accepted unit for dose equivalent for all types of radiation. The equivalent dose is obtained by multiplying the actual absorbed energy per kilogram (the exposure in Grays) by the weighting factor w_R unique to the type of radiation and the energy involved:

$$\text{Dose Equivalent (Sv)} = \text{Absorbed Dose (Gy)} \cdot \mathrm{w_R} \tag{37}$$

For X-rays and gamma rays, $w_{\mathrm{R}} = 1$, as these are low-LET radiation types. For neutrons, alphas, and other heavy charged particles, $w_{\mathrm{R}} > 1$.

Other nomenclature exists for these quantities. The weighting factor w_R is sometimes called the "Quality Factor", or. ("Higher quality" here means more lethal!) Also, an older alternative set of units were used in the past and still are used in the US. These are the rad for absorbed dose and the rem for dose equivalent. A rad of absorbed dose is 100 ergs per gram and is equal to 0.01 Gy. Dose rates are frequently quoted in expressions like "mR per hour", which means "millirems per hour", with the weighting (quality) factors already calculated in. The quality factor for X-ray and gamma-ray photons is one, as is the quality factor for electrons.

An additional calculation to determine dose must be done if the dose is nonuniform, i.e. certain areas of tissue are exposed to radiation and others are not, or if self-shielding is important. A set of "tissue weighting factors" (w_T) have been developed which can be used to convert the dose to a particular part of the body. Reference [56] gives a table of these factors as accepted by the ICRP. (The U.S. Nuclear Regulatory Commission uses an older and somewhat different set of these factors.) Then the effective dose E (in Sieverts) is given by

$$\mathrm{E} = \sum_{\mathrm{T}} w_T \sum_{\mathrm{R}} w_{\mathrm{R}} \mathrm{D}_{\mathrm{T,R}} \tag{38}$$

where $\mathrm{D}_{\mathrm{T,R}}$ is the absorbed dose (Grays). Note that the sum of all the tissue weighting factors is unity.

5.1.1 Neutrons

The quality factors used in the US for neutron exposure are given in Table 2. These are also given as an equivalent flux for a 1R exposure. (Note that the dose does not go to zero at low neutron energy, because the energy release from neutron capture reactions is taken into account.)

The International Commission on Radiological Protection (ICRP) has issued its own guidelines [24], which are slightly different from the ones above and are under regulatory review for adoption in the US. The weighting factor w_R is given by a set of equations, shown in Eq. (39). A graph of this weighting function is shown as Fig. 13.

$$w_{\mathrm{R}}(\mathrm{E_n}) = \begin{cases} 2.5 + 18.2e^{-\frac{1}{6}\log^2(\mathrm{E_n})}, & \mathrm{E_n} < 1\ \mathrm{MeV} \\ 5.0 + 17.0e^{-\frac{1}{6}\log^2(2\mathrm{E_n})}, & 1\ \mathrm{MeV} \le \mathrm{E_n} < 50\ \mathrm{MeV} \\ 2.5 + 3.25e^{-\frac{1}{6}\log^2(0.04\mathrm{E_n})}, & \mathrm{E_n} > 50\ \mathrm{MeV} \end{cases} \tag{39}$$

5.1.2 Photons

The dose rate to a small tissue sample in a beam of photons at a fixed energy $\mathrm{E}\gamma$ is given by

$$\dot{\mathrm{D}} = \phi \mathrm{E}_\gamma \left(\frac{\mu_{\mathrm{en}}}{\rho} \right). \tag{40}$$

Table 2 Neutron dose quality factors and fluences per US 10CFR20 regulations

E_n (MeV)	Quality factor (Q)	Fluence per unit dose equivalent (neutrons cm^{-2} rem^{-1})
2.5×10^{-8}	2	980×10^6
1×10^{-7}	2	980×10^6
1×10^{-6}	2	810×10^6
1×10^{-5}	2	810×10^6
1×10^{-4}	2	840×10^6
1×10^{-3}	2	980×10^6
1×10^{-2}	2.5	1010×10^6
1×10^{-1}	7.5	170×10^6
5×10^{-1}	11	39×10^6
1	11	27×10^6
2.5	9	29×10^6
5	8	23×10^6
7	7	24×10^6
10	6.5	24×10^6
14	7.5	17×10^6
20	8	16×10^6
40	7	14×10^6
60	5.5	16×10^6
1×10^2	4	20×10^6
2×10^2	3.5	19×10^6
3×10^2	3.5	16×10^6
4×10^2	3.5	14×10^6

Fig. 13 Dose weighting factor versus energy for neutrons (ICRP)

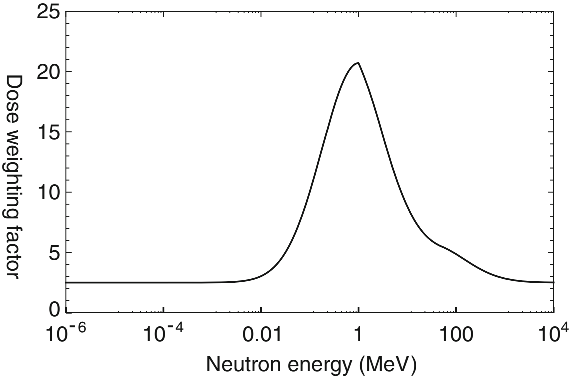

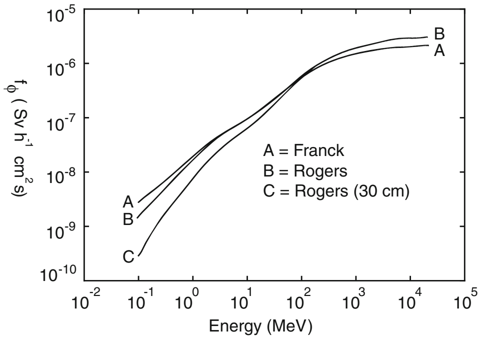

Fig. 14 Dose conversion factors, with units of Sievert per hour per photon per square centimeter per second, found in two different studies. *Curves* labeled *A* and *B* are maximum doses near the entrance point of the gamma, *curve C* is for a point 30 cm back from the entrance point. Data from Franck [17] and Rogers [46]. From [14]

Here μ_{en} is the mass energy-absorption coefficient, not to be confused with the mass attenuation factor μ. Tables of each are available at [23]. As an example, the NIST data for four-component soft tissue gives a value of $\mu_{\text{en}}/\rho = 3.073 \times 10^{-2}$ cm^2 g^{-1} at $E_\gamma = 1$ MeV. Thus a small sample would receive a dose of $1000 \times 3.073 \times 10^{-2} \times 1.6 \times 10^{-13} = 4.91 \times 10^{-12}$ joules per second per kilogram per photon per square centimeter per second (Gray per photon per square centimeter), for exposure to 1 MeV photons. A flux of one gamma per second would then give 3600 times this number, or 1.77×10^{-8} Sv h^{-1}. A thick target has some softening of the initial photon energy spectrum through collisions, but with a higher mass energy-absorption coefficient at lower energies, giving a slightly different result. Figure 14 gives results computed by two different authors with a simple phantom model for a human target.

5.2 Health Risks

The overall mortality risk from radiation at low doses ($<$0.01 Sv) has no direct epidemiological data to support it [34]. Risks are inferred from increased mortality rates at doses above 0.1 Sv and extrapolated downward, assuming a linear relationship between dose and increased mortality. A frequently used relationship is that a 1.0 Sv dose increases the risk of cancer by 5 %, or taken another way, there would be one additional death from cancer from low-level radiation exposure to a large population with an aggregated dose equivalent of 20 person-Sieverts. The data supporting this comes from Hiroshima and Nagasaki bomb survivors, people undergoing high dose medical procedures such as multiphasic abdominal and pelvic x-rays, nuclear industry workers, and large accidental exposures.

The linear, no-threshold risk model has remained a contentious point between researchers in the field and some outspoken members of the public. The points relevant to the arguments are (1) there is a large variation in radiation exposure in the general population in this range, (2) a large portion (about 25 %) of the public will get cancer not related to radiation, and (3) even very large statistical studies would not have sufficient size to show a small effect, given the nature of the statistical fluctuations expected. While some researchers insist that "no radiation dose is safe", others claim a "hormesis effect" is present, where small doses of radiation are actually beneficial.

In any case, radiation risk factors are elevated for women, children, and fetuses, and are lower for elderly people. Exposure to members of the public is limited to 1.0 mSv per year in the US by Sub-part D of the Code of Federal Regulations 10CF20 [57] and therefore forms the design maximum dose that a stowaway in a cargo container can be exposed to [30]. The International Commission on Radiological Protection (ICRP) uses this same number, and this is the standard adopted by many countries [24, 58].

In the case of an acute dose a quantity known as $\mathrm{LD}_{50/30}$ is worth noting: that is the dose that will kill 50 % of a population within 30 days. This is usually given as 4–4.5 Sv (400–450 rem).

5.2.1 Sample Radiation Exposure Calculations

Here are two sample problems for computation of dose and health risk for calculation of potential doses to stowaways in a cargo screening application.

First we consider a real system for which there are radiological measurements available. A source of 8.5 MeV neutrons was used to screen cargo by active interrogation. This system was built by Rapiscan and called the Pulsed Fast Neutron Analysis (PFNA) system [30]. The source had a measured neutron output flux of 1.0×10^7 n cm^{-2} s^{-1} at 1 m from the source in the forward direction. The system had a collimator so that the beam footprint was 12 cm high and 9 cm wide. A reference anthropomorphic phantom was provided by the National Institute of Health and placed at 2.06 m from the source as a proxy for a stowaway. The neutron beam was generated with a scanning arm that swept up and down so that the beam footprint covered the height of a container (8.5 ft or 2.6 m) at the position of the phantom. The phantom was placed on a movable table which moved at a 1 cm s^{-1} rate to simulate the actual x-y scan anticipated in the field. The phantom was fitted with neutron-sensitive film badges (containing polyethylene and CR-39 film) and exposed to the beam. The inverse square law gives a flux of $10^7/(2.06)^2 = 2.36 \times 10^6$ cm^{-2} s^{-1} at the position of the phantom. Using Table 2, we get a dose rate of 0.0982 rem s^{-1} for this source. The horizontal beam footprint (9 cm) traverses the dose measurement point in 9 s, and the vertical duty factor is 12 cm/206 cm = 0.046 because of the up-and down scanning. Thus we calculate an expected dose of $9 \cdot 0.0982 \cdot 0.46$ rem, or 40.9 mR (0.409 mSv). Actual measurement in the field gave a maximum dose per scan of 22 mR, in reasonable agreement because of overscanning and dwell in the scanning arm. This system, with appropriate interlocks, would thus meet the requirement of less than 100 mR per year, as it would not be expected that a stowaway would repeat this trip more than two or three times per year.

Next we consider the potential dose from a bremsstrahlung photon source derived from a 10 mA, 10 MeV electron beam on a tungsten target. This type of source might be imagined for NRF active interrogation. Here we use the data for thick-target bremsstrahlung from Reference [54]. We find the dose rate by integrating over the photon energy spectrum with the dose conversion factor shown in Fig. 14 (using the data from [46] for dose at the surface):

$$\dot{\mathrm{D}} = \frac{\dot{\mathrm{N}}_e}{\mathrm{R}^2} \int \mathrm{dEY(E)f}_{\phi}. \tag{41}$$

Here Y(E) is the photon yield per sterradian per electron. A 10 mA electron beam has $\dot{\mathrm{N}}_e = 6.25 \times 10^{16}$ electrons per second. If we take the distance R from the bremsstrahlung target to the potential unintentionally irradiated stowaway to be 150 cm, we find a dose of 26.5 Sv s^{-1}, or slightly less than 100,000 Sv h^{-1}. A lethal dose would take less than 1 s. This exceeds the NRC and ICRP standard by eight orders of magnitude, and also poses risks of food activation from photoneutrons.

6 Conclusions

Active interrogation schemes for interdiction of nuclear material have different requirements than systems designed for safeguards and arms control/treaty verification missions [48]. Three key parameters are the cost and size of the equipment involved, the radiation dose restrictions, and the time required for a measurement to be made. Additionally, active interrogation systems can become quite complex and technologically advanced, which may lead to reliability and availability issues. There is also a broad spectrum of operator training requirements, ranging from getting a “red light/green light” type of response from a simple radiation portal monitor to potentially having to tune femtosecond laser pulses in the field for some proposed laser Compton upshift NRF sources. Also important to consider in active interrogation systems, especially for cargo screening and interdiction, is how easily the measurement can be thwarted by judicious use of shielding. This is especially true for neutron interrogation, looking for either fission delayed neutrons or gammas, because hydrogenous material such as food, lumber, or many other substances found in commerce can easily attenuate the return signal by orders of magnitude. Systems can be designed so that they can report their own limitations, e.g. presence of hydrogen for neutron-based interrogation systems or presence of high-Z materials for NRF and delayed fission gamma-based systems.

Active interrogation for nonproliferation problems remains an active area of research worldwide. The annual budget for nuclear nonproliferation at the U.S. Department of Energy now (2015) stands at \$1.9 billion. While only a fraction of this goes for research into improved material assay techniques and the like, it is a substantial fraction. Similarly, the U.S. Department of Homeland Security, with its Domestic Nuclear Detection Office, with a research and development budget above \$200 million per year, has invested heavily in active interrogation systems. Research support in Europe and Japan for projects relating to active interrogation has also been strong.

7 Problems

1. A 10.5 MeV neutron source capable of producing 10^{12} neutrons per second (with 150 % of the isotropic flux in the forward direction) is available for use for cargo inspection.
   a. Find the dose rate, in Rem per minute, to a stowaway located at the midpoint of a cargo container if this source is located one foot underneath the container.
   b. Find the exposure time required for a lethal dose of this radiation.
   c. Assume that the container is loaded with plywood with a density of 0.6 g cm^{-3}. The thermal neutron flux at the center of the container is equal to 1.5×10^{-2} times the uncollided 10.5-MeV flux which would be in that position if the container were empty. Find the fission rate in a 100 g quantity of plutonium, 93 % ^{239}Pu. Assume that the Pu component is optically thin to thermal neutrons, and that $\sigma_f = 750b$ for ^{239}Pu.
2. Find the dose rate (in Rem per minute) for an (a) seated (average height 0.5 m) and (b) horizontal stowaway (on the container floor) immediately above a 10 MeV bremsstrahlung source with a Pb target and 5 mA beam energy. The target is 1 m below the container.

References

1. Accatino DSM, Bernstein A, Dougan JCA, Hall J, Loshak A, Manatt D, Meyer A, Pohl B, Prussin S, Walling R, Weirup D (2003) Detection of special nuclear material in cargo containers using neutron interrogation. UCRL-ID-155315. https://e-reports-ext.llnl.gov/pdf/244044.pdf
2. Argonne National Laboratory (1963) Reactor Physics Constants. Atomic Energy Commission. doi:10.2172/4620873. http://www.osti.gov/scitech/servlets/purl/4620873
3. Beckurts K, Wirtz K (1964) Slowing-down parameters. In: Neutron Physics. Springer, Berlin, pp 342–360. doi:10.1007/978-3-642-87614-1_16
4. Bernstein C, Prasad AR, Nfonsam V, Bernstein H (2013-05-22). doi:10.5772/53919. http://www.intechopen.com/books/export/citation/BibTex/new-research-directions-in-dna-repair/dna-damage-dna-repair-and-cancer
5. Bertozzi W, Caggiano JA, Hensley WK, Johnson MS, Korbly SE, Ledoux RJ, McNabb DP, Norman EB, Park WH, Warren GA (2008) Nuclear resonance fluorescence excitations near 2 Mev in ^{235} U and ^{239} Pu. Phys Rev C **78**, 041,601. doi:10.1103/PhysRevC.78.041601
6. Bertozzi W, Ledoux RJ (2005) Nuclear resonance fluorescence imaging in non-intrusive cargo inspection. Nucl Instrum Methods Phys Res Sect B: Beam Interact Mater Atoms 241(14),

820–825. doi:10.1016/j.nimb.2005.07.202. http://www.sciencedirect.com/science/article/pii/S0168583X05013303 (Proceedings of the Eighteenth International Conference on the Application of Accelerators in Research and Industry (CAARI 2004))

7. Blanc P, Tobin S, Croft S, Swinhoe M, Menlove H, Lee T (2010) Optimization of combined delayed neutron and differential die-away prompt neutron signal detection for characterization of spent nuclear fuel assemblies. Unclassified Report LA-UR-10-08013. http://permalink.lanl.gov/object/tr?what=info:lanl-repo/lareport/LA-UR-10-08013
8. Blanc P, Tobin SJ, Lee T, Hu J, Hendricks J, Croft S (2010) Delayed neutron detection with an integrated differential die-away and a delayed neutron instrument. Unclassified Report LA-UR-10-04125. http://permalink.lanl.gov/object/tr?what=info:lanl-repo/lareport/LA-UR-10-04125
9. Butkus R, Danielius R, Dubietis A, Piskarskas A, Stabinis A (2004) Progress in chirped pulse optical parametric amplifiers. Appl Phys B 79(6):693–700. doi:10.1007/s00340-004-1614-3
10. Chadwick M, Obložinský P, Herman M et al (2006) ENDF/B-VII.0: next generation evaluated nuclear data library for nuclear science and technology. Nucl Data Sheets 107(12):2931–3118. doi:10.1016/j.nds.2006.11.001. http://www.sciencedirect.com/science/journal/00903752
11. Chichester DL, Seabury EH (2008) Active interrogation using electronic neutron generators for nuclear safeguards applications. Preprint INL/CON-08-14196. http://www5vip.inl.gov/technicalpublications/documents/4096530.pdf
12. Church J, Slaughter D, Asztalos S, Biltoft P, Descalle MA, Hall J, Luu T, Manatt D, Mauger J, Norman E, Petersen D, Prussin S (2007) Signals and interferences in the nuclear car wash. Nucl Inst Methods Phys Res B 261(1–2), 351–355 (2007). doi:10.1016/j.nimb.2007.04.264
13. Dietrich SS, Berman BL (1988) Atlas of photoneutron cross sections obtained with monoenergetic photons. Atomic Data Nucl Data Tables 38(2):199–338. doi:10.1016/0092-640X(88)90033-2. http://www.sciencedirect.com/science/article/pii/0092640X88900332
14. Dooling JC Dose calculations using MAERS. Argonne National Laboratory Technical Report (Bremsstrahlung beamstops and collimators in APS beam line stations)
15. Engle LB, Fisher PC (1962) Energy and time dependence for delayed gammas from fission. Unclassified Report LAMS-2642. https://www.fas.org/sgp/othergov/doe/lanl/lib-www/la-pubs/00209999.pdf
16. Eriksson S, Mackey E, Lindstrom R, Lamaze G, Grogan K, Brady D (2013) Delayed-neutron activation analysis at NIST. J Radioanal Nucl Chem 298(3):1819–1822. doi:10.1007/s10967-013-2568-x
17. Franck JC (1988) Bremsstrahlung du faisceau stocke sur les molecules residuelles de la chambre avide de suder ACO. LURE EP 8801
18. Geddes CG, Rykovanov S, Matlis NH, Steinke S, Vay JL, Esarey EH, Ludewigt B, Nakamura K, Quiter BJ, Schroeder CB, Toth C, Leemans WP (2015) Compact quasi-monoenergetic photon sources from laser-plasma accelerators for nuclear detection and characterization. Nucl Instrum Methods Phys Res Sect B: Beam Interact Mater Atoms 350:116–121. doi:10.1016/j.nimb.2015.01.013. http://www.sciencedirect.com/science/article/pii/S0168583X15000269
19. Hall J, Asztalos S, Biltoft P, Church J, Descalle MA, Luu T, Manatt D, Mauger G, Norman E, Petersen D, Pruet J, Prussin S, Slaughter D (2007) The nuclear car wash: Neutron interrogation of cargo containers to detect hidden SNM. Nucl Instrum Methods Phys Res Sect B: Beam Interact Mater Atoms 261(12), 337–340. doi:10.1016/j.nimb.2007.04.263. http://www.sciencedirect.com/science/article/pii/S0168583X07007355 (Proceedings of the Nineteenth International Conference on the Application of Accelerators in Research and Industry)
20. Hamilton W (1975) The electromagnetic interaction in nuclear spectroscopy. North-Holland. https://books.google.com/books?id=CU6BAAAAIAAJ
21. Hartemann FV, Gibson DJ, Brown WJ, Rousse A, Phuoc KT, Mallka V, Faure J, Pukhov A (2007) Compton scattering x-ray sources driven by laser wakefield acceleration. Phys Rev ST Accel Beams 10, 011,301. doi:10.1103/PhysRevSTAB.10.011301
22. Heil R, Pitz H, Berg U, Kneissl U, Hummel K, Kilgus G, Bohle D, Richter A, Wesselborg C, Brentano PV (1988) Observation of orbital magnetic dipole strength in the actinide nuclei ^{232}Th and ^{238}U. Nucl Phys A 476(1):39–47. doi:10.1016/0375-9474(88)90371-5. http://www.sciencedirect.com/science/article/pii/0375947488903715

23. Hubbell JH, Seltzer SM (1996) Tables of X-ray mass attenuation coefficients and mass energy-absorption coefficients from 1 kev to 20 Mev for elements z = 1 to 92 and 48 additional substances of dosimetric interest. NIST Publication 5632. http://www.nist.gov/pml/data/xraycoef/
24. International Committee on Radiological Protection (2007) The 2007 recommendations of the International Commission on Radiological Protection. ICRP Publication 103. Ann ICRP 37:2–4
25. Jones JL, Blackburn BW, Norman DR, Watson SM, Haskell KJ, Johnson JT, Hunt AW, Harmon F, Moss C (2007) Status of the prototype pulsed photonuclear assessment (ppa) inspection system. Nucl Instrum Methods Phys Res Sect A: Accel Spectrom Detect Assoc Equip 579(1), 353–356 (2007). doi:10.1016/j.nima.2007.04.075. http://www.sciencedirect.com/science/article/pii/S0168900207006468 (Proceedings of the 11th Symposium on Radiation Measurements and Applications)
26. Jordan KA, Gozani T (2007) Detection of 235U in hydrogenous cargo with differential die-away analysis and optimized neutron detectors. Nucl Instrum Methods Phys Res Sect A: Accel Spectrom Detect Assoc Equip 579(1), 388–390. doi:10.1016/j.nima.2007.04.083. http://www.sciencedirect.com/science/article/pii/S0168900207006584 (Proceedings of the 11th Symposium on Radiation Measurements and Applications)
27. Jordan KA, Gozani T (2007) Pulsed neutron differential die away analysis for detection of nuclear materials. Nucl Instrum Methods Phys Res Sect B: Beam Interact Mater Atoms 261(12), 365–368. doi:10.1016/j.nimb.2007.04.294. http://www.sciencedirect.com/science/article/pii/S0168583X0700924X (Proceedings of the Nineteenth International Conference on The Application of Accelerators in Research and Industry)
28. Jordan KA, Vujic J, Gozani T (207) Remote thermal neutron die-away measurements to improve differential die-away analysis. Nucl Instrum Methods Phys Res Sect A: Accel Spectrom Detect Assoc Equip 579(1), 407–409. doi:10.1016/j.nima.2007.04.089. http://www.sciencedirect.com/science/article/pii/S0168900207006638 (Proceedings of the 11th Symposium on Radiation Measurements and Applications)
29. Keepin GR, Wimett TF, Zeigler RK (1957) Delayed neutrons from fissionable isotopes of uranium, plutonium, and thorium. Phys Rev 107:1044–1049. doi:10.1103/PhysRev.107.1044
30. Khan SM, Nicholas PE, Terpilak MS (2004) Radiation dose equivalent to stowaways in vehicles. Health Phys 483–492
31. Kneissl U, Pitz H, Zilges A (1996) Investigation of nuclear structure by resonance fluorescence scattering. Progr Particle Nucl Phys 37:349–433. doi:10.1016/0146-6410(96)00055-5. http://www.sciencedirect.com/science/article/pii/0146641096000555
32. Lamb WE (1939) Capture of neutrons by atoms in a crystal. Phys Rev 55:190–197. doi:10.1103/PhysRev.55.190
33. Leemans WP, Gonsalves AJ, Mao HS, Nakamura K, Benedetti C, Schroeder CB, Tóth C, Daniels J, Mittelberger DE, Bulanov SS, Vay JL, Geddes CGR, Esarey E (2014) Multi-gev electron beams from capillary-discharge-guided subpetawatt laser pulses in the self-trapping regime. Phys Rev Lett 113, 245,002. doi:10.1103/PhysRevLett.113.245002
34. Lin EC (2010) Radiation risk from medical imaging. Mayo Clinic Proc 85(12), 1142–1146. doi:10.4065/mcp.2010.0260. http://www.ncbi.nlm.nih.gov/pmc/articles/PMC2996147/
35. Metzger FR (1959) Resonance fluorescence in nuclei. Prog Nucl Phys 7:54–88
36. Negm H, Ohgaki H, Daito I, Hayakawa T, Zen H, Kii T, Masuda K, Hori T, Hajima R, Shizuma T, Kikuzawa N (2015) Reaction-yield dependence of the (γ, γ') reaction of 238u on the target thickness. J Nucl Sci Technol 52(6):811–820. doi:10.1080/00223131.2014.980348
37. Nelson RO, Chadwick MB, Michaudon A, Young PG (2001) High-resolution measurements and calculations of photon-production cross sections for ^{16}O(n,xγ) reactions induced by neutrons with energies between 4 and 200 MeV. Nucl Sci Eng 138, 105. http://www.ans.org/pubs/journals/nse/vv-138
38. Norman DR, Jones JL, Blackburn BW, Haskell KJ, Johnson JT, Watson SM, Hunt AW, Spaulding R, Harmon F (2007) Time-dependent delayed signatures from energetic photon interrogations. Nucl Instrum Methods Phys Res Sect B: Beam Interact Mater Atoms 261(12), 316–320. doi:10.1016/j.nimb.2007.04.288. http://www.sciencedirect.com/science/article/pii/S0168583X0700897X (Proceedings of the Nineteenth International Conference on The Application of Accelerators in Research and Industry)

39. O'Dell A Jr, Sandifer C, Knowlen R, George W (1968) Measurement of absolute thick-target bremsstrahlung spectra. Nucl Instrum Methods 61(3):340–346. doi:10.1016/0029-554X(68)90248-6. http://www.sciencedirect.com/science/article/pii/0029554X68902486
40. Particle Data Group (2014) Atomic and nuclear properties of materials for more than 300 materials. http://pdg.lbl.gov/2014/AtomicNuclearProperties/
41. Pruet J, Descalle MA, Hall J, Pohl B, Prussin SG (2005) Neutron and photon transport in seagoing cargo containers. J Appl Phys 97(9):094908. doi:10.1063/1.1887835. http://scitation.aip.org/content/aip/journal/jap/97/9/10.1063/1.1887835
42. Pruet J, McNabb DP, Hagmann CA, Hartemann FV, Barty CPJ (2006) Detecting clandestine material with nuclear resonance fluorescence. J Appl Phys 99(12):123102. doi:10.1063/1.2202005. http://scitation.aip.org/content/aip/journal/jap/99/12/10.1063/1.2202005
43. Quiter B, Ludewigt B, Mozin V, Wilson C, Korbly S (2011) Transmission nuclear resonance fluorescence measurements of ^{238}U in thick targets. Nucl Instrum Methods Phys Res Sect B: Beam Interact Mater Atoms 269(10):1130–1139. doi:10.1016/j.nimb.2011.02.081. http://www.sciencedirect.com/science/article/pii/S0168583X11002643
44. Quiter BJ, Laplace T, Ludewigt BA, Ambers SD, Goldblum BL, Korbly S, Hicks C, Wilson C (2012) Nuclear resonance fluorescence in ^{240}Pu. Phys Rev C 86, 034,307. doi:10.1103/PhysRevC.86.034307
45. Ragheb M (2013) Subcritical assemblies theory. NPRE 402 class notes. http://mragheb.com/NPRE%20402%20ME%20405%20Nuclear%20Power%20Engineering/Subcritical%20Assemblies%20Theory.pdf
46. Rogers DWO (1984) Fluence to dose equivalent conversion factors calculated with EGS3 for electrons from 100 keV to 20 GeV and photons from 11 keV to 20 GeV. Health Phys 46(4):891–914
47. Rose M, Laboratory BN, Commission UAE (1953) A Table of the Integral [psi] (x, T). BNL (Series). Brookhaven National Laboratory. https://books.google.com/books?id=a0Y7iPdy-RwC
48. Runkle RC, Chichester DL, Thompson SJ (2012) Rattling nucleons: new developments in active interrogation of special nuclear material. Nucl Instrum Methods Phys Res Sect A: Accel Spectrom Detect Assoc Equip 663(1):75–95. doi:10.1016/j.nima.2011.09.052. http://www.sciencedirect.com/science/article/pii/S016890021101847X
49. Rykovanov SG, Geddes CGR, Vay JL, Schroeder CB, Esarey E, Leemans WP (2014) Quasi-monoenergetic femtosecond photon sources from thomson scattering using laser plasma accelerators and plasma channels. J Phys B: Atom Mol Opt Phys 47(23), 234,013. http://stacks.iop.org/0953-4075/47/i=23/a=234013
50. Schear MA, Menlove HO, Evans LG, Tobin SJ, Croft S (2011) Spent fuel characterization using the differential die-away self-interrogation technique. Unclassified Report LA-UR-11-03423. http://permalink.lanl.gov/object/tr?what=info:lanl-repo/lareport/LA-UR-11-03423
51. Semenov VA (2014) Isotope-specific detection and assay: engineering solution with directional nuclear resonance fluorescence. PhD thesis, University of California, Berkeley
52. Shaw TJ, Strellis DA, Stevenson J, Keeley D, Gozani T (2009) Fissile material detection by differential die away analysis. In: McDaniel FD, Doyle BL (eds) American Institute of Physics Conference Series, vol 1099, pp 633–637. doi:10.1063/1.3120116
53. Sher R, Halpern J, Stephens WE (1951) Thresholds of photo-neutron reactions. Phys Rev 81:154–155. doi:10.1103/PhysRev.81.154.2
54. Tanaka S, Tanaka R, Nakai Y, Ozawa K Data on thick target bremsstrahlung produced by electrons. JAERI-M 83-019. http://www.iaea.org/inis/collection/NCLCollectionStore/_Public/14/804/14804537.pdf
55. Tice R, Setlow R (1985) Dna repair and replication in aging organisms and cells. Handbook of the Biology of Aging, pp 173–224. Van Nostrand Reinhold (1985)
56. United Nations Scientific Committee on the Effects of Atomic Radiation (2010) Sources and effects of ionizing radiation UNSCEAR 2008. Report to the General Assembly 1, 40. http://www.unscear.org/docs/reports/2008/09-86753_Report_2008_Annex_A.pdf

57. United States Government (2002) 10 FCR20 Subpart D—Radiation Dose Limits for Individual Members of the Public. http://www.nrc.gov/reading-rm/doc-collections/cfr/part020/part020-1301.html
58. Wrixon AD (2008) New icrp recommendations. J Radiol Protect 28(2), 161. http://stacks.iop.org/0952-4746/28/i=2/a=R02
59. Yevetska O, Enders J, Fritzsche M, von Neumann-Cosel P, Oberstedt S, Richter A, Romig C, Savran D, Sonnabend K (2010) Dipole strength in the $^{235}\mathrm{U}(\gamma, \gamma')$ reaction up to 2.8 mev. Phys Rev C 81, 044,309. doi:10.1103/PhysRevC.81.044309
60. Yoon JLJWY, Harker YD, Hoggan JM, Haskell KJ, VanAusdeln LA (2000) Proof-of-concept assessment of a photofission-based interrogation system for the detection of shielded nuclear material. Unclassified Report INEEL/EXT-2000-01523

Advanced Detection Technologies

Abstract Alternative technologies for gamma-ray photon and neutron detectors are presented. First, new scintillator materials are discussed, with some of the underlying physics of the scintillation process in inorganic scintillators. The performance of some new materials such as strontium iodide and some lanthanum compounds are discussed, along with growth techniques for these materials. Both single cystal growth and methods for the manufacture of transparent ceramics are covered. Next, the development of room temperature solid-state detector materials is explored, with some general properties to guide the search for new ternary and quaternary compounds. Next, alternatives to ^{3}He for neutron detection are discussed, including stilbene and new lithium compounds such as elpasolites. Finally, imaging techniques are explored. These include coded aperture arrays and Compton imaging detectors. The algorithms associated with coded aperture de-convolution are also discussed.

1 Introduction

The workhorse nuclear detectors are high purity germanium (HPGe) for laboratory high-resolution gamma spectroscopy, thallium-activated sodium iodide (NaI:Tl) for more portable/less expensive gamma detection with lower resolution requirements, and ^{3}He gas proportional counters for thermal neutrons. However, each of these has some drawbacks. High purity germanium detectors require liquid nitrogen or active cooling to liquid nitrogen temperature. HPGe detectors are expensive, which limits their deployment on a global scale for portal monitoring applications. They also have difficulty with harsh environments, and have low damage thresholds for exposure to fast neutrons. Sodium iodide detectors have poor linearity below 100 keV photon energies, have appreciable temperature sensitivity, and are hygroscopic and tend to yellow with age. ^{3}He detectors have been less frequently deployed since ^{3}He has become scarce, although this scarcity has been fairly well managed since 2014. So replacements for these common detectors have been an active area of research in recent years.

There have also been additional goals for the use of radiation detectors in nonproliferation applications. Instead of simply taking a spectrum with a given detector

E.C. Morse, *Analytical Methods for Nonproliferation*, Advanced Sciences and Technologies for Security Applications, DOI 10.1007/978-3-319-29731-6_9

in a radiation field, systems that can image the source have become very desirable. Also, demand for accurate hand-held devices that can detect and discriminate neutrons and gammas has increased, because first responders are frequently asked to be able to test for radiation in their investigations. The large number of devices of this type to be deployed dictates that they be manufactured cheaply, which means that alternative processing to the usual crystal growth methods are being explored. It is often anticipated that such devices will be networked, and processing algorithms are being developed for making sense of the networked signals and information.

This chapter explores recent research in each of the areas outlined above. Emphasis has been placed on the science issues in each of these areas, and what is under development, rather than what has come to market.

2 Advanced Scintillator Materials

The most desirable property of any scintillator detector is high energy resolution [15]. Since energy resolution $\propto 1/\sqrt{N_{h\nu}}$ as shown in Chap. "Detection Statistics", this means that the number of visible photons per keV of gamma energy is a primary criterion for a good scintillator. Linearity of the light output with gamma energy is also important (although there can be electronic compensation algorithms applied if necessary). The decay time of the light pulse should also be as short as possible. If neutrons are also present, it is very useful if the gamma and neutron induced optical decay characteristics are different enough that they can be discriminated. The spectrum of the emitted light is also important, as the photocathode efficiency of photomultiplier tubes is wavelength-dependent. Also, to provide a strong photoelectric absorption in the material, at least one of the atomic constituents should have an atomic number Z of 50 or higher. Finally, higher mass density translates to higher atomic number density, comparing similar atomic numbers, and this means greater gamma photon absorption probability.

It is useful at this point to describe the scintillation process in inorganic scintillators. Figure 1 shows the general process of scintillation in an inorganic scintillator with an activator at intermediate-to-late times since the first interaction with an energetic photon [25]. At very early times ($< 10^{-16}$ s), core electrons are scattered, and

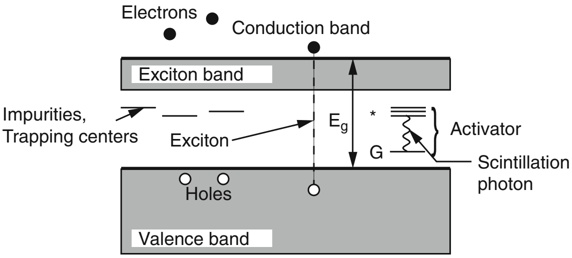

Fig. 1 Schematic of the scintillation mechanism in rare-earth-doped inorganic scintillators

these electrons quickly couple their excess energy to valence band electrons, creating electron-hole pairs. The valence band electrons are excluded from a forbidden energy range above the valence band and below the conduction band. Free electrons can migrate through the material at energies in the conduction band. In a pure crystal, recombination would happen relatively slowly, and photons generated in recombination events would have energies larger than the band gap energy (typically $4 \rightarrow 20\,\mathrm{eV}$), and most of the light would be re-absorbed. However if a small amount of dopant material is added such as cerium or europium, additional excited states can be made at these atomic sites which are inside the forbidden zone. The process usually starts by the activator atom absorbing a valence-band hole, which can be thought of as a positive charge which ionizes the activator atom. Then an electron in the conduction band falls into the activator atom's energy bands, typically in an excited state. In the case of cerium, these represent 4f and 5d orbital states in spectroscopic notation. These excitations can happen with electrons with energy less than that required to have an electron-electron collision, and these excited activator states typically de-excite to the ground state in the activator atom in about 10^{-8} s. The light produced by these de-excitations is typically in the visible range and the crystal is fairly transparent for these photons, since they are below band gap energy.

There is also the possibility of an electron-hole pair traveling together as a bound state known as an exciton. These excitons can also encounter a non-ionized activator atom and immediately excite the activator atom in a one-step process. There are other possibilities for the fate of excitons, however: they can become self-trapped by distorting the local crystalline lattice, which can lead to defect generation in the material. Also, other impurities in the material may represent traps for electrons and holes. Defects also represent potential traps. Finally, if there are interactions between the various excitation modes, than the multi-step processes can cause nonproportionality in the crystal's light output.

Generally the light output of a scintillator is a function of the band gap $\mathrm{E_g}$ in the material. Reference [15] suggests a relation:

$$\mathrm{N}_\gamma = \frac{\mathrm{E}_\gamma}{\beta \mathrm{E_g}} \qquad (1)$$

Here the coefficient β usually takes on a value of around2.5 for the better scintillators. Recent materials with sufficient light output to obtain better than 4 % resolution at 662 keV include $\mathrm{SrI_2{:}Eu}$, $\mathrm{LaBr_3{:}Ce}$, $\mathrm{LaCl_3{:}Ce}$, and GYGAG(Ce)($\mathrm{Gd_{1.5}Y_{1.5}Ga_{2.2}Al_{1.8}O_{12}{:}Ce}$) [12]. The current record-holder for the highest resolution is $\mathrm{SrI_2{:}Eu}$ at 2.6 % [14].

$\mathrm{SrI_2}$ must be grown using traditional crystal growth methods (vertical Bridgman method, [16], see Fig. 2) and suffers from a very long optical fall time of around 9 μs [22]. It is hygroscopic and also air-sensitive. It is also brittle, and it is difficult to grow large crystals. It may also suffer from nonuniformity, causing output to be sensitive to the source position. GYGAG, on the other hand, has been fabricated by a very different process [13, 32] . First, nanoparticles are generated by mixing the inorganic metal salts in an organic solvent, which is sent through a nozzle, forming

Fig. 2 Schematic of the vertical Bridgman method for crystal growth. From [16]. Used with permission, Springer

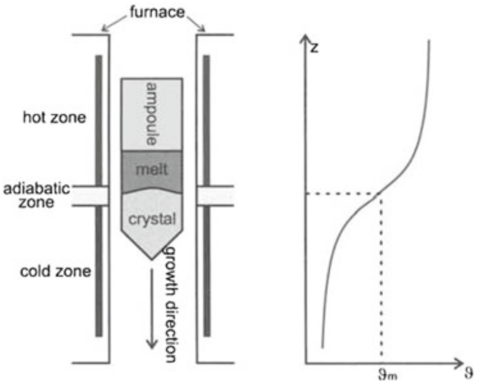

small droplets, and ignited. The particles collected have a size of around 10 nm. The particles are then pressed to make a "green body" and then progressively heat treated in air to 1200 °C which calcines and forms a crystalline structure in the material. These are then sintered in a vacuum furnace, which compresses the material and removes the oxygen. Finally, the material is hot isostatically pressed (HIP-ed) to get to the final density, forming a transparent ceramic. The material is mechanically tough, durable, and machinable. Also, the process lends itself to batch production. Many samples can be processed at once in a HIP machine, some of which have capacities up to 66 inches diameter. Although the energy resolution is not as good as SrI_2 (GYGAG has an energy resolution of $\approx 4\,\%$ at 662 keV), its potential for low manufacturing cost, combined with its durability, make it a desirable detector material for handheld devices.

Lanthanum-based scintillators (See Fig. 3 for a typical handheld device format.) ($LaBr_3$:Ce and $LaCl_3$:Ce) have been characterized extensively [26, 38]. Although these materials show excellent light output, they have the potential drawback that lanthanum has some radioactivity [21, 23]. ^{138}La, with an abundance of 0.09 % in natural La, has a half-life of 1.02×10^{11} y and has two decay branches: an electron capture to ^{138}Ba with a 65.6 % branching ratio, and a β^- decay to ^{138}Ce with a 34 % branching ratio. The Ba branch produces a 1436 keV gamma, and the Ce branch produces a 789 keV branch. These decay activities give $LaBr_3$ a specific activity of 1.62 Bq cm^{-3} and $LaCl_3$ a specific activity of 1.8 Bq cm^{-3}. These activities may ultimately limit the size of practical lanthanum-based detectors. However, in intermediate size ranges these activities may not interfere significantly in applications other than ultra-low counting, and in fact may lead to the possibility of self-calibration [21, 23, 26, 38] using this internal radioactivity. The use of the 1436 line, however, is complicated by the release of two characteristic x-rays around 31–32 keV simultaneously with the 1436 gamma, and these sum to be very close to the 1461 keV gamma of ^{40}K, always present in backgrounds. The 789 keV line is less prominent and can be muddled by the β^- continuum [23].

Fig. 3 Prototype handheld spectrometer based on LiYCl detector. Department of Homeland Security

3 Advanced Semiconductor Detectors

A comprehensive overview of the search for alternative semiconductor detectors is given in Ref. [29]. While cryogenic high purity germanium remains the definitive high-resolution gamma detector, other materials have been studied in hopes of developing a semiconductor detector that works well at room temperature. An ideal semiconductor detector would have at least one component with an atomic charge Z greater than 40 to maximize stopping power. The material should have a low dielectric constant to reduce system noise. Room temperature operation requires that the band-gap E_g be above 1.4 eV to avoid excessive leakage current, which also induces noise. High resolution requires the maximum generation of charge carriers (electron-hole pairs), which sets an upper limit on the band gap at around 2.2 eV.

The probability that either an electron or hole generated by a radiation-induced electron-hole pair created at some point x_0 in a detector modeled as an infinite slab are collected at electrodes located at $x = 0$ and $x = L$, the so-called charge collection efficiency, is given by the Hecht equation [19]:

$$\mathrm{CCE} = \frac{\lambda_e}{L}\left[1 - \exp\left(-\frac{(L - x_0)}{\lambda_e}\right)\right] + \frac{\lambda_h}{L}\left[1 - \exp\left(-\frac{(L - x_0)}{\lambda_h}\right)\right]. \quad (2)$$

Here λ_e and λ_h are the drift lengths for the electrons and holes, respectively, and these in turn are given as $\lambda_e = \mu_e \tau_e E$ and $\lambda_h = \mu_h \tau_h E$, where μ is the carrier mobility for each species (defined so that the velocities of the charge carriers are given by $v_{e,h} = \mu_{e,h} E$, where E is the electric field) and $\tau_{e,h}$ is the recombination lifetime for each charge carrier. Charge carrier lifetime-mobility products should be better than 10^{-2} cm^{2}V^{-1} for electrons and 10^{-3} cm^{2}V^{-1} for holes. (For comparison, these numbers are both greater than 1.0 in cryogenic Ge.) The requirement of a long charge carrier lifetime requires that a very low ($\ll$1 part per billion) concentration of trapping centers must be present in the material.

Since incomplete charge collection is usually the dominant source of statistical noise in a semiconductor detector, the mobility-lifetime product $\mu\tau$ for each species is the single most important parameter describing the performance of the material as a radiation detector. The search for better semiconductor detectors other than the elemental detectors (Ge, Si, and diamond) started with the study of binary compounds made with either one element from column III of the periodic table with one from column V, and binary II-VI compounds. (There are also IV-IV compounds as well, such as SiGe and SiC.) Reference [29] gives a list of these: the binary compounds with $1.4V < E_g < 2.2V$ include GaAs, InP, CdTe, AlSb, CdSe, BP, InN, AlAs, and HgS. Of these, CdTe has the highest $\mu\tau$ products of 3×10^{-3} and 2×10^{-4} cm^2 V^{-1} for electrons and holes, respectively–still a bit low compared to the desirable values given above.

The lackluster performance of the binary compounds has led to a look at ternary and quaternary compounds. As one might imagine, this creates a rather large parameter space. The list of candidate compounds can be pared down a bit by adding some useful rules. One rule is that the sizes of the individual atoms should be similar, and that the elemental lattice structure should be the same type, e.g. cubic or zincblende. Another rule is that the lattice constant should not change more than 15 % when one element is substituted for another. This is important so that the material has as few defects as possible, which can form trapping sites for the electrons and holes.

An example of a candidate ternary compound is $Cd_{1-x}Zn_xTe$, commonly referred to as CZT [31]. This material has a band gap which can be "engineered" by adjusting the stoichiometric coefficient x [28]:

$$E_g = 1.510 + 0.606x + 0.139x^2 \text{ eV}. \quad (3)$$

Raising the stoichiometric coefficient x increases the band gap, which decreases the number of electron-hole pairs generated by a gamma-ray photon, but also lowers the noise due to leakage current. The optimized value depends on the temperature of the detector: at −30 °C, x = 0.10 gives the highest resolution, while x = 0.7 optimizes the detector at room temperature [35]. Figure 4 shows a comparison of CZT with other detector materials.

Similarly, an effort has been carried out at Berkeley to develop a semiconductor from $Ga_2(Se_{1-x}Te_x)_3$ [1]. The motivation for studying this particular material stems from noting that the band gap in Ga_2Se_3 is between 2.0 and 2.6 eV (too high) and 1.0–1.2 eV for Ga_2Te_3 (too low). By adjusting the stoichiometric coefficient x, it is possible to create a material with the optimum band gap value of around 1.75 eV with x = 0.1. It appears difficult to get closer to a band gap of 1.4 eV as there seems to be a miscibility gap between $0.1 < x < 0.5$, and the Bridgman method tended to produce materials with cracks in this region [20].

It is interesting to note some of the techniques used to identify material properties for these semiconductor materials efforts. One of the most commonly used techniques for determining crystal structure is x-ray diffraction. This technique exploits the interference effect caused by the crystalline lattice constant d with the wavelength of an x-ray photon λ, given by the Bragg equation:

$$n\lambda = 2d \sin\theta, \tag{4}$$

where θ is the angle of the scattered radiation relative to the beam. Figure 5 shows the details of a setup used to measure the lattice parameters of a CZT crystal at

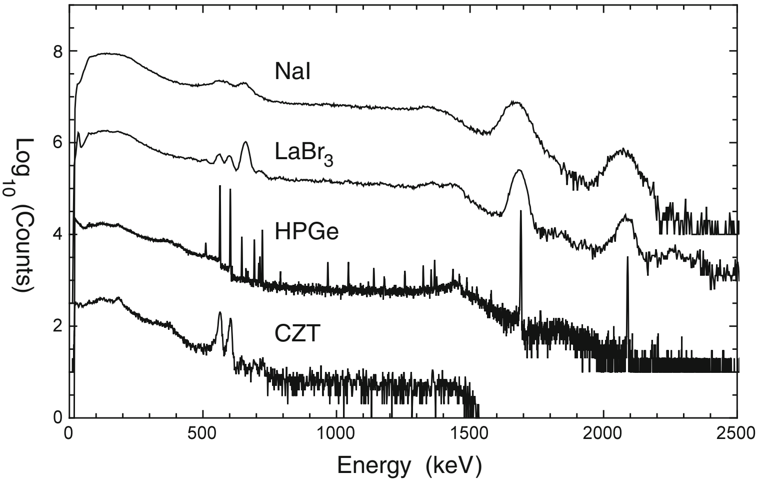

Fig. 4 Detector response comparison for CZT, high purity germanium (HPGe), $LaBr_3$, and NaI. Source was ^{122}Sb and ^{124}Sb. Response curves are shifted for clarity. Data courtesy of Lawrence Livermore National Laboratory. See also [37]

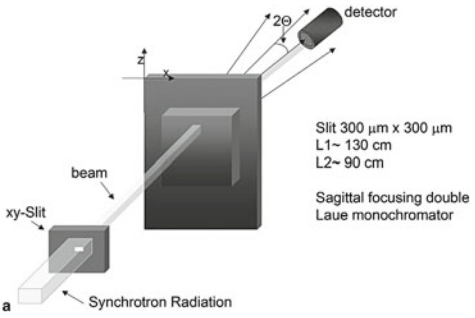

Fig. 5 Experimental setup used to measure crystalline properties in CZT. From [11]. Used with permission, Springer

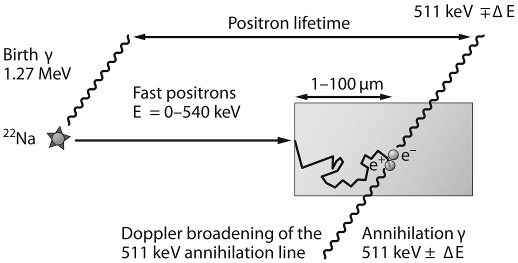

Fig. 6 Experimental setup for positron annihilation spectroscopy. From [36]. Used with permission, Springer

Brookhaven National Laboratory [11]. Band gap energies can be measured using photoluminescence. In this technique, a laser light source is used to create excitons at energies above the band gap energy, and the resulting de-excitation photons are measured with a spectrometer. The resulting spectrum has a peak which gives the band gap energy. Reference [28] gives an example of this technique applied to CZT. Another useful technique for characterizing semiconductors is positron annihilation spectrometry [1, 36]. In this technique, positrons, derived either from a radioactive source such as ^{22}Na, ^{59}Co, ^{64}Ge, or ^{68}Ge or from pair production from an energetic bremsstrahlung source, are deposited in the test material and the lifetime of the positrons is observed by a measurement of the time delay of production of 511 keV annihilation gammas from the time the production of gammas associated with the positron production. Figure 6 shows a typical scheme using ^{22}Na as a positron source, with the characteristic 1.27 MeV photon being used as a coincidence signal. The positron lifetime is affected by crystalline defects such as vacancies and interstitial atoms. Also, the momentum of the annihilating electron is carried through as a Doppler shift on the two 511 keV annihilating photons, and the differential energies of the 511 keV photons can be seen by two opposing detectors working in coincidence mode. These combined signatures can be used to characterize the type and concentration of defects in the material.

4 Alternatives to ^{3}He

4.1 *History and Background*

A shortage of ^{3}He was anticipated in 2008 [17]. Reasons for this shortage included a large demand for neutron detectors in radiation portal monitors, poor communication among U.S. Federal agencies in determining supply and demand (in part caused by classification issues regarding tritium inventory, from which ^{3}He is derived), and a sudden termination in Russian supply to the marketplace. Since that time, a coordinated working group has been formed within the U.S. government, and the actual needs have been assessed more carefully, resulting in a reduction in demand from 70,000 liters per year to less than 3,200 liters per year. The ^{3}He stockpile is expected to grow to more than 100,000 liters by 2020. Tritium for DOE purposes is still being produced at the Watts Bar Nuclear Plant Unit 1, operated by the Tennessee Valley Authority. The 12.3 year half-life for tritium to decay to ^{3}He assures that there will be ^{3}He for some years to come.

However, the momentum gained by the search for ^{3}He alternatives for neutron production has continued. Besides the availability and cost issues for ^{3}He, there has been a demand for detectors that can be adapted to shapes required for hand-held detectors such as shown in Fig. 3. This has led to research in various solid detection media.

4.2 *Stilbene*

Stilbene ($C_{14}H_{12}$) is one of the earliest scintillators discovered for detecting fast neutrons. It is a clear organic crystal. Its neutron detecting efficiency is about half that of anthracene, another organic crystal. Stilbene's crystalline structure causes it to be about thirty percent more efficient in one direction than another. Nevertheless, what makes it stand out is the difference in waveform between a high energy neutron and a gamma ray interacting in the scintillation medium. In its early history, however, the electronic circuits used to perform the pulse shape discrimination were not as fast or as accurate, and the gamma-to-neutron rejection ratios were in the range of about 1000:1 at 2.0 MeV neutron energy in a 1959 study [10], and headed towards unity at lower energies. Modern digital signal processing, however, has resulted in about a 5000:1 rejection ratio at 2.0 MeV and above 500:1 at 30 keV [30]. Thus stilbene can be regarded as a fair, but not perfect, ^{3}He alternative.

4.3 *CLYC, CLLB, and CLLC*

$Cs_2LiYCl_6:Ce^{3+}$ [33, 34], $Cs_2LiLaBr_6:Ce^{3+}$ (CLLB), and $Cs_2LiLaCl_6:Ce^{3+}$ (CLLC) are members of a crystalline family known as elpasolites, named after their discovery

Table 1 Properties of three elpasolite scintillator materials

	$Cs_2LiLaBr_6$:Ce^{3+} CLLC	$Cs_2LiLaBr_6$:Ce^{3+} CLLB	Cs_2LiYCl_6:Ce^{3+} CLYC
Density, g cm^{-3}	3.5	4.2	3.3
Emission, nm	290(CVL), 400(Ce^{3+})	410(Ce^{3+})	290(CVL) 390(Ce^{3+})
Decay time, ns	1 (CVL) 60, ≥400	55, ≥270	1 (CVL) 50, ∼1000
Max. light yield, ph/MeV	∼35,000	∼60,000	∼20,000
Light yield ph/n	∼110,000	∼180,000	∼70,000
GEE, MeV	∼3.1	3.2	∼3.1
Best ER 662 keV (%)	3.4	2.9	3.9
PSD	Excellent	Possible	Excellent

Data from [33]

in El Paso County, Colorado. All three of these detector materials contain lithium, for which the ^{6}Li component has a large reaction cross section (940 b at thermal neutron energy) for the reaction ^{6}Li(n,α)T with a positive Q of 4.78 MeV. (The natural abundance of ^{6}Li in natural Li is only 6.7 %, but enriched material is easily obtainable.) All three of these materials show excellent proportionality (within a few percent down to 15 keV), and have excellent light output. Table 1 gives some material properties for these compounds. In this table, "GEE" means the energy of a gamma ray which would give the same pulse height as a thermal neutron, ans "PSD" refers to the potential for pulse shape discrimination in the material. Also the materials show different emission wavelengths and decay times for scintillation photons arising from core valence luminescence (CVL) and from interactions with the Ce^{3+} activator (which can be further divided up into self-trapped excitons (STE) and prompt photon production by de-excitation). For neutrons, the slowest process dominates in CLYC and CLCC and that is the light produced from the decay of the STE with decay times up to 1 μs, whereas the neutrons do not produce any CVL light, which is produced with a 1.0 ns component. Differentiation of the neutron and gamma signals can be done with high accuracy. Furthermore, the different wavelengths for the scintillation light components affords the possibility of using two photomultipliers with different wavelength sensitivity to increase the gamma rejection ratio to near-^{3}He levels if desired. Figure 7 shows the differentiation of the neutron and gamma signals on CLYC based upon a relatively simple algorithm. A prototype handheld detector based on the CLYC material is shown as Fig. 3.

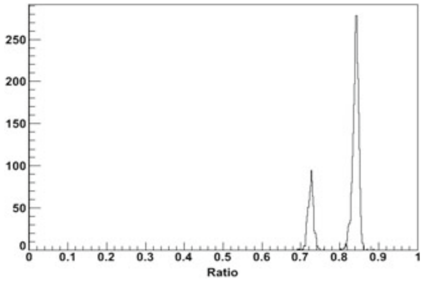

Fig. 7 Discrimination of neutrons from gammas in CLYC using the ratio of an integrated time slice of the output pulse to the total integrated pulse. From [34]

5 Imaging Detectors

5.1 Detector Arrays

Almost as soon as a new detector technology is developed, someone will make an array of them and try to get two- or three- dimensional images from the detector system. The need for detection systems that can localize a radiation source in two coordinate angles has special importance in determining the nature and location of threat signatures in homeland security applications. Oftentimes these systems have followed the lead of medical imaging systems which have been around for a long time. Reference [4] gives a description of the gamma camera used in medicine by the late 1950s. These systems have been optimized for small-to-intermediate sources located close by the imager, e.g. a thyroid gland or a heart injected with a tracer. For these systems, there can be one slab of scintillator material with a Pb collimator, and many photomultiplier tubes reading out the light signals through light pipes. A variation on this scheme known as SPECT (single photon emission computed tomography), can also use a coded aperture. Here a pseudo-random pattern of openings in a Pb slab is used to create a projection of photons on the detector slab or array which carries the angular information of the source location by the position of the shadows and illuminated areas on the detector.

The arrangement is somewhat different for far-field (3–50 m) detection of radioactive sources. These systems can utilize coded aperture imaging as well, but generally the systems are large enough in size to warrant an array of standard size scintillator crystals with each crystal coupled to an individual photomultiplier. Figure 8 shows an example of such a system at Berkeley. This system consists of 100 NaI scintillators, each a 10 cm cube, mounted in a 10×10 pattern. The coded aperture consists of an aluminum panel with circular holes in a 20×15 array. About fifty percent of the holes are covered with 25 mm thick Pb squares. The signals from each phototube are processed through a fast digitizer and these signals are sent through software to compose a two-dimensional image of the radiation field. Details of the software algorithm are described in [8], and some of the characteristic images obtained with test sources are shown. Typical resolution of a point source is about 60 cm at five meters standoff with a 10 μCi ^{137}Cs source (662 keV). The radiation data collected

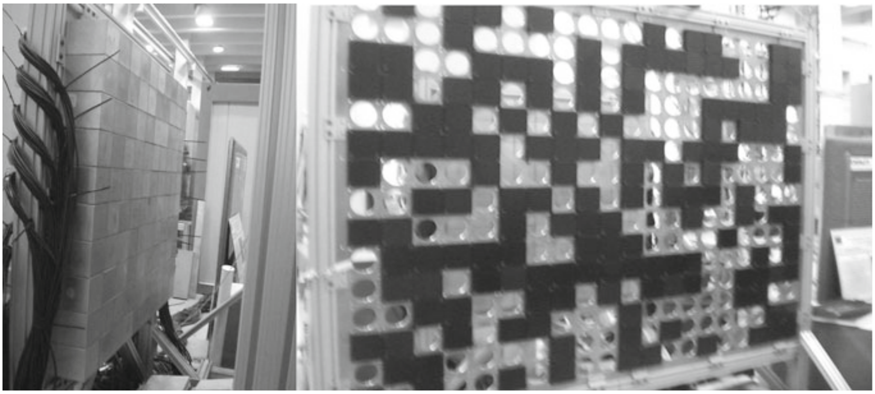

Fig. 8 A 10 × 10 imaging NaI array at Berkeley. *Left* the NaI array. *Right* the mask for the array. The *black squares* are 25 mm thick Pb plates

can be combined with the data from video cameras, which in turn can be put through image segmentation algorithms to try to identify the person or vehicle containing the source. The overall system has been named MVRDS, for "machine vision radiation detection system".

It is interesting to explore the mathematical details of the processing of coded-aperture signals. Let P stand for the information at the detector array (for "picture"). P is derived from a convolution of the actual image information O (the "Object") by the system function A, along with noise N:

$$\mathrm{P} = (\mathrm{O} * \mathrm{A}) + \mathrm{N}, \tag{5}$$

where the convolution operator * is defined by

$$(\mathrm{A} * \mathrm{B})(\mathrm{k}, \mathrm{l}) = \sum_{\mathrm{i}} \sum_{\mathrm{j}} \mathrm{A}(\mathrm{i}, \mathrm{j}) \mathrm{B}(\mathrm{i} + \mathrm{k}, \mathrm{j} + \mathrm{l}) \tag{6}$$

with indices i + k and j + l taken to be modulo the array size p. Note that the numbering goes from 0 to p-1, not 1 to p.

The deconvolution on the received data P is done by constructing a matrix G, chosen so that G ∗ A approximates a delta function. As an example, suppose that A is square p x p matrix with p being a prime integer equal to 4n + 1 for some integer n. Then a pseudorandom function based on Jacobi symbols can be constructed [18]:

$$\mathrm{A}(\mathrm{i}, \mathrm{j}) = \begin{cases} 0 & \mathrm{j} = 0 \\ 1 & \mathrm{j} \neq 0 \text{ and } \mathrm{i} = 0 \\ 1 - \left(\left(\frac{\mathrm{i}}{\mathrm{p}} \right) \left(\frac{\mathrm{j}}{\mathrm{p}} \right) + 1 \right) /2 & \text{else.} \end{cases} \tag{7}$$

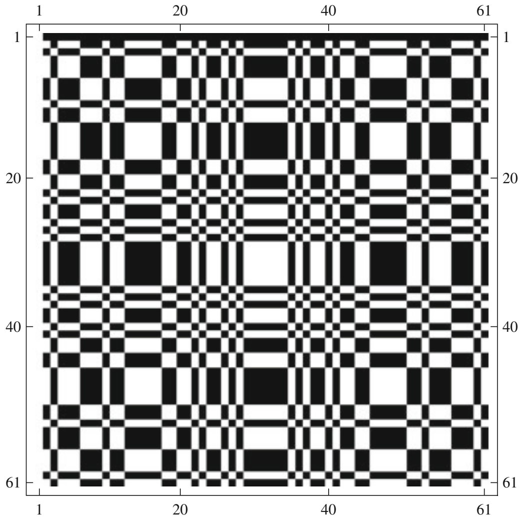

Fig. 9 A coded aperture array constructed using Jacobi symbols. Here $p = 61$

Here the Jacobi symbol $\left(\frac{a}{p}\right)$ is defined as

$$\left(\frac{a}{p}\right) = \begin{cases} 0 & \text{if } a = 0 \pmod{p} \\ +1 & \text{if } a \neq 0 \pmod{p} \text{ and for some integer } x,\ a = x^2 \pmod{p} \\ -1 & \text{if there is no such } x. \end{cases} \tag{8}$$

An example of a coded aperture array constructed with this method is shown as Fig. 9. For this choice of A, the appropriate decoding matrix G is given by

$$G(i,j) = \begin{cases} +1 & \text{if } A(i,j) = 1 \\ -1 & \text{if } A(i,j) = 0, \end{cases} \tag{9}$$

and the correlation gives

$$(A * G)(i,j) = \begin{cases} \frac{p^2}{2} - 2 & \text{if } i = j = 0 \\ -2A(i,j) & \text{else.} \end{cases} \tag{10}$$

Then the reconstructed image is given by

$$\hat{O} = P * G. \tag{11}$$

Figure 10 illustrates the process on an image which is a 61 × 61 bitmap of the Berkeley mascot Oski. A drawback of this simple deconvolution scheme is that the number of computational steps required for the deconvolution is proportional to p^4,

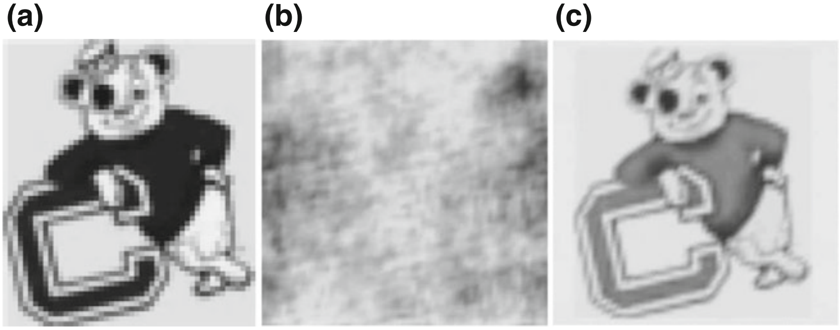

Fig. 10 Illustration of coded aperture encoding and decoding using the 61 × 61 coded aperture shown earlier. **a** Original image, **b** coded image, **c** decoded image

and this can become unwieldy unless some type of parallel processing environment can be utilized.

5.2 Compton Imaging

An alternative method for gamma-ray imaging exploits the energy-angle relationship in Compton scattering. Equation 23 in Chap. "Signatures and Background" can be re-written as:

$$\cos\theta = 1 - \mathrm{m_e c^2}\left(\frac{1}{\mathrm{E}_{\gamma'}} - \frac{1}{\mathrm{E}_{\gamma}}\right). \tag{12}$$

Suppose that a detector has an incident gamma ray and that gamma ray has a Compton scattering event within the detector. Suppose also that the scattered gamma is not absorbed in this detector, but impinges on a second detector which is in the form of a segmented array. Suppose that the scattered gamma from the first detector is completely absorbed in the second detector, either by deposition in a single cell of the second detector or by a track through two or more cells. In this way the total incident gamma energy E is known, and also the angle at which the scattered gamma with energy E′ can also be found. Since E and E′ are both known, the scattering angle for the Compton process in the first detector θ can be calculated. This angle then describes a locus of source points given by a cone with a symmetry axis around the line connecting the two detection locations. The process is repeated for each gamma interaction in the detection system of this type. The intersection of three or more cones generated by detected events, within some tolerance band, defines an absolute angle, both azimuthal and polar, for the direction of incoming radiation. Thus a two-dimensional image of source strength (and energy of the emitted gammas) can be constructed (Fig. 11).

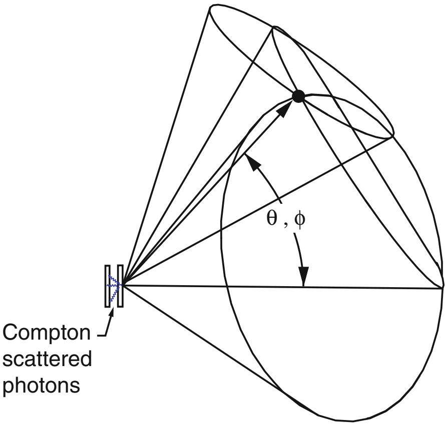

Fig. 11 Angular detection determination by three separate Compton events, showing the intersection of three back-calculated cones in angular space

More sophisticated forms of Compton imaging detectors can be created. Reference [7] gives an example of a Compton imaging system (also known as a Compton telescope) containing ten high-purity germanium slabs, each 8 cm × 8 cm × 1.5 cm, with thirty-seven strips on each side, running perpendicular to one another. The details of the device fabrication are given in [3]. The x and y locations of the gamma ray photon interactions are obtained from the charge signals collected from each set of strips on the two sides of the slab. The depth, or z-coordinate location, is determined by the difference in arrival times between the electron charge signal arriving at the positively biased set of strips and the hole charge signal arriving at the negative side [2]. The signals are processed using Compton kinematic discrimination (CKD) algorithms [5, 9, 24, 27]. The detector was launched on a balloon to observe extraterrestrial gamma-ray signals in the 300 keV–2 MeV range in 2005 and 2009 and successfully imaged the Crab Nebula from 6500 light years away–quite a standoff detection project! While this system is dwarfed by the Fermi Large Area Telescope, which works on the 20 MeV–50 GeV range and gives very high resolution images in real time and is based on pair production rather than Compton events [6], it is important to point out that the Fermi device cost around $ 690 million. The device described above is compact, much less expensive to fabricate, and might possibly find use in nuclear threat detection applications.

6 Concluding Remarks

The quest for low-cost, high-resolution, particle-discriminating, and efficient nuclear detection systems has been a constant since Becquerel's serendipitous detection of uranium alpha particles on photographic film in 1896. The need for better detectors in nuclear security and treaty verification programs has hastened the development of new technology in the area of solid-state detectors, scintillators, and imaging detectors. In some cases, older materials such as stilbene have been rediscovered. A great amount of cross-fertilization exists in detection research and development, with medical physics, high energy physics, and nuclear astrophysics bringing concepts forward which have been of great interest to the nonproliferation, arms control and treaty verification, and nuclear security communities.

7 Problems

1. A Compton upshift source is used for NRF inspection of cargo. The source makes 10^8 photons per pulse, 10^3 pulses per second, with a bandwidth of one percent centered on 1.733 MeV. The photons are distributed evenly inside a cone with a half-angle of two degrees. Assume that the source is one meter away from the underside of a cargo container, at its midpoint in length and width, and that a 5 kg spherical pit of 93 % enriched uranium ($\rho = 19.1\,\mathrm{g\,cm^{-3}}$) is at the geometric center of the cargo container, surrounded by plywood with a density of $0.6\,\mathrm{g\,cm^{-3}}$. The mass attenuation coefficient for plywood at 1.733 MeV is $0.054\,\mathrm{cm^2\,g^{-1}}$.

   a. Find the number of NRF photons per minute that would be detected by a gamma detector ($100\,\mathrm{cm^2}$ area and an efficiency of 0.2) located one meter from the outside of the container, at a small angle to the incoming photons. Note that the resonance integral $\int \sigma \mathrm{dE} = 30$ barn-eV at the 1.733 MeV resonance. (Note: use the thick-target efficiency factor

   $$\eta = \frac{\mathrm{n}\sigma_{\mathrm{NRF}}}{\mathrm{n}\sigma_{\mathrm{NRF}} + 2\mu} = 0.43$$

   and assume that the NRF resonance width $\ll \Delta E$ of the source.)

   b. If the beam were made to have much less angular divergence, what other detection method might be used?

2. Construct a pseudo-random mask using the Jacobi symbols with a size $\mathrm{p} = 73$. Plot a picture of this mask.
3. Decode the $\mathrm{p} = 61$ image codedimage.m located on the resource page for the book. The decoding correlation function Gtable61.m is also on the resource page. Plot the image.

References

1. Abdul-Jabbar N, Bourret-Courchesne E, Wirth B (2012) Single crystal growth of $\mathrm{Ga_2(Se_{1-x}Te_x)_3}$ semiconductors and defect studies via positron annihilation spectroscopy. J Cryst Growth 352(1):31–34. doi:10.1016/j.jcrysgro.2012.02.011. http://www.sciencedirect.com/science/article/pii/S0022024812001261. The proceedings of the 18th American conference on crystal growth and epitaxy

2. Amman M, Luke P (2000) Three-dimensional position sensing and field shaping in orthogonal-strip germanium gamma-ray detectors. Nucl Instrum Methods Phys Res Sect A: Accel Spectrom Detect Assoc Equip 452(1–2):155–166. doi:10.1016/S0168-9002(00)00351-X. http://www.sciencedirect.com/science/article/pii/S016890020000351X
3. Amman M, Luke P, Boggs S (2007) Amorphous-semiconductor-contact germanium-based detectors for gamma-ray imaging and spectroscopy. Nucl Instrum Methods Phys Res Sect A: Accel Spectrom Detect Assoc Equip 579(2):886–890. doi:10.1016/j.nima.2007.05.307. http://www.sciencedirect.com/science/article/pii/S0168900207012004
4. Anger HO (1958) Scintillation camera. Rev Sci Instrum 29(1):27–3. doi:10.1063/1.1715998. http://scitation.aip.org/content/aip/journal/rsi/29/1/10.1063/1.1715998
5. Aprile E, Bolotnikov A, Chen D, Mukherjee R (1993) A Monte Carlo analysis of the liquid xenon TPC as gamma-ray telescope. Nucl Instrum Methods Phys Res Sect A: Accel Spectrom Detect Assoc Equip 327(1):216–221. doi:10.1016/0168-9002(93)91446-T. http://www.sciencedirect.com/science/article/pii/016890029391446T
6. Atwood WB, Abdo AA, Ackermann M, Althouse W, Anderson B, Axelsson M, Baldini L, Ballet J, Band DL, Barbiellini G, Bartelt J, Bastieri D, Baughman BM, Bechtol K, Bdrde D, Bellardi F, Bellazzini R, Berenji B, Bignami GF, Bisello D, Bissaldi E, Blandford RD, Bloom ED, Bogart JR, Bonamente E, Bonnell J, Borgland AW, Bouvier A, Bregeon J, Brez A, Brigida M, Bruel P, Burnett TH, Busetto G, Caliandro GA, Cameron RA, Caraveo PA, Carius S, Carlson P, Casandjian JM, Cavazzuti E, Ceccanti M, Cecchi C, Charles E, Chekhtman A, Cheung CC, Chiang J, Chipaux R, Cillis AN, Ciprini S, Claus R, Cohen-Tanugi J, Condamoor S, Conrad J, Corbet R, Corucci L, Costamante L, Cutini S, Davis DS, Decotigny D, DeKlotz M, Dermer CD, de Angelis A, Digel SW, do Couto e Silva E, Drell PS, Dubois R, Dumora D, Edmonds Y, Fabiani D, Farnier C, Favuzzi C, Flath DL, Fleury P, Focke WB, Funk S, Fusco P, Gargano F, Gasparrini D, Gehrels N, Gentit FX, Germani S, Giebels B, Giglietto N, Giommi P, Giordano F, Glanzman T, Godfrey G, Grenier IA, Grondin MH, Grove JE, Guillemot L, Guiriec S, Haller G, Harding AK, Hart PA, Hays E, Healey SE, Hirayama M, Hjalmarsdotter L, Horn R, Hughes RE, Jhannesson G, Johansson G, Johnson AS, Johnson RP, Johnson TJ, Johnson WN, Kamae T, Katagiri H, Kataoka J, Kavelaars A, Kawai N, Kelly H, Kerr M, Klamra W, Kndlseder J, Kocian ML, Komin N, Kuehn F, Kuss M, Landriu D, Latronico L, Lee B, Lee SH, Lemoine-Goumard M, Lionetto AM, Longo F, Loparco F, Lott B, Lovellette MN, Lubrano P, Madejski GM, Makeev A, Marangelli B, Massai MM, Mazziotta MN, McEnery JE, Menon N, Meurer C, Michelson PF, Minuti M, Mirizzi N, Mitthumsiri W, Mizuno T, Moiseev AA, Monte C, Monzani ME, Moretti E, Morselli A, Moskalenko IV, Murgia S, Nakamori T, Nishino S, Nolan PL, Norris JP, Nuss E, Ohno M, Ohsugi T, Omodei N, Orlando E, Ormes JF, Paccagnella A, Paneque D, Panetta JH, Parent D, Pearce M, Pepe M, Perazzo A, Pesce-Rollins M, Picozza P, Pieri L, Pinchera M, Piron F, Porter TA, Poupard L, Rain S, Rando R, Rapposelli E, Razzano M, Reimer A, Reimer O, Reposeur T, Reyes LC, Ritz S, Rochester LS, Rodriguez AY, Romani RW, Roth M, Russell JJ, Ryde F, Sabatini S, Sadrozinski HFW, Sanchez D, Sander A, Sapozhnikov L, Parkinson PMS, Scargle JD, Schalk TL, Scolieri G, Sgr C, Share GH, Shaw M, Shimokawabe T, Shrader C, Sierpowska-Bartosik A, Siskind EJ, Smith DA, Smith PD, Spandre G, Spinelli P, Starck JL, Stephens TE, Strickman MS, Strong AW, Suson DJ, Tajima H, Takahashi H, Takahashi T, Tanaka T, Tenze A, Tether S, Thayer JB, Thayer JG, Thompson DJ, Tibaldo L, Tibolla O, Torres DF, Tosti G, Tramacere A, Turri M, Usher TL, Vilchez N, Vitale V, Wang P, Watters K, Winer BL, Wood KS, Ylinen T, Ziegler M (2009) The large area telescope on the Fermi gamma-ray space telescope mission. Astrophys J 697(2):1071. http://stacks.iop.org/0004-637X/697/i=2/a=1071
7. Bandstra MS, Bellm EC, Boggs SE, Perez-Becker D, Zoglauer A, Chang HK, Chiu JL, Liang JS, Chang YH, Liu ZK, Hung WC, Huang MHA, Chiang SJ, Run RS, Lin CH, Amman M, Luke PN, Jean P, von Ballmoos P, Wunderer CB (2011) Detection and imaging of the crab nebula with the nuclear compton telescope. Astrophys J 738(1):8. http://stacks.iop.org/0004-637X/738/i=1/a=8
8. Benson A, Bandstra M, Chivers D, Aucott T, Augarten B, Bates C, Midvidy A, Pavlovsky R, Siegrist J, Vetter K, Yee B (2013) The gamma-ray imaging framework. IEEE Trans Nucl Sci

60(2):528–532. doi:10.1109/TNS.2013.2245342

9. Boggs SE, Jean P (2000) Event reconstruction in high resolution compton telescopes. Astron Astrophys Suppl Ser 145(2):311–321. doi:10.1051/aas:2000107. http://aas.aanda.org/articles/aas/abs/2000/14/h2143/h2143.html
10. Brooks F (1959) A scintillation counter with neutron and gamma-ray discriminators. Nucl Instr Methods 4(3):151–163. doi:10.1016/0029-554X(59)90067-9. http://www.sciencedirect.com/science/article/pii/0029554X59900679
11. Carini G, Camarda G, Zhong Z, Siddons D, Bolotnikov A, Wright G, Barber B, Arnone C, James R (2005) High-energy x-ray diffraction and topography investigation of cdznte. J Electron Mater 34(6):804–810. doi:10.1007/s11664-005-0024-6
12. Cherepy N, Payne S, Sturm B, Kuntz J, Seeley Z, Rupert B, Sanner R, Drury O, Hurst T, Fisher S, Groza M, Matei L, Burger A, Hawrami R, Member, Shah K, Boatner L (2010) Comparative gamma spectroscopy with SrI_2(Eu), GYGAG(Ce) and Bi-loaded plastic scintillators. In: IEEE transactions on nuclear science, IEEE/NSS proceedings 2010
13. Cherepy NJ, Seeley ZM, Payne SA, Beck PR, Drury OB, ONeal SP, Figueroa KM, Hunter S, Ahle L, Thelin PA, Stefanik T, Kindem J (2013) Development of transparent ceramic Ce-doped gadolinium garnet gamma spectrometers. IEEE Trans Nucl Sci 60(3):2330–2335. doi:10.1109/TNS.2013.2261826. http://ieeexplore.ieee.org/stamp/stamp.jsp?arnumber=6520005
14. Cherepy NJ, Sturm BW, Drury OB, Hurst TA, Sheets SA, Ahle LE, Saw CK, Pearson MA, Payne SA, Burger A, Boatner LA, Ramey JO, van Loef EV, Glodo J, Hawrami R, Higgins WM, Shah KS, Moses WW (2009) SrI_2 scintillator for gamma ray spectroscopy. Proc SPIE 7449:74,490F–74,490F–6. doi:10.1117/12.830016
15. Dorenbos P (2002) Light output and energy resolution of Ce3+-doped scintillators. Nucl Instrum Methods Phys Res Sect A: Accel Spectrom Detect Assoc Equip 486(12):208–213. doi:10.1016/S0168-9002(02)00704-0. http://www.sciencedirect.com/science/article/pii/S0168900202007040. Proceedings of the 6th international conference on inorganic scintillators and their use in scientific and industrial applications
16. Dziuk G, Boschert S, Schmidt A, Siebert K, Bnsch E, Benz KW, Kaiser T (2003) Simulation of industrial crystal growth by the vertical Bridgman method. In: Jger W, Krebs HJ (eds) Mathematics key technology for the future. Springer, Berlin, pp 315–330. doi:10.1007/978-3-642-55753-8_26
17. Gillo J (2014) Stable isotope operations: Helium-3. In: 3rd federal workshop on isotope supply and demand (Nov 3, 2014). http://science.energy.gov/~/media/np/pdf/workshops/workshop-on-isotope-federal-supply-and-demand-2014/presentations/Jehanne_Workshop_2014_he3.pdf
18. Gottesman SR, Fenimore EE (1989) New family of binary arrays for coded aperture imaging. Appl Opt 28:4344–4352. doi:10.1364/AO.28.004344
19. Hecht K (1932) Zum mechanismus des lichtelektrischen primärstromes in isolierenden kristallen. Zeitschrift für Physik 77(3-4):235–245. doi:10.1007/BF01338917. http://dx.doi.org/10.1007/BF01338917
20. Huang GY, Abdul-Jabbar N, Wirth B (2014) Theoretical study of Ga_2Se3,Ga_2Te_3 and $Ga_2(Se_{1-x}Te_x)_3$: band-gap engineering. Acta Materialia 71:349–369. doi:10.1016/j.actamat.2014.03.010. http://www.sciencedirect.com/science/article/pii/S1359645414001578
21. Isaac MP, Hurley D, McDonald R, Norman E, Smith A (1997) A natural calibration source for determining germanium detector efficiencies. Nucl Instrum Methods Phys Res Sect A: Accel Spectrom Detect Assoc Equip 397(23):310–316. doi:10.1016/S0168-9002(97)00754-7. http://www.sciencedirect.com/science/article/pii/S0168900297007547
22. Jenkins D (2015) Novel scintillators and silicon photomultipliers for nuclear physics and applications. J Phys: Conf Ser 620(1):012,001. http://stacks.iop.org/1742-6596/620/i=1/a=012001
23. Kernan W (2006) Self-activity in lanthanum halides. IEEE Trans Nucl Sci 53(1):395–400. doi:10.1109/TNS.2006.869849
24. Kroeger R, Johnson W, Kurfess J, Phlips B, Wulf E (2002) Three-compton telescope: theory, simulations, and performance. IEEE Trans Nucl Sci 49(4):1887–1892. doi:10.1109/TNS.2002.801539

25. Lecoq P, Annenkov A, Gektin A, Korzhik M, Pedrini C (2006) Scintillation mechanisms in inorganic scintillators. In: Inorganic scintillators for detector systems, particle acceleration and detection. Springer, Berlin, pp 81–122. doi:10.1007/3-540-27768-4_3
26. Milbrath B, Runkle R, Hossbach T, Kaye W, Lepel E, McDonald B, Smith L (2005) Characterization of alpha contamination in lanthanum trichloride scintillators using coincidence measurements. Nucl Instrum Methods Phys Res Sect A: Accel Spectrom Detect Assoc Equip 547(23):504–510. doi:10.1016/j.nima.2004.11.054. http://www.sciencedirect.com/science/article/pii/S0168900205008909
27. Oberlack UG, Aprile E, Curioni A, Egorov V, Giboni KL (2000) Compton scattering sequence reconstruction algorithm for the liquid xenon gamma-ray imaging telescope (lxegrit). Proc SPIE 4141:168–177. doi:10.1117/12.407578
28. Olego DJ, Faurie JP, Sivananthan S, Raccah PM (1985) Optoelectronic properties of $Cd_{1-x}Zn_xTe$ films grown by molecular beam epitaxy on gaas substrates. Appl Phys Lett 47(11):1172–1174. doi:10.1063/1.96316. http://scitation.aip.org/content/aip/journal/apl/47/11/10.1063/1.96316
29. Owens A, Peacock A (2004) Compound semiconductor radiation detectors. Nucl Instrum Methods Phys Res Sect A: Accel Spectrom Detect Assoc Equip 531(12):18–37. doi:10.1016/j.nima.2004.05.071. http://www.sciencedirect.com/science/article/pii/S0168900204010575. Proceedings of the 5th international workshop on radiation imaging detectors
30. Prokuronov M, Golubev A, Demidov V, Rudskoi I, Smirnov G, Khaldeeva N, Shabalin A, Shubin S (2006) A digital method for pulse-shape discrimination between particles. Instrum Exp Tech 49(2):207–222. doi:10.1134/S0020441206020096
31. Schlesinger T, Toney J, Yoon H, Lee E, Brunett B, Franks L, James R (2001) Cadmium zinc telluride and its use as a nuclear radiation detector material. Mater Sci Eng: R: Rep 32(45):103–189. doi:10.1016/S0927-796X(01)00027-4. http://www.sciencedirect.com/science/article/pii/S0927796X01000274
32. Seeley Z, Cherepy N, Payne S (2013) Homogeneity of Gd-based garnet transparent ceramic scintillators for gamma spectroscopy. J Cryst Growth 379:79–83. doi:10.1016/j.jcrysgro.2012.11.042. http://www.sciencedirect.com/science/article/pii/S0022024812008391. Compound semiconductors and scintillators for radiation detection applications: a special tribute to the research of Michael Schieber
33. Shah K, Glodo J, van Loef E, Higgins W, Hawrami R, Shirwadkar U, Mukhopadhay S (2010) New detectors for gamma and neutron studies. DOE SBIR Phase II presentation. http://science.energy.gov/~/media/np/pdf/sbir%20sttr/presentations/shah_np_gamma_neutron_scintillators_1.pdf
34. Stonehill L (2012) A new scintillator for neutron and gamma detection: Cs_2LiYCl_6:Ce^{3+} (CLYC): overview and selected applications. Los Alamos Lab Tech Rep LA-UR-12-26565:1–41 (Nov 29, 2012). http://permalink.lanl.gov/object/tr?what=info:lanl-repo/lareport/LA-UR-12-26565
35. Toney J, Schlesinger T, James R (1999) Optimal bandgap variants of $cd_{1-x}zn_xte$ for high-resolution x-ray and gamma-ray spectroscopy. Nucl Instrum Methods Phys Res Sect A: Accel Spectrom Detect Assoc Equip 428(1):14–24. doi:10.1016/S0168-9002(98)01575-7. http://www.sciencedirect.com/science/article/pii/S0168900298015757
36. Tuomisto F (2010) Defect characterization in semiconductors with positron annihilation spectroscopy. In: Dhanaraj G, Byrappa K, Prasad V, Dudley M (eds) Springer handbook of crystal growth. Springer, Berlin, pp 1551–1579. doi:10.1007/978-3-540-74761-1_46
37. Vo D (2008) Comparison of portable detectors for uranium enrichment measurements. J Radioanal Nucl Chem 276(3):693–698. doi:10.1007/s10967-008-0619-5
38. Xiang Q, Tian D, Hao F, Chu C, Ding G, Zeng J, Luo F (2014) Self-calibration method for cerium-doped lanthanum bromide scintillator detector in the 0.12.0mev energy range. J Radioanal Nucl Chem 299(3):1439–1445. doi:10.1007/s10967-013-2782-6

Arms Control and Treaty Verification

Abstract Methods of detection unique to arms control and treaty verification are discussed here. The conditions and opportunities for detection in these enivronments are contrasted with portal monitoring and cargo screening environments. First, neutron multiplicity counting is covered, including both the technology involved and the mathematics required. Next, the Pu300, Pu600 and Pu900 plutonium analyses are explored. Next, neutron imaging methods are discussed from the historical perspective in the context of counting the number of warheads on a missile. The necessity for "information barriers" in this application is discussed. The use of anti-neutrino detectors to verify the operating power level of a nuclear reactor is also covered, and successful experiments of this technology are described. The dependence of the neutrino signal on the uranium-to-plutonium fission rate is discussed, and a simple analytical model for quantifying this effect is presented.

1 Introduction

Analytical methods used for arms control and treaty verification can be substantially different from techniques used for detection of clandestine nuclear material. Typically the expected result is known. The package size is typically much smaller than a cargo container. An inspection might be scheduled to determine whether a container contains a weapon component, and if so, what is the approximate mass of material involved. Because an open inspection may not be allowed because that would reveal design details that the party being inspected wants to keep secret, techniques must be used to remotely estimate the mass and other factors, such as ^{240}Pu content or date of manufacture, to ensure that the material contained is consistent with records.

Unlike cargo screening and other detection schemes being applied to a huge stream of test objects, oftentimes the number of test objects is small enough to employ more expensive and time-consuming tests with very high accuracy. Since a declaration of non-compliance in a weapon inspection scenario might very quickly escalate into a state diplomacy issue, the test methods employed must be very robust. The ideal situation is where the parties monitoring each other have a clear understanding of the physics involved in the test procedures, and have some agreement about their reliability. Members of weapon inspection teams often have prior background in

E.C. Morse, *Analytical Methods for Nonproliferation*, Advanced Sciences and Technologies for Security Applications, DOI 10.1007/978-3-319-29731-6_10

nuclear weapon designs of their own country, and will probably be aware of what information is considered sensitive. Some analysis systems are designed with "information barriers" built in, so that only the agreed-upon parameters are available.

Neutron multiplicity counting for plutonium assay is done with systems with large numbers of ^{3}He tubes with typical counting times of 30 min or more-hardly the type of procedure that would be done in a cargo inspection environment. These systems are large and expensive. The Pu300, Pu600, and Pu900 methods all require long counting times using high purity germanium detectors, and more suited to a low-background analytical laboratory than, say a repository building. Neutron imaging methods were used to provide self-radiography of a missile to determine the number of weapon packages on board in the case of multiple independent trajectory re-entry vehicle (MIRV) warheads. These systems have been made obsolete by changes in the terms of the inspection protocol, as well as the reduction of the number of warheads under the arms limitation agreement now in place. Neutrino methods for verification of power levels in nuclear reactors in order to verify the inventory of Pu isotopes potentially being produced. Here the detector systems have weight in tonnes and detection times of months–certainly quite a different detection methodology from cargo inspection!

2 Neutron Multiplicity Counting

As an example of a technique which would probably never be used in routine cargo inspection, we first consider neutron multiplicity counting. These systems require dozens of ^{3}He tubes and thirty or sixty minute counting times. These systems can determine the amount of fissile material to within a few percent, important in material accountability programs. Neutron multiplicity counting has become the standard method of plutonium assay for all phases of weapon-related plutonium, from initial manufacture to machining, stockpiling, and ultimately conversion into MOX fuel or other non-weapon formats. It is based upon the presence of spontaneous fission isotopes in the material, specifically ^{238}Pu, ^{240}Pu, and ^{242}Pu. Table 1 lists the spontaneous fission properties of nuclides of interest. Figure 1 shows the most important relationship: the probability distribution for spontaneous fission of ^{240}Pu versus the induced fission distribution for fast neutrons in ^{239}Pu. Typically, the fractions of these isotopes relative to the total plutonium present is measured by gamma-ray spectroscopy or mass spectrometry. Then the neutron multiplication in the material is determined by looking at the number of time-correlated neutrons coming out of the sample. Since the statistical distribution of neutrons per fission is different for the spontaneous fission in the nuclei just mentioned from neutron-induced fission in ^{239}Pu (and others), it is possible to determine the overall multiplication M in the sample. There can be a significant contribution to the total neutron rate from (α, n) reactions due to the presence of oxygen (^{17}O and ^{18}O), fluorine, beryllium, others. These reactions, however, produce only one neutron per reaction and thus

Table 1 Spontaneous fission yields of actinides of interest for multiplicity counting

Isotope A	Number of protons Z	Number of neutrons N	Total half-life	Spontaneous fission half-life (yr)	Spontaneous fission yield ($ns^{-1}g^{-1}$)	Spontaneous fission multiplicity ν	Induced thermal fission multiplicity ν
^{232}Th	90	142	1.41×10^{10} yr	$>1 \times 10^{21}$	$>6 \times 10^{-8}$	2.14	1.9
^{232}U	92	140	71.7 yr	8×10^{13}	1.3	1.71	3.13
^{233}U	92	141	$1.59 \times l0^{5}$ yr	1.2×10^{17}	8.6×10^{-4}	1.76	2.4
^{234}U	92	142	2.45×10^{5} yr	$2.1 \times l0^{l6}$	5.02×10^{-3}	1.81	2.4
^{235}U	92	143	7.04×10^{8} yr	3.5×10^{17}	2.99×10^{-4}	1.86	2.41
^{236}U	92	144	2.34×10^{7} yr	1.95×10^{16}	5.49×10^{-3}	1.91	2.2
^{238}U	92	146	4.47×10^{9} yr	8.20×10^{15}	1.36×10^{-2}	2.01	2.3
^{237}Np	93	144	2.14×10^{6} yr	1.0×10^{18}	1.14×10^{-4}	2.05	2.70
^{238}Pu	94	144	87.74 yr	4.77×10^{10}	2.59×10^{3}	2.21	2.9
^{239}Pu	94	145	2.41×10^{4} yr	5.48×10^{15}	2.18×10^{-2}	2.16	2.88
^{240}Pu	94	146	6.56×10^{3} yr	1.16×10^{11}	1.02×10^{3}	2.16	2.8
^{241}Pu	94	147	14.35 yr	(2.5×10^{15})	(5×10^{-2})	2.25	2.8
^{242}Pu	94	148	3.76×10^{5} yr	6.84×10^{10}	1.72×10^{3}	2.15	2.81
^{24l}Am	95	146	433.6 yr	1.05×10^{14}	1.18	3.22	3.09
^{242}Cm	96	146	163 days	$6.56 \times l0^{6}$	2.10×10^{7}	2.54	3.44
^{244}Cm	96	148	18.1 yr	1.35×10^{7}	1.08×10^{7}	2.72	3.46
^{249}Bk	97	152	320 days	1.90×10^{9}	1.0×10^{5}	3.40	3.7
^{252}Cf	98	154	2.646 yr	85.5	2.34×10^{12}	3.757	4.06

From [13]

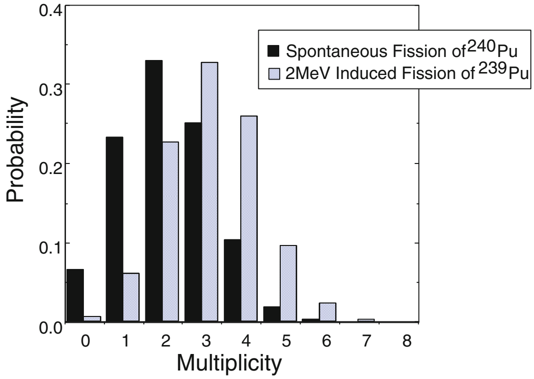

Fig. 1 Comparison of the neutron production probability distribution for spontaneous fission in ^{240}Pu versus induced fast fission in ^{239}Pu. From [12]

no coincident neutrons are present. Spontaneous fission, however, produces between zero and eight neutrons per event.

The distribution of the number of neutrons per fission event has been well-characterized for a number of isotopes. Studies of induced-fission multiplicity started in 1939 [3]. Table 2 shows the distribution of spontaneous fission neutrons for those

Table 2 Spontaneous and induced fission multiplicity distributions

P(ν)	^{238}Pu s.f.	^{240}Pu s.f	^{242}Pu s.f.	^{242}Cm s.f.	^{244}Cm s.f.	^{252}Cf s.f.	^{239} Pu 0.025 eV	^{239}Pu 2 MeV
0	0.052	0.066	0.068	0.021	0.015	0.002	0.011	0.006
1	0.205	0.232	0.230	0.147	0.116	0.026	0.099	0.061
2	0.380	0.329	0.334	0.327	0.300	0.127	0.275	0.227
3	0.225	0.251	0.247	0.327	0.333	0.273	0.327	0.326
4	0.108	0.102	0.099	0.138	0.184	0.304	0.205	0.259
5	0.028	0.018	0.018	0.037	0.043	0.185	0.073	0.096
6		0.002	0.003	0.003	0.009	0.066	0.010	0.022
7				0.001		0.015	0.001	0.003
8							0.002	0.001
ν_1	2.21	2.156	2.145	2.540	2.720	3.757	2.876	3.163
ν_2	3.957	3.825	3.794	5.132	5.939	11.962	6.748	8.240
ν_3	5.596	5.336	5.317	8.036	10.101	31.812	12.589	17.321

From [13]

isotopes with substantial spontaneous fission rates and compares those distributions to neutron-induced fission in ^{239}Pu for both thermal energy (0.25 eV) and for fast fission energy (2 MeV). It is fortunate that the most common (α, n) reaction (in oxygen) has an average neutron energy of 2.03 MeV, very close to the average energy of neutrons emitted in spontaneous fission of 1.96 MeV. Since other spontaneous fission nuclides can be present in plutonium, the effective ^{240}Pu content is what is actually measured, and it is given by:

$$^{240}\mathrm{Pu}_{\mathrm{eff}} = 2.52^{238}\mathrm{Pu} +^{240}\mathrm{Pu} + 1.68^{242}\mathrm{Pu} \tag{1}$$

Instead of working with the probability distributions directly, resulting in a nine-parameter set of equations, a set of three factorial moments are derived from the experimental multiplicity data for each isotope. These are given by:

$$\begin{aligned} \nu_1 &= \sum_{\nu=1}^{\max} \nu \mathrm{P}(\nu) \\ \nu_2 &= \sum_{\nu=2}^{\max} \nu(\nu-1)\mathrm{P}(\nu) \\ \nu_3 &= \sum_{\nu=3}^{\max} \nu(\nu-1)(\nu-2)\mathrm{P}(\nu) \end{aligned} \tag{2}$$

These are given in Table 2 as well.

The detectors used for multiplicity counting are arrays of ^{3}He tubes with a paraffin moderator and a well-type area for the sample. Typically, graphite reflectors are added top and bottom. Sample size capacities range from roughly a quart paint can size to 55 gallon drums and to standard waste containers of several meters on a side that can

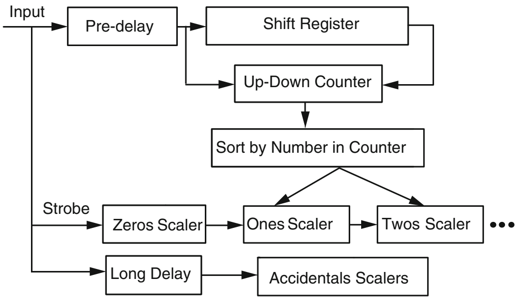

Fig. 2 Shift register electronics for multiplicity counting. From [12]

hold fourteen 55 gallon drums. The largest U.S.-built systems have 260 ^{3}He tubes pressurized to 10 atm and mounted in a 14.6 m × 2.6 m × 4.1 m high trailer. Typical detector efficiencies are 40–65 %.

A schematic diagram for the electronics is shown in Fig. 2. The typical gate length G for all coincidence counting intervals is 32 μs, with a 128-bit shift register running on a 4 MHz clock. Because of pulse pile-up at early times caused by the detector and counting electronics, a "pre-delay" is used to dismiss an early part of the signal which may not fit an exponential decay model. Typically, this pre-delay is about 3 μs. An innovative feature of the current design is a "derandomizer" circuit, which moves a detected event in time to the beginning of a clock pulse. This has been shown to reduce the errors due to pulse pile-up, which effects the higher-multiplicity events at high count rates. There are actually two sets of shift registers, one measuring all real multiplicities plus accidental ones due to independent events, called the R+A distribution, plus another one where a long time delay (up to 4096 μs) is used to determine accidental multiplicities, called the A distribution. A typical output from the shift register electronics is shown in Table 3. Notice that the events of multiplicity zero are higher in the A channel, but higher numbers of higher-multiplicity events are recorded in the R+A signal.

The signal processing proceeds as follows [7, 13]. First normalized probability distributions are made out of the R+A and A multiplicity data, resulting in a set of numbers $P_{R+A}(n)$ and $P_A(n)$ for both the R+A and A data. (Note that the R+A and A rates do not necessarily sum to the same number, because they are measuring two different time intervals. They should, however, have the same total count rate to within normal Poisson counting statistics.) Then factorial moments f_i and b_i (for "foreground" and "background") are formed in the manner given earlier in Eq. 2:

$$\begin{aligned} f_1 &= \sum_{n=1}^{\max} nP_{R+A}(n) \\ f_2 &= \sum_{n=2}^{\max} n(n-1)P_{R+A}(n) \\ f_3 &= \sum_{n=3}^{\max} n(n-1)(n-2)P_{R+A}(n) \end{aligned} \tag{3}$$

and similarly for the b_i.

Table 3 Multiplicity distribution for a 60-g plutonium oxide sample

Multiplicity	Counts in (R+A Gate) (f(i) distribution)	Counts (A Gate) (b(i) distribution)
0	26804360	29731130
1	8187530	6222207
2	1772831	1016603
3	325270	157224
4	53449	22387
5	8231	3093
6	1237	402
7	183	42
8	30	8
9	2	1
10	0	0

From [13]

The "singles" rate S is not the rate shown for multiplicity-one events but rather is the sum of all triggers. i.e. 37, 153, 123 total counts, divided by the counting time, for the data shown in Table 3. The "doubles" and "triples" rates are defined by S and the factorial moments:

$$\begin{aligned} \mathrm{D} &= \mathrm{S}(\mathrm{f}_1 - \mathrm{b}_1) \\ \mathrm{T} &= \mathrm{S}(\mathrm{f}_2 - \mathrm{b}_2 - 2\mathrm{b}_1(\mathrm{f}_1 - \mathrm{b}_1))/2. \end{aligned} \tag{4}$$

Not all doubles and triples happen within the timing window G. The exponential die-away time τ in the detector may be on the order of the timing window for optimum counting statistics. Thus the efficiency of collecting doubles, called the doubles gate fraction f_d, is given by

$$\mathrm{f}_\mathrm{d} = \mathrm{e}^{-\mathrm{P}/\tau}\left(1 - \mathrm{e}^{-\mathrm{G}/\tau}\right), \tag{5}$$

and the triples gate fraction is approximately f_d^2. The measured doubles rate D and triples rate T are then equated to the theoretical values through the following equations:

$$\begin{aligned} \mathrm{S} &= \mathrm{F}\varepsilon\mathrm{M}\nu_{\mathrm{s}1}(1+\alpha) \\ \mathrm{D} &= \frac{\mathrm{F}\varepsilon^2\mathrm{f}_\mathrm{d}\mathrm{M}^2}{2}\left[\nu_{\mathrm{s}2} + \left(\frac{\mathrm{M}-1}{\nu_{\mathrm{i}1}-1}\right)\nu_{\mathrm{s}1}(1+\alpha)\nu_{i2}\right] \\ \mathrm{T} &= \frac{\mathrm{F}\varepsilon^3\mathrm{f}_\mathrm{d}\mathrm{M}^3}{3}\left[\nu_{s3} + \left(\frac{\mathrm{M}-1}{\nu_{i1}-1}\right)[3\nu_{\mathrm{s}2}\nu_{\mathrm{i}2} + \nu_{\mathrm{s}1}(1+\alpha)\nu_{\mathrm{i}3}]\right. \\ &\quad \left. + 3\left(\frac{\mathrm{M}-1}{\nu_{\mathrm{i}1}-1}\right)^2 \nu_{\mathrm{s}1}(1+\alpha)\nu_{\mathrm{i}2}^2\right]. \end{aligned} \tag{6}$$

Here F is the spontaneous fission rate, ε is the neutron detection efficiency, M is the neutron leakage multiplication, α is the (α, n) to spontaneous fission ratio, f_d is the doubles gate fraction, f_t is the triples gate fraction, ν_{s1}, ν_{s2}, ν_{s3} are the factorial moments of the spontaneous fission distribution, and ν_{i1}, ν_{i2}, ν_{i3} are the factorial moments of the induced fission distribution.

The above yields a cubic equation in M:

$$a + bM + cM^2 + M^3 = 0 \tag{7}$$

where the coefficients are functions of S, D, and T:

$$\begin{aligned} a &= \frac{-6T\nu_{s2}(\nu_{i1} - 1)}{\varepsilon^2 f_t S(\nu_{s2}\nu_{i3} - \nu_{s3}\nu_{i2})} \\ b &= \frac{2D\left[\nu_{s3}(\nu_{i1} - 1) - 3\nu_{s3}\nu_{i2}\right]}{\varepsilon f_d S(\nu_{s2}\nu_{i3} - \nu_{s3}\nu_{i2})} \\ c &= \frac{6D\nu_{s2}\nu_{i2}}{\varepsilon f_d S(\nu_{s2}\nu_{i3} - \nu_{s3}\nu_{i2})} - 1 \end{aligned} \tag{8}$$

Once M is determined, the sample fission rate F is given by:

$$F = \frac{\left[\dfrac{2D}{\varepsilon f_d} - \dfrac{M(M-1)\nu_{i2}S}{\nu_{i1} - 1}\right]}{\varepsilon M^2 \nu_{s2}}. \tag{9}$$

The effective ^{240}Pu mass (in grams) is obtained from

$$m_{240} = \frac{F}{473.5} \tag{10}$$

And the oxide α is given by

$$\alpha = \frac{S}{F\varepsilon\nu_{s1}M} - 1. \tag{11}$$

As an example (for illustrative purposes only: some of the values chosen here are not necessarily accurate) we will take the data for the 60 g oxide sample given in Table 3. Using Eq. 5 with $G = 32$ μs and $\tau = 47$ μs and $P = 3$ μs gives a doubles fraction $f_d = 0.463$; however using $f_d = 0.485$ (with $f_T = f_D^2$) gives a more credible result. If we assume that $M \approx 1$, then we have $a + b + c + 1 = 0$, which gives (for $f_t = f_d^2$):

$$f_d = \frac{3\nu_{s2}T}{D\varepsilon\nu_{s3}}. \tag{12}$$

The resulting cubic equation has one positive root with $M = 1.0000$ as expected. This gives $\alpha = 1.23966$, a reasonable value for oxide scrap. Reference [12] does not

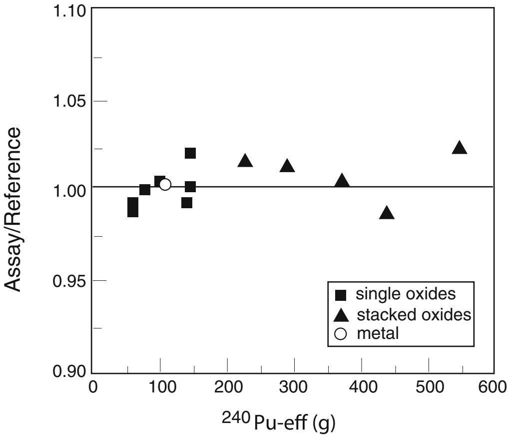

Fig. 3 Multiplicity assay results for for single and stacked plutonium samples using the Large Neutron Multiplicity Counter at Los Alamos. From [13]

give a counting time t_c, but we obtain the result:

$$m_{240}^{\mathrm{eff}} = \frac{29017}{t_c}.$$

Thus if this was a (fairly typical) 1800 s (30 min) count, the effective ^{240}Pu mass would be 16.1 g, or 30.4 % of the total plutonium mass, which represents fairly high burnup.

As a final note, we look at the accuracy of multiplicity counting. Figure 3 shows a set of measurements done on 10 gallon containers at Los Alamos containing either one or two Pu samples, each less than 2 kg and with ^{240}Pu content of around 6 %. One can see that overall variation in the assay value of the ^{240}Pu is less than 3 %, which is impressive because the accuracy of the "book value" of the plutonium is on the order of a few percent as well.

3 Pu300, Pu600, and Pu900 Methods

An important aspect of fissile material accountability consists of determining the time which has passed since the chemical separation of plutonium from other isotopes after its production in a reactor. The Pu-300 plutonium age method [4] uses high-resolution gamma spectroscopy to determine the age of a plutonium sample by comparing the intensity of two nearby lines in the gamma-ray energy histogram for a plutonium sample. The method uses the isotope ^{241}Pu, which typically is present in small quantities in all produced plutonium. Figure 4 shows the decay scheme for ^{241}Pu. ^{241}Pu decays to ^{241}Am by beta decay and to ^{237}U by alpha decay with a half-life of 14.35 y. The 432-y ^{241}Am isotope decays to ^{237}Np with branching ratios of 0.00149 % for the production of a 332 keV gamma ray and 0.000496 % for the

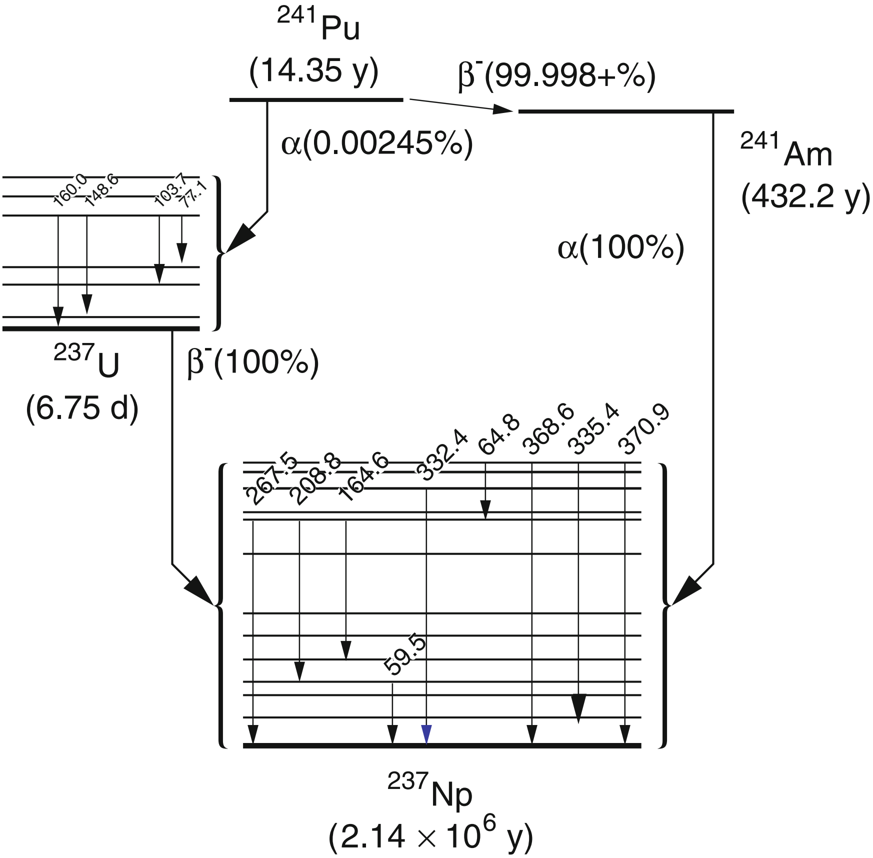

Fig. 4 Decay scheme for ^{241}Am, used for the Pu300 method of plutonium age determination. From [4]

production of a 335 keV gamma ray. Similarly, the 6.75-d ^{237}U isotope decays to ^{237}Np with branching ratios of 1.2 % for the production of a 332 keV gamma ray and 0.095 % for the production of a 335 keV gamma ray. The importance of these particular lines is that they are closely spaced in energy, and self-shielding effects are very similar with this close energy spacing, and thus the intensity ratios can be used to extract the age since separation. Although both isotopes in the decay chain produce the same gamma ray lines, they do so with different branching ratios. We can the give the number of photons produced at 332 and 335 keV as:

$$\begin{aligned} \mathrm{N}_{332} &= \mathrm{a}_1\mathrm{f}_1\lambda_{\mathrm{Pu}}\mathrm{e}^{-\lambda_{\mathrm{Pu}}t} + \mathrm{b}_1\lambda_{\mathrm{Am}}\left(1-\mathrm{e}^{-\lambda_{\mathrm{Pu}}\mathrm{t}}\right) \\ \mathrm{N}_{335} &= \mathrm{a}_2\mathrm{f}_1\lambda_{\mathrm{Pu}}\mathrm{e}^{-\lambda_{\mathrm{Pu}}t} + b_2\lambda_{\mathrm{Am}}\left(1-\mathrm{e}^{-\lambda_{\mathrm{Pu}}t}\right) \end{aligned} \tag{13}$$

with

$$\begin{array}{ll} \lambda_{Pu} = 0.693/14.35 & \lambda_{Am} = 0.693/432.7 \\ a_1 = 0.012 & a_2 = 0.00095 \\ b_1 = 0.0000149 & b_2 = 0.0000496 \\ f_1 = 0.000239. & \end{array} \tag{14}$$

This set of equations then gives an expression for the line pair ratio $r = N_{332}/N_{335}$ as:

$$r = \frac{N_{332}}{N_{335}} = \frac{2.3863\left(1 - e^{-0.0482927t}\right) + 13.85e^{-0.0482927t}}{7.943\left(1 - e^{-0.0482927t}\right) + 1.09648e^{-0.0482927t}}. \tag{15}$$

A plot of this line pair ratio as a function of time is shown as Fig. 5.

This can be converted into an expression for the time since separation t as:

$$t = t_0 \ln\left(k\frac{r_0 - r}{r - r_\infty} + 1\right) \tag{16}$$

where $r = N(332\,\text{keV})/N(335\,\text{keV})$ and

$$t_0 = 1/\lambda_{Pu},\ r_0 = a_1/a_2,\ r_\infty = b_1/b_2,\ k = \frac{a_2 f_1 \lambda_{Pu}}{b_2 \lambda_{Am}} \tag{17}$$

Which gives numerically:

$$t = 20.7071 \ln\left[1 + \frac{0.138208(12.6154 - r)}{r - 0.300403}\right] \tag{18}$$

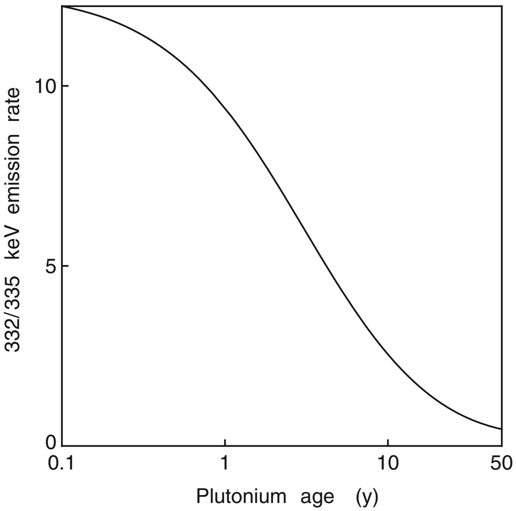

Fig. 5 332.4–335.4 keV intensity ratio for Pu as a function of time since separation

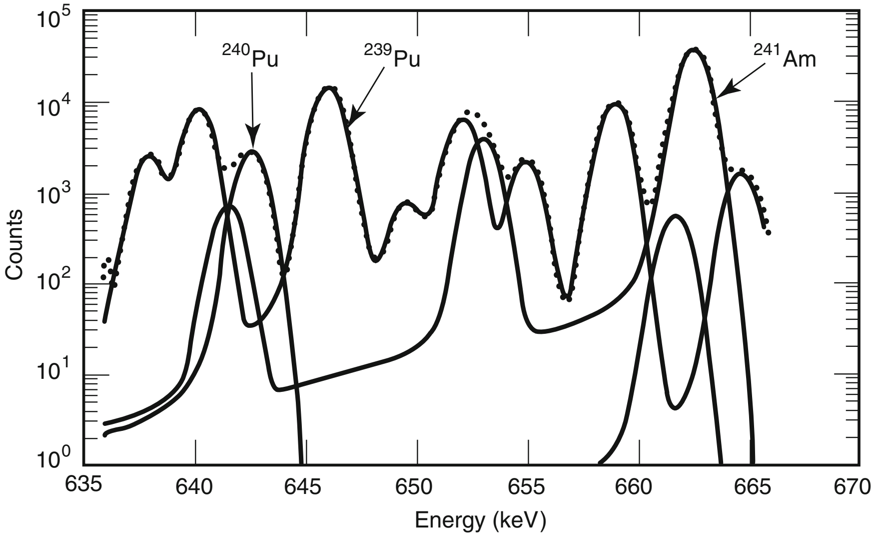

Fig. 6 Gamma ray spectrum for a plutonium sample around 635–670 keV. *Dotted line* shows total counts. From [4]

The Pu600 method similarly uses nearby lines in the 600 keV region of the gamma-ray histogram for Pu isotopic mixtures to determine the isotopic composition. In this case the contributors are ^{239}Pu, ^{240}Pu, and ^{241}Am. In particular, there is a line at 642.5 keV in ^{240}Pu and one at 646.0 keV in ^{239}Pu. A typical spectrum is shown as Fig. 6. Because of the presence of an interfering line from ^{241}Am at 641.5 keV (with a branching ratio of 7.1×10^{-6} %), special analysis is required. Another peak in ^{241}Am at 662.4 keV (branching ratio 3.64×10^{-4}%) has little interference from plutonium gammas, and thus the interfering peak at 641.5 can be subtracted. This leaves a relatively accurate measurement of the ^{239}Pu/^{240}Pu ratio, thus revealing whether or not the sample is weapon-grade (<7 %) plutonium.

The Pu900 analysis uses a gamma ray emitted by de-excitation of ^{17}O from its first excited state at 870.7 keV to determine whether the sample is metal or oxide. This gamma was originally thought to be due to ^{17}O(α, α') inelastic reactions, although further measurements at the Pacific Northwest National Laboratory have shown that the dominant mechanism is actually a reaction on nitrogen: ^{14}N(α, n)^{17}O*, which produces the same gamma. However, the presence of this gamma in large quantities rules out the possibility that the sample is plutonium metal, which is the attribute to be determined. An additional measurement technique to determine the presence of oxide is the measurement of 2438.0 and 2788.8 keV peaks from the ^{18}O(α, n)^{21}Ne reaction. While these peaks are weaker and at higher energies (where high purity Ge detectors have lower efficiency), the measurement of strong peaks at these energies rules out the presence of Pu metal [4].

4 Neutron Imaging

The current strategic arms reduction treaty (START) between the United States and Russia, called "new START" entered into force on February 5, 2011 after ratification by the U.S. Senate and both the Duma and the Federation Council in Russia. It will stay in force for ten years, with a renewal possible after that time. The terms of the agreement allow for ten on-site re-entry vehicle inspections each year at ICBM bases, air bases, and on submarines. The requirements for these inspections, primarily designed to count the number of warheads on a particular (randomly selected) weapon, are to check that number against the declared inventory. For this purpose, there cannot be a cover (such as a nose cone) over the payload package of the weapon, but each independent warhead can be covered to mask design details. This has obviated any current need for more remote warhead-counting schemes such as neutron imaging. Reference [1], an assessment of technologies for re-entry vehicle on-site inspections (RVOSIs) conducted by the U.S. Defense Nuclear Agency in 1994 stated that "We found no clear indication that the use of a technology would eliminate intrusiveness or operational impact concerns associated with the visual inspection protocol, and technologies are unlikely to offer cost savings over visual inspections." However, some background on neutron imaging techniques that have been developed is given here for completeness and historical interest.

Reference [11] describes the inspection regime possibilities from a 1987 perspective, and gives a preliminary design for an in-silo neutron radiography system. The INF (Intermediate-Range Nuclear Forces) treaty, ratified in May 1988, allowed for on-site inspections at U.S. and Russian military bases and specifically allowed radiation detection devices to be used in these tests. This was found to be helpful because of the different neutron radiation fields generated depending on the number of warheads. Reference [14] gives a discussion of the deployment of a large polyethylene-moderated ^{3}He detector array (with single output) used in Russia to map the neutron fields surrounding SS-20 (three warheads) and SS-25 (single warhead) missiles. The flux maps generated were clearly distinct. In 1990–1991, several U.S. national laboratories participated in technology demonstrations at the F. E. Warren Air Force Base near Cheyenne, Wyoming. These tests were aimed at warhead counting using remote radiation detection using the Peacekeeper missiles located there, which had as many as ten MIRV warheads each. Reference [24] describes a Livermore-developed system called the Gamma Ray Imaging Spectrometer, using a coded-aperture gamma detector array, similar to the one described in Chap. "Advanced Detection Technologies", mounted in an existing payload package transport truck used at the site. Reference [8] describes a Los Alamos-made detector tested at the site. This detector was constructed with four boron-loaded plastic scintillators (type BC454), each 7.6 cm diameter and 20 cm long, used in a diamond-shaped pattern with a polyethylene neutron collimator. The electronics package would tag events where the front scintillator saw a fast neutron recoil, primarily on hydrogen, with a time-correlated boron neutron capture pulse from one of the other three scintillators. (The detector, originally used for neutron detection in space, is described in [15].) This afforded a ±20° horizontal

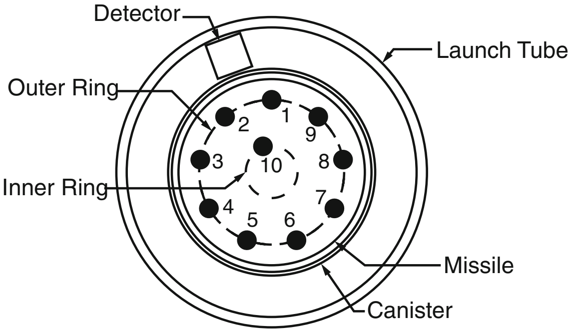

Fig. 7 Peacekeeper missile payload layout and detector geometry for LASL measurements. From [8]

and ±50° vertical sensitivity. The detector was transported around the perimeter of the missile at the height of the warheads. The test geometry is shown in Fig. 7. The Peacekeeper missile warhead placement had nine of ten warheads in an outer circle, with a tenth one closer to center. The tests performed by LASL showed a clear variation in neutron signal (variation of approximately a factor of two) for the outer nine warheads, but failed to pick up the tenth warhead farther inside the missile payload. Reference [17] provides some additional historical perspective on these tests.

Since that time, other neutron imaging systems have emerged. An excellent example of current imaging capability is given in [19]. Here four Eljen EJ301 scintillators were arranged in a plane, and another seven were placed 45 cm behind. Energy deposition in the first set of detectors was recorded, and that information was combined with time-of-flight information from a coincident signal in the rear set. From that a back-projection cone could be constructed, similar to the case of Compton imaging described in Chap. "Advanced Detection Technologies". The combination of many such cones then yields an image. In these tests, a ^{252}Cf source could be properly imaged at 30 m standoff distance, and the source could be imaged through the walls of a seagoing ocean tanker. Angular resolution of order ±10° was obtained.

Coded aperture techniques have also been explored for neutron imaging. Reference [16] describes a system fabricated at Oak Ridge National Laboratory for imaging of fast neutrons. The system used a polyethylene mask for neutron scattering and included a lead shield for gamma attenuation. It showed an angular resolution of about one degree, and could easily identify configurations of mixed oxide fuel pin segments from several meters away, even with concrete-block shielding. The system was also tested in an active-interrogation mode to detect ^{235}U with a neutron generator in a pulsed mode, using the die-away portion of the signal following each pulse. Similarly, a thermal neutron imager was developed at Brookhaven National Laboratory [23], using a cadmium mask. In this study, photoneutrons generated from an accelerator were used to expose a depleted uranium target, and the delayed-fission neutrons were detected after thermalization in a two-dimensional ^{3}He-filled wire chamber.

A good review of the full gamut of image-based warhead counting methods is given in [20]. The authors make the point that all of these systems are very intrusive, and can reveal too much information about the weapons under inspection without sufficient information barriers. The authors recommend that should any of these systems be developed further, the information barrier and image reconstruction algorithms should be developed together rather than separately.

5 Neutrino Methods

Verification of the total number of fissions produced at a nuclear reactor is paramount in determining if the spent nuclear fuel has been properly accounted for. One method available to do this is by looking at the total number of anti-neutrinos produced by the reactor, produced by beta decay of fission product nuclei. At typical reactor power levels (gigawatts thermal), about 10^{21} anti-neutrinos per second are produced. A typical neutrino production reaction would be, for example [2]:

$$^{86}_{35}\mathrm{Br} \rightarrow ^{86}_{36}\mathrm{Kr} + \bar{\nu} + \mathrm{e}^{-} \qquad \mathrm{Q} = 7.626\ \mathrm{MeV} \tag{19}$$

This fission product is produced cumulatively in 1.8 % of all thermal-neutron induced fissions in ^{235}U, and has a 55.1 s half-life. Generally the energy released in beta decay is split between the neutrino and the electron with 30–40 % going to the electron and the remainder to the antineutrino. Typically one fission produces a total of 12 MeV in neutrino energy in the beta decay products, most of which are in isotopes with half-lives shorter than a few hours, so that the neutrino signal tracks the reactor power level fairly closely.

The most common method of detecting antineutrinos is to use the inverse beta decay process on hydrogen:

$$\bar{\nu}_{\mathrm{e}} + \mathrm{p} \rightarrow \mathrm{n} + \mathrm{e}^{+}. \tag{20}$$

This reaction has a threshold of about 1.81 MeV. The cross section is given by [10]:

$$\sigma(\mathrm{E}_{\bar{\nu}}) = 8.85 \times 10^{-44}(\mathrm{E}_{\bar{\nu}} - (\mathrm{m_n} - \mathrm{m_p}))((\mathrm{E}_{\bar{\nu}} - (\mathrm{m_n} - \mathrm{m_p}))^2 - \mathrm{m_e^2})^{1/2}\ \mathrm{cm}^2, \tag{21}$$

where the masses and the neutrino energy are in MeV. It is useful to plot the product of this cross section multiplied by the energy spectrum of the antineutrinos produced in fission in ^{235}U and ^{239}Pu, and this is shown in Fig. 8. The integrated cross sections are 6.38×10^{-43} cm^2 for ^{235}U and 4.18×10^{-43} cm^2 for ^{239}Pu. Thus an interaction rate for antineutrinos in a (say, water, molecular weight = 18, two protons) detector located a distance R away from the reactor running at a power level P with a mass m of water can be calculated as:

$$\dot{\mathrm{N}} = \frac{\mathrm{P}}{\mathrm{E_f}} \cdot \frac{2\mathrm{mN_A}}{18} \cdot \frac{\sigma}{4\pi \mathrm{R}^2}. \tag{22}$$

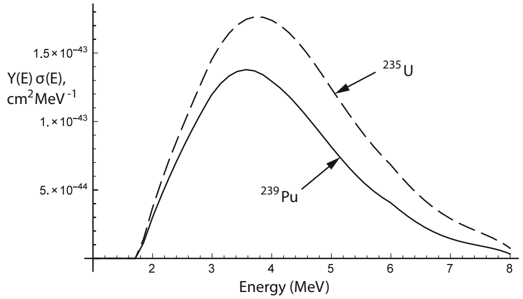

Fig. 8 p($\bar{\nu}$, e$^+$)n cross section multiplied by neutrino yield per MeV per fission in ^{235}U and ^{239}Pu. Data from [10]

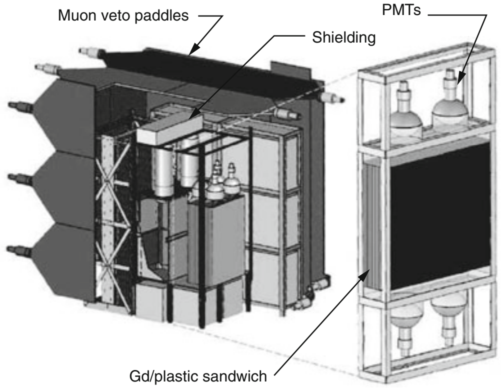

Fig. 9 Neutrino detector deployed at the San Onofre Nuclear Generating Station. From [21]

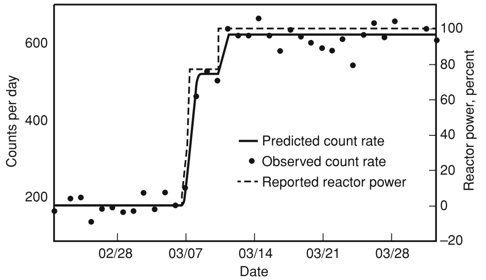

Fig. 10 Neutrino counts per day at the SONGS site. From [22]

A prototype 1000 kg liquid scintillator detector was developed by Livermore and Sandia and was deployed at the San Onofre Nuclear Generating Station (SONGS) in 2003 [22]. This detector is shown as Fig. 9. With a 25 m standoff from the reactor core, this gives about 4000 antineutrino interactions per day for fresh fuel (no initial ^{239}Pu inventory). The performance of this detector is shown in Fig. 10. As one can see from the figure, about 400 excess anti-neutrino events were seen each day when the reactor was at full power, showing about a 10 % efficiency.

The physics processes in this detector include independent and time-correlated measurement of the produced positron and the neutron shown in Eq. 20. The positron undergoes almost immediate annihilation and thus the production of two 511 keV gamma rays; these result in a fast light pulse in the photomultiplier tubes coupled to the scintillator. The neutron coming out of this reaction would thermalize and then interact with a gadolinium dopant added to the liquid scintillator at 0.1 % concentration. The thermal neutron would be absorbed in the Gd (with a 49,000 barn cross section at thermal energies), which would produce about 9 MeV in photons from the (n, γ) reactions. This second light pulse would typically occur some tens of microseconds after the positron annihilation event, and the coincident light pulses with the correct timing signature would form the counts. A competing signal masquerading as a true antineutrino reaction is formed by cosmic-ray muons, however. These events could be minimized by placing the detector underground (with about 10 m of equivalent earth covering) and by providing an anti-coincidence signal from a set of scintillators surrounding the central detectors, called the "muon veto paddles".

The efficiency reduction from 100 % is due in part to the addition of the Gd activator, which lowers the optical transparency of the scintillator medium, and to light coupling efficiency related to the scintillators and the coupling to the photomultiplier tubes, given the index of refraction of the scintillating fluid. While the experiment was concluded to be a success, other issues may prevent this system from being practical. First, the distance from the reactor is critical because of the inverse-square law involved. Fortunately for the SONGS detector, a convenient location was available near the reactor core: this was the "tendon gallery" at the bottom of the containment structure and underground, where the steel cables for the confinement structure are tethered in a way that they can be inspected. (The underground feature helps a great deal with the muon problem.) Not all reactors have this feature, nor will all nuclear reactor facilities be compliant with letting a team of international inspectors set up there. Second, the organic scintillator chosen had a low flash point and might be considered as a dangerous addition to a nuclear reactor facility because of flammability issues. (Consider asking a utility company to tolerate a tonne of flammable liquid 25 m from the reactor!) Third, some knowledge is required about the composition of the initial fuel, the core parameters for calculating ^{239}Pu infill, and other issues.

To address some of these issues, Livermore and Sandia built a second-generation prototype which they called the SONGS-2 detector [21]. It was similar in size but used a solid plastic scintillator medium, undoped, but interleaved in 2 cm sheets with a set of Mylar sheets which have been painted with a 1.0 mm thickness of a Gd paint. The undoped plastic scintillator sheets were then coupled to the photomultiplier tubes. This lowered the light self-attenuation in the scintillator medium, and the segregated Gd-painted areas would produce neutron capture gammas with enough energy to have access to the plastic scintillator. This design was somewhat successful. A third prototype was built, and this time a water-based scintillator was used with Gd doping. This design had a lower manufacturing cost as a feature, but the problem of lower light output emerged, because water interacts with electrons from gamma scattering only through the Cerenkov effect (where electrons with a speed greater than c/n, where n is the index of refraction, create light). This process is about 100 times less efficient than the light production in a plastic or liquid organic scintillator, but nevertheless would lend itself to much larger detectors at greater standoff range.

Unfortunately, The SONGS experiments ended in January 2012 due to the closure of both reactors active on the site until this time.

Other antineutrino detectors have been developed around the world. The Nucifer Reactor Neutrino Monitor has been assembled at the CEA-Saclay laboratory in France and has been operating since 2012 [5]. It uses a 0.8 m^3 volume organic scintillator doped with 0.2 % Gd with plastic scintillator muon veto, similar to the SONGS-2 design. It is located 7 m from the 70 MW Saclay research reactor. The observed neutrino rate is 276 ± 14 events per day. The use of this detector with the smaller research reactor is noteworthy, because this class of reactor probably forms a bigger proliferation threat than the large power reactors. It is also worth noting some earlier neutrino experiments done by a Russian team working at the Rovno nuclear power plant in what is now Ukraine between 1983 and 1991 [18]. Their detector was a large volume of distilled water with an array of sixteen ^{3}He tubes. The inverse beta decay reaction on hydrogen produced fast neutrons which thermalized in the water. Background subtraction was done using data during reactor refueling periods.

5.1 Reactor Antineutrino Detection Time Dependence

Over time a fraction of the fission power in LEU-fueled reactors is due to ^{239}Pu because it is bred by the fertile conversion of ^{238}U. A small quantity of other isotopes are also produced, in particular ^{241}Pu, which also has a thermal fission cross section. There are also fast fissions in the ^{238}U, which is the majority component in LEU fuel. Over time the antineutrino interactions are somewhat fewer, as the plutonium antineutrino integrated cross section is about 66 % of the uranium antineutrino integrated cross section. The relevant energy-averaged cross sections for antineutrino detection using the inverse beta reaction on protons is shown in Table 4, along with the energy produced per fission reaction in the relevant isotopes. If the initial distribution of isotopes in the reactor fuel is known, then one can simulate the relative rate of neutrino detection as a function of time, and consequently of the burnup in the core. A simple set of rate equations can be set up of the form

$$\frac{\mathrm{dn_i}}{\mathrm{dt}} = -\mathrm{n_i}(\sigma_\mathrm{f}^\mathrm{i} + \sigma_\mathrm{c}^\mathrm{i}) + \mathrm{n_{i-1}}\sigma_\mathrm{c}^\mathrm{i-1}, \tag{23}$$

Table 4 Data for calculation of antineutrino detection from a reactor using the inverse beta decay reaction

Isotope	Energy-Averaged cross section per fission (10^{-43} cm^2)	Energy release per fission (MeV)
^{235}U	6.38	201.7 ± 0.6
^{239}Pu	4.18	210 ± 0.9
^{238}U	8.89	205.0 ± 0.9
^{241}Pu	5.76	212.4 ± 1.0

Data from [6]

where the subscripts “f” and “c” stand for fission and capture, respectively. The reactor power is then proportional to $\sum \sigma_{\mathrm{f}}^{\mathrm{i}} \mathrm{E}_{\mathrm{f}}^{\mathrm{i}} \mathrm{n}_{\mathrm{i}}$. The antineutrino detection rate per unit power can then be calculated from

$$\dot{\mathrm{N}}_{\bar{\nu}_{\mathrm{e}}} \propto \frac{\sum \sigma_{\bar{\nu}_{\mathrm{e}}}^{i} \sigma_{\mathrm{f}}^{\mathrm{i}} \mathrm{n}_{\mathrm{i}}}{\sum \sigma_{\mathrm{f}}^{\mathrm{i}} \mathrm{E}_{\mathrm{f}}^{\mathrm{i}} \mathrm{n}_{\mathrm{i}}}. \tag{24}$$

As an example, a simulation of the antineutrino output for a US-made pressurized water reactor (PWR) is shown here as Fig. 11. Here the initial fuel load was taken to be 3.5 % enriched in ^{235}U with the balance as ^{238}U. The cross sections must be averaged over the neutron energy spectrum for the particular reactor type. Reference [9] contains a full set of appropriately averaged cross sections for a US-made PWR.

The coupled rate equations given in Eq. 23 can be solved in an analytic closed form. The relative neutrino detection rate can then be calculated using Eq. 24. If the total fission power is integrated over time, one can also switch from time as a variable in the antineutrino observation rate to burnup in its usual unit of megawatt-days per tonne of heavy metal (MWd/THM). One can see the individual contributions to the neutrino signal in Fig. 11 as well as the total. At medium burnup, say 20,000 MWd/THM, the relative antineutrino rate has dropped about 10 %. The accuracy, of course, depends on knowledge of the actual initial enrichment and whether there are initial Np or Pu isotopes in the “clean” fuel. It also depends on the flux distribution in the reactor, the practices used for fuel shuffle, and some other variables, but a fairly

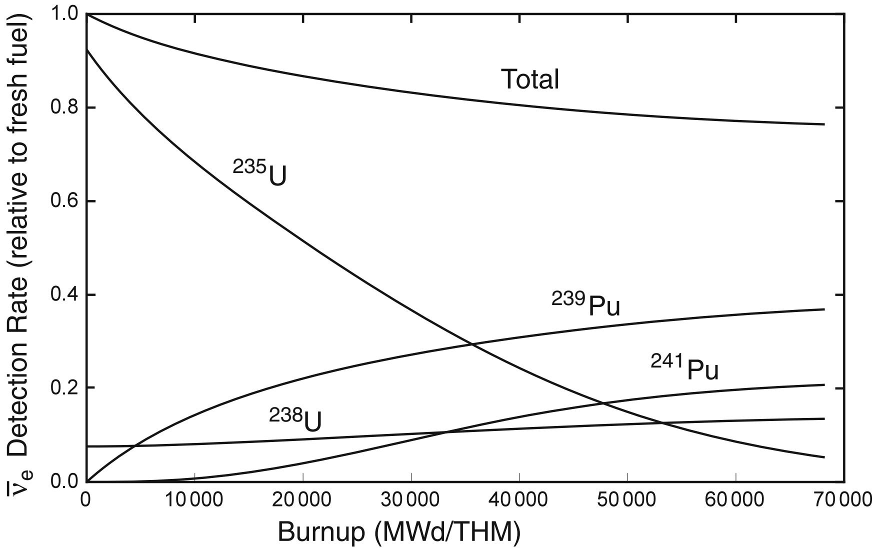

Fig. 11 Simulation of neutrino detection rate as a function of burnup for a U.S.-made pressurized water reactor. Cross section data from [9]

strong case can be made that diversion of significant quantities of fissile material can be ruled out by antineutrino monitoring if the reactor core constituents are well known.

6 Concluding Remarks

A wide variety of analytical techniques have been developed specifically for various arms control and treaty verification regimes. The shifting goals and requirements for arms control and treaty verification have resulted in some of these technological approaches becoming little more than of historical interest, while other technologies have become routine and adopted by other countries. The continued development of neutrino detectors is an example of the latter. If these can be made cheaply, reliably, and tamper-proof, this may lead to an IAEA standard for deployment at all power reactors and research reactors in all NPT countries.

Detection methods for arms control and treaty verification must be made non-intrusive and contain provably robust information barriers. When one sees the information available from multiplicity counting and the Pu300, Pu600, and Pu900 methods, it becomes more clear as to why the new START treaty adopted an open nose cone inspection regime.

7 Problems

1. Download and read http://www.lanl.gov/orgs/n/n1/FMTTD/neut_mc/pdfs/LA_13422_M.pdf. Use the data in Table 5.8 in this document to obtain moments f_1, f_2, b_1, b_2 from the data. Use the factorial moments for Pu spontaneous fission and induced fission from the data in Table 5.8. Use the expressions in Eq. 3 in this chapter to obtain the singles, doubles, and triples rates. Then use Eqs. 10 and 11 in this chapter to obtain the ^{240}Pu mass and the oxide (n, α) coefficient α. Assume an 1800 s counting time and a 56 % efficient detector.
2. A Pu sample is analyzed and the following gamma ray counts are obtained: 332 keV: 75,100; 335 keV: 68,500.
   a. Using the Pu300 method, estimate the age of the sample, i.e. time since separation.
   b. Find the $2 - \sigma$ uncertainty in that age.

References

1. Abe MC (1994) Reentry vehicle on-site inspection technology study. Technical Report, DNA-TR-94-22. http://www.dtic.mil/dtic/tr/fulltext/u2/a285960.pdf
2. Aleklett K, Nyman G, Rudstam G (1975) Beta-decay properties of strongly neutron-rich nuclei. Nucl Phys A 246(2):425–444. doi:10.1016/0375-9474(75)90657-0. http://www.sciencedirect.com/science/article/pii/0375947475906570
3. Anderson HL, Fermi E, Szilard L (1939) Neutron production and absorption in uranium. Phys Rev 56:284–286. doi:10.1103/PhysRev.56.284
4. Archer D, Gosnell T, Luke J, Nakae L (2001) Pu300, Pu600, and Pu900 systems. In: Technology R&D for arms control. U.S. Department of Energy National Nuclear Security Administration Defense Nuclear Nonproliferation Programs. http://fissilematerials.org/library/doe01b.pdf
5. Bazoma J, Boireau G, Bouvet L, Buck C, Bui V, Collin A, Communeau V, Cormon S, Coulloux G, Cribier M, Cucoanes A, Deschamp H, Dumonteil E, Durand V, Fallot M, Fechner M, Fischer V, Gaffiot J, Gautier M, Giot L, Guillon B, Guilloux G, Granelli R, Haser J, Kato Y, Lasserre T, Latron L, Legou P, Lenoir M, Letourneau A, Lhuillier D, Lindner M, Martino J, Mention G, Mercier G, Mueller T, Nghiem TA, Onillon A, Pedrol N, Pelzer J, Pequignot M, Piret Y, Pleurel N, Porta A, Prono G, Scola L, Starzinski P, Varignon C, Vilajosana T, Vivier M, Yermia F (2014) The Nucifer reactor neutrino monitor. In: IAEA Safeguards Symposium. https://www.iaea.org/safeguards/symposium/2014/home/eproceedings/sg2014-papers/000011.pdf
6. Bernstein A, Baldwin G, Boyer B, Goodman M, Learned J, Lund J, Reyna D, Svoboda R (2010) Nuclear security applications of antineutrino detectors: Current capabilities and future prospects. Sci Global Secur 18:3. doi:10.1080/08929882.2010.529785
7. Böhnel K (1985) The effect of multiplication on the quantitative determination of spontaneously fissioning isotopes by neutron correlation analysis. Nucl Sci Eng 90(1). doi:10.13182/NSE85-2
8. Byrd R, Auchampaugh G, Moss C, Feldman W (1991) Warhead counting using neutron scintillators: detector development, testing, and demonstration. In: Conference Record of the 1991 IEEE Nuclear Science Symposium and Medical Imaging Conference, pp 1305–1309, vol 2. doi:10.1109/NSSMIC.1991.259136
9. Croff AG, Bjerke MA, Morrison GW, Petrie LM (1978) Revised uranium-plutonium cycle PWR and BWR models for the ORIGEN computer code. Oak Ridge National Laboratory. doi:10.2172/6787757. http://www.osti.gov/scitech/servlets/purl/6787757
10. Davis BR, Vogel P, Mann FM, Schenter RE (1979) Reactor antineutrino spectra and their application to antineutrino-induced reactions. Phys Rev C 19:2259–2266. doi:10.1103/PhysRevC.19.2259
11. DeVolpi A (1987) Neutron radiographic techniques for nuclear arms control applications. In: Barton JP, Farny G, Person JL, Röttger H (eds) Neutron radiography. Springer, Netherlands, pp 805–807. doi:10.1007/978-94-009-3871-7_99
12. Ensslin N, Krick M, Pickrell M, Reilly D, Stewart J (1991) Passive neutron multiplicity counting. In: Reilly D, Ensslin N, Smith, S Jr, Kreiner S (eds) Passive nondestructive assay of nuclear materials, vol LA-UR-07-1402. U.S. Nuclear Regulatory Commission
13. Ensslin N, Harker WC, Krick MS, Langner DG, Pickrell MM, Stewart JE (1998) Application guide to neutron multiplicity counting. Los Alamos Manual, LA-13422-M. http://permalink.lanl.gov/object/tr?what=info:lanl-repo/lareport/LA-13422-M
14. Ewing RI, Marlow KW (1990) A fast-neutron detector used in verification of the inf treaty. Nucl Instrum Methods Phys Res Sect A: Accel Spectrom Detect Assoc Equip 299(1):559–561. doi:10.1016/0168-9002(90)90843-U. http://www.sciencedirect.com/science/article/pii/016890029090843U
15. Feldman W, Auchampaugh G, Byrd R (1991) A novel fast-neutron detector for space applications. Nucl Instrum Methods Phys Res Sect A: Accel Spectrom Detect Assoc Equip 306(1–2):350–365. doi:10.1016/0168-9002(91)90342-N. http://www.sciencedirect.com/science/article/pii/016890029190342N

16. Hausladen P, Blackston M (2009) Passive and active fast-neutron imaging in support of AFCI safeguards campaign. Oak Ridge National Laboratory Technical Report, ORNL/TM-2009/210. http://info.ornl.gov/sites/publications/files/Pub21226.pdf
17. Johnson M, Doyle JE, Murphy C (2011) Recovering START institutional knowledge. Los Alamos National Laboratory Unclaasified Report, LA-UR-11-03284. http://permalink.lanl.gov/object/tr?what=info:lanl-repo/lareport/LA-UR-11-03284
18. Kuvshinnikov A, Mikaelyan L, Nikolaev S, Skorokhvatov M, Etenko A (1991) Measuring the $\bar{\nu}_e + p \rightarrow n + e^+$ cross-section and beta decay axial constant in a new experiment at Rovno NPP reactor. JETP Lett 54:253–257
19. Mascarenhas N, Brennan J, Krenz K, Marleau P, Mrowka S (2009) Results with the neutron scatter camera. IEEE Trans Nucl Sci 56(3):1269–1273. doi:10.1109/TNS.2009.2016659
20. McDonald B, Seifert A, White T, Robinson S, Miller E, Jarman K, Misner A, Pitts WK (2011) Image-based verification: Some advantages, challenges, and algorithm-driven requirements. PNNL Report, PNNL-SA-80551. https://www.nti.org/media/pdfs/McDonaldetal2011_Image-based_Verif_Some_Adv_Chall_Algdriven_reqs.pdf?_=1439478341
21. Meissner C (2008) Antineutrino detectors improve reactor safeguards. Sci Technol Rev. https://str.llnl.gov/str/JulAug08/pdfs/07.08.4.pdf
22. Parker A (2006) Monitoring nuclear reactors with antineutrinos. Sci Technol Rev. https://str.llnl.gov/str/JanFeb06/pdfs/01_06.4.pdf
23. Vanier PE, Forman L, Norman DR (2009) Thermal neutron imaging in an active interrogation environment. Brookhaven National Laboratory Technical report, BNL-90269-2009-CP. https://www.bnl.gov/isd/documents/70294.pdf
24. Ziock K, Hailey C, Gosnell T, Lupton J, Harrison F (1992) A gamma-ray imager for arms control. IEEE Trans Nucl Sci 39(4):1046–1050. doi:10.1109/23.159757

Public Policy and Proliferation

Abstract The structure of international, national, and non-governmental agencies that participate in the worldwide activity to control nuclear proliferation is discussed here. The International Atomic Energy Agency (IAEA) is described from the standpoints of its organization, reporting functions, the treaties behind its functions, and the technical support that it provides. Its role in safeguards and verification, upholding the standards of the Additional Protocol, and promoting peaceful uses of nuclear energy are detailed. Next, the organizations within the US government involved in nuclear proliferation are discussed: these include the Departments of Homeland Security, Energy, State, and Justice. The US Intelligence Community, with its seventeen individual branches is discussed. The nonproliferation-relevant activities in the US Nuclear Regulatory Commission are also outlined. Next the role of non-governmental organizations (NGOs) is discussed. Their activities include promoting international peace and security, publicizing nuclear construction and service activities, and providing guidance and advocacy on export control issues related to nuclear proliferation.

1 Introduction

This chapter outlines the basic mechanisms and structures by which the world's nuclear "haves" and "have-nots" communicate with each other and develop policies and treaties. It also serves to introduce readers contemplating a career in nonproliferation, arms control, and treaty verification to the institutions and projects where they might find a job someday.

2 The International Atomic Energy Agency (IAEA)

The IAEA was established on 29 July 1957 as an independent organization. It reports to the United Nations General Assembly and Security Council. Its purpose is to promote the peaceful uses of nuclear energy and to prevent the development and use

E.C. Morse, *Analytical Methods for Nonproliferation*, Advanced Sciences
and Technologies for Security Applications, DOI 10.1007/978-3-319-29731-6_11

of nuclear weapons. The original headquarters were in Geneva, Switzerland, but since 1979 the IAEA has been headquartered in Vienna, Austria. Operational liaison offices are located in Geneva, Switzerland, and New York. Regional offices are located in Toronto, Canada, and Tokyo, Japan. Four main technical thrust areas for the IAEA are Nuclear Energy, Nuclear Safety and Security, Nuclear Sciences and Applications, and Safeguards and Verification. These technical areas also support the policy-making bodies of the IAEA known as the General Conference and the Board of Governors. The agency's Secretariat has approximately 2,300 scientific, technical, and administrative personnel overall, representing over 100 countries. Nuclear engineers, nuclear physicists, and safeguards inspectors make up the largest professional group in the agency. Almost all other types of scientists are involved as well, along with lawyers, computer experts, and other professionals. Most professional appointments are limited to 5 years and never more than 7 years. This relatively high-turnover environment is intended to keep a fresh flow of ideas into the agency, and it forms an ideal environment for early-career professionals.

2.1 Verification and Safeguards

Article III of the Nonproliferation Treaty (NPT, see Appendix A) calls out "comprehensive safeguard agreements". These give IAEA the authority to verify that the description of nuclear material and nuclear-related activities is complete and accurate. Currently there are such agreements for 174 of the 182 NPT member states [1]. Verification activities can include on-site inspections, evaluations, visits, installation of seals, and remote surveillance with cameras. IAEA does the accounting for all "source and special fissionable material" usable for producing nuclear weapons, specifically ^{233}U, ^{235}U, and ^{239}Pu.

Safeguards activities include the following: Nuclear material accountancy consists of a conventional audit of the materials from a record-keeping viewpoint. Design information verification consists of determining whether or not a facility's technical design is consistent with its stated use and that use for other purposes has not been attempted. Environmental sampling can detect trace quantities of isotopes of interest (particularly ^{233}U, ^{235}U, and ^{239}Pu), and analysis can determine whether or not highly enriched U or weapons-grade Pu have been present at the facility. Material accountability is determined by counting, weighing and performing certain non-destructive assay tests, such as radiation detection, on the material. In some cases destructive analysis techniques are used on small samples. Containment and surveillance technologies such as cameras and seals can be installed at a facility to detect unauthorized access or undeclared operation. To date almost 300 remote surveillance systems, with the ability to communicate directly with IAEA headquarters, have been installed at nuclear facilities.

2.2 Additional Protocol

The original safeguard agreements contained in Article III of the NPT have been found to be less than fully effective in some cases. The rules by which IAEA inspectors could gain access to sites were structured such that material could be relocated before visits could occur. Also, some activities such as nuclear research and development, import/export traffic, and U and Th production were not adequately addressed. The Additional Protocol program was designed to cut access time to as little as two hours and called for automatic visa renewals for inspectors. Not only do current stockpiles of U and Th have to be reported, but total production of these materials, whether or not they have been traded outside the country, must be disclosed.

As of July 2015 there have been 146 Additional Protocols signed and 126 are in force [2]. While the Additional Protocols have greatly increased the reporting requirements for the member states, they have resulted in more transparency in accounting for any activity even only loosely coupled to nuclear weapon production.

2.3 Peaceful Uses of Nuclear Energy

Article IV of the NPT gives IAEA the responsibility to promote the development of peaceful uses for nuclear energy, especially in developing countries. The IAEA gives the member states the right to exchange equipment, materials, and information toward this end. The IAEA publishes a vast amount of technical and scientific material pertaining to nuclear energy in general. IAEA divides this effort among three major divisions: Nuclear Energy, Nuclear Safety and Security, and Nuclear Sciences and Applications.

3 Nuclear Nonproliferation Activities Within the US Government

In 2010, the US government announced an inter-agency plan called the Global Nuclear Detection Architecture (GNDA). The participants in this plan include the Department of Homeland Security (DHS), the Department of Defense (DOD), the Department of Energy (DOE), the State Department, the Department iof Justice (DOJ), the Intelligence Community (IC), and the Nuclear Regulatory Commission (NRC). Consolidating and coordinating nonproliferation efforts across such a broad range of government interests has been a daunting task, but this type of collaboration is absolutely necessary.

3.1 DHS: The Domestic Nuclear Detection Office (DNDO)

DNDO is the lead agency for domestic nuclear detection as it relates to the threat of nuclear terrorism and illicit trafficking of nuclear material. DNDO partners with international, federal, state, local, tribal, and private sector entities to fulfill this mission. DNDO also has custody of the nuclear forensics program in the US, in partnership with the National Nuclear Security Administration (NNSA) arm of DOE. The forensics effort also has links to the US Federal Bureau of Investigation (FBI), the DOD (especially the Defense Threat Reduction Agency (DTRA)), the State Department, and the Office of the Director of National Intelligence. DNDO's support of new technologies, such as ^{3}He alternatives and advanced solid state and scintillator detectors have been described in Chap. "Arms Control and Treaty Verification".

DNDO has also partnered with the European Commission, through its Joint Research Center, in a 3 year program (from 2010 to 2013) to characterize nine different detection systems. This effort, known as the Illicit Trafficking Radioactive Assessment Program+10 (ITRAP+10), compared nearly 100 instruments available on the commercial market. The results of these tests will be shared with the international community along with U.S. agencies at the federal, state, and local levels.

DNDO also has trained more than 8,500 US federal, state, and local officers and first responders in radiation detection. DNDO also has administered an Academic Research Initiative (ARI) program which has supported hundreds of undergraduate and graduate students interested in professional development for a future workforce in the area of nuclear security.

Also, DNDO launched a program under the aegis of the Global Initiative to Combat Nuclear Terrorism, or GICNT, which is carried out within the GICNT Nuclear Detection Working Group (NDWG). This effort is comprised of 82 countries working together. This resulted in a coordinating meeting in Marrakech, Morocco for a 1 year activity which led to a third volume of a series entitled "Guidelines for Planning and Organization", which was approved at the GICNT meeting in 2013.

3.2 DNDO Nuclear Forensics Efforts

A document entitled Nuclear Security Summit Communiqué and Work Plan was generated in 2010 which has become a blueprint for international collaboration to strengthen nuclear security. One of the focus areas in this plan was to develop nuclear forensic methods to trace the origin of interdicted nuclear materials, help identify smuggling networks, and aid in prosecution of illicit trafficking. The program also aims at identifying weaknesses in security measures in place to detect clandestine nuclear and radiological material. DNDO is also committed to training exercises related to nuclear forensics for scientists as well as law enforcement personnel, including crime scene management. Tabletop exercises have been held in 15 member nations in the GICNT.

DNDO has provided expertise to the IAEA and interagency US partners to develop databases for national nuclear forensics libraries. These databases help countries determine whether radioactive material outside of regulatory control are consistent with material being held inside their regulatory control, i.e. to determine whether interdicted material was in transit from another country or if it might have been the result of theft within the country.

DNDO has also supported the development of a common language, or lexicon, for standardization of terms related to nuclear and radiological material in order to enable more precise communication among its international partners regarding these materials. It is hoped that tightening the language being used in nuclear interdiction cases will bring confidence in international collaboration relating to policing in these matters.

DNDO also supports an educational program entitled the National Nuclear Forensics Expertise Development Program for support of graduate and post-graduate students at universities, along with junior faculty awards and undergraduate mentoring activities.

3.3 National Nuclear Security Administration (NNSA)

The NNSA is charged with stewardship of the nuclear weapon stockpile for the United States. The nuclear weapons laboratories, including Lawrence Livermore National Laboratory, the Los Alamos National Scientific Laboratory, and Sandia National Laboratory are directly under the control of the NNSA, and NNSA supports activities at other Department of Energy laboratories including Pacific Northwest National Laboratory, Idaho National Laboratory, Brookhaven National Laboratory, Oak Ridge National Laboratory, and Argonne National Laboratory. The NNSA has an Office of Defense Nuclear Nonproliferation which interacts with many other national and international partners on a wide range of issues relating to nuclear nonproliferation. The NNSA has the primary responsibility for handling and disposal of nuclear and radiological material within the US, as well as various other WMD materials.

The Nuclear Nonproliferation Program is divided into six offices, including the Office of Global Threat Reduction, the Office of Nonproliferation Research and Development, The Office of Nonproliferation and International Security, the Office of International Material Protection and Cooperation, the Office of Fissile Material Disposition, and the Office of International Operations.

The Office of Global Threat Reduction is charged with securing nuclear and radiological materials worldwide and reducing the quantity of these materials where possible. A system called Materials Protection, Control and Accounting has been put in place and has now been applied to almost all Russian nuclear material and warhead sites. Of particular interest in this regard is the facility at Mayak, which is the largest and longest running part of the Russian nuclear production effort. The new storage facility was developed in a joint US-Russian effort. This facility has been used for downblending weapon-grade uranium for use as nuclear fuel as well as the dismantling of plutonium weapon components. The Office has also been involved with the conversion of 57 reactors in 32 countries from HEU to LEU fuel. This has resulted in the return of 765 kg of HEU to Russia and over 1,200 kg of HEU to the US. There also has been a program to secure buildings with nuclear and radiological materials, and 545 buildings worldwide of this nature have been secured. Additionally, over 29,000 US radiological sources have been recovered by NNSA through this Office.

The Office of Nonproliferation Research and Development has been at the forefront of the advanced radiation detection equipment described in Chaps. "Advanced Detection Technologies" and "Arms Control and Treaty Verification". This Office has also been responsible for the development of enhanced ground and space based systems for the detection of nuclear explosions.

The Office of Nonproliferation and International Security is charged with ensuring transparency in nuclear weapon reduction efforts, strengthening nuclear safeguards, and developing protection and export control for other countries possessing nuclear material. It is also tasked with transitioning nuclear weapon design expertise and infrastructure to peaceful efforts in international partner countries, and improving interaction and cooperation in nuclear weapon states towards this end. Thousands of nuclear weapon scientists in the former Soviet Union, Iraq, and Libya in over 200 facilities have been engaged under this program.

The Office of Fissile Materials Disposition is responsible for the disposition of surplus US weapon grade plutonium and HEU and Russian plutonium by converting this material into mixed-oxide (MOX) fuel for consumption in power reactors. Under this program, over 352 MT of former Soviet weapons HEU has been downblended for use in US power plants. This material, representing the equivalent of 14,000 nuclear weapons, provided more than ten percent of electricity production in the US over more than two decades. Additionally 108 tonnes of US HEU has been downblended (equal to 2,376 nuclear weapons). A program is underway to complete a MOX fuel fabrication facility in the US, with the goal of using this facility to convert 68 MT of US and Russian weapon-grade plutonium to MOX fuel. This Office also gave support to the closure of the weapon-grade plutonium production reactor at Seversk in Russia, thus ending all weapon-grade plutonium in Russia.

3.4 The Department of State

The US Department of State has a Bureau of International Security and Nonproliferation. The Bureau is organized into thirteen offices, ten of which are involved in nuclear nonproliferation issues. These are the Office of Cooperative Threat Reduction, the Office of Counterproliferation Initiatives, the Office of Export Control Cooperation, the Office of Missile, Biological, and Chemical Nonproliferation, the Office of Multilateral Nuclear and Security Affairs, the Office of the Nonproliferation and Disarmament Fund, the Office of Nuclear Energy, Safety, and Security, the Office of Regional Affairs, the Office of Threat Reduction, and the Office of WMD Terrorism.

The Office of Cooperative Threat Reduction is tasked with reducing the risk of WMD threats by states of concern and terrorist groups through diplomatic means. States of concern with US diplomatic channels have included Iraq, Libya, and former Soviet Union nations. Former WMD experts working in these countries have been engaged through this office in order to reduce the risk of their cooperation with terrorist organizations, non-state actors, and proliferant states.

The Office of Counterproliferation Initiatives works at developing counterproliferation initiatives designed to interdict or deny shipments of WMD materials and their delivery systems, and checks compliance with UN Security Council Resolution 1540, as discussed in Chap. "Introduction".

The Office of Export Control Cooperation develops and coordinates export control issues as they pertain to the possibility of nuclear proliferation. This Office manages the export control system and related border security issues. The Office also coordinates export control issues with its international partners, and tries to maintain consistency in export control policies worldwide.

The Office of Missile, Biological, and Chemical Nonproliferation, in addition to its biological and chemical nonproliferation interests, also works to impede the development of missile delivery systems for both nuclear and chemical/biological WMD delivery. They also monitor associated materials and technology for missile development.

The Office of Multilateral Nuclear and Security Affairs is the lead organization for stewardship of a number of international treaties, including the Treaty on the Non-Proliferation of Nuclear Weapons, budgetary and policy support for various IAEA-directed activities including safeguards, nuclear security, and shared technical knowledge, and G-7 and EU nonproliferation and disarmament summit meetings. The Chairman of the interagency Subcommittee on International Safeguards and Monitoring is from this Office. This Office also plays a role in various discussions, within the US government and internationally, on safeguards, nonproliferation, security, and nuclear disarmament.

The Office of Nonproliferation and Disarmament Fund coordinates, evaluates, and executes projects aimed at high-priority, short-timescale activities which have a profound effect on arms control and nonproliferation. Typically the Office has about 35–45 active projects with a total budget of around USD 150 million. Examples of past projects have included the removal of about 100 pounds of HEU fuel from the reactor facility at the Vinca Institute in Belgrade, Serbia and the removal of various nuclear infrastructure items from Libya.

The Office of Nuclear Energy, Safety, and Security is the responsible party within the State Department for coordination of peaceful uses of nuclear energy abroad, with emphasis on export control issues, nuclear safety, and physical protection of the facilities involved. The agency coordinates with Department of Energy and IAEA personnel on issues related to civilian nuclear safety, waste management, and nuclear fuel cycles as they pertain to proliferation risks and dirty bombs. This Office is also involved in carrying out an international program to convert research and test reactors to lower enrichment fuel, and to help with secure repatriation of HEU developed in this way.

The Office of Regional Affairs concentrates on diplomatic responses needed to specific regional nuclear proliferation issues posed by countries such as Iran, North Korea, and Syria. It also develops diplomacy for "nuclear-have" countries such as India, Pakistan, and China.

The Office of Threat Reduction works with international partners to develop coordinated global efforts to reduce the risk of WMD development. Although it focuses on biological threats, it has a charter for nuclear weapons threats as well, through the pathway of its outreach program to domestic and international non-government organizations (NGOs).

The Office of WMD Terrorism is charged with reducing the threat of WMD terrorism through building international partnerships to defend against terrorism. This Office is the charged with diplomatic efforts especially aimed at stopping nuclear smuggling. The Office helps connect US experts in nuclear security, border security, and radiation detection with their international counterparts. It chairs the Nuclear Trafficking Response Group. It works with other agencies on developing expertise in nuclear forensics. It also serves as the US point of contact for the IAEA Incident and Trafficking Database.

3.5 The Department of Defense

The Department of Defense (DoD) set up the Defense Threat Reduction Agency (DTRA) in 1998. It was the continuation and consolidation of several previous nuclear-related agencies within DoD: the Defense Special Weapons Agency (1996–1998), the Defense Nuclear Agency (1971–1996), the Defense Atomic Support Agency (1959–1971), the Armed Forces Special Weapons Project (1947–1959), and the Manhattan Project (1942–1946). It is the Combat Support Agency for all WMD threats, including nuclear. DTRA has the prime military responsibility for minimizing the effect of a domestic nuclear event within the US. It also has the charge to reduce the risk of such an event, and to conduct a research program in support of nuclear threat reduction. It is headquartered in Fort Belvoir, Virginia and has a staff of about 2000 people, and an annual operating budget of about USD 420 million.

Part of DTRA's charter is to assist in the implementation of the Nunn-Lugar Cooperative Threat Reduction (CTR) Program, enacted in 1991. This treaty established the destruction of a large part of the nuclear arsenal in the US as well as the former Soviet Union (FSU). DTRA staff have assisted in the destruction of FSU military equipment in three FSU countries (Ukraine, Belarus, and Kazakhstan). The Nunn-Lugar program has four objectives:

1. Dismantle FSU WMD and associated infrastructure,
2. Consolidate and secure FSU WMD and related technology and materials,
3. Increase transparency and encourage higher standards of conduct, and
4. Support defense and military cooperation with the objective of preventing proliferation.

To date CTR has resulted in the deactivation of 7,616 warheads, 2,531 missiles (ICBMs, SLBMs, and ASMs), 1,187 launchers and silos destroyed, and 33 submarines decommissioned [3].

3.6 The US Department of Justice

The Department of Justice has jurisdiction over the Federal Bureau of Investigation (FBI). Within the FBI, a Weapons of Mass Destruction Directorate (WMDD) was established in 2006, and it was tasked with collecting intelligence related to attempts at developing, importing, or stealing WMD components in the US. In 2011, a National Security Branch was established within the FBI, and the efforts for counterterrorism, counterintelligence, and WMD were combined into one branch with a senior Bureau official presiding. Also included in this branch are activities in counterproliferation and the Terrorist Screening Center. Additionally the Branch includes the High-Value Detainee Interrogation Group, for intelligence gathering for collecting intelligence from key terror suspects.

The FBI is the lead organization in the US for gathering counterintelligence. Since proliferation attempts are often done by international organizations, the FBI partners with agencies with an international charter, which includes the Department of Homeland Security and the Department of Commerce's Office of Export Enforcement. The Export Enforcement Coordination Center, run by the Immigration and Customs Enforcement (ICE) group at DHS, acts as a conduit for information between federal law enforcement and the intelligence community as pertains to potential export control violations. The National Counterproliferation Center, which is managed by the Office of National Intelligence, assists the intelligence community regarding matters of potential nuclear trafficking, and helps with predicting future WMD threats.

3.7 The US Intelligence Community

The US Intelligence Community consists of 17 separate organizations. They are: Air Force Intelligence, Army Intelligence, the Central Intelligence Agency, Coast Guard Intelligence, the Defense Intelligence Agency, the Department of Energy, the Department of Homeland Security, the Department of State, the Department of the Treasury, the Drug Enforcement Administration, the Federal Bureau of Investigation, Marine Corps Intelligence, the National Geospatial-Intelligence Agency, the National Reconnaissance Office, the National Security Agency, Navy Intelligence, and the Office of the Director of National Intelligence. Of these, the Central Intelligence Agency (CIA) has the largest international impact, while the FBI has the largest presence in potential nuclear issues domestically. Whereas the FBI functions both as a law enforcement agency and as an intelligence gathering agency, the CIA's role is purely intelligence gathering internationally, i.e. espionage. The CIA's efforts are complemented by the National Security Agency (NSA), which is largely involved in electronic surveillance and code-breaking. While there has been a view among some that these agencies compete in some cases and fail to share information, in recent years information sharing has been streamlined. The appointment of a Director of National Intelligence has improved the situation since this position was established in 2004. The Director of National Intelligence is responsible for integrating information from all the intelligence sources into the President's Daily Briefing.

3.8 The Nuclear Regulatory Commission (NRC)

The NRC is responsible for controlling all SNM used for commercial and other peaceful purposes. In order to comply with U.S. government non-proliferation commitments, the NRC must engage in various activities outside of its normal function in regulating nuclear reactors from a safety viewpoint. These activities include implementing international safeguards treaties and reviewing import and export licenses. The NRC maintains a Nuclear Materials Management and Safeguards System (NMMSS). It is through this system that domestic nuclear safeguards are applied in conformance with the US's Safeguards Agreement (SA) with IAEA. The NRC also helps provide compliance to the Nuclear Non-Proliferation Treaty (NPT) and the Additional Protocol (AP) to the U.S.-IAEA SA, and places requirements on the U.S. government that the NRC helps to implement. Regulations in the US Code of Federal Regulations (CFR) 10CFR Part 75 and Part 110 contain requirements which help to ensure that the US meets its IAEA nonproliferation requirements as long as the NRC and Agreement State licensees, applicants, and certificate holders comply with the terms of these 10 CFR regulations. Additionally, however, under international safeguard rules, the NRC would be obliged to report the location of all civilian nuclear facilities, give information on the location of source and special nuclear materials, to track and report on imports and exports involving source material, special nuclear material and certain dual-use items, and give access to the civilian nuclear facilities to conduct inspections. However, as a nuclear weapons state under the NPT, the U.S. is not obligated to undergo international safeguards. The U.S. IAEA Safeguards Agreement and the U.S. Additional Protocol are both subject to a national security exclusion. Nonetheless, the US has agreed to all of the reporting conditions and site access conditions given above, except in those cases where the US determines that national security might be jeopardized. (In practice, the IAEA has never visited a US nuclear power plant.)

The NRC also gives technical assistance to the IAEA. The NRC works to enhance international safeguards and verification programs managed by IAEA. The Subgroup on Safeguards Technical Support (SSTS) and other US government organizations that NRC is involved with assist the IAEA in developing the technical capabilities useful for enhancing verification regimes worldwide. The NRC works multilaterally with other US agencies to improve both domestic and international nonproliferation standards.

4 Non-governmental Organizations (NGOs)

4.1 The Center for Export Controls (CEC)—Moscow

The CEC advises exporters of materials, equipment, and services from Russia on possible issues pertaining to the potential use of these products and services for WMD development. The CEC helps exporters set up training programs for development of export controls for dual-use technology. The CEC also advises exporters on setting up internal compliance programs, developing licensing documentation, and issuance of international contracts for dual-use technology.

4.2 The Center for International Trade and Security, University of Georgia (CITS)

The CITS conducts research and does teaching in the area of nuclear security, arms control, nonproliferation, and regional security. It also explores US-Russia and US-India foreign relations. An important focus for the Center's work are evaluations of nonproliferation and arms control issues from the standpoint of export controls. These analyses include National Export Control Focus, U.S. Industry Evaluations, Export Control Regime Evaluations, and an Export Control Database Project. The latter is useful for government, academics, policymakers, and other NGOs.

4.3 The Center for Nonproliferation Studies (CNS)

The CNS is the largest nonproliferation-related NGO in the US, with more than 40 specialists and 70 graduate students. Its headquarters are in Monterey, California and there are also offices in Washington, DC and Almaty, Kazakhstan. The CNS has four major thrust areas: the Chemical and Biological Weapons Nonproliferation Program, the International Organization and Nonproliferation Program, the Newly Independent States Nonproliferation Program, and the East Asia Nonproliferation Program. The CNS publishes two region-specific newsletters based on the last two programs: the NIS Export Control Observer and NIS Asian Export Control Observer.

4.4 The Institute for Science and International Security (ISIS)

The ISIS is committed to providing public information regarding science and public policy issues related to national security. ISIS is focused on export control issues regarding nuclear technology. ISIS tries to assist commercial enterprises which might otherwise become engaged in the exportation of sensitive nuclear-related materials, equipment, or services.

4.5 The Nuclear Threat Initiative (NTI)

The NTI provides public information regarding the nuclear, biological, chemical weapons, and missile programs of a selection of countries. NTI promotes citizen involvement in public policy issues involving WMD proliferation risks.

4.6 The Stimson Center

The Henry L. Stimson Center is a nonprofit, nonpartisan institution concerned with international peace and security. The Export Controls section provides news and information relevant to current WMD-precursor export control issues.

4.7 The Stockholm International Peace Research Institute (SIPRI)

The SIPRI concerns itself with national and multilateral export control issues in Europe. SIPRI offers analysis of national arms export controls, multilateral export control regimes, and international organizations providing support to export control efforts.

4.8 The Wisconsin Project on Nuclear Arms Control

The Wisconsin Project is the developer of The Risk Report. This report provides current unclassified intelligence on worldwide WMD programs. The Project has investigated sales of proliferation-related technology for more than two decades. The

Project has identified thousands of buyers linked to WMD and missile proliferation. By tracking and exposing the movement of weapons and dual-use goods, the Project has been instrumental in changing export control policies worldwide.

References

1. International Atomic Energy Agency: IAEA Safeguards Serving Nuclear Non-Proliferation. IAEA (2015). https://www.iaea.org/sites/default/files/safeguards_web_june_2015.pdf
2. International Atomic Energy Agency: Status of the Additional Protocol. IAEA (2015). https://www.iaea.org/safeguards/safeguards-legal-framework/additional-protocol/status-of-additional-protocol
3. U.S. Department of Defense-Defense Threat Reduction Agency: CTR program measures and Scorecard URL http://www.dtra.mil/Portals/61/Documents/CTR%20Scorecards/Nunn-Lugar%20CTR%20Scorecard%202014.pdf

Appendix A
The Treaty on the Non-proliferation of Nuclear Weapons

Notification of the Entry into Force

1. By letters addressed to the Director General on 5, 6 and 20 March 1970 respectively, the Governments of the United Kingdom of Great Britain and Northern Ireland, the United States of America and the Union of Soviet Socialist Republics, which are designated as the Depositary Governments in Article IX. 2 of the Treaty on the Non-Proliferation of Nuclear Weapons, informed the Agency that the Treaty had entered into force on 5 March 1970.
2. The text of the Treaty, taken from a certified true copy provided by one of the Depositary Governments, is reproduced below for the convenience of all Members.

Treaty on the Non-proliferation of Nuclear Weapons

The States concluding this Treaty, hereinafter referred to as the "Parties to the Treaty".

Considering the devastation that would be visited upon all mankind by a nuclear war and the consequent need to make every effort to avert the danger of such a war and to take measures to safeguard the security of peoples, Believing that the proliferation of nuclear weapons would seriously enhance the danger of nuclear war.

In conformity with resolutions of the United Nations General Assembly calling for the conclusion of an agreement on the prevention of wider dissemination of nuclear weapons, Undertaking to co-operate in facilitating the application of International Atomic Energy Agency safeguards on peaceful nuclear activities.

Expressing their support for research, development and other efforts to further the application, within the framework of the International Atomic Energy Agency safeguards system, of the principle of safeguarding effectively the flow of source and special fissionable materials by use of instruments and other techniques at certain strategic points.

E.C. Morse, *Analytical Methods for Nonproliferation*, Advanced Sciences
and Technologies for Security Applications, DOI 10.1007/978-3-319-29731-6

Affirming the principle that the benefits of peaceful applications of nuclear technology, including any technological by-products which may be derived by nuclear-weapon States from the development of nuclear explosive devices, should be available for peaceful purposes to all Parties to the Treaty, whether nuclear-weapon or non-nuclear-weapon States.

Convinced that, in furtherance of this principle, all Parties to the Treaty are entitled to participate in the fullest possible exchange of scientific information for, and to contribute alone or in co-operation with other States to, the further development of the applications of atomic energy for peaceful purposes.

Declaring their intention to achieve at the earliest possible date the cessation of the nuclear arms race and to undertake effective measures in the direction of nuclear disarmament.

Urging the co-operation of all States in the attainment of this objective.

Recalling the determination expressed by the Parties to the 1963 Treaty banning nuclear weapon tests in the atmosphere, in outer space and under water in its Preamble to seek to achieve the discontinuance of all test explosions of nuclear weapons for all time and to continue negotiations to this end.

Desiring to further the easing of international tension and the strengthening of trust between States in order to facilitate the cessation of the manufacture of nuclear weapons, the liquidation of all their existing stockpiles, and the elimination from national arsenals of nuclear weapons and the means of their delivery pursuant to a Treaty on general and complete disarmament under strict and effective international control.

Recalling that, in accordance with the Charter of the United Nations, States must refrain in their international relations from the threat or use of force against the territorial integrity or political independence of any State, or in any other manner inconsistent with the Purposes of the United Nations, and that the establishment and maintenance of international peace and security are to be promoted with the least diversion for armaments of the world's human and economic resources.

Have agreed as follows:

Article I

Each nuclear-weapon State Party to the Treaty undertakes not to transfer to any recipient whatsoever nuclear weapons or other nuclear explosive devices or control over such weapons or explosive devices directly, or indirectly; and not in any way to assist, encourage, or induce any non-nuclear-weapon State to manufacture or otherwise acquire nuclear weapons or other nuclear explosive devices, or control over such weapons or explosive devices.

Article II

Each non-nuclear-weapon State Party to the Treaty undertakes not to receive the transfer from any transferor whatsoever of nuclear weapons or other nuclear explosive devices or of control over such weapons or explosive devices directly, or indirectly; not to manufacture or otherwise acquire nuclear weapons or other nuclear explosive devices; and not to seek or receive any assistance in the manufacture of nuclear weapons or other nuclear explosive devices.

Article III

1. Each Non-nuclear-weapon State Party to the Treaty undertakes to accept safeguards, as set forth in an agreement to be negotiated and concluded with the International Atomic Energy Agency in accordance with the Statute of the International Atomic Energy Agency and the Agency's safeguards system, for the exclusive purpose of verification of the fulfillment of its obligations assumed under this Treaty with a view to preventing diversion of nuclear energy from peaceful uses to nuclear weapons or other nuclear explosive devices. Procedures for the safeguards required by this Article shall be followed with respect to source or special fissionable material whether it is being produced, processed or used in any principal nuclear facility or is outside any such facility. The safeguards required by this Article shall be applied on all source or special fissionable material in all peaceful nuclear activities within the territory of such State, under its jurisdiction, or carried out under its control anywhere.
2. Each State Party to the Treaty undertakes not to provide: (a) source or special fissionable material, or (b) equipment or material especially designed or prepared for the processing, use or production of special fissionable material, to any non-nuclear-weapon State for peaceful purposes, unless the source or special fissionable material shall be subject to the safeguards required by this Article.
3. The safeguards required by this Article shall be implemented in a manner designed to comply with Article IV of this Treaty, and to avoid hampering the economic or technological development of the Parties or international co-operation in the field of peaceful nuclear activities, including the international exchange of nuclear material and equipment for the processing, use or production of nuclear material for peaceful purposes in accordance with the provisions of this Article and the principle of safeguarding set forth in the Preamble of the Treaty.
4. Non-nuclear-weapon States Party to the Treaty shall conclude agreements with the International Atomic Energy Agency to meet the requirements of this Article either individually or together with other States in accordance with the Statute of the International Atomic Energy Agency. Negotiation of such agreements shall commence within 180 days from the original entry into force of this Treaty. For States depositing their instruments of ratification or accession after the 180-day period, negotiation of such agreements shall commence not later than the date of such deposit. Such agreements shall enter into force not later than eighteen months after the date of initiation of negotiations.

Article IV

1. Nothing in this Treaty shall be interpreted as affecting the inalienable right of all the Parties to the Treaty to develop research, production and use of nuclear energy for peaceful purposes without discrimination and in conformity with Articles I and II of this Treaty.
2. All the Parties to the Treaty undertake to facilitate, and have the right to participate in. the fullest possible exchange of equipment, materials and scientific and technological information for the peaceful uses of nuclear energy. Parties to the Treaty in a position to do so shall also cooperate in contributing alone or together with other States or international organizations to the further development of the applications of nuclear energy for peaceful purposes, especially in the territories of non-nuclear-weapon States Party to the Treaty, with due consideration for the needs of the developing areas of the world.

Article V

Each Party to the Treaty undertakes to take appropriate measures to ensure that, in accordance with this Treaty, under appropriate international observation and through appropriate international procedures, potential benefits from any peaceful applications of nuclear explosions will be made available to non-nuclear-weapon States Party to the Treaty on a non-discriminatory basis and that the charge to such Parties for the explosive devices used will be as low as possible and exclude any charge for research and development. Non-nuclear weapon States Party to the Treaty shall be able to obtain such benefits, pursuant to a special international agreement or agreements, through an appropriate international body with adequate representation of non-nuclear-weapon States. Negotiations on this subject shall commence as soon as possible after the Treaty enters into force. Non-nuclear-weapon States Party to the Treaty so desiring may also obtain such benefits pursuant to bilateral agreements.

Article VI

Each of the Parties to the Treaty undertakes to pursue negotiations in good faith on effective measures relating to cessation of the nuclear arms race at an early date and to nuclear disarmament, and on a treaty on general and complete disarmament under strict and effective international control.

Article VII

Nothing in this Treaty affects the right of any group of States to conclude regional treaties in order to assure the total absence of nuclear weapons in their respective territories.

Article VIII

1. Any Party to the Treaty may propose amendments to this Treaty. The text of any proposed amendment shall be submitted to the Depositary Governments which shall circulate it to all Parties to the Treaty. Thereupon, if requested to do so by one-third or more of the Parties to the Treaty, the Depositary Governments shall convene a conference, to which they shall invite all the Parties to the Treaty, to consider such an amendment.
2. Any amendment to this Treaty must be approved by a majority of the votes of all the Parties to the Treaty, including the votes of all nuclear-weapon States Party to the Treaty and all other Parties which, on the date the amendment is circulated, are members of the Board of Governors of the International Atomic Energy Agency. The amendment shall enter into force for each Party that deposits its instrument of ratification of the amendment upon the deposit of such instruments of ratification by a majority of all the Parties, including the instruments of ratification of all nuclear-weapon States Party to the Treaty and all other Parties which, on the date the amendment is circulated, are members of the Board of Governors of the International Atomic Energy Agency. Thereafter, it shall enter into force for any other Party upon the deposit of its instrument of ratification of the amendment.
3. Five years after the entry into force of this Treaty, a conference of Parties to the Treaty shall be held in Geneva, Switzerland, in order to review the operation of this Treaty with a view to assuring that the purposes of the Preamble and the provisions of the Treaty are being realised. At intervals of five years thereafter. a majority of the Parties to the Treaty may obtain, by submitting a proposal to this effect to the Depositary Governments, the convening of further conferences with the same objective of reviewing the operation of the Treaty.

Article IX

1. This Treaty shall be open to all States for signature. Any State which does not sign the Treaty before its entry into force in accordance with paragraph 3 of this Article may accede to it at any time.
2. This Treaty shall be subject to ratification by signatory States. Instruments of ratification and instruments of accession shall be deposited with the Governments of the United Kingdom of Great Britain and Northern Ireland, the Union of Soviet

Socialist Republics and the United States of America, which are hereby designated the Depositary Governments.

3. This Treaty shall enter into force after its ratification by the States, the Governments of which are designated Depositaries of the Treaty, and forty other States signatory to this Treaty and the deposit of their instruments of ratification. For the purposes of this Treaty, a nuclear weapon State is one which has manufactured and exploded a nuclear weapon or other nuclear explosive device prior to 1 January, 1967.
4. For States whose instruments of ratification or accession are deposited subsequent to the entry into force of this Treaty, it shall enter into force on the date of the deposit of their instruments of ratification or accession.
5. The Depositary Governments shall promptly inform all signatory and acceding States of the date of each signature, the date of deposit of each instrument of ratification or of accession, the date of the entry into force of this Treaty, and the date of receipt of any requests for convening a conference or other notices.
6. This Treaty shall be registered by the Depositary Governments pursuant to Article 102 of the Charter of the United Nations.

Article X

1. Each Party shall in exercising its national sovereignty have the right to withdraw from the Treaty if it decides that extraordinary events, related to the subject matter of this Treaty, have jeopardized the supreme interests of its country. It shall give notice of such withdrawal to all other Parties to the Treaty and to the United Nations Security Council three months in advance. Such notice shall include a statement of the extraordinary events it regards as having jeopardized its supreme interests.
2. Twenty-five years after the entry into force of the Treaty, a conference shall be convened to decide whether the Treaty shall continue in force indefinitely, or shall be extended for an additional fixed period or periods. This decision shall be taken by a majority of the Parties to the Treaty.

Article XI

This Treaty, the English, Russian, French, Spanish and Chinese texts of which are equally authentic, shall be deposited in the archives of the Depositary Governments. Duly certified copies of this Treaty shall be transmitted by the Depositary Governments to the Governments of the signatory and acceding States.

IN WITNESS WHEREOF the undersigned, duly authorised, have signed this Treaty. DONE in triplicate, at the cities of London, Moscow and Washington, the first day of July, one thousand nine hundred and sixty-eight.

Appendix B
The Atomic Energy Act

The AEA, as amended, sets forth the procedures and requirements for the U.S. governments negotiating, proposing, and entering into nuclear cooperation agreements with foreign partners. The AEA, as amended, requires that U.S. peaceful nuclear cooperation agreements contain the following nine provisions:

1. Safeguards: Safeguards, as agreed to by the parties, are to be maintained over all nuclear material and equipment transferred, and all special nuclear material used in or produced through the use of party, irrespective of the duration of other provisions in the agreement or whether the agreement is terminated or suspended for any reason. Such safeguards are known as “safeguards in perpetuity.”
2. Full-scope IAEA safeguards as a condition of supply: In the case of non-nuclear weapons states, continued U.S. nuclear supply is to be conditioned on the maintenance of IAEA full-scope safeguards over all nuclear materials in all peaceful nuclear activities within the territory, under the jurisdiction, or subject to the control of the cooperating party.
3. Peaceful use guaranty: The cooperating party must guarantee that it will not use the transferred nuclear materials, equipment, or sensitive nuclear technology, or any special nuclear material produced through the use of such, for any nuclear explosive device, for research on or development of any nuclear explosive device, or for any other military purpose.
4. Right to require return: An agreement with a non-nuclear weapon state must stipulate that the United States has the right to require the return of any transferred nuclear materials and equipment, and any special nuclear material produced through the use thereof, if the cooperating party detonates a nuclear device, or terminates or abrogates an agreement providing for IAEA safeguards.
5. Physical security: The cooperating party must guarantee that it will maintain adequate physical security for transferred nuclear material and any special nuclear material used in or produced through the use of any material, or production or utilization facilities transferred pursuant to the agreement.
6. Retransfer rights: The cooperating party must guarantee that it will not transfer any material, Restricted Data, or any production or utilization facility transferred

E.C. Morse, *Analytical Methods for Nonproliferation*, Advanced Sciences and Technologies for Security Applications, DOI 10.1007/978-3-319-29731-6

pursuant to the agreement,or any special nuclear material subsequently produced through the use of any such transferred material, or facilities, to unauthorized persons or beyond its jurisdiction or control, without the consent of the United States.

7. Restrictions on enrichment or reprocessing of U.S.-obligated material: The cooperating party must guarantee that no material transferred, or used in, or produced through the use of transferred material or production or utilization facilities, will be reprocessed or enriched, or with respect to plutonium, uranium- 233, HEU, or irradiated nuclear materials, otherwise altered in form or content without the prior approval of the United States.
8. Storage facility approval: The cooperating party must guarantee not to store any plutonium, uranium-233, or HEU that was transferred pursuant to a cooperation agreement, or recovered from any source or special nuclear material transferred, or from any source or special nuclear material used in a production facility or utilization facility transferred pursuant to the cooperation agreement, in a facility that has not been approved in advance by the United States.
9. Additional restrictions: The cooperating party must guarantee that any special nuclear material, production facility, or utilization facility produced or constructed under the jurisdiction of the cooperating party by or through the use of transferred sensitive nuclear technology, will be subject to all the requirements listed above.

Appendix C
The Area Under the ROC Curve for Gaussian Probability Distributions

The formula for the area under the curve (AUC) for a receiver operator characteristic (ROC) derived from gaussian probability distributions is derived here.

Let the probability distribution of the positives be given by

$$p(x) = \frac{1}{\sqrt{2\pi}\sigma_1} \exp\left(-\frac{(\mathrm{x} - \mu_1)^2}{2\sigma_1^2}\right)$$

Note that $\int_{-\infty}^{+\infty} \mathrm{p(x)dx} = 1$.

Similarly, let the probability distribution of the negatives be given by

$$\mathrm{n(x)} = \frac{1}{\sqrt{2\pi}\sigma_2} \exp\left(-\frac{(x - \mu_2)^2}{2\sigma_2^2}\right)$$

The true positive rate TPR(x) is given by the integral of the positive rate from the threshold x to infinity, i.e.

$$\begin{aligned}\mathrm{TPR(x)} &= \int_{\mathrm{x}}^{\infty} \mathrm{p(x')dx'} \\ &= \tfrac{1}{\sqrt{2\pi}\sigma_1} \int_{\mathrm{x}}^{\infty} \exp\left(-\frac{(\mathrm{x}' - \mu_1)^2}{2\sigma_1^2}\right)\mathrm{dx}' \\ &= \tfrac{1}{2}\mathrm{erfc}\left(\tfrac{\mathrm{x} - \mu_1}{\sqrt{2}\sigma_1}\right)\end{aligned}$$

and the false positive rate FPR(x) is given similarly by

$$\begin{aligned}\mathrm{FPR(x)} &= \int_{\mathrm{x}}^{\infty} \mathrm{n(x')dx'} \\ &= \tfrac{1}{2}\mathrm{erfc}\left(\tfrac{\mathrm{x} - \mu_2}{\sqrt{2}\sigma_2}\right)\end{aligned}$$

E.C. Morse, *Analytical Methods for Nonproliferation*, Advanced Sciences and Technologies for Security Applications, DOI 10.1007/978-3-319-29731-6

The area under the curve (AUC) is given by

$$
\begin{aligned}
\mathrm{AUC} &= \int_0^1 \mathrm{TPR}\ |\mathrm{d(FPR)}| \\
&= \int_{-\infty}^{+\infty} \mathrm{TPR(x)} \left| \frac{\mathrm{d(FPR(x))}}{\mathrm{dx}} \right| \mathrm{dx} \\
&= \int_{-\infty}^{+\infty} \mathrm{TPR(x)n(x)dx} \\
&= \int_{-\infty}^{+\infty} \frac{1}{2}\mathrm{erfc}\left(\frac{\mathrm{x}-\mu_1}{\sqrt{2}\sigma_1}\right) \left[\frac{1}{\sqrt{2\pi}\sigma_2} \exp\left(-\frac{(\mathrm{x}-\mu_2)^2}{2\sigma_2^2}\right)\right] \mathrm{dx}
\end{aligned}
$$

This integral is essentially a double integral, since erfc is an integral over a gaussian. We deal with this by replacing the function erfc with a substitution

$$
\mathrm{erfc}\left(\frac{\mathrm{x}-\mu_1}{\sqrt{2}\sigma_1}\right) = -\frac{2}{\sqrt{\pi}} \int_0^{+\infty} \exp\left(-\left(\frac{\mathrm{x}-\mu_1}{\sqrt{2}\sigma_1} - \mathrm{x}'\right)^2\right) \mathrm{dx}' + 2
$$

The AUC integral contains two terms; call them I_1 and I_2, with I_2 standing for the part of the above expression for the AUC with the $+2$ term in the above expression for erfc, and I_1 representing the part with the double integral. I_2 integrates easily:

$$
\mathrm{I}_2 = \int_{-\infty}^{+\infty} \frac{1}{2}(2) \left[\frac{1}{\sqrt{2\pi}\sigma_2} \exp\left(-\frac{(\mathrm{x}-\mu_2)^2}{2\sigma_2^2}\right)\right] \mathrm{dx} = 1.
$$

The other term results in a double integral

$$
\begin{aligned}
\mathrm{I}_1 = -\frac{1}{2}\frac{2}{\sqrt{\pi}} \int_{-\infty}^{+\infty} &\left[\int_0^{+\infty} \exp\left(-\left(\frac{\mathrm{x}-\mu_1}{\sqrt{2}\sigma_1} - \mathrm{x}'\right)^2\right) \mathrm{dx}'\right] \\
&\times \left[\frac{1}{\sqrt{2\pi}\sigma_2} \exp\left(-\frac{(\mathrm{x}-\mu_2)^2}{2\sigma_2^2}\right)\right] \mathrm{dx}
\end{aligned}
$$

Both integrals have fixed end points, so the order of integration can be reversed:

$$
\begin{aligned}
\mathrm{I}_1 = -\frac{1}{2}\frac{1}{\sqrt{2\pi}\sigma_2}\frac{2}{\sqrt{\pi}} \int_0^{+\infty} \int_{-\infty}^{+\infty} &\left[\exp\left(-\left(\frac{\mathrm{x}-\mu_1}{\sqrt{2}\sigma_1} - \mathrm{x}'\right)^2\right)\right] \\
&\times \left[\exp\left(-\frac{(\mathrm{x}-\mu_2)^2}{2\sigma_2^2}\right)\right] \mathrm{dx}\,\mathrm{dx}'
\end{aligned}
$$

We can evaluate the inner integral by completing the square. The result is

$$
\mathrm{I}_1 = \frac{\sigma_1}{\sqrt{\pi}\sqrt{\sigma_1^2+\sigma_2^2}} \int_0^{\infty} \exp\left[-\frac{\mathrm{x}'^2\sigma_1^2}{\sigma_1^2+\sigma_2^2} - \frac{\mathrm{x}'\left(2\sqrt{2}\mu_1\sigma_1 - 2\sqrt{2}\mu_2\sigma_1\right)}{2\left(\sigma_1^2+\sigma_2^2\right)} - \frac{\mu_1^2 - 2\mu_2\mu_1 + \mu_2^2}{2\left(\sigma_1^2+\sigma_2^2\right)}\right] \mathrm{dx}'
$$

And this gives

$$\mathrm{AUC} = \mathrm{I}_1 + \mathrm{I}_2 = 1 - \frac{1}{2}\mathrm{erfc}\left(\frac{\mu_1 - \mu_2}{\sqrt{2}\sqrt{\sigma_1^2 + \sigma_2^2}}\right) = \frac{1}{2} + \frac{1}{2}\mathrm{erf}\left(\frac{\mu_1 - \mu_2}{\sqrt{2}\sqrt{\sigma_1^2 + \sigma_2^2}}\right)$$

or equivalently

$$\mathrm{AUC} = \frac{1}{2}\mathrm{erfc}\left(-\frac{\mu_1 - \mu_2}{\sqrt{2}\sqrt{\sigma_1^2 + \sigma_2^2}}\right).$$

Glossary

Actinide Elements with atomic number between 89 and 103

Adsorption A process where a gas, liquid or dissolved solid adheres to a surface

Alpha emission spectroscopy Analysis of a sample by the energy distrubution of alpha particles

Areal density The product of mass density and thickness

Asymptotic Limits of functions at extreme values of parameters

Avogadro's constant Number of atoms in a gram-mole $= 6.02 \times 10^{23}$

Boltzmann law Equation relating density and pressure variations with potential energy in thermodynamic equilibrium

Boltzmann transport equation An equation describing the movement of particles in velocity space, physical space, and time

Boltzmann's constant Constant relating average energy and temperature in a gas or plasma

Boosting Weapon yield enhancement by use of fusion reactions

Bragg equation An equation showing the X-ray diffraction angles in X-ray in a crystal

Breit-Wigner form A model of the energy dependence of a resonant state in an atom or nucleus

Bremsstrahlung Radiation produced by the interaction of electrons with atomic nuclei

Bridgman method A crystal-growing method in which a melting zone travels slowly through the powder charge

Brunt-Väisälä frequency A frequency of stable oscillation in the atmosphere caused by buoyancy

Burnup Consumption of fissile material due to fission reactions

BWR Boiling Water Reactor

Calcines Heating a solid material to drive off water, oxygen, and other gases

Carbogenic molecular sieve Molecular sieve containing folded graphite or other carbon-based structure

Cerenkov effect Production of light be electrons in a medium where the electrons are traveling faster than the light speed in that medium

E.C. Morse, *Analytical Methods for Nonproliferation*, Advanced Sciences and Technologies for Security Applications, DOI 10.1007/978-3-319-29731-6

Child-Langmuir limit Limit of current in a beam of charged particles due to electrostatic space charge

Compton collisions Elastic collisions between electrons and photons

Compton kinematic discrimination Algorithm to use Compton-scattetred photons to generate a two-dimensional image

Compton upshift Production of high-energy photons by interaction of low energy photons with an electron beam

Convolving Taking an integration of a source term with a propagation function

Core valence luminescence Radiative recombination of holes in the upper core band into the valence band

Coriolis forces Force acting on a moving object in a rotating system

Cosmogenic Created by interaction of airborne and surface nuclei with cosmic rays

Coulombic forces Repulsive electrostatic forces between nuclear particles

Démarche An official diplomatic protest or request

De-excitation Return of a nucleus or atom to its ground, or lowest energy, state

Debye temperature A temperature in a solid equivalent to the energy of the highest vibrational state

Decoupled A condition where an underground nuclear explosion is not well connected to the surrounding rock

Desorption A process where a gas or liquid is released from a solid material

Deuteron photodissociation The splitting of a deuteron into a proton and a neutron

Die-away time Time for a reduction in neutron count rate by a factor of $\mathrm{e} = 2.718$

Dielectric constant The ratio of the electrical permittivity of a material to that of free space

Discrete ordinate methods Neutron transport equations using a rid in space and groups of energy and angle

Doppler broadening Increase in spectral line width due to random thermal motion

Doppler shift A shift in frequency of a wave caused by the velocity of the generator or observer

e-folding The time or distance for a signal to be attenuated by a factor of $\mathrm{e} = 2.718$

Eikonal A theory of wave propagation which assumes that changes in the medium happen slowly

Electron Capture Capture of an electron by an atomic nucleus

Eutectoid A material that has two distinct phases coming lead together

Even-even actinides Actinides with an even number of both protons and neutrons

Exciton A quantum-mechanical state in which an electronhole pair travel together

Fano factor Reduction in statistical variance due to collective effects

Faraday cups Electrodes for collecting charged particles

Fermat's principle A principle that says that the path that a wave will take is the one which takes the minimum time

Fermi age model A method of treating the slowing down of fast neutrons to thermal energies

Fick's law Equation relating diffusive flux to concentration gradient

Fractionation Changes in elemental concentrations due to variations in transport properties

Fuel shuffle Movement of fuel rods in a reactor to even out the burnup

Gamma-ray spectroscopy Identification of nuclei through gamma-ray emissions

Gaussian distribution Limiting form of a Poisson distribution when the mean becomes large

Graphite-moderated reactor A reactor using graphite to slow fission neutrons to thermal energies

Green body An intermediate phase of creating a ceramic

Green's function kernel An expression used to solve a differential equation with a source term

Hecht equation An equation describing the efficiency of charge collection in a semiconductor

Heisenberg relation An expression for the uncertainty of the positionmomentum product or the energy time product and Planck's constant $\hbar$

High-Z elements Elements with a high atomic number, such as U or Pb

Highly enriched uranium Uranium containing more that 20 % ^{235}U

Histogram A plot of the number of events observed for each measurement value

Hot isostatic press A method to increase the density of a material by using heat and pressure, usually with an inert gas

Hydroacoustic Acoustic wave traveling through water

Hygroscopic Prone to absorb water

Indium resonance energy The energy at which a large cross section for capture exists in indium at 1.46 eV

Inverse barns Fluence in units of 10^{+24} cm^{-2}

Jacobi symbol A mathematical operator on two integers that returns a single integer

Kalinowski line A line in Xe isotope ratio space separating reactor produced Xe from nuclear explosive produced Xe

Lagrangian fluid model A fluid description where the coordinate system moves with the fluid

Lamb wave An atmospheric wave which is localized to the earth's surface

Laplacian operator $\frac{\partial^2}{\partial x^2} + \frac{\partial^2}{\partial y^2} + \frac{\partial^2}{\partial z^2}$

Laser wakefield acceleration Production of high-energy particles by intense laser pulses

Love wave A wave located near the surface of a solid or liquid with a motion perpendicular to the direction of travel and in the plane of the surface

Mach number Ratio of velocity to speed of sound

Mass attenuation coefficient Gamma attenuation coefficient divided by mass density

Mass spectrometry Analysis of a sample by the atomic mass distribution in the material

Matthews correlation coefficient Metric for the quality of a binary qualifier

Maxwellian An energy distribution following Maxwell-Boltzmann statistics, i.e. $\mathrm{f(E)}\ \alpha\sqrt{\mathrm{E}}\mathrm{exp}(-\mathrm{E}/\mathrm{T})$

Millibarn 10^{-27} cm^2

Miscibility The ability of two substances to exist in solution together

Monte Carlo Computational method based on random numbers

Natural abundance The fraction of an isotope of an element that is found naturally compared to all isotopes of that element

Nebulizer Device for making fog-like mixtures

Neutron capture Capture of a neutron by an atomic nucleus

Odd-odd nuclide A nuclide with an odd number of both protons and neutrons

Orbital states Energy states in an atom

Pig Shieldded container for radioactive materials

Poisson distribution Distribution expected for any number of uncorrelated events

PWR Pressurized Water Reactor

Quaternary Having four distinct parts

Radioxenon radioactive xenon isotopes

Rayleigh wave A wave located near the surface of a solid or liquid with an elliptical motion

RMS thermal velocity The root-mean-square average velocity of particles at some temperature

Roentgen Unit of radiation exposure, roughly equal to rads

Saggital focusing double Laue monochromator A device used in X-ray diffraction analysis

Scintillation detector A radiation detector based on conversion of nuclear particles or gamma rays into low-energy photons

Self-attenuation Absorption of gamma rays or particles within the material generating them

Sintered Conversion of a material into a high-density format using heat and pressure

SOFAR channel Acoustic waveguide in seawater at 500–1000 m depth

Solid-state germanium detectors Radiation detectors based on conversion of gamma rays into electron-hole pairs in germanium

Spallation Breakup of nuclei by energetic particles

Species One isotope of an element

Spline Connection of data points using smooth algebraic functions

Sterradian Unit of solid angle $= \int \mathrm{d}\cos\theta\,\mathrm{d}\phi$

Stoichiometric coefficient The subscripts in a chemical formula showing the number of atoms per molecule

Sublimation Conversion of a substance from a solid to a gas without an intermediate liquid phase

Surface-barrier semiconductor diode detectors Detectors used for α counting with a metallic contact on the back side and no diffused n-type layer

T-phase seismic wave Seismic wave resulting from a hydroacoustic wave

Ternary Having three distinct parts

Thermal neutron cross sections Neutron cross sections averaged over a thermal energy spectrum

Torr Unit of pressure equal to one mm Hg. 1.0 atm $\approx$ 760 torr

Vitrified Converted into a glass-like substance

Wavenumber $2\pi/\lambda$, where λ is the wavelength

WGU Weapon Grade Uranium; enriched to $>90\,\%$ ^{235}U

Yukawa kernel An alternative to the Fermi age model useful for hydrogenous media

Index

E.C. Morse, *Analytical Methods for Nonproliferation*, Advanced Sciences and Technologies for Security Applications, DOI 10.1007/978-3-319-29731-6